Politecnico di Torino

ScuDo
Scuola di Dottorato ~ Doctoral School
WHAT YOU ARE, TAKES YOU FAR

Doctoral Dissertation
Doctoral Program in Physics (36^{th}cycle)

Electric field effect on magnetic interface phenomena

By

Adriano Di Pietro

******

Supervisor(s):
Dr. G. Durin, Supervisor

Doctoral Examination Committee:
Prof. Rocío Yanes Díaz , Referee, Universidad de Salamanca
Prof. Salvatore Perna , Referee, Università degli studi di Napoli
Prof. E.F, Politecnico di Torino
Prof. G.H, Politecnico di Torino
Prof. I.J, Politecnico di Torino

Politecnico di Torino
2024

Declaration

I hereby declare that, the contents and organization of this dissertation constitute my own original work and does not compromise in any way the rights of third parties, including those relating to the security of personal data.

Adriano Di Pietro
2024

* This dissertation is presented in partial fulfillment of the requirements for **Ph.D. degree** in the Graduate School of Politecnico di Torino (ScuDo).

"A Anna ed Ezio, i miei meravigliosi nonni"

Acknowledgements

Writing these acknowledgements has been a great challenge for me as I realized that, the more i thought about them, the more the simple message of gratitude at the bottom of it all got corrupt.

I'll try to just go with the feeling:

My first thought runs to Nonna Anna and Nonno Ezio: I started this path with you 2 guys by my side and sadly, I cannot walk with you through end line. I just wanted to tell you that all your sacrifices have led to my best life and for this you have my never ending gratitude. I also thank my family Paola, Enrico and Flavio whom with never ending support, gave me the tools follow all my dreams without fear.

My mind immediately goes to Ilaria, who blessed me with her incredible support along this admittedly difficult road. Words stop being useful pretty soon when describing your impact on basically everything. From the deepest part of my heart: thank you.

I'd like of course to thank the whole group at INRIM, starting with my Supervisor Gianfranco Durin: thanks for giving me the chance to be part of this awesome project and for the support throughout! Special thanks to Alessandro Sola and Alessandro Magni for the countless coffee breaks talking life, science and everything in between. A huge thank you to Vittorio Basso and Patrizio Ansalone for blessing me with some extremely deep physics talks. These discussions are truly at the heart of what a PhD should be.

A huge thank you goes to Prof. Silvia Picozzi and all the SPIN group in Chieti, composed by Lei Qiao, Baishun Yang and Srdjan Stavrić. You guys helped me close so many gaps in my DFT knowledge! A special mention to Silvia and Lei for saving

one of my papers from certain disaster! It meant much more to me than you probably realize.

I must of course thank all the colleagues of the MagnEFi ITN which was brilliantly coordinated by Liza Herrera and Clare Desplats. Some of my fondest memories during these 3 years are with you guys, from the Turin Meeting to the Crete Conference... What a ride together! I have of course to add a special mention to Rohit, Gyan, Adrien and Mouhad for making me feel at home even when I was far away from mine. Closely related to this: my deep gratitude also goes to Liza Herrera, Felipe Garcìa-Sànchez, Luis Lopez-Diaz and Reinoud Lavrijsen for having me hopping around your labs and sharing a lot of time and knowledge with me. I cannot close this small paragraph without mentioning my dear friend Giovanni, whom I really wish all the best for his bright future even though he cursed our MagnEFi group chat with one of the most vile memes I have ever witnessed: thanks for ruining Harry Potter for everyone.

I think with a message like this, less is more and therefore I stop here. Thanks to everyone for making this a truly incredible journey.

Abstract

Understanding the principles governing the electrical manipulation of magnetization properties in materials is crucial for the advancement of magnetic memory devices. This Dissertation investigates the direct and indirect effects of electric fields on magnetic interface phenomena, spanning scales from the atomistic to the micromagnetic level.

In order to have a solid starting place to understand the results of this dissertation, we spend some time to establish a theoretical background both on the microscopic (atomistic) scale as well as on the micrometer scale.

Special attention is given to the pivotal role of spin-orbit coupling in contemporary magnetism research landscape, with special emphasis on magneto-crystalline anisotropy and chiral exchange interactions such as Dzyaloshinskii-Moriya interaction. We also discuss current research into innovative electrical methods for altering these crucial aspects of magnetism.

After having laid the theoretical foundations of magnetism on these different length scales, we discuss some of the main numerical aspects of 2 pillars of modern computational material science, namely density functional theory and micromagnetism.

In the result section, we start by discussing some experimental observations on the multilayer Ta/$Co_{20}Fe_{60}B_{20}$/HfO_2 and the discovery of so called "multiple magneto-ionic regimes", i.e. different reversibility regimes of the magnetization reversal process in response to the application of an electric field at this particular ferromagnet/oxide interface.

We follow up by showing ab initio calculations delving deeper in the microscopic mechanism governing this behavior. We discuss a plausible explanation for this behavior by closely inspecting the different effects Oxygen can have on the

magneto-crystalline anisotropy of the material depending on its precise positioning and penetration depth.

Departing from the atomistic approach, the thesis introduces a micromagnetic formulation inspired by non-abelian field theories, facilitating a compact matrix notation for DMI and Kitaev exchange interactions in arbitrary crystallographic point groups.

In the final part of the thesis we implement the matrix notation of the DMI tensors in collective coordinate models to efficiently describe the static and dynamic properties of magnetic domain walls in nanowires with perpendicular magnetic anisotropy. In doing so we discover a highly non trivial interplay of the different DMI tensor components (diagonal, antisymmetric and symmetric traceless) in the canting angle response of the domain wall to an in plane field. We also discover a non-linear enhancement of the Walker breakdown field in the presence of some combinations of Dzyaloshinskii-Moriya tensor components and propose systems with S_4 symmetry as promising candidates to experimentally display our theoretically formulated predictions.

Contents

List of Figures **xiii**

List of Tables **xxvi**

Nomenclature **xxvii**

1 Introduction **1**

1.1 How is memory stored today? 1

1.2 What about tomorrow? The end of Moore's Law 2

1.3 Tomorrows data storage technology 3

1.3.1 What is Spintronics? 3

1.3.2 Where is Spintronics in today's memory storage market? . . 4

1.3.3 Electric field control of interfacial magnetism 6

1.4 The approach used in this dissertation 7

1.5 Outline of the dissertation 9

2 Theoretical Background **11**

2.1 Microscopic models for magnetic order 11

2.1.1 The Hubbard model 12

2.2 Going beyond the Heisenberg model 19

2.2.1 Spin-orbit coupling: a small effect at the base of magnetism as we know it . . . 19
2.3 Microscopic origin of magneto-crystalline anisotropy . . . 23
2.3.1 SOC as the source of magneto-crystalline anisotropy . . . 23
2.3.2 Origin of orbital magnetic moment anisotropy in 3*d* transition metals . . . 32
2.3.3 Interfacial perpendicular magnetic anistoropy at ferromagnet/oxide interfaces . . . 34
2.3.4 Magneto-ionic control of interfacial magnetism . . . 35
2.3.5 Recent advances in magneto-ionic research . . . 37
2.4 Chiral interactions: Extended Heisenberg model . . . 38
2.4.1 Microscopic origin of DMI . . . 39
2.4.2 An overview of DMI materials . . . 43
2.4.3 Direct and indirect electric field control of DMI . . . 47
2.4.4 Conclusion . . . 48

3 The continuum limit: Micromagnetism 52

3.1 Exchange energy density . . . 53
3.1.1 The Dzyaloshinskii-Moriya Interaction . . . 60
3.2 Magnetic Anisotropy . . . 62
3.3 The micromagnetic energy functional and the variational principle . 68
3.3.1 Variational principle for the DMI term . . . 70
3.4 Magnetism in lower dimensions: interfacial effects . . . 72
3.4.1 Magnetic ordering in low dimensional magnetic systems . . 72
3.4.2 Magnetic anisotropy in low dimensions . . . 74
3.4.3 The interfacial Dzyaloshinskii-Moriya interaction . . . 75
3.4.4 Characteristic scales in micromagnetism . . . 80
3.5 The Landau-Lifshitz Gilbert equation . . . 81

3.6 Magnetic domain walls 85
3.6.1 Collective coordinate models 86
3.6.2 The Bloch profile 88
3.6.3 Dynamical equations for the DW - the $q-\phi-\Delta$ model . . . 91
3.6.4 Static configurations in the $q-\phi-\Delta$ model with chiral interactions 93
3.6.5 Field driven DW motion 97

4 The geometrization of micromagnetic exchange 101
4.1 A simple example of non trivial parallel transport 102
4.2 Global symmetries vs. local symmetries 103
4.2.1 Local vs. global symmetries for magnetic interactions . . . 106
4.3 Non trivial parallel transport and Heisenberg exchange 107

5 Computational Methods 111
5.1 The basics of density functional theory 111
5.1.1 The many-body Schrödinger equation 112
5.1.2 The Born Oppenheimer approximation 113
5.1.3 Density Functional Theory 114
5.1.4 The Hohenberg-Kohn Theorems 115
5.1.5 The Kohn-Sham equations 116
5.1.6 Ab initio methodology for magnetic exchange parameters . 122
5.2 Numerical principles for micromagnetic solvers 128
5.2.1 Discretizing the magnetization field 129
5.2.2 Finite difference version of the effective field terms 131

6 Results 134

6.1 Multiple magneto-ionic regimes in $Ta/Co_{20}Fe_{60}B_{20}/HfO_2$ . . . 135
6.1.1 Introduction . . . 135
6.1.2 Experimental setup . . . 136
6.1.3 Magneto-ionic Regimes I and II . . . 137
6.1.4 Discussion . . . 140
6.1.5 Conclusions . . . 144
6.2 Ab-initio study of magneto-ionic mechanisms in ferromagnet/oxide multilayers . . . 145
6.2.1 Introduction . . . 145
6.2.2 Methods and computational details . . . 147
6.2.3 Results . . . 151
6.2.4 Discussion . . . 153
6.2.5 Conclusion . . . 156
6.3 Gauge theory applied to magnetic lattices . . . 158
6.3.1 Introduction . . . 158
6.3.2 Continuum limit of Heisenberg exchange on arbitrary lattices . . . 160
6.3.3 Gauge covariant derivatives and the DMI tensor . . . 167
6.3.4 DMI tensor decomposition and ground state selection criterion 170
6.3.5 Discussion . . . 172
6.3.6 Conclusions . . . 174
6.4 Domain wall statics and dynamics in the presence of arbitrary Dzyaloshinskii-Moriya interaction tensors . . . 175
6.4.1 Energy density in the presence of arbitrary DMI tensors . . . 177
6.4.2 Collective coordinate models with arbitrary DMI . . . 179
6.4.3 In plane field driven DW titling in the presence of arbitrary DMI tensors . . . 182

6.4.4 Intrinsic DW tilting in the presence of D_b and D_s 186
6.4.5 Measuring D_a and D_s DMI contributions with IP fields . . . 188
6.4.6 Domain-wall dynamics in the presence of arbitrary DMI tensors 190
6.4.7 Conclusion 195

7 Summary of results and future outlook 197
7.1 Summary of results 197
7.2 Future outlook 198

References 202

Appendix A The limits of the Hubbard model 220
A.1 The non-interacting limit $U = 0$ 220
A.2 The non-hopping case $t = 0$ 221

Appendix B Quasi degenerate perturbation theory 223

Appendix C Moriya's derivation of DMI 227
C.1 The x-component 227
C.2 The y-component 229
C.3 The z-component 229

Appendix D The finite difference code to compute exotic DMI terms in thin films 231

List of Figures

1.1 Semi-logarithmic plot of the number of transistors on microchip as a function of the years. We can easily see how it has roughly doubled every 2 years since the 1950's. Reproduced from https://ourworldindata.org/. 3

1.2 Spin valve based on the GMR effect. The ferromagnetic layers are indicated by the "FM" label and the non-magnetic spacer by the "NM" label. As can be seen, depending on the relative orientation of the the magnetic layers, the spin polarized electrons experience different resistances. 4

1.3 Log-Log plot reporting the total write access time (ns) vs. the total write access energy (fJ) for different spintronics based device concepts: (SD) spin diffusion, (STT) spin-transfer-torque, (SHE) spin Hall effect, (DW) domain wall motion (ME) magnetoelectric switching, (IMA) in-plane magnetic anisotropy, (PMA) perpendicular magnetic anisotropy. The red star on the bottom right designates the preferred corned (i.e. low write access time and low energy requirements). Reproduced from [1]. 5

1.4 Comparison of several application-related features between the four types of (ME) switching. The terms in the first 2 rows represent, C: capacitance of the dielectric, V: the applied voltage, R: electrical resistance of the dielectric, t_0: duration of the voltage pulse. In the voltage controlled exchange scheme (i.e. the second column from the left), the heat dissipation arises from the leakage current and dielectric loss due to magnetic hysteresis. In this context we have P_s: switched polarization, V: critical voltage for polarization switching, A: electrode area. We highlight how charge accumulation effects, despite promising in almost all aspects (fast, reliable, scalable), unfortunately display a very small ME coefficient α_E, therefore requiring very high fields for application. Figure re-adapted from [2]. 8

1.5 Different length scales and corresponding salient features of magnetism. Reproduced from [3] 9

2.1 Graphical representation of a Hubbard lattice. We display the 2 competing interactions of kinetic energy (t) and Coulomb repulsion (U). 15

2.2 Schematic representation of the hopping mechanism in the half filled lattice ($U/t \ll 1$ limit) of eq.(2.11) 16

2.3 Basics of Rashba spin-splitting (a) Non spin polarized band dispersion in the absence of Rashba SOC (b) Dispersion relation for a non-magnetic free electron gas in the presence of Rashba SOC (see eq.(2.40)) The blue and red parabolas represent the spin split bands. 22

2.4 Orbital momentum anisotropy in a crystal field with tetragonal symmetry. For simplicity, we assume large exchange splitting and consider only the minority spin band. The inclusion of SOC in lowest order perturbation theory (see 2.3.1) results in new states with anisotropic orbital magnetic moment (units of $\hbar$). The indicated orbital momenta for SQA alignment $\boldsymbol{S} \parallel z$-axis and $\boldsymbol{S} \parallel x-$ or $y-$axis results for only mixing spins in the minority band. Reproduced from [4] 32

2.5 (a) Layer-resolved orbital moment anisotropy ($\Delta\mu$) and magnetic anisotropy (MA) energy. Middle: Schematic representation of the crystalline structures calculated. Fe, Mg, and O are represented by large, medium, and small balls, respectively. (b) DOS with SOC for averaged out-of-plane ($d_{z^2-r^2}+d_{xz}+d_{yz}$) and IP Fe-3d orbitals ($d_{x^2-y^2}+d_{xy}$) for Fe at the interface (Fe5). Inset: a simple picture showing that PMA is produced by the hybridization of Fe out-of-plane orbitals ($d_{3z^2-r^2}$,d_{xz},d_{yz}) and O p_z orbitals. This hybridization leads to an uncompensated charge occupation in Fe in-plane orbitals ($d_{x^2-y^2}$,d_{xy}) and results in an enhanced out-of-plane orbital moment. Reproduced from [5] 36

2.6 Schematic representation of the favored magnetic order promoted by the different terms of the extended Heisenberg model of eq.(2.95). $J_{ij} \lessgtr 0$ represents antiferromagnetic or ferromagnetic order. $\boldsymbol{D}_{ij} \neq 0$ represents canted magnetic order as a consequence of DMI and $\overset{\leftrightarrow}{\Gamma}_{ij}$ represents 2 site anisotropy. 42

2.7 Schematic representation of the Moriya rules relating the local symmetries of a pair of spins $\boldsymbol{S}_A$ and $\boldsymbol{S}_B$ and the direction of the DMI. . 44

2.8 Relationship between crystal symmetry and microscopic DM vector. Sketch of the DM vector in a C_{2v} (a,c), C_{4v} (b) C_{3v} (d) and a C_4 symmetric unit cell (e). Mirror planes are indicated by the black dashed lines. Atoms in the top layer are indicated by blue circles while atoms in the bottom layer are indicated by smaller red circles. The green arrows on the bonds represent the DM vector while the orange arrows represent an effective micromagnetic DM vector (discussed at length later in 3.1.1) . We highlight how the C_{2v} case (a,c) is of particular interest as the Moriya rules in this case would allow for multichiral magnetisation configuration, i.e. winding magnetic structures with opposite Néel-type chirality. We also emphasize how the centrosymmetry of structure (e) forbids the presence of DM interaction. 45

2.9 Unit cell of MnSi which is part of the $P2_13$ space group. 45

2.10 Diagrammatic representation of a typical system displaying interfacial DMI. The exchange interaction between neighboring spins $\hat{\boldsymbol{S}}_i$ and $\hat{\boldsymbol{S}}_j$ is mediated by a heavy metal ion which introduces a strong SOC in the interfacial region. In accordance with the 5^{th} Moriya rule, the DM vector $\boldsymbol{D}_{ij}$ lies parallel to the vector $\boldsymbol{r}_i \times \boldsymbol{r}_j$. 47

2.11 Correlation between DMI and the electric surface dipole moment. In panel (a), the planar averaged charge density difference $\Delta\rho(z)$ is illustrated for O absorption on Fe/Ir(011) across various oxygen coverages. The dashed red, blue, and gray lines depict the approximate equilibrium positions of the O, Fe, and topmost Ir atoms on the fully relaxed surface. In panel (b), the relationship between O coverage and the alterations in the surface dipole moment, DMI, and (c) relative Fermi energy is explored. (d-e) Isosurface plot of the charge density difference $\Delta\rho(z)$ for a coverage of 0.25 (d) and 0.75 ML (e), with blue and red isosurfaces indicating areas of charge accumulation and depletion respectively. Reproduced from[6]. . . . 49

2.12 (a) Schematic representation of the setup composed of a Ta/CoFeB/TaOx trilayer with the additional ZrO_2 layer and Indium Tin oxide (ITO) electrode. (b) Schematic cross section of the sample. (c) iDMI measured with Brillouin light scattering (BLS) vs. top Ta-thickness. (d,e) MOKE images of current skyrmion induced motion (CIM) at zero applied gate voltage. (g,h) MOKE images of skyrmion current induced motion (CIM) at $V_g = +3.5V$ applied gate voltage. The in plane current density is represented by the white arrow and the out of plane magnetic field of $\mu_0 H_z = 80$ μT. In the initial state (d,e), skyrmions move in the direction of the current indicating CW chirality ($D < 0$). Under positive gate voltage, the skyrmions move against the current density direction, indicating a CCW chirality ($D > 0$). (f,g) Schematic representation of CW and CCW skyrmions. Reproduced from [7] 50

3.1 Schematic representation of them micromagnetic limit. The magnetization inside the cells is averaged and considered constant. The details of the atomic structure are neglected. 54

3.2 Depiction of the incidence matrix of an undirected graph (left) and the edge-node incidence matrix of a directed graph (right) 57

3.3 Simple cubic (SC) nearest neighbors cluster represented as a directed graph 59

3.4 Magnetic anisotropy energy landscapes: (a) isotropic (b) *easy-axis* anisotropy along z (c) *easy-plane* anisotropy in the $x-y$ plane (d) *easy-cone* anisotropy (e-f) sixth order anisotropy energy landscapes. Readapted from [8]. 63

3.5 Schematic representation of how the division in magnetic domains is a means to minimize the presence of magnetic surface and volume charges. The demagnetizing field stabilizes configurations displaying flux closure. 66

3.6 Schematic representation of a thin film system. As can be seen the coordination number is decreased in the surface layers 73

3.7 Projection of the magnetization vector $\boldsymbol{m}$ on the basal plane of chiral skyrmions and antiskyrmions in non-centrosymmetric ferromagnets. The m and γ parameters correspond to the ones reported in Tab.3.2. . 79

3.8 Illustration of the mechanical analogy of a spinning top of fixed length M_s pointing in the direction $\boldsymbol{m}$ precessing around the z-axis. The coordinates of the vector in the space-fixed reference frame are parameterized by the angles (θ, ϕ, ψ) and the body fixed frame $\{\hat{e}_1, \hat{e}_2, \hat{e}_3\}$ 83

3.9 Schematic representation of the precessional trajectory of the magnetization $\boldsymbol{m}$ around the effective field H_{eff} for the case (a) undamped precession (b) damped precession with Gilbert's assumption (eq.(3.102)) (c) damped precession with additional nutation motion as a consequence of inertial terms present in eq.(3.103) 84

3.10 Magnetic domains observed via Kerr microscopy. (a) Perspective view of the magnetic domains of an iron whisker. (b) Top view of the magnetic domains present in a NiFe thin film. Reproduced from [3]. 86

3.11 (a) untilted DW configuration in semi-infinite nanowire geometry (infinite length along x and finite width w along y). The collective coordinates needed to treat the dynamics of such a system are reported on the bottom and are the DW position q, the internal DW magnetization angle ϕ and the DW width Δ. (b) tilted DW configuration in a semi-infinite nanowire geometry. An additional collective coordinate is needed to treat the dynamics of such a system, namely the canting angle χ, ... 88

3.12 Depiction of the Bloch profile $\theta(x)$ as reported in eq.(3.114) 89

3.13 (a) Néel DWs (b) Bloch DWs 91

3.14 (a) Schematic of the tilted DW. (b) Micromagnetic configuration of a 100 nm wide track with DM D = 2 mJ/m^2 and a transverse magnetic field $H_y = 100$ mT. (c) DW tilt angle χ as a function of H_y for several values of D and (d) as a function of D for $H_y = 100$ mT. Dots are the results of micromagnetic simulations, whereas the continuous lines are the results of the collective coordinates model. Reproduced from [9] 95

3.15 (a) DW velocity as a function of the applied field in the presence (D = 0.5 mJ/m^2) and absence ((D = 0 mJ/m^2) of DMI. A clear shift in the Walker (red dashed line) field is visible for the case with present DMI. After Walker breakdown is achieved, the DW velocity drops down significantly (b) DW internal magnetisation angle $\Delta\phi$ as a function of applied field H_z in the presence (D = 0.5 mJ/m^2) and absence ((D = 0 mJ/m^2) of DMI. The dynamical equilibrium angle ϕ_0 is constant for higher values of the applied field in the case where DMI is present in the system. After H_w is reached, the DW motion starts precessing. Reproduced by [10]. 99

4.1 parallel transport of a vector on a curved surface along the path $A \to B \to C \to A$ 102

4.2 Diagrammatic representation the concept of parallel transport in the Heisenberg model while in the presence and absence of SOC. 108

5.1 Conceptual diagram showing the essential steps of the self-consistent calculation (scf), which is at the heart of all main DFT codes. 120

5.2 Exemplary case of the 4 state method for the calculation of the J_{12}^{zy} coefficient of the exchange matrix of eq.(6.19) 126

5.3 Exemplary case of the 4 state method for the calculation of the A_1^{zy} and the $A_1^{zz} - A_1^{yy}$ coefficients of the single ion anisotropy matrix of eq.(5.57) 128

5.4 Schematic representation of the material discretization used for micromagnetic simulations 129

6.1 Graphic representation of the magneto-ionic stack covered with the ionic liquid $[EMI]^+[TFSI]^-$ and the counter electrode made of ITO 137

6.2 Hall voltage response to the progressive oxidation induced upon exposure to a gate voltage G_V = -2 V. Different exposure times t drive the system from the initial state (IPA-(a)) through regime I (b) into PMA (c) and back to IPA through regime II (d). 138

6.3 Remanence as a function of gating time in (a) non-annealed (as-grown) samples under G_V = -2.3 V (circles), G_V = -2 V (squares) and G_V = -1.7 V (triangles). (b) Remanence as a function of gating time in samples annealed at 180 °C (half open square) and 350 °C (open squares) under G_V = -2 V. 140

6.4 (a) Hysteresis loops for the (irreversible) IPA $\rightarrow$ PMA transition under the application of $G_V = +4V$ in the first magneto-ionic regime. (b) First hysteresis loops for the PMA $\rightarrow$ IPA transition (solid line) and subsequent 10 cycles (dotted lines) in regime II. (c) Magnetic remanence as a function of the cycle number in regime II. 141

6.5 Proposed magneto-ionic mechanism for regimes I and II. (a) When $G_V < 0$, oxygen species migrate towards the ferromagnetic (CoFeB) layer. After a certain amount of time, PMA is achieved, indicating that some optimum in surface coverage has been achieved. (b) If $G_V < 0$ keeps being applied, oxygen species continue to be incorporated in the CoFeB layer, resulting in a gradual return to the IPA (Regime II), shown in (c). (d) If the voltage sign is reversed $G_V > 0$, mobile oxygen species can migrate back to the top electrode. For the same applied voltage G_V there is no reversibility in regime I ((b) towards (e)) while full reversibility is achieved in regime II ((c) toward (f)). 142

6.6 Sketch of the different interfacial configurations. Unit cells (I) and (II) represent Fe/O interfaces while unit cells (III) and (IV) represent the Fe/HfO_2 interfaces. 150

6.7 Magneto-crystalline anisotropy energy (MCAE) comparison of the pure Fe/HfO_2 interface (structures (III) and (IV)). The θ angle of the spin quantization axis (SQA) from eq.(6.2) is shown in the inset of (a). (a,b) MCAE for the ground state of the Fe/HfO_2 unit cell with frontal O-Fe distance of (a) $\Delta z_{(\text{O-Fe})} = 5.76$ a_B (equilibrium) and (b) $\Delta z_{(\text{O-Fe})} = 3.76$ a_B (shifted). $\Delta z_{(\text{O-Fe})}$ represents the interplanar distance of the interstitial oxygen species from the Fe surface respectively (marked with the dashed line) (c) Fe/HfO_2 unit cell with frontal oxygen positioning. (d,e) Ground state of the Fe/HfO_2 unit cell with interstitial interplanar O-Fe distance of (d) $\Delta z_{(\text{O-Fe})} = 5.34$ a_B (equilibrium) and (e) $\Delta z_{(\text{O-Fe})} = 3.34$ a_B (shifted). (f) Fe/HfO_2 unit cell with interstitial oxygen positioning. The K_1 represents the value of the MCAE and is given by $E(\theta = 0) - E(\theta = \pi/2)$. 152

6.8 Magneto-crystalline anisotropy energy (MCAE) (θ from eq.(6.2)) in the Fe/HfO_2 setup shown with shifted oxygen species at the interface. (a) MCAE of the mixed surface in its ground state. (b) MCAE of the mixed surface with a frontal O-Fe distance of 5.78 a_B . (c) Side view of the Fe/HfO_2 unit cell with the mixed setup. The $\Delta z_{\text{(O-Fe)1}}$ and $\Delta z_{\text{(O-Fe)2}}$ denote the interplanar distance of the frontal and interstitial oxygen species from the Fe surface respectively (marked with the dashed line). 153

6.9 Magneto-crystalline anisotropy energy (MCAE) as a function of the frontal and interstitial oxygen atoms interplanar distance as depicted in Fig.6.8-(c). (a) Effect of frontal oxygen shifts ($\Delta z_{\text{(O -Fe)2}}$ variable) while the interstitial oxygen is kept fixed at a distance $\Delta z_{\text{(O -Fe)2}} = 2.53\, a_B$ from the FM surface.(b) Effect of frontal oxygen shifts ($\Delta z_{\text{(O -Fe)2}}$ variable) while the interstitial oxygen is kept fixed at a distance $\Delta z_{\text{(O -Fe)2}} = 1.96\, a_B$ from the FM surface. The initial interplanar distance of the frontal oxygen atoms is $\Delta z_{\text{(O -Fe)2}} = 6.94\ a_B$ in both (a) and (b) 154

6.10 (a) Energetic cost of shifting interstitial and frontal oxygen atoms in the mixed interface setup displayed in panel (c) of Fig. 6.8. The starting positions are $\Delta z_{\text{(O-Fe)1}} = 2.53\ a_B$ for the interstitial oxygen atom and $\Delta z_{(O-Fe)2} = 6.94\ a_B$ for the frontal oxygen atoms (i.e. the setup of panel (a) in Fig. 6.8) (b) MCAE at different frontal oxygen positions $\Delta z_{\text{(O-Fe)2}}$ represented in panel (d) of Fig. 6.8. The starting positions are $\Delta z_{(O-Fe)1} = -0.08\ a_B$ for the interstitial oxygen atom and $\Delta z_{\text{(O-Fe)2}} = 6.94\ a_B$ for the frontal oxygen atoms (i.e the setup of panel (c) in Fig. 6.8). Positive values on the y-axis indicate that the system has IP magnetic anisotropy. 155

6.11 Hypothesis for the mechanism governing the different magneto-ionic regimes in CoFeB/HfO_2 multilayers. (a) Ground state of the system. (b) Irreversible magnetization switching via interstitial sites occupied by migrating oxygen species. (c) Reversible magnetization switching via frontal oxygen shifts. The bottom cartoon in all three panels represents the magnetization direction and the switching process. . . 155

6.12 a) Heisenberg model on a cubic lattice. We indicate the lattice sites with indices i, j b) Decomposition of the cubic lattice in nearest neighbour clusters using the Voronoi tassellation [11]. In this decomposed lattice we use the k index to identify the cell and α, β indices to indicate the nearest neighbors. c) Continuum limit performed on the cell from b). The cell index k becomes continuous $d^3\boldsymbol{r}$ and the atomic moments become a continuous function of space $\boldsymbol{m}(\boldsymbol{r})$ 161

6.13 Directed graph representing the nearest neighbors (n.n) on the cubic lattice. The vertices are represented by v_i and the edges by l_i. 163

6.14 Directed graph representing the nearest neighbors (n.n) on a C_{6v}. The vertices are represented by v_i and the edges by l_i. 165

6.15 2 different basis choices to represent the lattice vectors in the C_{6v} geometry. We only depict the basis choice in the C_6 plane as along the z-axis the choice is trivial. 166

6.16 Symmetric exchange components $\hat{\boldsymbol{\Xi}}_{ij} := \Xi_{ij}$ from eq.(6.18) as a function of all 32 non-centrosymmetric crystallographic point groups as imposed by the Neumann principle (6.47). The generators are expressed in the basis used in [12]. 169

6.17 DMI tensor components $(\hat{\boldsymbol{Q}})_{ij} := Q_{ij}$ from eq.(6.48) as a function of all 21 non-centrosymmetric crystallographic point groups as imposed by the Neumann principle of eq.(6.47). The 11 centrosymmetric point groups have a vanishing DMI tensor and are not shown. The generators are expressed in the basis used in [12]. 170

6.18 DMI tensor components for all 21 non-centrosymmetric crystallographic point groups as imposed by the Neumann principle [13]. The 11 centrosymmetric point groups have a vanishing DMI tensor and are not shown. The components D_a, D_s, D_b, D_t are the ones shown in the decomposition of eq.(6.65), while terms of the form D_{ij} are combinations of D_a, D_s, D_b, D_t. 179

6.19 (a) Scheme of the system used in the micromagnetic simulations. We show the dimensions $L_x = 1\ \mu$m , $L_y = 160$ nm and $L_z = 0.6$ nm as well as the internal DW angle ϕ and the DW tilt angle χ. (b) ϕ and χ angles in the case of $\chi > 0$ (i.) ϕ and χ angles in the case of $\chi > 0$ (ii.) (c) Schematic representation of the internal DW angle (the colored arrows in the middle of the domain wall indicate the orientation of the magnetization in the $x-y$ plane) stabilized by the presence of the different DMI tensor components of eq.(6.80) in the presence of an applied IP field 181

6.20 a-c) Internal DW magnetization (the orange arrows in the middle of the domain wall indicate the orientation of the magnetization in the $x-y$ plane) angle stabilized by 3 different representative DMI tensors in the absence of an applied IP field (d-e) Internal DW magnetization angle stabilized by 2 different representative DMI tensors in the presence of an applied IP field. The mirrored image of the tilted domain wall in (d) and (e) is included for clarity. The DMI tensor components are expressed in mJ/m^2. 184

6.21 Comparison of Micromagnetic simulations [14] and numerical minimization of the energy density of eq.(6.80) for (a) The tilting angle χ as a function of the D_{21} DMI tensor component of in the case of a C_{2v} symmetric DMI. (b) Tilting angle χ as a function of the D_s DMI tensor component of in the case of a S_4 symmetric DMI in the case of $D_b = 0$. (c) Tilting angle χ as a function of the D_s DMI tensor component of in the case of a S_4 symmetric DMI in the case of $D_b = 1.5$ mJ/m^2. (d) Tilting angle χ as a function of the D_b DMI tensor component of in the case of a T symmetric DMI with an IP applied field in the y-direction of magnitude $\mu_0 H_y = 100$ mT (e) Tilting angle χ as a function of the D_b DMI tensor component of in the case of a T symmetric DMI with an IP applied field in the x-direction of magnitude $\mu_0 H_x = 100$ mT. 186

6.22 (a) DW angle $\phi + \chi$ as a function of the off-diagonal DMI tensor components D_s in the S_4 symmetric case. (b) DW angles as a function of the diagonal DMI tensor components D_b ($D_b/D_s \ll 1$ limit) in the S_4 symmetric case. (c) intrinsic DW tilting in the presence of simultaneous presence of D_s and D_b for 3 representative cases. . . . 188

6.23 (a) DW tilting angle χ response to an H_y field sweep from -200 mT to $+200$ mT in the case of pure D_a (blue dots) and pure D_s (orange squares) contributions to DMI. As can be seen the 2 responses overlap almost completely. (b) DW tilting angle χ response to a rotating IP field with H_y and H_x components (see eq.(6.93) in the case of pure D_a and pure D_s contributions to DMI. The dashed curves are obtained by fitting the energy minimum of eq.(6.80) onto the results obtained via micromagnetic simulations using D_a and D_s as the fitting parameters. 189

6.24 Comparison of Micromagnetic simulations [14], numerical minimization (6.101) and analytical estimate (see eq.(6.105)) for the DW Walker breakdown H_W. (a) DW velocity v_{DW} as a function of an applied out-of-plane field H_z. The different curves show the velocity profile for different values of the symmetric component of a C_{2v} symmetric DMI tensor (see inset of (c)). (b) DW velocity v_{DW} as a function of an applied out-of-plane field H_z. The different curves show the velocity profile for different values of the anti symmetric component of a C_{2v} symmetric DMI tensor (see inset of (d)). (c) Comparison of simulation results, numerical maximization of eq.(6.103) and analytical estimate (see eq.(6.105)) of the Walker breakdown as a function of the symmetric component of a C_{2v} symmetric tensor. (d) Comparison of simulation results, numerical maximization of eq.(6.103) and analytical estimate (see eq.(6.105)) of the Walker breakdown as a function of the anti symmetric component of a C_{2v} symmetric tensor. 193

6.25 (a) 3D plot of eq.(6.105) (b) Plot of the analytical formula for the WB field H_W as a function of the off-diagonal $\tilde{D}'$ component (see eq.(6.105)). The different curves represent the behavior of the WB field for different diagonal DMI D_b values. At $D_b = 0$ (i.e the blue curve) we recover the linear behavior. The peak velocities are reported on the second y-axis shown in red. (c) Comparison of WB field calculated from a micromagnetic simulation with a DMI tensor compatible with S_4 symmetry ($D_l = 1.3$ mJ/m^2 and free D_b) and the analytical estimate of eq.(6.105). The peak velocities are reported on the second y-axis shown in red. 195

A.1 (a) Nearest neighbors in the SC lattice (b) Dispersion relation ε_k. To allow for a 3D visualization, the k_z-component is set to 0. 221

B.1 Effect of the unitary operator S acting on the matrix H 224

B.2 Decomposition of a matrix H in a diagonal ($\mathscr{H}^0$), block diagonal ($\mathscr{H}^1$) and non block-diagonal matrix ($\mathscr{H}^2$) component 224

List of Tables

2.1 $\langle \mu_i, \sigma_1 | \boldsymbol{L} \cdot \boldsymbol{S} | \mu_j, \uparrow \rangle$ Matrix elements for $3d$-orbitals. 28

2.2 $\langle \mu_i, \sigma_1 | \boldsymbol{L} \cdot \boldsymbol{S} | \mu_j, \downarrow \rangle$ Matrix elements for $3d$-orbitals. 29

3.1 The form of micromagnetic Dzyaloshinskii-Moriya energy density $\mathscr{E}_{DMI}$ for all 11 non-centrosymmetric point groups 61

3.2 $\phi(\psi) = m\psi + \gamma$ solutions for the 11 different non-centrosymmetric crystallographic point groups. D and D' refer to the DMI forms reported in Table.3.1 80

6.1 Total energy difference between the relaxed structures of Fig.6.6 . . 150

Nomenclature

Roman Symbols

α	Gilbert damping
α_E	Magneto-electric coefficient
$\boldsymbol{\Omega}$	Angular velocity vector
$\boldsymbol{B}$	Magnetic field due to current
$\boldsymbol{D}$	Microscopic Dzyaloshinskii-Moriya vector
$\boldsymbol{d}$	Micromagnetic Dzyaloshinskii-Moriya vector
$\boldsymbol{H}$	Magnetic field in vacuum
$\boldsymbol{H}_{\text{eff}}$	Effective field
$\boldsymbol{H}_d$	Demagnetizing field
$\boldsymbol{M}$	Magnetization vector
$\boldsymbol{m}$	Normalized magnetization vector
χ	Domain wall canting angle
Δ	Domain wall width
γ	Gyromagnetic ratio
$\hat{\boldsymbol{\Xi}}$	Anisotropic symmetric exchange tensor
$\hat{\boldsymbol{Q}}$	DMI tensor
$\hbar$	Planck constant
$\mathscr{E}$	Micromagnetic energy density of the system
$\mathscr{F}$	Rayleigh dissipation function
$\mathscr{H}$	Hamiltonian
$\mathscr{L}$	Lagrangian function
μ_0	Magnetic permeability of free space
μ_B	Bohr magneton
$\partial V = S$	Surface of the magnetic body
ϕ	Internal domain wall angle
σ_{DW}	Energy density of a magnetic domain wall
$\overleftrightarrow{\Gamma}$	Microscopic Kitaev exchange tensor
$\overleftrightarrow{I}$	Inertial tensor
$\overleftrightarrow{N}$	Demagnetizing tensor
ξ	Spin orbit coupling parameter
A	Micromagnetic exchange constant
$c, c^\dagger$	Fermionic annihilation and creation operators
c	Speed of light in a vacuum
E	Microscopic energy of the system
J	Microscopic Heisenberg exchange parameter

K_0, K_1 etc. Magnetocrystalline anisotropy coefficients

K_u Uniaxial anisotropy coefficient

M_s Saturation magnetization

Q Domain wall polarization

Q Quality factor of the material

q Domain wall position

T Kinetic energy in the Hubbard model

t Sample thickness

U Coulomb energy in the Hubbard model

V Volume of the magnetic body

AFM Antiferromagnet

BCC Body centered cubic

CCM Collective coordinate model

CMOS Complementary metal-oxide-semiconductor

DFT Density functional theory

DMI Dzyaloshinkii-Moriya interaction

DMI Dzyaloshinskii Moriya interaction

DRAM Dynamic Random Access Memory

DW Domain wall

FFT Fast Fourier transform

FM Ferromagnet

GMR Giant magneto resistance

HM Heavy metal

IL Ionic liquid

IP In plane

IPA In plane magnetic anisotropy

IT Information technology

KS Kohn Sham

LLG Landau Lifshitz Gilbert equation

MAE Magnetic anisotropy energy

MCAE Magneto crystalline anisotropy energy

ME Magneto electric

ML Monolayer

NM Non-magnetic

OAM Orbital atomic moment

OOP Out of plane

Ox Oxide

PMA Perpendicular magnetic anisotropy

RAM Random access memory

RHS Right hand side

RKKY Ruderman–Kittel–Kasuya–Yosida interaction

SC Simple cubic

SD Spin diffusion

SHE Spin Hall effect

SOT Spin orbit torque

SQA Spin quantization axis

SRAM Static Random Access Memory

SRT Spin reorientation transition

STT Spin transfer torque

Thz Terahertz

VCMA Voltage control of magnetic anisotropy

WB Walker breakdown

WS Wigner Seitz cell

Chapter 1

Introduction

1.1 How is memory stored today?

Nowadays, the vast majority of memory storage technology in computers relies entirely on the physics of semiconductors and transistors. Memory, in its primary form, exists as Random Access Memory (RAM), which is volatile and necessitates a continuous power supply for data retention. At the core of computer memory lies the memory cell, which serves as the fundamental unit for representing a single binary bit of information (either 0 or 1).

There are two primary types of memory cells utilized in modern computers: firstly, we have Dynamic Random Access Memory (DRAM) which constitutes the prevalent form of main system memory in computer architectures. Each DRAM memory cell comprises a transistor and a minute capacitor. The storage of information is achieved through charge accumulation or depletion within the capacitor but unfortunately, owing to the nature of capacitors, charge leakage occurs over time, making periodic refreshing of the memory cells necessary to sustain data integrity.

Secondly, we have Static Random Access Memory (SRAM) which is employed as cache memory or in limited quantities on the processor chip itself. SRAM exhibits superior performance and reliability when compared to DRAM, albeit at higher cost and power consumption. An SRAM cell is constructed using flip-flop circuits and employs multiple transistors to retain a single bit of information. Unlike DRAM, SRAM does not mandate regular refreshing, thereby enhancing speed and responsiveness.

It appears evident that the physics involved in memory storage revolves around the manipulation of charge and voltage levels within these memory cells. By precisely controlling the applied voltage across specific components within the memory cell, information can be encoded as a pattern of electrical charges or their absence. These patterns are subsequently interpreted as binary values, wherein charged components represent logical "1" and discharged components represent logical "0".

1.2 What about tomorrow? The end of Moore's Law

Moore's law, originally formulated to describe the scaling of transistor sizes (see Fig.1.1), has also found relevance in the realm of data storage technology where the rapid growth in memory capacity per unit surface area (currently moving toward the 5 Tb/in^2 mark), now faces 2 significant technological challenges: first of all, the higher density of transistor elements has caused Joule heating to become a serious threat to both performance and environmental impact of computing devices. Secondly, a more fundamental barrier looms with the advent of quantum mechanical wave-like behavior manifested by electrons when the feature size approaches the limits of the mesoscopic scale (around the nanometer scale). This quantum barrier undermines the traditional notion of a transistor as a binary element therefore signalling the effective end of the Moore's Law era.

At the same time, the rapid expansion of the IT industry has resulted in a significant increase in demand for energy, with some estimates claiming that 20-30 % of the global energy production will be devoted to this growing sector by 2030. We are faced with a major challenge to the IT ecosystem: on the one side we are dealing with the presence of 2 major walls, Joule heating and quantum effects at the nanoscale, while human development is moving at incredible speed towards them with fundamental and applied research being the only possibilities to steer the wheel and prevent the crash. To successfully move and thrive in the post-Moore era, we need to rethink our computing architectures, starting at their very core: the physical principles that we use to encode information.

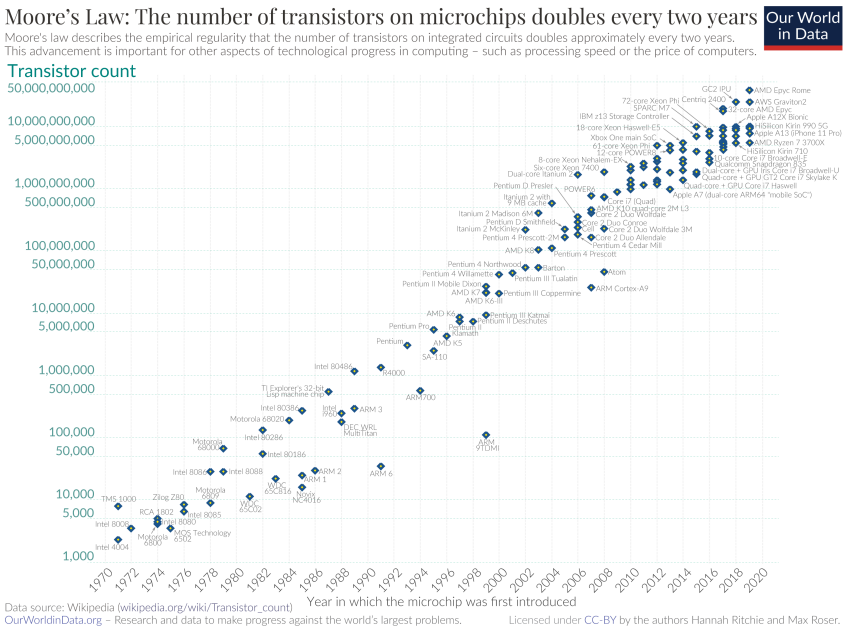

Fig. 1.1 Semi-logarithmic plot of the number of transistors on microchip as a function of the years. We can easily see how it has roughly doubled every 2 years since the 1950's. Reproduced from https://ourworldindata.org/.

1.3 Tomorrows data storage technology

1.3.1 What is Spintronics?

Spintronics, also known as spin electronics, is a branch of solid-state physics that explores the interplay between charge and spin transport in magnetic nanostructures. While the concept of electron spin dates back to the early 20th century, exploiting this intrinsic property of materials for technological applications has always been a formidable challenge.

A significant milestone in the field of Spintronics can be attributed to Albert Fert and Peter Grüenberg, who independently discovered the phenomenon of giant magneto-resistance (GMR) [15, 16] which awarded them the Nobel Prize of 2007. Their discovery involved observing changes in the resistivity of a magnetic multilayer composed of a sequence of 2 ferromagnetic layers interspersed with a non magnetic spacer layer. What they observed is that, when the magnetization in the layers is parallel, the electrons encounter low resistance while in the case of antiparallel alignment, electrons encounter strong resistance. This leads to the realization of two

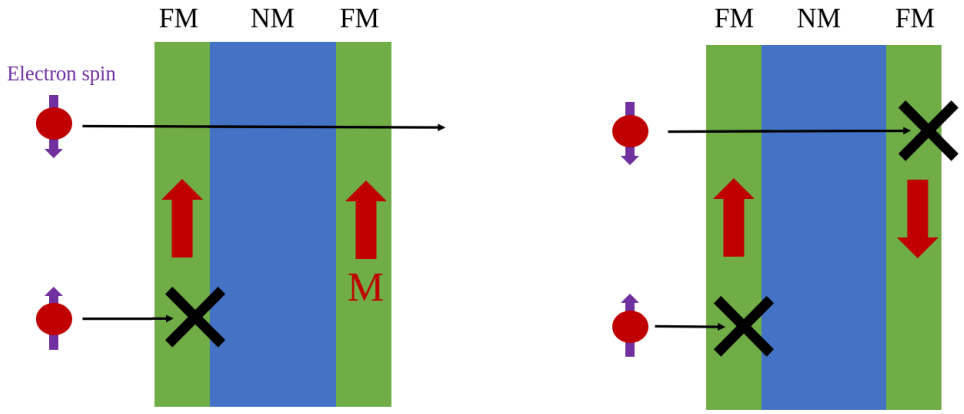

Fig. 1.2 Spin valve based on the GMR effect. The ferromagnetic layers are indicated by the "FM" label and the non-magnetic spacer by the "NM" label. As can be seen, depending on the relative orientation of the the magnetic layers, the spin polarized electrons experience different resistances.

resistance states, namely, a low and high resistance state in immediate analogy with the high (”0”) and low (”1”) resistive state of a CMOS transistor used in conventional computing (Fig.1.2).

The discovery of GMR opened up new opportunities for research into novel physics and innovative computational devices that could couple spin and charge transport, as opposed to pure charge transport. As a result, countless spintronic devices have been proposed, some even commercialized, and new discoveries continue to emerge every day in high-impact research journals, indicating that Spintronics is a fervent and growing scientific field.

1.3.2 Where is Spintronics in today’s memory storage market?

The conventional DRAM technology, despite its advantages, is being sought to be replaced in the industry due to its volatile nature. While flash memory offers inherent non-volatility as it does not rely on capacitors, it faces limited endurance posing a challenge for long-term reliability. Spintronic concepts, on the other hand, hold significant promise in the pursuit of alternative memory solutions as they couple inherent non-volatility and theoretically infinite endurance, making them highly desirable for next-generation memory technologies.

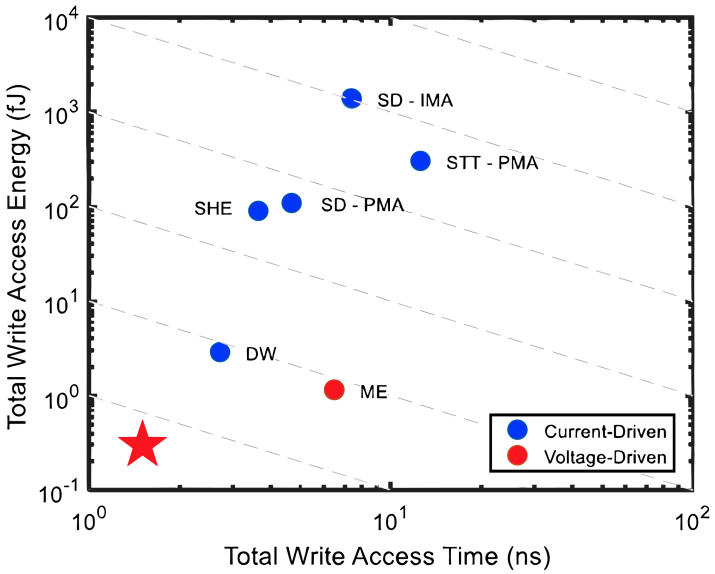

Fig. 1.3 Log-Log plot reporting the total write access time (ns) vs. the total write access energy (fJ) for different spintronics based device concepts: (SD) spin diffusion, (STT) spin-transfer-torque, (SHE) spin Hall effect, (DW) domain wall motion (ME) magnetoelectric switching, (IMA) in-plane magnetic anisotropy, (PMA) perpendicular magnetic anisotropy. The red star on the bottom right designates the preferred corned (i.e. low write access time and low energy requirements). Reproduced from [1].

Benchmarking the performance of spin-based or magnetic memories with high endurance provides valuable insights into the trade-offs between write energy and time costs associated with the physical principles at the base of the encoding mechanism (Fig.1.3). In the following we provide a brief survey on some of the concepts underlying the main ideas in today's spintronics community: by observing the top right of Fig.1.3 we first notice how the development of in plane anisotropy (IPA) devices is being superseded by their perpendicular magnetic anisotropy (PMA) counterparts as a consequence of faster operation speed, lower energy consumption and higher storage density potential.

Spin diffusion (SD) writing and spin Hall Effect (SHE) mechanisms offer high energy efficiency compared to Spin-Transfer-Torque (STT) methods because of their lower resistance writing path, which enables operation at smaller voltages. Furthermore, domain wall (DW) memories exhibit the potential for even smaller driving currents, pushing the boundaries of activation energies in memory switching. However, it is important to note that the thus far mentioned alternative memory concepts still rely on (spin-polarized) currents for their operation: although the required cur-

rents are significantly smaller compared to CMOS-compatible counterparts, concerns regarding Joule heating persist.

In contrast, magneto-electric (ME) memories stand out as having the lowest energy cost among the considered types. These memory concepts aim at altering the magnetization state of a material (i.e. writing information) with purely electrical effects and therefore rely solely on the charging and discharging of capacitors, eliminating the need for current-induced torques.

Despite their potential, the industry has thus far successfully developed only spin-transfer torque (STT) memories, which have been commercially available since 2007 (the first to introduce them to the market being Freescale.inc). The remaining memory schemes mentioned are still at various stages of research and development. Notably, memories based on magneto-electric effects are the least mature, despite their significant promise due to their remarkably low power requirements.

1.3.3 Electric field control of interfacial magnetism

The coupling between electricity and magnetism in solid-state insulators was initially proposed by Pierre Curie in 1894 [17], who based his reasoning on simple symmetry considerations. Building upon this idea, in 1959 Landau and Lifshitz [18] postulated the linear nature of this effect in magnetic crystals of specific symmetry classes, thereby proposing the electric field control of magnetization with the relationship

$$\mu_0 \Delta M = \alpha_E \Delta E, \tag{1.1}$$

where ΔM represents the change in magnetization, ΔE denotes the applied electric field, α_E represents the magneto-electric coefficient and μ_0 is the vacuum permeability. The existence of this linear effect in the antiferromagnetic compound Cr_2O_3 was predicted by Dzyaloshinskii [19] in the same year and subsequently confirmed by experiments in 1960 [20].

Since the 1960s, the field of magneto-electrics has expanded significantly beyond the realm of linear magneto-electric effects with experimental discoveries of both linear and nonlinear magneto-electric effects in single-phase multiferroics [21–23]. The 1970's have set the stage for new explorations in this field, witnessing many new magneto-electric effects in piezoelectric-magnetic heterostructures [24]. The

2000's on the other hand, have seen a rise in the exploration of magneto-electric effects in magnetic-dielectric heterostructures [25, 26], where the thin film magnetic components is electrically addressed through non piezoelectric gate dielectrics. During these years of intense scientific development, the advent of ab initio simulations has provided theorists with the capability to explain and predict experimental observations in solid state systems with increasing precision.

The great scientific and technological pull factor of magneto-electric (ME) effects lies in their ability to convert between magnetic and electric free energy without the need for electrical current, thus minimizing heat dissipation. As mentioned in the previous section, all competitive new data storage technologies that rely on information encoding based on the direction of a magnetization vector (e.g. STT, SD) still function based on current based manipulation. The converse ME effect, observed in magnetic/dielectric heterostructures, revolves around the ability to switch the magnetization of the magnetic layer by applying a voltage across the dielectric layer and therefore presents an opportunity to address the issue of overheating: the theoretical lower limit of energy dissipation for ME switching is in the attojoule range, approximately four orders of magnitude lower than STT magnetization switching [27].

In magnetic/dielectric heterostructures, ME switching can occur through various physical mechanisms, including the transfer of voltage-induced strains [28–30], voltage-modified interfacial spin polarized charge density [31, 32], voltage-induced switching of interfacial exchange coupling/other exchange mechanism [33–36] and, finally, voltage-induced surface chemistry manipulation [37–40]. In Fig.1.3 we report and highlight some of the main application-relevant features of the 4 mentioned ME switching mechanisms.

1.4 The approach used in this dissertation

Magnetism stands as one of the captivating domains in physics where the quantum mechanical nature of our reality transcends the microscopic realm and manifests itself at the macroscopic level, allowing for easily observable phenomena. It is therefore natural to assume that this makes magnetism in the solid state a rich and intricate field that can be explored across various length scales (see Fig.1.5), from the very small atomistic scale to the macroscopic scale going beyond the mm.

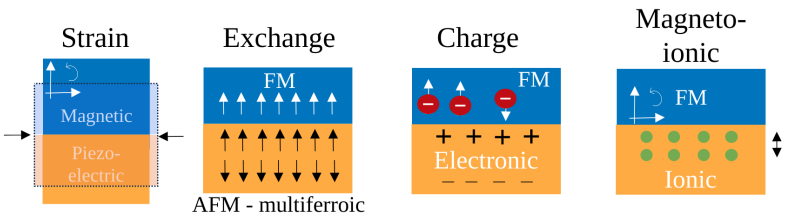

Energy supply	CV²	CV²	CV²	CV²
Heat dissipation	$V^2 t_0 / R$	$2 P_s V A + V^2 t_0 / R$	$V^2 t_0 / R$	$V^2 t_0 / R$
Switching speed	Fast	Fast	Fastest	Slow
Reliability	High	Moderate	High	Moderate
Size scalability	Low	Low	High	High
180° ME switching	✓	✓	✓	✗
State-of-the-art α_E (s/m)	8 x 10^{-6}	1 x 10^{-7}	3 x 10^{-9}	2 x 10^{-8}

Fig. 1.4 Comparison of several application-related features between the four types of (ME) switching. The terms in the first 2 rows represent, C: capacitance of the dielectric, V: the applied voltage, R: electrical resistance of the dielectric, t_0: duration of the voltage pulse. In the voltage controlled exchange scheme (i.e. the second column from the left), the heat dissipation arises from the leakage current and dielectric loss due to magnetic hysteresis. In this context we have P_s: switched polarization, V: critical voltage for polarization switching, A: electrode area. We highlight how charge accumulation effects, despite promising in almost all aspects (fast, reliable, scalable), unfortunately display a very small ME coefficient α_E, therefore requiring very high fields for application. Figure re-adapted from [2].

From the theoretical and computational point of view, magnetism is a particularly rich field where contributions can be made using a wide range of formalisms and mathematical tools: while quantum mechanics lies at the heart of magnetism, we can be largely oblivious of its principles while studying hysteretic properties of magnetic materials, for example.

In this context, the influence of an electric field on the magnetic properties of solid-state materials is indeed a topic that can be addressed across very different length scales, spanning from atomic bonds to Weiss domains.

Within this dissertation, we have produced contributions to the understanding of both the direct and indirect effects of an electric field on magnetic properties across various scales. Specifically, the scientific contributions presented in this work pertain to the phenomenology and mathematical models related to the first two levels of the diagram in Fig.1.5—namely, the atomistic scale of $\approx$ Å to the scale of Weiss domains ranging from 1-1000 nm.

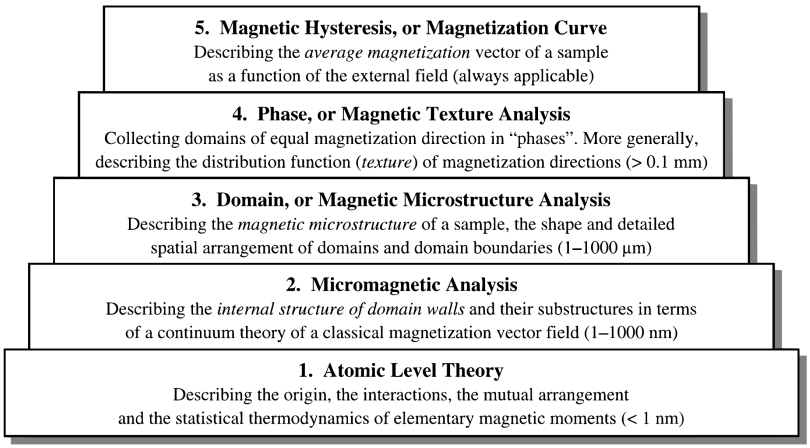

Fig. 1.5 Different length scales and corresponding salient features of magnetism. Reproduced from [3]

1.5 Outline of the dissertation

In this dissertation we mainly focus on the study of 2 of the mentioned ME switching mechanisms: we address the effect of electrically induced surface chemistry changes on interfacial magnetization (magneto-ionics) and the effect of the electric field on magnetic exchange interactions in magnetic thin films. The dissertation is structured into three main parts: an initial theoretical section, a section on the computational implementation of the theory, and a final results section.

In Chapters 2 and 3, we establish the theoretical foundation for understanding magnetism in the solid state. Chapter 2 delves into the origin of magnetic ordering at the atomic level, discussing modern models of magnetism and the crucial role of Spin-Orbit Coupling (SOC) in dictating the appearance of magnetocrystalline anisotropy and chiral exchange interactions. Chapter 3 focuses on transitioning from the atomistic theory to micromagnetism through the continuum limit, a vital component for studying magnetic phenomena at the scale of real devices. Special attention is given to defining chiral interactions (see Chapter 4) in the continuum, which is pivotal for some of the subsequent results.

Chapter 5 addresses two key pillars of modern computational material science: density functional theory and finite element codes for micromagnetic simulations. While not delving deeply into their implementations, we provide general information

about these formalisms relating them to the approaches outlined in the preceding theory section.

With the necessary theoretical and computational foundation, we then move on to discuss the main results of the dissertation in Chapter 6. We begin by examining an experimental observation related to magneto-ionic mechanisms in HM/FM/Oxide multilayers, in which I participated as a co-author. Next, we delve into ab-initio calculations designed to explain trends observed in the experimental setting. The following two sections shift focus to chiral interactions in FM thin films and their connection to symmetry breaking induced by an electric field. The first of such works is of pure theoretical character and describes a locally covariant formulation of micromagnetism in magnetic lattices that allows to easily derive all allowed forms of chiral interactions. The second and final discussed work in this dissertation is of computational nature and describes the behavior of magnetic domain walls in the presence of arbitrary chiral interaction. It builds directly upon the previous work as it uses the same compact formalism allowing for a remarkably simple analytical derivation of some models for domain wall dynamics. We conclude the dissertation by hinting at new avenues for research that have emerged from the results obtained.

Chapter 2

Theoretical Background

The observation of magnetic properties in solids can be traced back as far as 2500 years in the past. Despite its ancient observation, our comprehension of the microscopic mechanisms underlying magnetism have only truly emerged in the last century and a half. The challenge of capturing the intricate features of magnetism through physical models has been formidable, and its enigmas could only be truly unraveled with the introduction of quantum mechanics. In the subsequent discussion, we present a concise overview of key models of magnetism in solid state systems both on the atomistic and the micrometer scale, emphasizing how diverse forms of magnetic interactions manifest in the solid state as a consequence of many-body electron interactions.

2.1 Microscopic models for magnetic order

The understanding of magnetization in isolated atoms relies on the quantum mechanics of the hydrogen atom, combined with the consideration of electron spin. However, most of the intriguing aspects of magnetism occur in the solid state, where magnetic atoms are arranged in lattices with long-range order. In a solid, the introduction of chemical bonds between atoms disrupts the spherical symmetry that characterizes the central potential of an isolated atom and, consequently, the nature of magnetism undergoes fundamental changes in this context.

Creating effective models to describe magnetic ordering in solids has long been a formidable challenge for physicists, which in its most advanced formulations, still

persists to this day. The complex interplay of electronic interactions, lattice structures, and other factors make the theoretical understanding of magnetic phenomena a highly intricate pursuit.

We pick up the story from the early 20^{th} century, when Werner Heisenberg [41] in one of his many pioneering contributions, showed that spin-independent Coulomb interaction, when coupled with the Pauli exclusion principle, can generate an effective spin-spin interaction. In Heisenberg's picture of ferromagnetism, the founding assumption is that the electrons contributing to the magnetic order are localized near the atomic nucleus and their spin "communicates" with neighbouring spins via the so called "exchange interaction".

While Heisenberg's model provided fundamental qualitative insights, it failed to make accurate quantitative predictions, suggesting that electron spins should almost always align antiferromagnetically. This discrepancy necessitated further refinements to the model.

An alternative perspective was later proposed by Felix Bloch [42], who considered the itinerant nature of electrons as crucial in determining ferromagnetic ordering mechanisms. Bloch's model led to a series of investigations that employed band-theoretical methods and mean field approximations to make quantitative predictions. The basic strategy of these approximations involved treating electrons with up and down spins as distinct particle species and imposing self-consistency conditions. However, this approach introduces a fundamental limitation by breaking the symmetry of the problem: treating electrons as distinguishable particles reduces the continuous $SU(2)$ symmetry to a discrete Z_2 symmetry, posing a challenge in capturing the full complexity of magnetic systems.

2.1.1 The Hubbard model

The Hubbard model emerges in the middle ground between these 2 points of view and allows to treat the localization of the electrons as a parameter, rather than a fixed assumption of the model. The central idea behind the Hubbard model is in fact to explore the interplay between two competing energies in the formation of electronic states in a multi-atom and multi-electron system. At its core, it is a tight-binding model [43] of localized electrons hopping on a lattice (see Fig.2.1), with the key assumptions underlying the validity this model being summarized as follows: the

Hubbard Hamiltonian accounts for the magnetic ground state through the balance of the hopping energy and the Coulomb energy under the assumption that the involved particles (electrons) are Fermions and therefore follow the Fermi-Dirac statistics.

- The *hopping energy* is associated with the motion of electrons of like-spin to move between neighboring atoms. It favors delocalization (large band dispersion) and in second quantized form, the term describing such behavior is given by

$$T = -\sum_{i \neq j} t_{ij} c^{\dagger}_{j\sigma} c_{i\sigma}. \tag{2.1}$$

- The *Coulomb energy* acts as a repulsive force only between electrons of opposite spin located on the same atom. In second quantized form, the term describing such behavior is given by

$$U = u \sum_{i} n_{i,\uparrow} n_{i,\downarrow}. \tag{2.2}$$

The Hubbard Hamilotnian is then given by the sum of these 2 contributions, taking into account all the atomic sites of the lattice (see Fig.2.1):

$$\mathscr{H} = -\sum_{i,j,\sigma} t_{ij} c^{\dagger}_{j\sigma} c_{i\sigma} + u \sum_{i} n_{i,\uparrow} n_{i,\downarrow} \tag{2.3}$$

The Fermionic statistics are incorporated in the model by imposing the canonical anti-commutation relations for the electron creation and annihilation operators

$$\{c_{i\sigma}, c^{\dagger}_{j\sigma'}\} = \delta_{ij} \delta_{\sigma\sigma'}. \tag{2.4}$$

This model has three dimensionless parameters that determine the different regimes at which it can operate:

- $u/t \rightarrow$ Coulomb energy vs. kinetic energy.
- $T/t \rightarrow$ Temperature vs. kinetic energy.
- Average electron occupation $n = \frac{1}{N} \sum_{i\sigma} \langle n_{i\sigma} \rangle \in [0, 2]$.

Furthermore, two trivial yet extremely important limits of this model are

- $n \ll 1$ i.e the particle inter-spacing is much larger than the lattice constant and the electrons are essentially free to move. In this limit, we expect a metallic behavior.

- $n = 2$ in this case all sites are occupied and electrons are not free to move anymore (Pauli blocking). In this regime we expect an insulating behavior.

The non trivial physics of the Hubbard model occurs near half filling, i.e $n \approx 1$, when the ground state is determined by the interplay of kinetic energy, the Pauli exclusion principle and Coulomb repulsion. In the following, we briefly discuss the features of this regime in 2 distinct limits, namely the weak and strong interacting limits :

- $\frac{u}{t} \ll 1$: in the weak interacting limit we expect the nearly half filled model to have similar properties to metallic systems. There are however some important non perturbative contributions that can cause the behavior to stray from the expectations.

- $\frac{u}{t} \gg 1$: In the strongly interacting limit, doubly occupied states actually cost a large energy (due to the larger value of u). This means that the conduction band is jammed and electron mobility is hindered: in this regime we have what is known as a Mott insulating phase.

The Mott insulating phase

The way to study the Mott insulating phase is to start from the huge degeneracy of the system at $t = 0$, $n = 1$ (see Appendix A), where the energy of the system remains unaltered upon spin flips at the individual sites. Using that as a starting point, we can study degenerate perturbation theory and find out the effects of a small but finite hopping amplitude, performing a Schrieffer-Wolff transformation of the Hamiltonian (see Appendix B for an in depth discussion)

$$\mathscr{H} = T + U \rightarrow \mathscr{H}' = e^{-A}\ \mathscr{H}\ e^{A}. \tag{2.5}$$

We use the Baker-Campbell-Hausdorff (BCH) formula to expand the exponential in a series. The validity of the series expansion is guaranteed by the fact that we choose

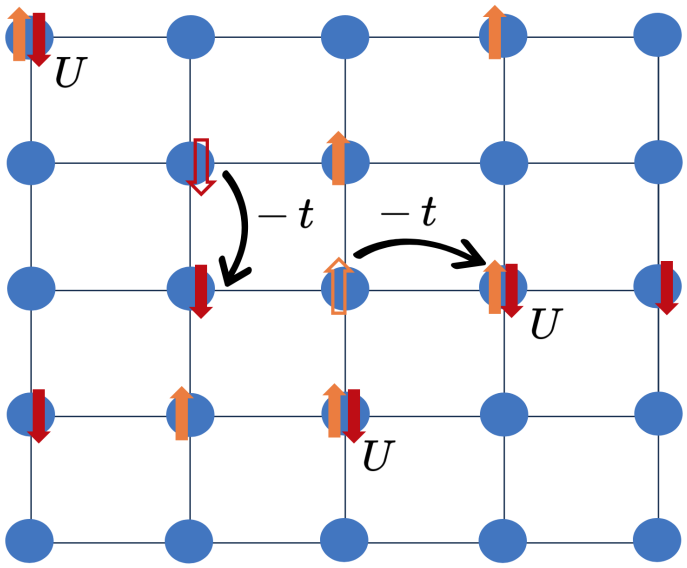

Fig. 2.1 Graphical representation of a Hubbard lattice. We display the 2 competing interactions of kinetic energy (t) and Coulomb repulsion (U).

$A \propto t$ and we consider the limit $t/u \ll 1$

$$\mathscr{H}' \approx \underbrace{U+T}_{\mathscr{H}} + T - [A,U] - [A,T] + \frac{1}{2}[A,[A,U]] + \mathscr{O}(t^2). \tag{2.6}$$

To eliminate first order terms in T, we select A such that $[A,U] = T$

$$\Rightarrow \mathscr{H}' = U - \frac{1}{2}[A,T] + \mathscr{O}(t^2). \tag{2.7}$$

To determine the matrix elements of the new Hamiltonian we use the eigenbasis of the operator U which is constituted (at half filling) by states having one electron per atomic site.

$$U|n\rangle = E_n|n\rangle \tag{2.8}$$

$$\Rightarrow \langle n|T|m\rangle = \langle n|A|m\rangle (E_m - E_n) \tag{2.9}$$

$$\langle n|\mathscr{H}'|m\rangle = -\frac{1}{2}\langle n|[A,T]|m\rangle \tag{2.10}$$

$$= -\frac{1}{2}\sum_l \langle n|T|l\rangle\langle l|T|m\rangle \left(\frac{1}{E_l - E_n} - \frac{1}{E_m - E_l}\right). \tag{2.11}$$

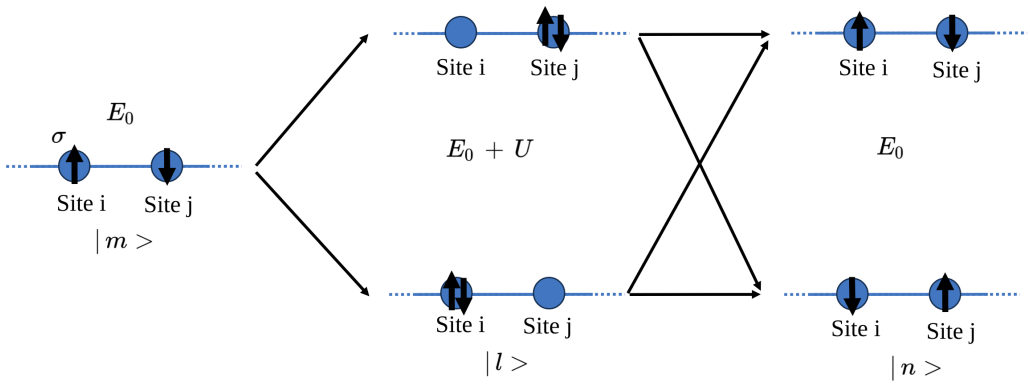

Fig. 2.2 Schematic representation of the hopping mechanism in the half filled lattice ($U/t \ll 1$ limit) of eq.(2.11)

Eq.(2.11) shows that, to second order, the action of the Hamiltonian on the eigenstates of U can be visualized as a virtual hopping to intermediate states $|l\rangle$ Since the ground state of the unperturbed Hamiltonian has all sites occupied, the only allowed virtual excitations are states with one doubly occupied state, i.e $E_l - E_n = u$, $E_m - E_l = -u$ (see Fig.2.2). This allows us to simplify (2.11) to

$$\Rightarrow \langle n| \mathscr{H}' |m\rangle = -\frac{1}{u} \sum_l \langle n| T |l\rangle \langle l| T |m\rangle . \tag{2.12}$$

Since the $\{|l\rangle\}$ states constitute a complete basis, we now have a way of expressing the matrix elements of the perturbed Hamiltonian

$$\Rightarrow \langle n| \mathscr{H}' |m\rangle = -\frac{1}{u} \langle n| T^2 |m\rangle . \tag{2.13}$$

From Hubbard to the Heisenberg models

At this point we are in the position to analyze the behavior of the effective Hamiltonian derived from the half filled, strongly interacting limit of the Hubbard model. Our goal here is to demonstrate that, indeed, in this limit the physics of the Hubbard model is captured by the familiar Heisenberg Hamiltonian. To do so, we start from the Schrieffer-Wolff approach described above and couple it with the more didactic procedure followed by [44]. Since we are interested in obtaining the effective Hamiltonian in operator form, we rewrite the effective Hamiltonian matrix element

$\langle n|\,\mathscr{H}'\,|m\rangle$ of eq.(2.12) in operator form

$$\mathscr{H}' = \sum_{n,m} |n\rangle\langle n|\,\mathscr{H}'\,|m\rangle\langle m| \tag{2.14}$$

$$= -\frac{1}{u}\sum_{n,m} |n\rangle\langle n|\,T^2\,|m\rangle\langle m| \tag{2.15}$$

We can now identify $\sum_n |n\rangle\langle n| = \sum_m |m\rangle\langle m| = \mathscr{P}_0$ with 2 projection operators that ensure we are acting on the correct subspace, i.e the subspace spanned by the degenerate eigenstates of the unperturbed Hamiltonian U. Recalling the form of the hopping term T from (2.1), we are able to write the effective Hamiltonian of eq.(2.14) as

$$\mathscr{H}' = \mathscr{P}_0\left(-\frac{1}{u}\sum_{i\neq j}\sum_{k\neq l}\sum_{\sigma\eta} t_{ij}t_{kl}c^\dagger_{i\sigma}c_{j\sigma}c^\dagger_{k\eta}c_{l\eta}\right)\mathscr{P}_0 \tag{2.16}$$

The introduction of the projection operators $\mathscr{P}_0$ allows us to significantly simplify the sum because of the following: $\mathscr{P}_0$ projects onto states where all sites are occupied by exactly one electron, is acted upon the operator string $c^\dagger_{i\sigma}c_{j\sigma}c^\dagger_{k\eta}c_{l\eta}$, and is projected on states of the same nature. Recalling $i \neq j$ and $k \neq l$, one can see that the only non vanishing terms are of the form

$$\mathscr{P}_0\; c^\dagger_{i\sigma}c_{j\sigma}c^\dagger_{k\eta}c_{l\eta}\;\mathscr{P}_0 = c^\dagger_{i\sigma}c_{j\sigma}c^\dagger_{k\eta}c_{l\eta}\,\delta_{il}\delta_{jk} \tag{2.17}$$

$$\Rightarrow \mathscr{H}' = \mathscr{P}_0\left(-\frac{1}{u}\sum_{ik}\sum_{\sigma\eta}|t_{ik}|^2 c^\dagger_{i\sigma}c_{k\sigma}c^\dagger_{k\eta}c_{i\eta}\right)\mathscr{P}_0, \tag{2.18}$$

where we have used the fact $t_{ik} = t^*_{ki}$. To proceed towards the desired result, we use fermionic anticommutator relations yielding

$$= \mathscr{P}_0\left(-\frac{1}{u}\sum_{lk}\sum_{\sigma\eta}|t_{ik}|^2 c^\dagger_{l\sigma}c_{l\eta}(\delta_{\sigma\eta} - c^\dagger_{k\eta}c_{k\sigma})\right)\mathscr{P}_0 \tag{2.19}$$

$$= \mathscr{P}_0\,\frac{1}{u}\left(\sum_{lk}|T_{ik}|^2\sum_{\sigma} c^\dagger_{l\sigma}c_{l\sigma} - \sum_{\sigma\eta} c^\dagger_{l\sigma}c_{l\eta}c^\dagger_{k\eta}c_{k\sigma})\right)\mathscr{P}_0. \tag{2.20}$$

To establish a connection with the spin operators in second quantization, we notice

$$\sum_{\sigma\eta} c^\dagger_{l\sigma} c_{l\eta} c^\dagger_{k\eta} c_{k\sigma} \tag{2.21}$$

$$= \sum_{\sigma} (\underbrace{c^\dagger_{l\sigma} c_{l\sigma}}_{n_{l\sigma}} \underbrace{c^\dagger_{k\sigma} c_{k\sigma}}_{n_{k\sigma}} + c^\dagger_{l\sigma} c_{l-\sigma} c^\dagger_{k-\sigma} c_{k\sigma}), \tag{2.22}$$

allowing us to rewrite the effective Hamiltonian as

$$\mathscr{H}' = \mathscr{P}_0 \frac{1}{u} \left(\sum_{l\neq k} |t_{ik}|^2 \sum_{\sigma} (n_{l\sigma} n_{k\sigma} + c^\dagger_{l\sigma} c_{l-\sigma} c^\dagger_{k-\sigma} c_{k\sigma} - n_{l\sigma}) \right) \mathscr{P}_0. \tag{2.23}$$

We are now finally in a position to introduce the spin operators in second quantization

$$S^z_i = \frac{1}{2} \sum_{\sigma} n_{i\sigma}, \tag{2.24}$$

$$S^i_{\pm} = c^\dagger_{i\pm} c_{i\mp} \tag{2.25}$$

$$S_x = \frac{1}{2}(S_+ + iS_y), \tag{2.26}$$

$$S_y = \frac{1}{2i}(S_+ - iS_-), \tag{2.27}$$

$$\boldsymbol{S}_k \cdot \boldsymbol{S}_l = S^z_l S^z_k + \frac{1}{2} \sum_{\sigma} S_{l\sigma} S_{k-\sigma}. \tag{2.28}$$

The first term of eq.(2.23) can be tackled by noticing that, on the subspace spanned by the eigenstates of U, the 2 relations

$$\mathscr{P}_0 \left(\sum_{\sigma} n_{k\sigma} n_{l\sigma} \right) \mathscr{P}_0 = \mathscr{P}_0 (2S^z_k S^z_l + 1/2) \mathscr{P}_0, \tag{2.29}$$

$$\mathscr{P}_0 \sum_{\sigma} n_{k\sigma} \mathscr{P}_0 = \mathscr{P}_0^2 = \mathscr{P}_0, \tag{2.30}$$

hold true, and therefore we can rewrite eq.(2.23) as

$$\Rightarrow \mathscr{H}' = \mathscr{P}_0 \frac{1}{u} \left(\sum_{l\neq k} |t_{ik}|^2 \left((2S^z_k S^z_l + (1/2 - 1) + \sum_{\sigma} S_{l\sigma} S_{k-\sigma} \right) \right) \mathscr{P}_0 \tag{2.31}$$

$$= \mathscr{P}_0 \frac{1}{u} \left(\sum_{k\neq l} |t_{kl}|^2 (2\boldsymbol{S}_k \cdot \boldsymbol{S}_l - \frac{1}{2}) \right) \mathscr{P}_0, \tag{2.32}$$

which, upon changing indices and dropping the projectors $\mathscr{P}_0$, corresponds to the famous Heisenberg Hamiltonian:

$$\mathscr{H}' = \sum_{i \neq j} -J_{ij} \boldsymbol{S}_j \cdot \boldsymbol{S}_j + const. \tag{2.33}$$

where we define the exchange coupling as

$$J_{ij} = \frac{2|t_{ij}|^2}{u}. \tag{2.34}$$

and a minus sign to make the notation consistent with the convention $J_{ij} > 0 \Rightarrow$ ferromagnetic ground state $J_{ij} < 0 \Rightarrow$ antiferromagnetic ground state (see Fig.2.6). We have therefore successfully established that the ground state properties of the spin degree of freedom in the half-filled Hubbard model in the strong interacting limit $u/t \gg 1$ are described by the Heisenberg model.

Up until now, all the considerations regarding magnetic ordering, while of fundamental qualitative relevance, failed to capture one essential feature of magnetic materials: even established that magnetic ordering exists in our system, how can we predict in which direction the macroscopic magnetization is going to point in an experimental setting? In other words, while we were able to build a model that wants all spins to align (or anti-align) with each other in the ground state, we are still completely oblivious as to which direction in space all these spins should be pointing towards. It turns out that we are missing one key ingredient to describe magnetism in real system: spin-orbit coupling.

2.2 Going beyond the Heisenberg model

2.2.1 Spin-orbit coupling: a small effect at the base of magnetism as we know it

Spin-orbit coupling (SOC) describes the coupling of the spin degree of freedom of electrons $\boldsymbol{S}$ with their orbital angular momentum $\boldsymbol{L}$. The energy scale of this interaction is typically about 10-100 times smaller than typical exchange energy described in the previous section, nevertheless it is of fundamental importance

in magnetism. Here we briefly outline the origin of this interaction, providing a quantum mechanical interpretation of the effect and finally show how its introduction in some models describing magnetic ordering, builds a much more realistic picture of magnetism.

The physical origin of atomic SOC

We sketch the physical origin of SOC by using the simplified picture of an electron orbiting around its static nucleus. When an electron of mass m and momentum $\boldsymbol{p}$ moves across the electric field $\boldsymbol{E}$ generated by the central potential of the nucleus, Lorentz invariance dictates that in the co-moving reference frame of the electron an additional magnetic field of the form $\boldsymbol{B} \propto \boldsymbol{p} \times \boldsymbol{E}/c^2$ is present. The electron spin $\boldsymbol{S}$ interacts with this magnetic field, which tries to align it along its direction. To account for this effect in the Hamiltonian we introduce an energy penalty for the electron spin misaligning from the effective magnetic field perceived by the orbiting electron

$$\mathscr{H}_{SOC} = \frac{e\hbar}{2m_e^2c^2}\boldsymbol{S}\cdot(\boldsymbol{p}\times\boldsymbol{E}). \tag{2.35}$$

At this point we express the electric field generated by the atomic core via a simple central field Ansatz

$$\boldsymbol{E} = -\nabla\Phi = -\nabla\frac{Ze}{4\pi\varepsilon_0 r}. \tag{2.36}$$

Taking advantage of the central symmetry of the problem (i.e the potential only depends on the radius) we can rewrite the differential operator as $\nabla\Phi(r) \to \frac{\boldsymbol{r}}{r}\frac{d\Phi(r)}{dr}$, allowing us to recover the familiar SO coupling term

$$\boldsymbol{E} = \frac{Ze}{4\pi\varepsilon_0 r^3}\boldsymbol{r} \tag{2.37}$$

$$\Rightarrow \mathscr{H}_{SOC} = -\frac{e\hbar}{2m_e^2c^2}\boldsymbol{S}\cdot(\boldsymbol{p}\times\nabla\Phi) = -\frac{e\hbar^2}{2m_e^2c^2}\frac{1}{r}\frac{\mathrm{d}\Phi(r)}{\mathrm{d}r}\boldsymbol{S}\cdot\boldsymbol{L} = \xi_{nl}(r)\boldsymbol{S}\cdot\boldsymbol{L}, \tag{2.38}$$

where we have used the fact that $\boldsymbol{p} \times \boldsymbol{r} = \hbar \boldsymbol{L}$. To highlight the energy scale of SO interaction, we define the expectation value $\zeta_{nl} = \langle \xi_{nl}(r) \rangle > 0$

$$\zeta_{nl} = \int_0^\infty R_{nl}(r) \xi_{nl}(r) R_{nl}^*(r) r^2 dr, \tag{2.39}$$

where $R_{nl}(r)$ represents the radial part of the hydrogen ground state wave function. The spin-orbit parameter ζ_{nl} can be computed [45], revealing the following general trends

- The SOC energy is of the order of $10 - 100$ meV in $3d$ transition metals, making it considerably weaker than the exchange interaction ≈ 1 eV and ligand field splitting effects.
- The strength of the SOC scales with Z^4, meaning it becomes very strong for heavier elements.
- It is of particular relevance for rare earth elements, which together with a higher Z, possess partially shielded $4f$ electrons that are less influenced from ligand field effects.

Despite its modest strength in $3d$ systems, SOC has the fundamental role of connecting the magnetic ground state of the system to the crystal lattice, introducing the so called magnetocrystalline anisotropy phenomenon which is at the heart of a lot of technological concepts involving magnetic materials.

SOC in solid state systems: Rashba SOC and Dresselhaus SOC

As described above, an electron with momentum $\boldsymbol{p}$ moving across an electric field $\boldsymbol{E}$ experiences an effective magnetic field $\boldsymbol{B}_{eff} \approx \boldsymbol{E} \times \boldsymbol{p}/mc^2$ in its rest frame, which induces a momentum-dependent Zeeman energy. In the presence of a central potential, this yields the usual Russell-Saunders form of SOC of eq.(2.38). In systems with structural inversion symmetry broken along the growth direction $\hat{e}_z$ (such as quantum wells or material interfaces), the spin sub-bands are split (see Fig.2.3), and the spin degree of freedom appears to be bound to the linear momentum of the electrons implying the spin is sensitive to his orbital environment. One could attribute this splitting to the electric field resulting from the interface electric field, i.e. set $\boldsymbol{E} = E_z \hat{e}_z$ in eq.(2.38) and obtain the famous Rashba SOC term

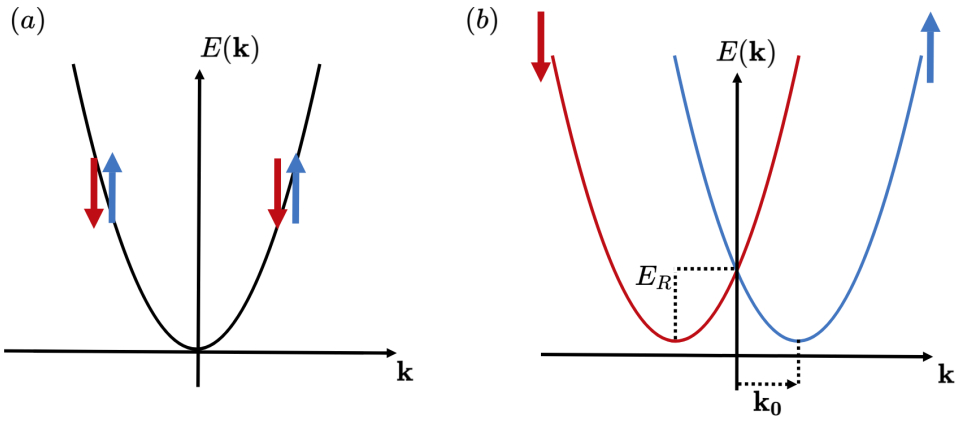

Fig. 2.3 Basics of Rashba spin-splitting (a) Non spin polarized band dispersion in the absence of Rashba SOC (b) Dispersion relation for a non-magnetic free electron gas in the presence of Rashba SOC (see eq.(2.40)) The blue and red parabolas represent the spin split bands.

$$\mathscr{H}_R = \frac{\alpha_R}{\hbar}(\hat{e}_z \times \boldsymbol{k}) \cdot \boldsymbol{\sigma} \tag{2.40}$$

which indeed yields the correct symmetry properties of the band structure. Relating the parameter α_R to the experimental observations however immediately shows the limits of this approach, as relating it to the interface electric field ends up vastly underestimating the effect. The correct physical picture is indeed more intricate [46] and reveals how the absence of inversion symmetry has the important additional effect of distorting the Bloch Wave functions such that they acquire a finite, momentum dependent orbital magnetic moment which is then coupled to the spin degree of freedom via the intra-atomic Russell-Saunders SOC. One of the first microscopic scenarios for Rashba spin splitting at the surface of Au was based on a minimal tight binding model assuming only (s,p) orbitals being the drivers of the mechanism [47]. Indeed, going through the detailed calculations highlights how $\alpha_R \propto \xi \cdot \gamma$, where ξ encodes the strength of the atomistic SOC and γ parametrizes the magnitude of inversion symmetry breaking along $\hat{e}_z$. It was later shown how γ is determined by the asymmetry of the Bloch functions in the vicinity of the nuclei and can in principle be influenced by external electric fields [48]. We emphasize how the shape of the Rashba SOC term is indeed a consequence of the symmetry properties of the symmetry breaking at the surface and that more complex symmetry breaking

patterns found in e.g. bulk materials can indeed lead to richer forms of SOC, called Dresselhaus SOC.

2.3 Microscopic origin of magneto-crystalline anisotropy

2.3.1 SOC as the source of magneto-crystalline anisotropy

A very clear and rigorous theoretical treatment of magnetocrystalline anisotropy in 3*d* transition metals appears with Patrick Bruno [49], who derived his model by computing the change in energy as a consequence of SOC in a tight binding model. In the following we show the steps of the derivation of [49, 50]. The assumptions of the model can be summarized as follows:

- The 3*d* electrons in the Bruno model are located on a lattice and do not interact with each other via Coulomb repulsion. This situation is perfectly captured by the non interacting limit of the Hubbard model ($U = 0$) discussed in Appendix A. We emphasize how this actually implies that, in the Bruno model, magnetic exchange interaction is not considered, i.e. it is a model purely addressing the interaction of electrons with the crystal field as a consequence of spin orbit coupling.
- Without SOC, the unperturbed Hamiltonian can be written in second quantized form as follows

$$\mathscr{H}_0 = -\sum_{<i,j>,n,\sigma} t_{ij}(c^{\dagger}_{jn\sigma}c_{in\sigma} + h.c.) \tag{2.41}$$

  or, in momentum space,

$$\mathscr{H}_0 = -\sum_{\boldsymbol{k},n,\sigma} \varepsilon_n(\boldsymbol{k})c^{\dagger}_{n\sigma}(\boldsymbol{k})c_{n\sigma}(\boldsymbol{k}) \tag{2.42}$$

  Where n represents the energy level index, σ the spin index, i, j the lattice site locations and $\boldsymbol{k}$ the crystal momentum.

- The eigenstates with energies $\varepsilon_n(\boldsymbol{k})$ of this Hamiltonian are Bloch functions of the form

$$|\boldsymbol{k}, n, \sigma\rangle = \sum_{\mu} a_{n,\mu,\sigma}(\boldsymbol{k}) \, |\boldsymbol{k}, \mu, \sigma\rangle \tag{2.43}$$

  where μ indicates the sub-orbitals corresponding to the main quantum number n. In the case of $3d$ elements $\mu \in \{d_{yz}, d_{zx}, d_{xy}, d_{x^2-y^2}, d_{3z^2-r^2}\}$.

- The system is perturbed by the presence of SOC which, in the Slater-Koster (SK) basis (2.43), can be expressed as follows [49, 50]

$$\mathscr{H}_{SOC} = \xi \sum_{\mu_1,\mu_2,\sigma_1,\sigma_2} \langle \mu_1, \sigma_1 | \mathbf{L} \cdot \mathbf{S} | \mu_2, \sigma_2 \rangle \times \sum_{k} c^{\dagger}_{\mu_1,\sigma_1}(\mathbf{k}) c_{\mu_2,\sigma_2}(\mathbf{k}), \tag{2.44}$$

  where we have used the fact that the SOC operator is diagonal in the momentum index. The matrix elements $\langle \sigma_1, \mu_1 | \mathbf{L} \cdot \mathbf{S} | \sigma_2, \mu_2 \rangle$ are expressible analytically and are reported in [51, 52].

At this point we can proceed and compute the second order energy correction as a consequence of SOC. The validity of the perturbational approach is guaranteed by the fact that in $3d$ metals, the energy scale of SOC, ξ, is indeed $10-100$ times smaller than crystal field splitting effects ($\approx 1eV$). To second order in perturbation theory the energy correction can be written as

$$\delta E = \sum_{exc.} \frac{|\langle gr | \mathscr{H}_{SOC} | exc. \rangle|^2}{E_{gr} - E_{exc}} \tag{2.45}$$

Where $\langle gr|$ indicates the metallic, unperturbed state of the system. Since the spin-orbit coupling operator is a one body operator diagonal in $\mathbf{k}$, we only need to take in account excited states $|exc.\rangle$ of the form

$$|exc.\rangle = c^{\dagger}_{n_2\sigma_2}(\mathbf{k}) c_{n_1\sigma_1}(\mathbf{k}) \, |gr\rangle \, , \tag{2.46}$$

as all the other ones would disappear in the evaluation of the expectation value by means of the Wick theorem

$$\Rightarrow \delta E = \sum_{\substack{k,n_1,n_2 \\ \sigma_1,\sigma_2}} \frac{\langle gr | \mathscr{H}_{SOC} c^{\dagger}_{n_2\sigma_2} c_{n_1\sigma_1} | gr \rangle \, \langle gr | c^{\dagger}_{n_1\sigma_1} c_{n_2\sigma_2} \mathscr{H}_{SOC} | gr \rangle}{\varepsilon_{n_1,\sigma_1}(\mathbf{k}) - \varepsilon_{n_2,\sigma_2}(\mathbf{k})}. \tag{2.47}$$

If we change the basis to the SK basis according to (2.43) we have

$$c^{\dagger}_{n_2\sigma_2}(\mathbf{k}) = \sum_{\mu} a_{n_2\mu\sigma_2} c^{\dagger}_{\mu\sigma_2}(\mathbf{k}), \tag{2.48}$$

allowing us to rewrite (2.3.1) as

$$\delta E = \sum_{\substack{k,n_1,n_2\\ \sigma_1,\sigma_2}} \sum_{\substack{\alpha,\beta\\ \gamma,\delta}} \frac{\langle gr|\mathscr{H}_{SOC} c^{\dagger}_{\alpha\sigma_2} c_{\beta\sigma_1}|gr\rangle \langle gr|c^{\dagger}_{\gamma\sigma_1} c_{\delta\sigma_2} \mathscr{H}_{SOC}|gr\rangle a_{n_2,\alpha,\sigma_2} a^{*}_{n_1,\beta,\sigma_1} a^{*}_{n_2,\delta,\sigma_2} a_{n_1,\gamma,\sigma_1}}{\varepsilon_{n_1,\sigma_1}(\mathbf{k}) - \varepsilon_{n_2,\sigma_2}(\mathbf{k})}. \tag{2.49}$$

We remark how the momentum k label is implicit since we assume spin orbit coupling does not cause scattering to different momenta k'. We can now have a look at the matrix element contraction

$$\langle gr|\mathscr{H}_{SOC} c^{\dagger}_{\alpha\sigma_2} c_{\beta\sigma_1}|gr\rangle \langle gr|c^{\dagger}_{\gamma\sigma_1} c_{\delta\sigma_2} \mathscr{H}_{SOC}|gr\rangle . \tag{2.50}$$

By expressing the spin orbit coupling operator in the SK basis (2.44) we have

$$\begin{aligned}(2.50) = \xi^2 \sum_{\substack{\mu_{1\cdots4}\\ \bar{\sigma}_{1\cdots4}\\ k}} & \underbrace{\langle gr|c^{\dagger}_{\mu_2\bar{\sigma}_2} c_{\mu_1\bar{\sigma}_1} c^{\dagger}_{\alpha\sigma_2} c_{\beta\sigma_1}|gr\rangle}_{:=A} \underbrace{\langle gr|c^{\dagger}_{\gamma\sigma_1} c_{\delta\sigma_2} c^{\dagger}_{\mu_4\bar{\sigma}_4} c_{\mu_3\bar{\sigma}_3}|gr\rangle}_{:=B} \times \\ & \times \langle \mu_2,\bar{\sigma}_2|\mathbf{L}\cdot\mathbf{S}|\mu_1,\bar{\sigma}_1\rangle \langle \mu_4,\bar{\sigma}_4|\mathbf{L}\cdot\mathbf{S}|\mu_3,\bar{\sigma}_3\rangle \end{aligned} \tag{2.51}$$

The summations are simplified by the delta functions produced by the A and B terms

$$A = \delta_{\mu_2,\beta}\delta_{\mu_1,\alpha}\delta_{\bar{\sigma}_2,\sigma_1}\delta_{\bar{\sigma}_1,\sigma_2}, \tag{2.52}$$

$$B = \delta_{\mu_3,\gamma}\delta_{\mu_4,\delta}\delta_{\bar{\sigma}_3,\sigma_1}\delta_{\bar{\sigma}_4,\sigma_2}. \tag{2.53}$$

Performing the summations and plugging in (2.49) we have

$$\delta E = \xi^2 \sum_{\substack{k,n_1,n_2\\ \sigma_1,\sigma_2}} \sum_{\mu_{1\cdots4}} \frac{\langle \mu_1,\sigma_1|\mathbf{L}\cdot\mathbf{S}|\mu_2,\sigma_2\rangle \langle \mu_3,\sigma_2|\mathbf{L}\cdot\mathbf{S}|\mu_4,\sigma_1\rangle a^{*}_{n_1,\mu_1,\sigma_1} a_{n_1,\mu_4,\sigma_1} a^{*}_{n_2,\mu_3,\sigma_2} a_{n_2,\mu_2,\sigma_2}}{\varepsilon_{n_1,\sigma_1}(\mathbf{k}) - \varepsilon_{n_2,\sigma_2}(\mathbf{k})}. \tag{2.54}$$

To rid ourselves of the sum over n_1, n_2 , we can now introduce the generalized density of states

$$n_{\mu_1,\mu_2,\sigma}(\mathbf{k},\varepsilon) = \sum_n a^*_{n,\mu_1,\sigma}(\mathbf{k}) a_{n,\mu_2,\sigma}(\mathbf{k}) \delta(\varepsilon - \varepsilon_{n,\sigma}(\mathbf{k})), \tag{2.55}$$

which allows us to introduce the notation

$$\begin{aligned}\Rightarrow \delta E = -\xi^2 \int_{\varepsilon_2<\varepsilon_F<\varepsilon_1} \frac{d\varepsilon_1\, d\varepsilon_2}{\varepsilon_2 - \varepsilon_1} \sum_{\substack{\mu_{1\cdots4}\\ \sigma_1,\sigma_2,k}} \underbrace{\left(\sum_{n_1} a^*_{n_1,\mu_1,\sigma_1} a_{n_1,\mu_4,\sigma_1} \delta(\varepsilon_1 - \varepsilon_{n_1,\sigma_1}(\mathbf{k})) \right)}_{n_{\mu_1,\mu_4,\sigma_1}(\mathbf{k},\varepsilon_1)} \\ \times \underbrace{\left(\sum_{n_2} a^*_{n_2,\mu_3,\sigma_2} a_{n_2,\mu_2,\sigma_2} \delta(\varepsilon_2 - \varepsilon_{n_2,\sigma_2}(\mathbf{k})) \right)}_{n_{\mu_3,\mu_2,\sigma_3}(\mathbf{k},\varepsilon_2)} \times \langle \mu_1,\sigma_1|\mathbf{L}\cdot\mathbf{S}|\mu_2,\sigma_2\rangle \langle \mu_3,\sigma_2|\mathbf{L}\cdot\mathbf{S}|\mu_4,\sigma_1\rangle\end{aligned} \tag{2.56}$$

$$\begin{aligned}\delta E = \sum_{\lambda,\sigma_1,\sigma_2,k} \underbrace{\int_{\varepsilon_2<\varepsilon_F<\varepsilon_1} \frac{d\varepsilon_1\, d\varepsilon_2}{\varepsilon_2 - \varepsilon_1} n_{\mu_1,\mu_4,\sigma_1}(\mathbf{k},\varepsilon_1) n_{\mu_3,\mu_2,\sigma_3}(\mathbf{k},\varepsilon_2)}_{\mathscr{A}(\theta,\sigma_1,\sigma_2)} \\ \times \langle \mu_1,\sigma_1|\mathbf{L}\cdot\mathbf{S}|\mu_2,\sigma_2\rangle \langle \mu_3,\sigma_2|\mathbf{L}\cdot\mathbf{S}|\mu_4,\sigma_1\rangle\end{aligned} \tag{2.57}$$

where we have condensed the μ index summation in the λ symbol, i.e.

$$\sum_\lambda \equiv \sum_{\mu_{1\cdots4}} \tag{2.58}$$

It can be shown [49], that the invoking the following properties of the SOC matrices

$$\langle \mu_1,\sigma_1|\mathbf{L}\cdot\mathbf{S}|\mu_2,\sigma_2\rangle \langle \mu_3,\sigma_2|\mathbf{L}\cdot\mathbf{S}|\mu_4,\sigma_1\rangle = \langle \mu_1,-\sigma_1|\mathbf{L}\cdot\mathbf{S}|\mu_2,-\sigma_2\rangle \langle \mu_3,-\sigma_2|\mathbf{L}\cdot\mathbf{S}|\mu_4,-\sigma_1\rangle \tag{2.59}$$

$$\Rightarrow \langle \mu_1,\sigma_1|\mathbf{L}\cdot\mathbf{S}|\mu_2,\sigma_2\rangle \langle \mu_3,\sigma_2|\mathbf{L}\cdot\mathbf{S}|\mu_4,\sigma_1\rangle = \mathrm{Re}(\langle \mu_1,\sigma_1|\mathbf{L}\cdot\mathbf{S}|\mu_2,\sigma_2\rangle \langle \mu_3,\sigma_2|\mathbf{L}\cdot\mathbf{S}|\mu_4,\sigma_1\rangle) \tag{2.60}$$

and

$$\mathrm{Re}(\langle \mu_1,\sigma|\mathbf{L}\cdot\mathbf{S}|\mu_2,-\sigma\rangle \langle \mu_3,-\sigma|\mathbf{L}\cdot\mathbf{S}|\mu_4,\sigma\rangle) = const. - \langle \mu_1,\uparrow|\mathbf{L}\cdot\mathbf{S}|\mu_2,\uparrow\rangle \langle \mu_3,\uparrow|\mathbf{L}\cdot\mathbf{S}|\mu_4,\uparrow\rangle . \tag{2.61}$$

The notation can be simplified significantly. Plugging (2.61) in (2.57) and neglecting the constant offset when we sum over the spin indices we have

$$\delta E = -\xi^2 \sum_{\lambda} \langle \mu_1, \uparrow | \mathbf{L}\cdot\mathbf{S} | \mu_2, \uparrow \rangle \langle \mu_3, \uparrow | \mathbf{L}\cdot\mathbf{S} | \mu_4, \uparrow \rangle \times \\ \times (\mathscr{A}(\uparrow,\uparrow,\lambda) - \mathscr{A}(\uparrow,\downarrow,\lambda) - \mathscr{A}(\downarrow,\uparrow,\lambda) + \mathscr{A}(\downarrow,\downarrow,\lambda)). \tag{2.62}$$

By redefining $(\mathscr{A}(\uparrow,\uparrow,\lambda) - \mathscr{A}(\uparrow,\downarrow,\lambda) - \mathscr{A}(\downarrow,\uparrow,\lambda) + \mathscr{A}(\downarrow,\downarrow,\lambda)) \equiv G(\lambda)$ we can simplify the notation and obtain

$$\delta E = -\xi^2 \sum_{\lambda} \langle \mu_1, \uparrow | \mathbf{L}\cdot\mathbf{S} | \mu_2, \uparrow \rangle \langle \mu_3, \uparrow | \mathbf{L}\cdot\mathbf{S} | \mu_4, \uparrow \rangle \times G(\lambda). \tag{2.63}$$

Explicitly evaluating of the matrix elements $\boldsymbol{L}\cdot\boldsymbol{S}$ and exploiting the symmetry properties of considered system, one can obtain different expressions for magneto-crystalline anisotropy [49]. For a mono atomic thin film hosting $3d$-orbitals (see Tables 2.1 and 2.2) with (001) or (111) orientation one obtains the expression

$$\delta E = K_0 + K_1 \sin^2(\theta), \tag{2.64}$$

while for a (110) orientation we have

$$\delta E = K_0 + K_1 \sin^2(\theta) + K_2 \sin^2(\theta)\cos(2\phi), \tag{2.65}$$

where the $K_i(\xi, G(\lambda))$ coefficients are all functions of the spin orbit coupling parameter ξ and the $G(\lambda)$ function which relates the anisotropy coefficients to the band structure of the material.

Table 2.1 $\langle \mu_i, \sigma_1 | \boldsymbol{L} \cdot \boldsymbol{S} | \mu_j, \uparrow \rangle$ Matrix elements for $3d$-orbitals.

$\langle \mu_i, \sigma_1 \vert \boldsymbol{L} \cdot \boldsymbol{S} \vert \mu_j, \sigma_2 \rangle$	$\vert xy\uparrow\rangle$	$\vert yz\uparrow\rangle$	$\vert zx\uparrow\rangle$	$\vert x^2-y^2\uparrow\rangle$	$\vert 3z^2-r^2\uparrow\rangle$
$\langle xy\uparrow\vert$	0	$i\sin(\theta)\sin(\phi)/2$	$-i\sin(\theta)\cos(\phi)/2$	$i\cos(\theta)$	0
$\langle yz\uparrow\vert$	$-i\sin(\theta)\sin(\phi)/2$	0	$i\cos(\theta)/2$	$-i\sin(\theta)\cos(\phi)/2$	$-i\sqrt{3}\sin(\theta)\cos(\phi)/2$
$\langle zx\uparrow\vert$	$i\sin(\theta)\cos(\phi)/2$	$-i\cos(\theta)/2$	0	$-i\sin(\theta)\sin(\phi)/2$	$-i\sqrt{3}\sin(\theta)\sin(\phi)/2$
$\langle x^2-y^2\uparrow\vert$	$-i\cos(\theta)$	$i\sin(\theta)\cos(\phi)/2$	$i\sin(\theta)\sin(\phi)/2$	0	0
$\langle 3z^2-r^2\uparrow\vert$	0	$i\sqrt{3}\sin(\theta)\sin(\phi)/2$	$-i\sqrt{3}\sin(\theta)\sin(\phi)/2$	0	0
$\langle xy\downarrow\vert$	0	$(i\cos(\theta)\sin(\phi)-\cos(\phi))/2$	$-(i\cos(\theta)\cos(\phi)+\sin(\phi))/2$	$-i\sin(\theta)$	0
$\langle yz\downarrow\vert$	$(\cos(\phi)-i\cos(\theta)\sin(\phi))/2$	0	$-i\sin(\theta)/2$	$-(\sin(\phi)+i\cos(\theta)\cos(\phi))/2$	$-\sqrt{3}(\sin(\phi)+i\cos(\theta)\cos(\phi))/2$
$\langle zx\downarrow\vert$	$-(\sin(\phi)+i\cos(\theta)\cos(\phi))/2$	$i\sin(\theta)/2$	0	$(\cos(\phi)-i\cos(\theta)\sin(\phi))/2$	$-\sqrt{3}(\sin(\phi)-i\cos(\theta)\sin(\phi))/2$
$\langle x^2-y^2\downarrow\vert$	$i\sin(\theta)$	$(\sin(\phi)+\cos(\theta)\cos(\phi))/2$	$(-\cos(\phi)+i\cos(\theta)\sin(\phi))/2$	0	0
$\langle 3z^2-r^2\downarrow\vert$	0	$\sqrt{3}(\sin(\phi)+i\cos(theta))/2$	$\sqrt{3}(\cos(\phi)-i\cos(\theta)\sin(\phi))/2$	0	0

Table 2.2 $\langle \mu_i, \sigma_1 | \boldsymbol{L} \cdot \boldsymbol{S} | \mu_j, \downarrow \rangle$ Matrix elements for $3d$-orbitals.

$\langle \mu_i, \sigma_1 \vert \boldsymbol{L} \cdot \boldsymbol{S} \vert \mu_j, \sigma_2 \rangle$	$\vert xy\downarrow\rangle$	$\vert yz\downarrow\rangle$	$\vert zx\downarrow\rangle$	$\vert x^2-y^2\downarrow\rangle$	$\vert 3z^2-r^2\downarrow\rangle$
$\langle xy\uparrow\vert$	0	$(i\cos(\theta)\sin(\phi)+\cos(\phi))/2$	$(-i\cos(\theta)\cos(\phi)+\sin(\phi))/2$	$-i\sin(\theta)$	0
$\langle yz\uparrow\vert$	$-(\cos(\phi)+i\cos(\theta)\sin(\phi))/2$	0	$-i\sin(\theta)/2$	$(\sin(\phi)-i\cos(\theta)\cos(\phi))/2$	$\sqrt{3}(\sin(\phi)-i\cos(\theta)\cos(\phi))/2$
$\langle zx\uparrow\vert$	$(\sin(\phi)-i\cos(\theta)\cos(\phi))/2$	$i\sin(\theta)/2$	0	$-(\cos(\phi)+i\cos(\theta)\sin(\phi))/2$	$\sqrt{3}(\sin(\phi)+i\cos(\theta)\sin(\phi))/2$
$\langle x^2-y^2\uparrow\vert$	$i\sin(\theta)$	$-(\sin(\phi)-i\cos(\theta)\cos(\phi))/2$	$(\cos(\phi)+i\cos(\theta)\sin(\phi))/2$	0	0
$\langle 3z^2-r^2\uparrow\vert$	0	$-\sqrt{3}(\sin(\phi)-i\cos(theta))/2$	$-\sqrt{3}(\cos(\phi)+i\cos(\theta)\sin(\phi))/2$	0	0
$\langle xy\downarrow\vert$	0	$-i\sin(\theta)\sin(\phi)/2$	$i\sin(\theta)\cos(\phi)/2$	$-i\cos(\theta)$	0
$\langle yz\downarrow\vert$	$i\sin(\theta)\sin(\phi)/2$	0	$-i\cos(\theta)/2$	$i\sin(\theta)\cos(\phi)/2$	$i\sqrt{3}\sin(\theta)\cos(\phi)/2$
$\langle zx\downarrow\vert$	$-i\sin(\theta)\cos(\phi)/2$	$i\cos(\theta)/2$	0	$i\sin(\theta)\sin(\phi)/2$	$i\sqrt{3}\sin(\theta)\sin(\phi)/2$
$\langle x^2-y^2\downarrow\vert$	$i\cos(\theta)$	$-i\sin(\theta)\cos(\phi)/2$	$-i\sin(\theta)\sin(\phi)/2$	0	0
$\langle 3z^2-r^2\downarrow\vert$	0	$-i\sqrt{3}\sin(\theta)\sin(\phi)/2$	$+i\sqrt{3}\sin(\theta)\sin(\phi)/2$	0	0

Relation between magneto-crystalline anisotropy and orbital magnetic moment anisotropy

To elucidate the physical origin of magneto-crystalline anisotropy detailed above, it is instructive to compute the second order perturbational correction of the angular momentum as a consequence of SOC. We write the expectation value of the orbital magnetic moment in the presence of SOC in second order perturbation theory

$$\langle \boldsymbol{L} \rangle = \sum_{exc} \frac{\langle gr|\boldsymbol{L}|exc\rangle \langle exc|H_{s.o}|gr.\rangle}{E_{gr} - E_{exc}}, \tag{2.66}$$

where the orbital angular momentum operator in second quantized form can be expressed as

$$\boldsymbol{L} = 4 \sum_{\mu_1,\mu_2,\sigma,\zeta} \langle \mu_2|\boldsymbol{L}_\zeta|\mu_1\rangle \sum_k c^\dagger_{\mu_2,\sigma}(\boldsymbol{k}) c_{\mu_1,\sigma}(\boldsymbol{k}), \tag{2.67}$$

with ζ representing the spin quantization axis. Since the angular momentum operator is diagonal in the spin index (i.e. it cannot induce spin flipping), only matrix elements of the spin orbit coupling operator that do not include spin flipping terms can survive the summation over excited states. We can evidence them by decomposing the spin-orbit coupling operator $\boldsymbol{L}\cdot\boldsymbol{S}$ as

$$\boldsymbol{L}\cdot\boldsymbol{S} = L_\zeta S_\zeta + \frac{1}{2}(L_+ S_- + L_- S_+) \tag{2.68}$$

where $S_\pm$ and $L_\pm$ represent spin and angular momentum raising/lowering operators. The only surviving terms of the $\sum_{exc}$ summation are the ones involving the term $L_\zeta S_\zeta$. An analogous calculation procedure as the one described in Section.6.2.2 [50] allows us to write the expectation value in (2.66) as

$$\langle \boldsymbol{L} \rangle = -4\xi \sum_{\lambda,\sigma} \mathscr{A}(\lambda,\sigma,\sigma) \langle \mu_1|\boldsymbol{L}|\mu_2\rangle \langle \mu_3|\boldsymbol{L}|\mu_4\rangle \langle \sigma|\boldsymbol{S}|\sigma\rangle \tag{2.69}$$

If we now project onto the SQA, we obtain

$$\langle L_\zeta \rangle = -4\xi \sum_{\lambda,\sigma} \mathscr{A}(\lambda,\sigma,\sigma) \langle \mu_1 | L_\zeta | \mu_2 \rangle \langle \mu_3 | L_\zeta | \mu_4 \rangle \langle \sigma | S_\zeta | \sigma \rangle \tag{2.70}$$

$$= -4\xi \sum_{\lambda} [\mathscr{A}(\lambda,\uparrow,\uparrow) - \mathscr{A}(\lambda,\downarrow,\downarrow)] \langle \mu_1 | L_\zeta | \mu_2 \rangle \langle \mu_3 | L_\zeta | \mu_4 \rangle . \tag{2.71}$$

$$= -4\xi (\langle L_\zeta^\uparrow \rangle - \langle L_\zeta^\downarrow \rangle) \tag{2.72}$$

From the decomposition of eq.(2.68), we can derive the useful identity

$$\langle \mu\ \sigma | \boldsymbol{L}\cdot\boldsymbol{S} | \mu'\ \sigma \rangle = \langle \mu\ \sigma | L_\zeta S_\zeta | \mu'\ \sigma \rangle = \frac{\sigma}{2} \langle \mu\ \sigma | L_\zeta | \mu'\ \sigma \rangle \tag{2.73}$$

which allows us to rewrite the $\langle L_\zeta \rangle$ of (2.71) as

$$\langle L_\zeta \rangle = -4\xi \sum_{\lambda} \mathscr{A}(\lambda,\uparrow,\uparrow) \langle \mu_1 \uparrow | \boldsymbol{L}\cdot\boldsymbol{S} | \mu_2 \uparrow \rangle \langle \mu_3 \uparrow | \boldsymbol{L}\cdot\boldsymbol{S} | \mu_4 \uparrow \rangle - \tag{2.74}$$

$$\mathscr{A}(\lambda,\downarrow,\downarrow) \langle \mu_1 \downarrow | \boldsymbol{L}\cdot\boldsymbol{S} | \mu_2 \downarrow \rangle \langle \mu_3 \downarrow | \boldsymbol{L}\cdot\boldsymbol{S} | \mu_4 \downarrow \rangle . \tag{2.75}$$

Having rewritten $\langle L_\zeta \rangle$ in this form allows us to draw some similarities with the energy correction due to spin-orbit coupling δE in (2.63). If we neglect spin flipping terms $\propto \langle \mu\ (\uparrow\downarrow) | \boldsymbol{L}\cdot\boldsymbol{S} | \mu'\ (\downarrow\uparrow) \rangle$ and assume that the majority spin channel is fully occupied (i.e. we have a vanishing orbital momentum $\langle L_\zeta^\uparrow \rangle = 0$) we immediately see how the energy correction δE becomes proportional to the orbital magnetic moment component projected onto the spin quantization axis

$$\delta E = 4\xi \langle L_\zeta^\downarrow \rangle , \tag{2.76}$$

or, recalling the relationship between orbital magnetic moment and orbital moment $\boldsymbol{m}_\zeta^o = -\mu_B \langle L_\zeta \rangle$ we have another important result from the Bruno model [49]

$$\delta E = -\frac{4\xi}{\mu_B} m_\zeta^o . \tag{2.77}$$

The explicit dependence of the orbital magnetic moment on the spin quantization axis ζ clearly shows the anisotropic nature of this energy contribution. The relation (2.77) tells us that in a $3d$-transition metal where the majority spin channel is completely occupied, the energy is minimized in the direction where the orbital magnetic moment is the largest. We remark how this statement is in general only

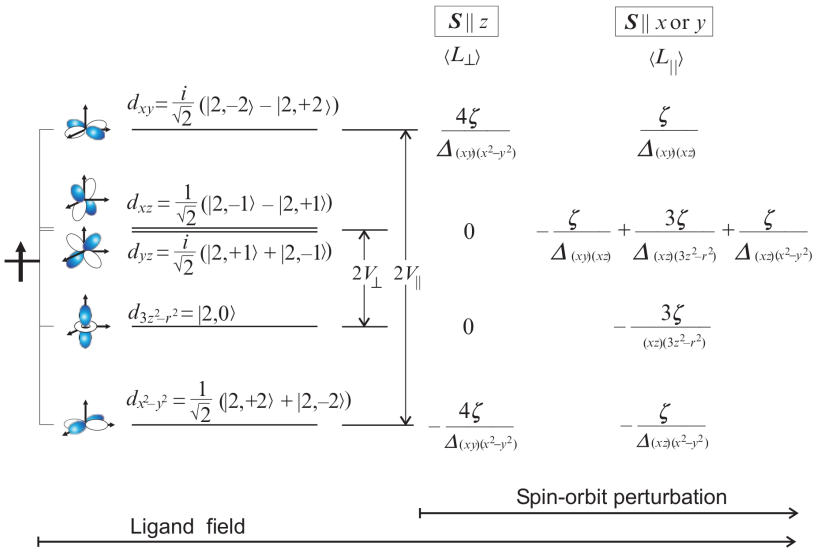

Fig. 2.4 Orbital momentum anisotropy in a crystal field with tetragonal symmetry. For simplicity, we assume large exchange splitting and consider only the minority spin band. The inclusion of SOC in lowest order perturbation theory (see 2.3.1) results in new states with anisotropic orbital magnetic moment (units of $\hbar$). The indicated orbital momenta for SQA alignment $\boldsymbol{S} \parallel z$-axis and $\boldsymbol{S} \parallel x-$ or $y-$axis results for only mixing spins in the minority band. Reproduced from [4]

true given the mentioned assumptions and in the most general cases, spin flipping terms also have to be taken into account [50].

2.3.2 Origin of orbital magnetic moment anisotropy in $3d$ transition metals

Thus far, we have successfully established a relation between the minimum energy state of an electronic system with the direction in which the orbital magnetic moment is maximized via eq.(2.77). We emphasize however, that the underlying causes of the anisotropic orbital magnetic moment in $3d$ magnetic transition metals remain to be cleared. In order to provide an intuitive picture of the underlying physical picture, we illustrate the textbook case of a Co monolayer [4].

In the context of $3d$ transition metals, the otherwise degenerate energy levels of the d-shell experience a splitting due to the bonding environment created by the crystal field [4]. This splitting results in the emergence of new d-orbitals that possess

a significant energy separation (≈ 1 eV): e.g. in the case of Co, the tetragonal bonding environment imposes a crystal field that uplifts the degeneracy of the d-orbitals ($d_{xy}, d_{xz}, d_{yz}, d_{3z^2-r^2}, d_{x^2-y^2}$) (see Fig.2.4). However, the symmetry of the crystal field environment imposes constraints on the new eigenstates of the Hamiltonian, mandating them to be strictly real and thereby prohibiting the presence of any orbital angular momentum [53]. According to eq.(2.77), this would imply a vanishing orbital moment anisotropy and, consequently, no MCA. As easily imaginable at this point, the missing ingredient to recover the correct answer lies in the key role played by SOC in 3d transition metals. Although the magnitude of SOC is considerably smaller than that of the crystal field effects ($\xi \approx 1\%$ of the crystal field splitting), this effect plays a crucial role by modifying the eigenstates as linear combinations of the pure d-orbitals allowed by the crystal field environment. Importantly, the broken time reversal symmetry resulting from SOC allows for the reinstatement of the orbital magnetic moment that had been suppressed by the crystal field environment. The expression for the orbital moment of a perturbed state $|n\rangle$ in the presence of SOC can be now be written as

$$\langle L_\zeta^n \rangle = \xi \sum_{m \neq n} \frac{|\langle d_n^\uparrow | L_\zeta | d_m^\uparrow \rangle|^2}{\Delta_{nm}} \tag{2.78}$$

where the sum runs over all zero-order spin-up states $|d_m^\uparrow\rangle$ and Δ_{nm} represents the energy separation of the 2 states. From the right side of Fig.2.4, we see that the orbital magnetic moment for each of the perturbed orbitals is different depending on orientation of the spin quantization axis, i.e. it is anisotropic. This anisotropy as well as the orbital moment however, vanishes if we sum over all the states implying that a partially filled d-shell is necessary to display finite orbital magnetic moment anisotropy and by consequence, magnetocrystalline anisotropy. By use of the crystal field concepts described above, we can now discuss the results for a Co ML: the crystal field in the tetrahedral bonding environment of a Co monolayer induces the energy splitting of the molecular d-orbitals with the characteristic $V_\parallel > V_\perp$ [4], which implies

$$2V_\parallel = \Delta_{(xy)(x^2-y^2)}, \tag{2.79}$$

$$2V_\perp = \Delta_{(yz)(3z^2-r^2)}. \tag{2.80}$$

where $\Delta_{(n)(m)}$ denotes the difference between orbital states d_m and d_n. Assuming a completely filled spin-down band and a partially filled spin-up band, we obtain

$$m^o_{\zeta=x} = \mu_B \left(\frac{3\xi}{\Delta_{(xz)(3z^2-r^2)}} + \frac{\xi}{\Delta_{(xz)(x^2-y^2)}} \right) = \frac{\xi \mu_B}{2V_\parallel} \left(\frac{3}{R} + \frac{2}{R+1} \right), \tag{2.81}$$

$$m^o_{\zeta=z} = \mu_B \frac{4\xi}{\Delta_{(xy)(x^2-y^2)}} = \frac{2\xi \mu_B}{V_\parallel}, \tag{2.82}$$

where we have defined $R = V_\perp / V_\parallel$ and used the fact that $\Delta_{(xz)(x^2-y^2)} = V_\parallel + V_\perp$ as can be seen from Fig.2.4. Plugging these expressions in eq.(2.77), we immediately see that the easy axis imposed by the magneto-crystalline anisotropy lies out of plane for the case $R > 1$ and in plane for $R < 1$.

2.3.3 Interfacial perpendicular magnetic anistoropy at ferromagnet/oxide interfaces

Interfacial perpendicular magnetic anistoropy (iPMA) was first observed in FM metal/Oxide interfaces in 2002 [54] where the experimental setup consisted of a Platinum underlayer surmounted by 0.6 nm thick layer of Co and an Aluminum layer of varying thickness. The experiment aimed to investigate the changes in magnetic properties of Co resulting from controlled oxidation of the Aluminum layer, both in ambient air and in the presence of an oxygen plasma. The key observations were as follows:

- Following brief exposures to oxygen, the hysteresis loop of the Co layer displayed a slanted shape, accompanied by the absence of an anomalous Hall signal for the out-of-plane (OOP) magnetization component. This indicated the presence of an in-plane (IP) magnetic anisotropy, despite the Platinum underlayer's expected induction of SOC effects.

- With longer exposures to oxygen, two notable changes occurred: a square hysteresis loop with 100% remanence emerged, and an anomalous Hall signal appeared for the OOP component of the Co layer, indicating a transition from IP to OOP magnetization. Importantly, the 100% remanence suggested that the Co layer itself had not been oxidized.

To shed light on the underlying physical explanation of oxygen control of interfacial magnetic anisotropy, we examine a toy model with similar characteristics, namely an Fe/MgO thin films which has been investigated thoroughly both experimentally [55–57] and with first principles calculations [58, 59]. A key difference from the textbook case described previously in 2.3.2 is the presence of oxygen atoms in the vicinity of 3*d* ferromagnetic Fe atoms on the surface which result in a more complex bonding environment. The physical understanding of the observed phenomena can nonetheless be effectively captured, at least qualitatively, by the Bruno model outlined in eq.(2.77). Far away from the surface, the crystal field environment of the Fe atoms results in an very small orbital magnetic moment anisotropy (we remark that because of the presence of SOC, an anisotropy contribution is present, albeit roughly 100 smaller that the surface contribution) (see Fig.2.5-(a)) At the surface however, the bonding environment is significantly different due to the absence of neighboring Fe atoms and the presence of oxygen species coming from the MgO layer. In particular, the geometric positioning of O induces a strong hybridization between the Op_z and OOP 3d orbitals of iron which significantly reduces the electronic occupation of 3d orbitals with out-of-plane (OOP) character ($d_{3z^2-r^2}$,d_{xz},d_{yz}) compared to those with in-plane (IP) character ($d_{x^2-y^2}$,d_{xy}). This can be easily seen in Fig.2.5-(b), where the DOS integrated over all occupied states in the presence of SOC is calculated and reveals a difference of about 3% between the OOP and IP orbitals for Fe atoms at the interface with MgO. The resulting undercompensation of IP orbitals, coupled with the presence of SOC, results in a magnetic anisotropy energy that favors an OOP magnetization easy axis.

2.3.4 Magneto-ionic control of interfacial magnetism

As theoretically motivated (see 2.3.3 and 2.3.2), the properties of metal/oxide bilayers are heavily influenced by the oxygen stoichiometry and defect structure at the interface between these materials. Therefore, the ability to electrically tune these properties presents a promising new way for dynamically controlling magnetism with low-power and high-efficiency. The magnetism community has long been exploring the concept of inducing electric field effects on magnetization through direct field effects, aiming to induce band shifting or charge accumulation effects [60, 61]. More recently however, a novel approach to manipulating the magnetic properties of thin films involves harnessing the ionic transport in metal oxides driven by an electric

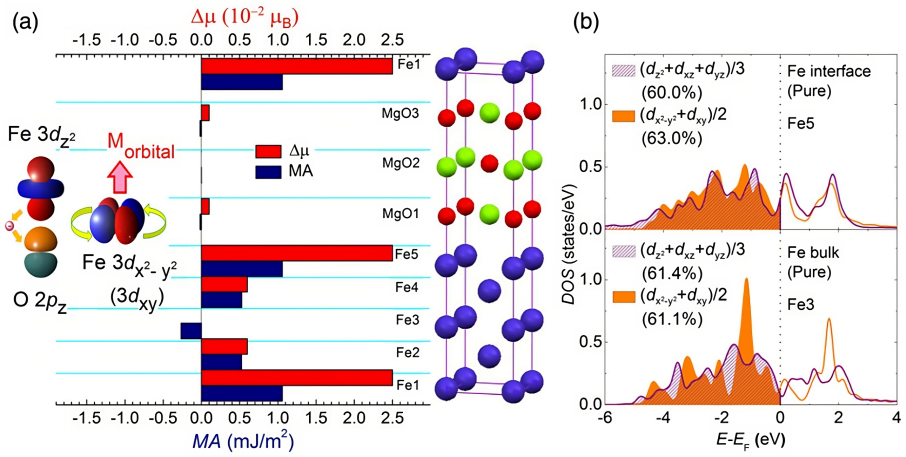

Fig. 2.5 (a) Layer-resolved orbital moment anisotropy ($\Delta\mu$) and magnetic anisotropy (MA) energy. Middle: Schematic representation of the crystalline structures calculated. Fe, Mg, and O are represented by large, medium, and small balls, respectively. (b) DOS with SOC for averaged out-of-plane ($d_{z^2-r^2} + d_{xz} + d_{yz}$) and IP Fe-3d orbitals ($d_{x^2-y^2} + d_{xy}$) for Fe at the interface (Fe5). Inset: a simple picture showing that PMA is produced by the hybridization of Fe out-of-plane orbitals ($d_{3z^2-r^2}$,d_{xz},d_{yz}) and O p_z orbitals. This hybridization leads to an uncompensated charge occupation in Fe in-plane orbitals ($d_{x^2-y^2}$,d_{xy}) and results in an enhanced out-of-plane orbital moment. Reproduced from [5]

field, which has led to the emergence of a new branch of nanomagnetism called "magneto-ionics".

A notable example of magneto-ionic control of magnetization was reported in 2015, where a Co/Oxide bilayer demonstrated direct in situ voltage-driven migration of O^{2-} ions, resulting in a toggle switch effect on the interfacial magnetic anisotropy already with 2V [38]. Subsequent developments revealed that the switching speed and stability of the switching process are heavily influenced by the material properties of the capping layer atop the magnetic one. For instance, the insertion of H^+-ions at Co/GdOx interfaces has shown reliable switching with no degradation after $>$ 2000 voltage cycles [39], while the use of yttria-stabilized zirconia (YSZ) [40] as a capping material exhibited a 100$\times$ acceleration of the switching process. These results suggest that further advancements in engineering proton-conducting materials could lead to even more substantial improvements in switching speed.

Another crucial aspect that requires attention is the seemingly unreliable reversibility of the switching process depending on the specific oxide employed. In a study by Fassatoui et al.[62], reversible voltage induced magnetization switching was observed in Pt/CoFe/AlOx and Pt/CoFe/TbOx samples, while the reversibility was

absent in the case of Pt/CoFe/MgO setup. The authors attributed this phenomenon to the distinct ionic mobility properties of the oxides in contact with the metallic ferromagnetic material, where AlOx and TbOx exhibited predominant ionic mobility from mobile oxygen species [62], while MgO displayed a significant ionic mobility component from Mg under the effect of a gate voltage. Furthermore, a study by Gilbert et al. (2016) [63] analyzed the ionic penetration of oxygen species in polycrystalline AlOx/GdOx/Co(15 nm) samples, revealing that oxygen species can penetrate through the entire magnetic layer with a sufficiently long application of gate voltage. The study also demonstrated that the reversibility of the magnetization switching depends on the depth of oxygen penetration, with shallow oxygen concentration near the surface resulting in fully reversible switching and deeper oxygen penetration leading to the loss of reversibility.

2.3.5 Recent advances in magneto-ionic research

One of the main strengths of magneto-ionic manipulation of interfacial magnetism is its potential to operate devices at significantly low energy levels compared to traditional current-based methods (magneto-ionic manipulation requires only 10 aJ/bit of energy [64] against the typical 10 fJ/bit [65] of VCMA). Another crucial advantage from a material perspective is the ability to induce non-volatile changes, offering functional plasticity and allowing for the creation of devices that can retain their magnetization state without the need for continuous power input.

However, despite these strengths, the field of magneto-ionics is still in its growth phase, and numerous challenges remain to be addressed:

- Magneto-ionic processes are slow in nature, which hinders their practical implementation.
- The driving factors at the basis of reversibility and robustness of induced magnetization changes are still debated in the community.
- Oxygen-based magneto-ionics, which has received considerable attention in the past decade, requires additional thermal assistance to enhance mobility and efficiency of magnetization change [63]. Furthermore, the penetration of oxygen ions into materials through ionic conduction channels can lead to irreversible changes and lattice distortion in the magnetic layer.

In response to these challenges, research groups are actively exploring various solution strategies. One such approach involves the use of N ions instead of O ions as the drivers of magneto-ionic changes [37]: the study compares nitrogen magneto-ionics in CoN to oxygen magneto-ionics in Co_3O_4 and shows that nitrogen transport occurs uniformly, creating a plane-wave-like migration front, without assistance of diffusion channels. Moreover, the use of N ions can reduce the threshold voltages required for effect, also indicating that this approach significantly reduces the timescales needed for magnetization changes, from hours to seconds. Another successful step forward involves the use of H^+ ions (protons) for magneto-ionic manipulation [39]. Although fast, the reduced size of the protons makes it challenging to identify the penetration depth in the magnetic layer. Furthermore, a deep implantation of the protons in the magnetic material has severe consequences regarding the reversibility of the magneto-ionic changes, presenting a new set of considerations for practical implementation. A third interesting path being pursued is the so called the "structural-ion" approach [66]: this approach aims at incorporating the migrating ions into the target material in its as-deposited state, therefore reducing structural distortions and leading to improved endurance of magneto-ionic manipulations. These research directions hold promise for overcoming the existing challenges and advancing the field of magneto-ionic manipulation towards practical applications.

2.4 Chiral interactions: Extended Heisenberg model

When magnetic systems display inversion symmetry breaking, the presence of spin-orbit coupling triggers the appearance of new forms of magnetic exchange that favor perpendicular alignment of neighboring spins, in contrast to Heisenberg exchange which only favors parallel or anti-parallel alignment. The Dzyaloshinskii-Moriya [67, 68] interaction (DMI) was first predicted by Igor Dzyaloshinskii, who hypothesized the presence of such an interaction to motivate weak ferromagnetic signatures in the antiferromagnet $\alpha-Fe_2O_3$. Tôru Moriya later formulated a robust mathematical derivation of this type of interaction by introducing a spin-orbit coupling term in a tight binding model and obtaining an effective Hamiltonian via a Schrieffer-Wolff transformation similar to the one discussed in 2.1.1.

While first discovered in 1958, the DMI has gained exponentially growing attention in the scientific community over the last 13 years due to its strong influence on many exotic spintronics phenomena. Nowadays the DMI has become essential for understanding and predicting many magnetism phenomena, such as weak ferromagnetism, spin glasses, cuprates, multiferroics, chiral and topological magnetism in heterostructures, thin film and bulk materials. Furthermore, this particular form of interaction is of great importance for future applications in the IT industry because it's at the heart of many physical phenomena relevant for novel computing architectures: to mention a few instances, DMI is a fundamental ingredient for stabilizing topological magnetic structures such as skyrmions and antiskyrmions [69–71], while at the same time being very important for the significant enhancement of magnetic domain wall velocity.

Tailoring the DMI in magnetic materials is of great importance for the future of material science, but despite much research, many challenging questions regarding the origins of DMI in magnetic materials still remain open to this day. In this section we first provide a derivation of DMI from a microscopic point of view, following the derivation by Tôru Moriya [67]. We then continue by describing some of the systems where DMI can be found, highlighting how contradicting discoveries are still being made to this day. We conclude by providing an overview of some of the methods used to manipulate chiral interactions in magnetic materials, paying special attention to the role of chemisorbed oxygen [7, 6] and of electric fields [58] in magnetic thin films.

2.4.1 Microscopic origin of DMI

In order to show how the presence of SOC can induce the appearance of chiral interactions in magnetic systems lacking inversion symmetry, we show the results of the pioneering work of Tôru Moriya [67]. Moriya successfully adapted Anderson's superexchange model [72] to account for SOC, showing how an effective spin model with these characteristics indeed resulted in the appearance of a spin-spin interaction favoring a canted magnetic order. Since it is based on the a superexchange model, Moriya indeed based his model on a tight-binding approach [43] rather than the Hubbard model approach we showed in 2.1.1. Despite this apparent discrepancy, the 2 approaches are very similar and can indeed be brought in contact as was done later [73].

We introduce atomic orbitals $|n,i,\uparrow\downarrow\rangle$, which are eigenfunctions of the Hamiltonian $\mathscr{H}_1$

$$\mathscr{H}_1 = \frac{\boldsymbol{p}^2}{2m} + V(\boldsymbol{r}) + \frac{\hbar}{2m^2c^2}\boldsymbol{S}\cdot(\nabla V(\boldsymbol{r})\times\boldsymbol{p}) \tag{2.83}$$

at one single isolated atom and are characterized by n: the orbital state of the electron, i: the atomic site and $\uparrow\downarrow$: the spin state. Correspondingly we define the creation and annihilation operators $c^{\dagger}_{ni\uparrow\downarrow}, c_{ni\uparrow\downarrow}$ of the electron in the state $|\psi_{n,i,\uparrow\downarrow}\rangle$. The one electron Hamiltonian written in terms of annihilation and creation operators is expressed as follows

$$\mathscr{H} = \mathscr{H}_0 + \mathscr{H}_{SOC} = \sum_n \sum_i \varepsilon_{ni}[c^{\dagger}_{ni\uparrow}c_{ni\uparrow} + c^{\dagger}_{ni\downarrow}c_{ni\downarrow}] \tag{2.84}$$

$$\begin{aligned}
&+ \sum_{i\neq j}\sum_{n,n',\sigma} b_{ji,n'n}\left(c^{\dagger}_{n'j\sigma}c_{ni\sigma} + c^{\dagger}_{ni\sigma}c_{n'j\sigma}\right) + \\
&+ \mathscr{C}^{x}_{ji,n'n}\left(c^{\dagger}_{n'j\sigma}c_{ni-\sigma} - c^{\dagger}_{ni\sigma}c_{n'j-\sigma}\right) - \\
&- i\mathscr{C}^{y}_{ji,n'n}\left(c^{\dagger}_{n'j-\sigma}c_{ni\sigma} + c^{\dagger}_{ni\sigma}c_{n'j-\sigma}\right) + \\
&+ \mathscr{C}^{z}_{ji,n'n}(2\sigma)\left(c^{\dagger}_{n'j\sigma}c_{ni\sigma} - c^{\dagger}_{ni\sigma}c_{n'j\sigma}\right),
\end{aligned} \tag{2.85}$$

where the $\mathscr{C}$ and b coefficients represent the following one body Hamiltonian matrix elements[1]

$$\mathscr{C}^{\pm}_{ji,n'n} = \langle 0|c_{n'j\mp}\mathscr{H}_1 c^{\dagger}_{ni\pm}|0\rangle\,, \tag{2.86}$$

$$b_{ji,n'n} \pm \mathscr{C}^{z}_{ji,n'n} = \langle 0|c_{n'j\pm}\mathscr{H}_1 c^{\dagger}_{ni\pm}|0\rangle\,. \tag{2.87}$$

In order to find the effective Hamiltonian via the Schrieffer-Wolf transformation, we proceed with a method similar to the one employed in 2.1.1, assuming an unperturbed ground state that is highly degenerate in the spin variable but not in the orbital index. Following the procedure to derive an effective Hamiltonian via the Schrieffer-Wolff transformation (see Appendix B), we write

$$\mathscr{H}' = \frac{1}{u}\mathscr{P}_0 T^2 \mathscr{P}_0, \tag{2.88}$$

[1] here the spin index $\uparrow\downarrow$ is converted to $\pm$ because it needs to be related to some algebraic operations.

where the projector $\mathscr{P}_0$ acts on an arbitrary state and projects it on the subspace spanned by the eigenstates of $\mathscr{H}_0$ (a perfectly insulating state where each site is occupied by an electron). In analogy to before, u represents the energy cost of a doubly occupied site. Moriya showed that the terms $\propto b^2$ of eq.(2.88) yield the symmetric spin exchange part already seen in the Heisenberg Hamiltonian (see 2.1.1), the terms $\propto \mathscr{C}b$ yield spin-spin interaction terms that promote perpendicular alignment of the spins (this later became known as the Dzyaloshinskii-Moriya interaction) and, finally, the terms $\propto \mathscr{C}^2$ generate effective spin-spin interactions that can be interpreted as a 2-site anisotropy terms

$$\propto b^2 \Rightarrow J_{ij}\boldsymbol{S}_i \cdot \boldsymbol{S}_j, \tag{2.89}$$

$$\propto \mathscr{C}b \Rightarrow \boldsymbol{D}_{ij} \cdot (\boldsymbol{S}_i \times \boldsymbol{S}_j), \tag{2.90}$$

$$\propto \mathscr{C}^2 \Rightarrow \boldsymbol{S}_i^T \overleftrightarrow{\Gamma}_{ij} \boldsymbol{S}_j, \tag{2.91}$$

where the effective spin model parameters $J_{ij}, \boldsymbol{D}_{ij}, \overleftrightarrow{\Gamma}_{ij}$ are related to the tight binding parameters via

$$J_{ij} = \frac{2|b_{ij,nn'}|^2}{u}, \tag{2.92}$$

$$\boldsymbol{D}_{ij} = \boldsymbol{D}_\alpha(j,i) := \frac{4i}{u}[b_{ji,n'n}\mathscr{C}_{ij,nn'} - \mathscr{C}_{ji,n'n}b_{ij,nn'}], \tag{2.93}$$

$$\overleftrightarrow{\Gamma}_{ij} = \boldsymbol{C}_{ij,nn'} \otimes \boldsymbol{C}_{ji,n'n} + \boldsymbol{C}_{ji,n'n} \otimes \boldsymbol{C}_{ij,nn'} - \mathbb{I} \otimes (\boldsymbol{C}_{ij,nn'} \cdot \boldsymbol{C}_{ji,n'n}) \tag{2.94}$$

A rigorous derivation of the DMI term is provided in Appendix C. The so-obtained effective spin model can finally be expressed in the familiar form

$$\mathscr{H}' = \sum_{<i,j>} -J_{ij}\boldsymbol{S}_i \cdot \boldsymbol{S}_j + \boldsymbol{D}_{ij} \cdot (\boldsymbol{S}_i \times \boldsymbol{S}_j) + \boldsymbol{S}_i^T \overleftrightarrow{\Gamma}_{ij} \boldsymbol{S}_j. \tag{2.95}$$

which is also known as the extended Heisenberg model for magnetic interactions. This model is at the basis of an incredibly vast wealth of physical phenomena, many of which are sill being explored today. The ordinary Heisenberg exchange term $\propto J_{ij}$ favors either parallel or antiparallel alignment, with the easy axis of the global alignment being decided by other sources of magnetic anisotropy (such as MCA as described in sec.6.2.2 - see Fig.2.6).

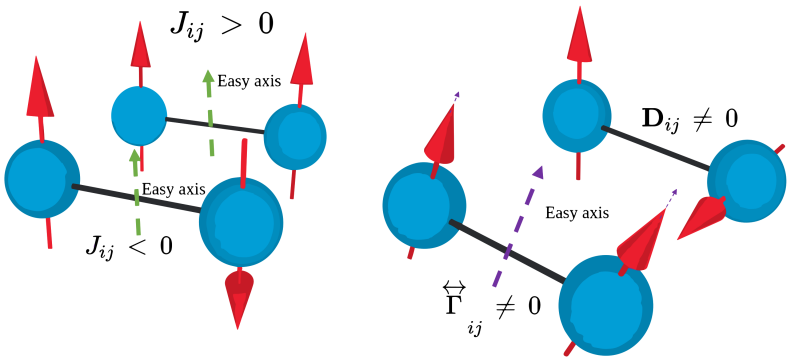

Fig. 2.6 Schematic representation of the favored magnetic order promoted by the different terms of the extended Heisenberg model of eq.(2.95). $J_{ij} \lessgtr 0$ represents antiferromagnetic or ferromagnetic order. $\boldsymbol{D}_{ij} \neq 0$ represents canted magnetic order as a consequence of DMI and $\overleftrightarrow{\Gamma}_{ij}$ represents 2 site anisotropy.

The DMI term $\propto \boldsymbol{D}_{ij}$ instead favors perpendicular alignment of neighboring spins as depicted in Fig.2.6 and the direction in which this perpendicular alignment is favoured is indeed dependent on the direction of the DM vector, which is also constrained by the crystal symmetry as discussed in the following 2.4.1.

Finally, the term $\propto \overleftrightarrow{\Gamma}_{ij}$ favors the alignment of neighboring spins according to an easy axis different from the one dictated by magnetocrystalline anisotropy. We emphasize that this term is highly non-trivial and can be interpreted as a 2-site anisotropy as opposed by the single-ion anisotropy addressed by the Bruno model (see Fig.2.6): the underlying mechanism is very different. In the Bruno model, the electrons on the single atom interact with the crystal field and acquire an anisotropy due to SOC: the electron-electron interaction is completely neglected. In this case, the magnetic moments in the effective spin model align as a consequence of spin-spin interactions coupled with the presence of SOC: this 2 site anisotropy is a consequence of electrons interacting. This last term is very often neglected because the strength of this interaction goes with the square of spin orbit coupling terms $\propto \mathscr{C}^2$ and is therefore negligibly small in most (but not all) systems.

Crystal symmetry and allowed DMI vectors: the Moriya rules

As noted by Moriya himself in his seminal paper of 1960 [67] and inspired by the Neumann Principle of crystallography, the symmetry of the crystal can reveal in which cases the DM between neighboring magnetic atoms is present or not.

We emphasize however 2 important points: firstly, in the microscopic case, the symmetries relevant for the determination of the DM vector are not the global symmetries of the crystallographic point group but the local symmetries of the atomic environment around the relevant atom; secondly the (local) crystal symmetry can only predict the direction of the DM vector and not it's strength. In the following we report the 5 Moriya rules useful for determining the direction of the DM vector. Given 2 selected atoms positioned at sites A and B, with the point bisecting the straight line segment denoted AB, we can in general formulate the following statements:

- When a center of inversion is located at C, the DM vector $\boldsymbol{D}_{AB} = 0$ on that given bond (2.7-(a)).
- When there is a mirror $\hat{\pi}$ including A and B, $\boldsymbol{D}_{AB} \perp \hat{\pi}$.
- When a mirror plane $\hat{\pi}$ perpendicular to AB passes through C, $\boldsymbol{D}_{AB} \parallel$ to $\hat{\pi}$ or $\boldsymbol{D}_{AB} \perp AB$ (2.7-(b)).
- When a 2-fold rotation axis C_2 is perpendicular to AB and passes through C, $\boldsymbol{D}_{AB} \perp C_2$ (2.7-(c)).
- When there is an n-fold axis C_n ($n \geq 2$) along AB, $\boldsymbol{D}_{AB} \parallel AB$. (Fig.2.7-(d))
- When there is a 2-fold axis C_2 along $\perp$ AB, $\boldsymbol{D}_{AB} \perp AB$ (Fig.2.7-(e)).
- In the case that the magnetic interaction between neighboring atoms is mediated by a third one via a superexchange mechanism ([74]) the orientation of the DM vector is obtained from the relation $\boldsymbol{D}_{AB} \propto \boldsymbol{r}_A \times \boldsymbol{r}_B$, where $\boldsymbol{r}_A$ and $\boldsymbol{r}_B$ represent the position vectors of the magnetic ions relative to the 3rd ion mediating the superexchange interaction (see Fig.2.7-(f) and Fig.2.10).

For some exemplary cases demonstrating the Moriya rules, please refer to Fig.2.8.

2.4.2 An overview of DMI materials

In general, DMI exists between any pair of magnetic atoms with local inversion symmetry breaking and is therefore a quite common feature in magnetic materials. We remark however, how in general it is a second order effect compared to ordinary Heisenberg exchange and magneto-crystalline anisotropy, making it quite elusive to

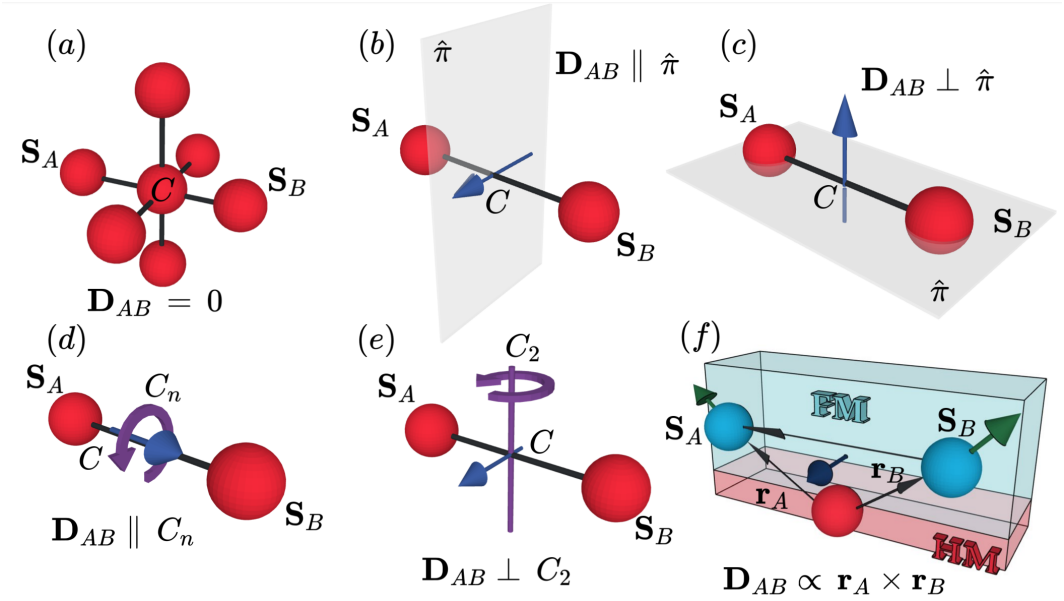

Fig. 2.7 Schematic representation of the Moriya rules relating the local symmetries of a pair of spins $\boldsymbol{S}_A$ and $\boldsymbol{S}_B$ and the direction of the DMI.

detect experimentally. In the following we provide a brief overview of the typical DMI materials, paying special attention to bulk and thin film systems, which have gained significant scientific interest in recent years.

B20-chiral magnets

B20-type chiral magnets, such as MnSi [75], $Fe_{1-x}Co_xSi$ [76], and FeGe [77], are historically significant as they were the first compounds to demonstrate stable skyrmionic states. This is due to the fact that these alloys belong to the non-centrosymmetric space group $P2_13$ (see Fig.2.9), which allows for the emergence of Bulk DMI. Ab initio calculations reveal that the strength of the DMI in these systems is determined by the SOC of the 3*d* atoms and strong 3*d*-*p* hybridization with the *p* atoms of Si or Ge, mediating magnetic interactions [78].

Experiments have shown that the chirality of the spin spirals (which is linked to the strength of the DMI) in these systems can be adjusted by altering the relative concentrations of 3*d* and *p* elements [79] in the compound. These systems are particularly interesting because they show excellent agreement between experimental data and ab-initio calculations, which remarkably reproduce the mentioned composition dependence of the DMI strength.

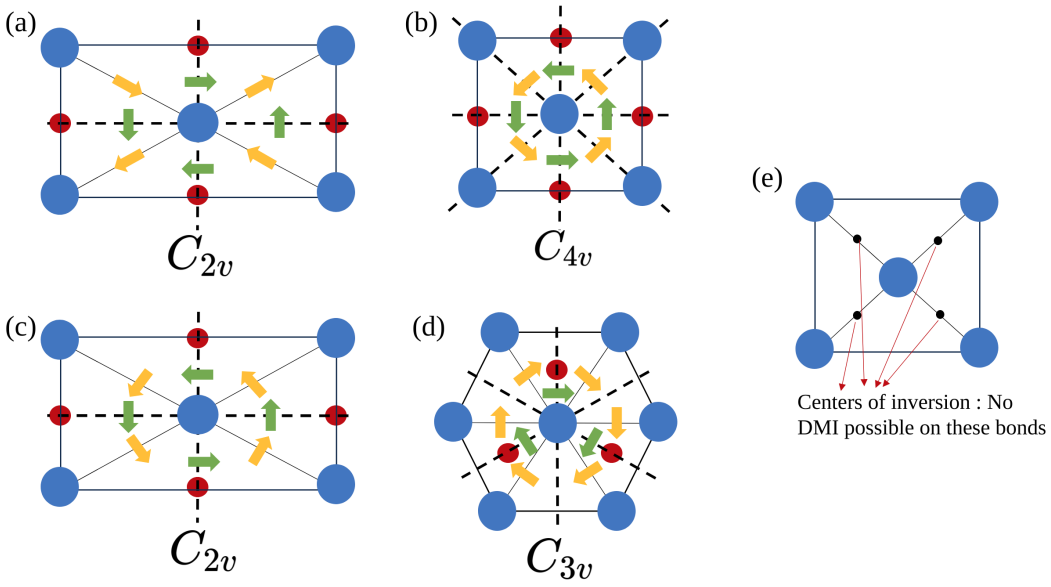

Fig. 2.8 Relationship between crystal symmetry and microscopic DM vector. Sketch of the DM vector in a C_{2v} (a,c), C_{4v} (b) C_{3v} (d) and a C_4 symmetric unit cell (e). Mirror planes are indicated by the black dashed lines. Atoms in the top layer are indicated by blue circles while atoms in the bottom layer are indicated by smaller red circles. The green arrows on the bonds represent the DM vector while the orange arrows represent an effective micromagnetic DM vector (discussed at length later in 3.1.1) . We highlight how the C_{2v} case (a,c) is of particular interest as the Moriya rules in this case would allow for multichiral magnetisation configuration, i.e. winding magnetic structures with opposite Néel-type chirality. We also emphasize how the centrosymmetry of structure (e) forbids the presence of DM interaction.

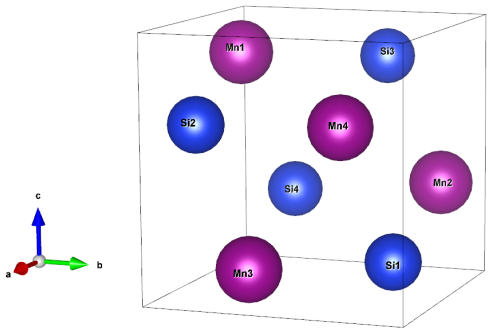

Fig. 2.9 Unit cell of MnSi which is part of the $P2_13$ space group.

Magnetic thin-film heterostructures

The interesting combination of intrinsic inversion symmetry breaking and strong SOC provided by the interplay of heavy metal (HM) atoms located at the interface of HF/FM heterostructures has made these systems an ideal platform for the study of chiral magnetism. Layer resolved ab-initio calculations have proven of central importance in revealing some general features of interfacial DMI in a variety of heterostructures [80]. It was found that the predominant contribution to DMI in these systems is localized in the interfacial ferromagnetic layer, while the dominating SOC contribution is located in the adjacent HM (heavy metal) layer.

These findings confirm the validity of the assumptions of the Fert-Levy model [81, 74], which considers interface DMI as a consequence of anisotropic superexhcnage mediated by heavy metal atoms in heterostructures. Moreover, the ab-initio analysis has also highlighted the great importance of $3d/5d$ orbital hybridization at the interface in determining the strength and sign of DMI in heterostructures and further contributes to improving our understanding of interfacial magnetism. Recent studies have revealed that ferromagnetic interfaces exhibit interface DMI even in the absence of heavy metal (HM) atoms, which has been attributed to the Rashba effect. Similarly to interface DMI, the dominant DMI contribution in these systems is mainly located in the first FM layer. In contrast to ordinary interface DMI observed in the Fert-Levy model, the spin orbit contribution of Rashba-DMI is also located in the first FM layer.

This discovery was first established through ab-initio investigations of Co/graphene [82], while at the same time unveiling a linear correlation between Rashba-DMI and the Rashba splitting parameter α_R in close quantitative agreement with experimental data. The electric field provides an interesting gateway for low energy manipulation of chiral interactions in FM thin films as it has been demonstrated to modulate the interfacial DMI induced by the Rashba effect [83–86]. Recent research has shown that electric field control of Rashba-induced DMI allows for efficient current-driven domain-wall motion and magnetization switching, highlighting its potential in the development of advanced spintronic devices [80, 87–91].

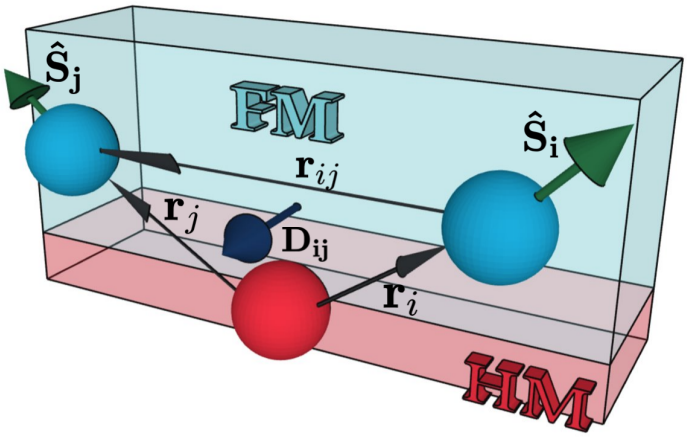

Fig. 2.10 Diagrammatic representation of a typical system displaying interfacial DMI. The exchange interaction between neighboring spins $\hat{\boldsymbol{S}}_i$ and $\hat{\boldsymbol{S}}_j$ is mediated by a heavy metal ion which introduces a strong SOC in the interfacial region. In accordance with the 5^{th} Moriya rule, the DM vector $\boldsymbol{D}_{ij}$ lies parallel to the vector $\boldsymbol{r}_i \times \boldsymbol{r}_j$.

2.4.3 Direct and indirect electric field control of DMI

As established in 2.4.1, DMI is an important magnetic interaction that has been attracting significant attention in the scientific community due to it's central role in many exotic phenomena of magnetism, as well as being a key parameter for the manipulation of topological magnetic structures in future spintronics based devices.

While some of the key ingredients to stabilize sizable DMI seem to have been established (inversion symmetry breaking and the presence of SOC), some other very important properties of this exotic magnetic interaction are still under intense scrutiny. Most notably, a clear correlation between the strength of DMI and the band structure of materials has not been ultimately identified yet, making the choice of good DMI materials more a matter of experience rather than the result of a choice based on hard data from a large database.

Even without a clear view on all the facets of this interesting magnetic parameter, several strategies to improve and control DMI in magnetic thin films have been demonstrated. In particular we highlight ref. [80] where the authors describe three approaches to efficiently tune the DMI in ultrathin magnetic films. The first approach involves using NM/FM/Pt trilayers with inverse stacking of FM/Pt and FM/NM structures characterized by DMI with opposite chiralities, which allows the

enhancement of DMI up to 50% as compared to the corresponding FM/Pt bilayers. The second approach is to cap Co/Pt structure with an oxidized layer, which can cause a dramatic DMI enhancement due to the Rashba type DMI. Finally, the paper demonstrates that DMI magnitude can be modulated using an electric field with an efficiency factor comparable to that of the electric field control of perpendicular magnetic anisotropy in transition metal/oxide interfaces.

Among the various strategies to manipulate DMI suggested in [80], the use of an electric field is of particular interest for applications because of the promise of fast operations times and low energy costs. There are several ways in which an electric field might be employed to tailor this magnetic interaction. One additional way to address DMI via electric field resides in the possibility to piezoelectrically manipulate the strain properties of a material as shown in ref. [92]: there the authors present experimental results and micromagnetic simulations that demonstrate electric-field control of skyrmions through strain-mediated magnetoelectric coupling in ferromagnetic/ferroelectric multiferroic heterostructures. The paper also shows the process of non-volatile creation of multiple skyrmions, reversible deformation and annihilation of a single skyrmion by performing magnetic force microscopy with in situ electric fields.

Another interesting way to control DMI in magnetic thin films has been shown to be the controlled oxidation of FM surfaces [6]. It was shown via ab-initio simulations, that the magnitude and sign of DMI can be controlled by tuning the oxygen coverage of the magnetic film. The origin of this mechanism is to be identified in the efficient modulation of surface electric dipoles via strongly electronegative ions such as oxygen (see Fig.2.11). This concept has also been recently followed up in an experimental setting [7], where the controlled oxidation of a CoFeB layer was shown to successfully switch the sign of DMI (See Fig.2.12).

2.4.4 Conclusion

In the preceding sections, we have explored the emergence of various types of magnetic order arising from electron many-body interactions. These models hold fundamental significance and their predictive capacity is greatly enhanced by ab-initio methods, which allow the calculation of energy in magnetic systems, conse-

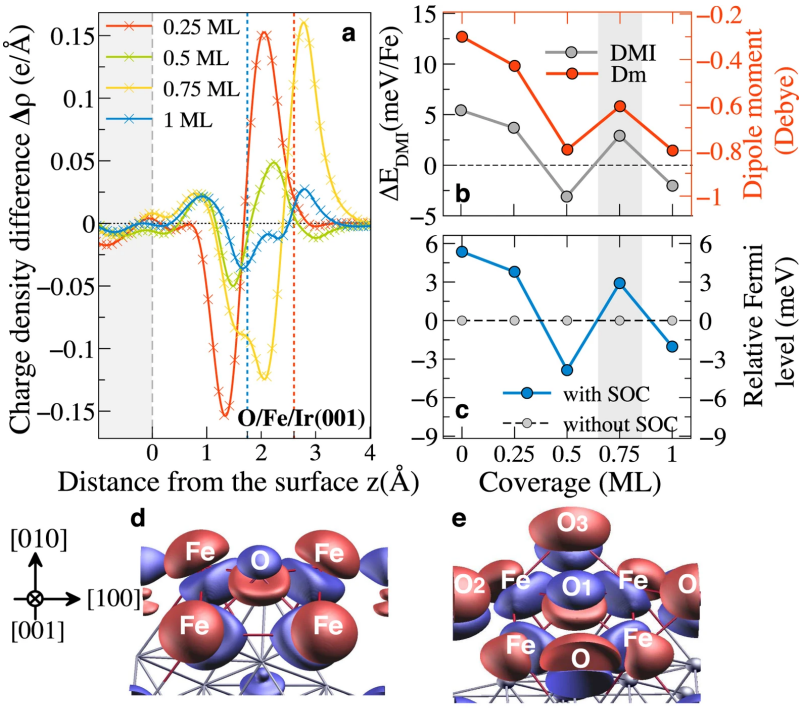

Fig. 2.11 Correlation between DMI and the electric surface dipole moment. In panel (a), the planar averaged charge density difference $\Delta\rho(z)$ is illustrated for O absorption on Fe/Ir(011) across various oxygen coverages. The dashed red, blue, and gray lines depict the approximate equilibrium positions of the O, Fe, and topmost Ir atoms on the fully relaxed surface. In panel (b), the relationship between O coverage and the alterations in the surface dipole moment, DMI, and (c) relative Fermi energy is explored. (d-e) Isosurface plot of the charge density difference $\Delta\rho(z)$ for a coverage of 0.25 (d) and 0.75 ML (e), with blue and red isosurfaces indicating areas of charge accumulation and depletion respectively. Reproduced from[6].

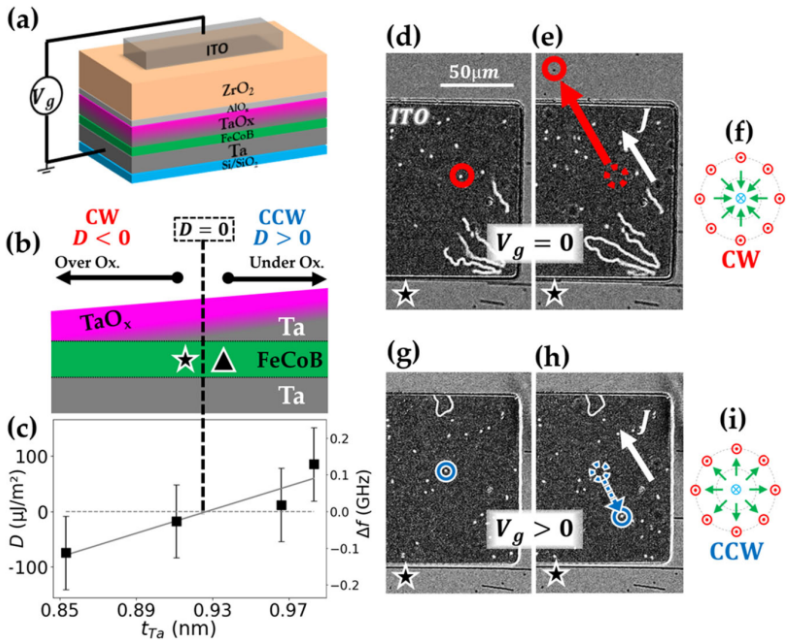

Fig. 2.12 (a) Schematic representation of the setup composed of a Ta/CoFeB/TaOx trilayer with the additional ZrO_2 layer and Indium Tin oxide (ITO) electrode. (b) Schematic cross section of the sample. (c) iDMI measured with Brillouin light scattering (BLS) vs. top Ta-thickness. (d,e) MOKE images of current skyrmion induced motion (CIM) at zero applied gate voltage. (g,h) MOKE images of skyrmion current induced motion (CIM) at $V_g = +3.5V$ applied gate voltage. The in plane current density is represented by the white arrow and the out of plane magnetic field of $\mu_0 H_z = 80\ \mu$T. In the initial state (d,e), skyrmions move in the direction of the current indicating CW chirality ($D < 0$). Under positive gate voltage, the skyrmions move against the current density direction, indicating a CCW chirality ($D > 0$). (f,g) Schematic representation of CW and CCW skyrmions. Reproduced from [7]

quently enabling the extraction of crucial parameters such as anisotropy constants and exchange tensor components through energy mapping techniques (see 5.1.6).

However, when investigating material characteristics observable at larger scales, such as the dynamics of magnetic domain walls or the expansion dynamics of magnetic bubbles, microscopic models alone are insufficient in providing conclusive answers. To fully comprehend and analyze these other facets of magnetism in the solid state, we require a formalism that disregards many microscopic degrees of freedom and selectively retains the relevant ones necessary for modeling the prominent features at the scale of micrometers rather than individual atoms.

In the next chapter we introduce micromagnetism, a formalism that aims to elevate the microscopic theory of magnetism to a continuum theory thereby unlocking a wealth of valuable tools for studying the dynamics of magnetic materials on the micrometer scale.

Chapter 3

The continuum limit: Micromagnetism

In the previous chapter, we have spent some time setting the stage for a theory of magnetism that works on the atomic scale. The dynamical behavior of magnetic moments on the experimental scale is however something that is impossible to capture with purely atomistic ab-initio approaches: at nano- and micro-scales we therefore have to implement other theoretical predictive models which, while keeping some of the essential features of atomistic magnetism, adopt some fundamental approximations. As an example for the necessity of multi-scale approaches, atomistic theories regarding magnetic systems do not take in account the presence of the dipolar interaction and therefore fail to capture many of the features of experimental systems such as the formation of Weiss Domains and other magnetization patterns.

Micromagnetism [93, 94] is a theoretical framework used to describe the behavior of magnetic materials at the micrometer scale, i.e. on length scales where the material consists of regions that are large enough to be treated as continuous, but small enough to reveal details of magnetic domains (see Fig.3.1).

One of the key advantages of micromagnetism is its ability to model large-scale systems with a good degree of accuracy, while still being computationally efficient. This makes it an ideal tool for studying the behavior of magnetic materials in applications such as magnetic storage devices, spintronics, and magnetic sensors.

Within micromagnetism, magnetic materials are not considered as ensembles of atoms with interacting electrons, but rather as an ensemble of interacting magnetic moments. Ferromagnetic materials allow for a big simplification because of exchange interactions, which, up to a characteristic length scale := λ favor parallel alignment of magnetic moments. Averaging the microscopic magnetization inside of regions of the material smaller than $d^3\boldsymbol{r} < \lambda^3$ allows us to formally define the macroscopic magnetization $\boldsymbol{M}(\boldsymbol{r})$ as a continuous function of space, effectively promoting our theory of magnetism to a continuum theory. It is also assumed that the magnetic moments inside the volume $d^3\boldsymbol{r}$ reach their thermodynamic equilibrium value on a time scale much smaller (i.e. much faster) than the system as a whole reaches its equilibrium configuration.

Within this framework, the label quantifying how likely a configuration is going to manifest itself is provided by the internal energy, which is promoted to a functional of the magnetization $E[\boldsymbol{M}(\boldsymbol{r})]$. The ground state of the system is identified via the variational principle

$$\delta E[\delta \boldsymbol{M}(\boldsymbol{r})] = 0, \tag{3.1}$$

where $\delta E[\delta \boldsymbol{M}(\boldsymbol{r})]$ indicates the variation of the energy functional for a variation of the magnetization field $\delta \boldsymbol{M}(\boldsymbol{r})$ under the constraint $|\boldsymbol{M}|/M_s = 1\text{m}$ where M_s indicates the saturation magnetization of the sample.

Despite these differences, micromagnetism and ab-initio methods can be complementary approaches, as they can provide different levels of detail and insights into the behavior of magnetic materials. For example, DFT can be used to calculate the magnetic properties of a material, which can then be used as input for micromagnetic simulations to study the dynamics of the magnetization under different external conditions.

In the following we are going to provide a brief overview of the different energy contributions composing the energy functional $E[\boldsymbol{M}(\boldsymbol{r})]$

3.1 Exchange energy density

The exchange interaction is an energy contribution associated to the relative orientation of spins in the system and is directly related to the Heisenberg exchange interaction discussed 2.1.1. In the following we consider a lattice in which the state

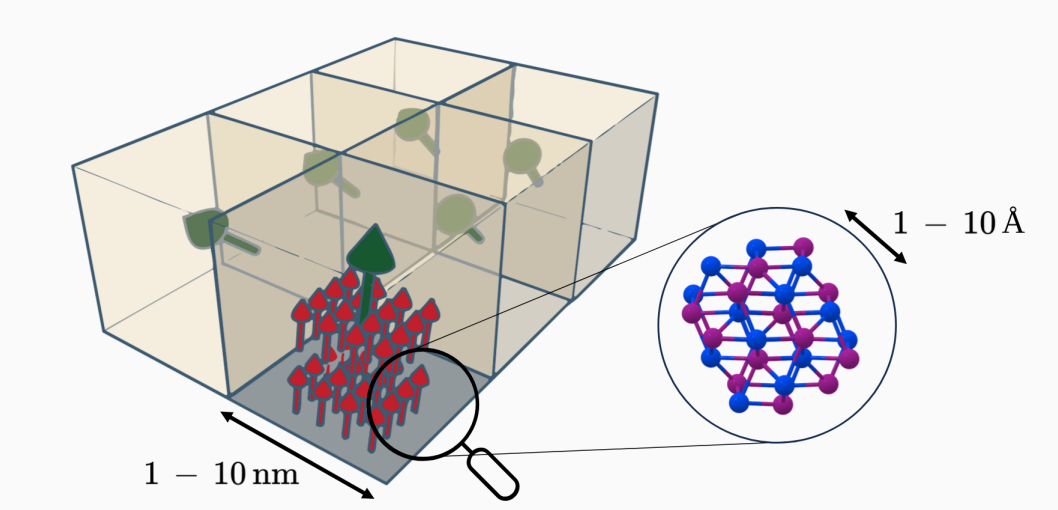

Fig. 3.1 Schematic representation of them micromagnetic limit. The magnetization inside the cells is averaged and considered constant. The details of the atomic structure are neglected.

of the electrons in the unit cell is identical except for the relative orientation of their spin. Let $\boldsymbol{S}_i \equiv \boldsymbol{S}(\boldsymbol{r}_i)$ represent the unit vector pointing in the direction of the average magnetization of the $i-$th unit cell located in $\boldsymbol{r}_i$, the total Heisenberg exchange energy in the system can be quantified as follows

$$E_{exch} = -\sum_{\langle i,j \rangle} J_{ij} \boldsymbol{S}_i \cdot \boldsymbol{S}_j, \tag{3.2}$$

where J_{ij} represents the energy cost of misalignment of spins $\boldsymbol{S}_i, \boldsymbol{S}_j$ per unit cell volume. Despite the similarity to the quantum mechanical version of the Heisenberg model discussed in Chapter 2, this expression treats the localized spins as vectors quantities and not as a quantum mechanical operators acting on electron wave-functions. In the micromagnetic approximation we suppose the changes in magnetization occur on length scales much larger than the lattice constant, therefore we can assume that the spins are misaligned by a small amount and we can Taylor expand as follows

$$\boldsymbol{S}(\boldsymbol{r}_j) \approx \boldsymbol{S}(\boldsymbol{r}_i) + \sum_A \frac{\partial \boldsymbol{S}(\boldsymbol{r}_i)}{\partial x_A} \left[\Delta \boldsymbol{r}_{ij}\right]_A + \sum_{A,B}^{3} \frac{\partial^2 \boldsymbol{S}(\boldsymbol{r}_i)}{\partial x_A \partial x_B} \left[\Delta \boldsymbol{r}_{ij}\right]_A \left[\Delta \boldsymbol{r}_{ij}\right]_B, \tag{3.3}$$

where we have defined $\left[\Delta \boldsymbol{r}_{ij}\right]_A := \left[\boldsymbol{r}_i - \boldsymbol{r}_j\right] \cdot \hat{e}_A$. The assumption of small misalignment also allows us to write

$$\boldsymbol{S}_i \cdot \boldsymbol{S}_j = \cos\theta_{ij} \approx 1 - \theta_{ij}^2, \tag{3.4}$$

which, together with the assumption of unit length $|\boldsymbol{S}(\boldsymbol{r}_i)|^2 = 1$, yields

$$\theta_{ij}^2 \approx \sum_{A,B} \frac{\partial \boldsymbol{S}(\boldsymbol{r}_i)}{\partial x_A} \cdot \frac{\partial \boldsymbol{S}(\boldsymbol{r}_i)}{\partial x_B} \left[\Delta \boldsymbol{r}_{ij}\right]_A \left[\Delta \boldsymbol{r}_{ij}\right]_B \tag{3.5}$$

which finally allows us to write the exchange energy as

$$E_{exch} = \frac{1}{2} \sum_{\langle i,j \rangle} J_{ij} \sum_{A,B} \frac{\partial \boldsymbol{S}(\boldsymbol{r}_i)}{\partial x_A} \cdot \frac{\partial \boldsymbol{S}(\boldsymbol{r}_i)}{\partial x_B} \left[\Delta \boldsymbol{r}_{ij}\right]_A \left[\Delta \boldsymbol{r}_{ij}\right]_B \tag{3.6}$$

$$= \sum_{i,A,B} \Xi_{AB}(\boldsymbol{r}_i) \frac{\partial \boldsymbol{S}(\boldsymbol{r}_i)}{\partial x_A} \cdot \frac{\partial \boldsymbol{S}(\boldsymbol{r}_i)}{\partial x_B}, \tag{3.7}$$

where we have defined

$$\Xi_{AB}(\boldsymbol{r}_i) = \frac{1}{2} \sum_{j \in N.N \boldsymbol{r}_i} J_{ij} \left[\Delta \boldsymbol{r}_{ij}\right]_A \left[\Delta \boldsymbol{r}_{ij}\right]_B \tag{3.8}$$

as an anisotropic exchange tensor. The sum over j is restricted to all the nearest neighbors (N.N) of $\boldsymbol{S}(\boldsymbol{r}_i)$ and therefore depends on the crystalline structure of the material. We can now let the unit cell volume shrink to $d^3\boldsymbol{r}$ in order to convert the sum over i to a volume integral and the atomic spins to a continuous magnetization field $\boldsymbol{m}(\boldsymbol{r})$, obtaining

$$E_{exch} = \int_V \sum_{A,B} \Xi_{AB} \frac{\partial \boldsymbol{m}(\boldsymbol{r})}{\partial x_A} \cdot \frac{\partial \boldsymbol{m}(\boldsymbol{r})}{\partial x_B} d^3\boldsymbol{r} \tag{3.9}$$

Using graph theory to sum over nearest neighbors

The derivation of the continuum exchange energy density from Döring [93] which we reformulated above, although fairly straightforward, faces an issue: computing the elements of Ξ_{AB} for symmetric anisotropic exchange is neither easy nor systematic, especially when dealing with crystallographic point groups that go beyond the

simplest cases. This difficulty arises from the challenge of easily identifying the $\Delta \boldsymbol{r}_{ij}$ terms in equation (3.8)

Since crystal structures are nets, which are special sub-classes of graphs, an interesting trend emerging in recent years has been to use the toolkit of graph theory, an important branch of mathematics, to treat similar problems. In the following we provide an overview of the basics of graph theory, keeping the discussion focused on the parts that can help us understand how a crystal can be analyzed with this formalism.

A graph $G = (X,U)$ consists of a set of *vertices* labelled $X = \{v_1, v_2, \cdots v_i, \cdots v_n\}$ and *edges* corresponding to pairs of vertices $(i, j), \cdots$ labelled $U = \{l_1, l_2, \cdots, l_j, \cdots, l_m\}$. If a pair of vertices (i, j) is distinguished from a pair (j, i), then we are talking about a directed edge and the graph as a whole is referred to as a *directed graph*. Vertices connected by an edge or more are called *neighbors* and the set of neighbors of that vertex is called its *neighborhood*. The *coordination* of a vertex is the number of edges incident on it and if all the vertices of the graph have the same coordination, e.g. n, the graph is called *n-regular*. To formulate predictions and perform calculations it is useful to associate different matrices to the graphs of interest. The *undirected incidence matrix* $\hat{B}$ of an undirected graph $G = (X,U)$ is as $n \times m$ matrix where n is the number of vertices and m is the number of edges respectively, such that

$$B_{ij} = \begin{cases} 1 \text{ if vertex } v_i \text{ is incident with edge } l_j \\ 0 \text{ otherwise} \end{cases} . \tag{3.10}$$

If the graph $G = (X,U)$ is directed, then the incidence matrix $\hat{C}$ becomes

$$C_{ij} = \begin{cases} +1 \text{ if edge } l_j \text{ leaves vertex } v_i \\ -1 \text{ if edge } l_j \text{ enters vertex } v_i \\ 0 \text{ otherwise} \end{cases} . \tag{3.11}$$

We report an exemplary case in Fig.3.2. We now proceed and show how, using some of the basics of graph theory introduced above, it is possible to streamline the process of performing sums over nearest neighbors such as the one in eq.(3.8) by mapping it onto a simple matrix multiplication. First of all, we notice how $\Delta \boldsymbol{r}_{ij}$ in eq.(3.8) represents the vector connecting sites i and j, making it an object that can

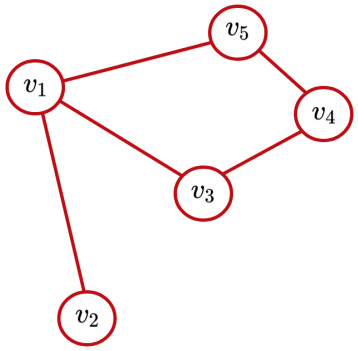

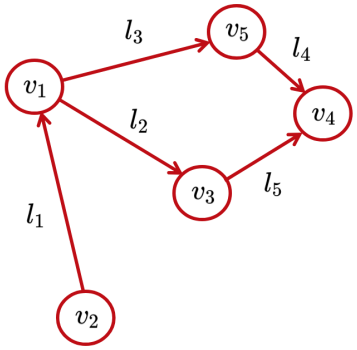

$$\hat{B} = \begin{bmatrix} v_1 \\ v_2 \\ v_3 \\ v_4 \\ v_5 \end{bmatrix} \begin{pmatrix} 0 & 1 & 1 & 0 & 1 \\ 1 & 0 & 0 & 0 & 0 \\ 1 & 0 & 0 & 1 & 0 \\ 0 & 0 & 1 & 0 & 1 \\ 1 & 0 & 0 & 1 & 0 \end{pmatrix} \begin{matrix} [v_1 & v_2 & v_3 & v_4 & v_5] \end{matrix}$$

$$\hat{C} = \begin{bmatrix} v_1 \\ v_2 \\ v_3 \\ v_4 \\ v_5 \end{bmatrix} \begin{pmatrix} -1 & 1 & 1 & 0 & 0 \\ 1 & 0 & 0 & 0 & 0 \\ 0 & -1 & 0 & 0 & 1 \\ 0 & 0 & 0 & -1 & -1 \\ 0 & 0 & -1 & 1 & 0 \end{pmatrix} \begin{matrix} [l_1 & l_2 & l_3 & l_4 & l_5] \end{matrix}$$

Fig. 3.2 Depiction of the incidence matrix of an undirected graph (left) and the edge-node incidence matrix of a directed graph (right)

be easily related to an edge-node incidence matrix as the one reported in (3.11). To show how such a connection can be made, we demonstrate the case of a simple cubic (SC) lattice.

First of all, we identify the cluster of nearest neighbors surrounding atom i as a directed graph with vertex set

$$X = \{v_1, v_2, v_3, v_4, v_5, v_6\}$$

and edge set

$$U = \{(v_1, v_2), (v_1, v_3), (v_1, v_4), (v_1, v_5), (v_1, v_6)\} = \{l_1, l_2, l_3, l_4, l_5\}$$

which allows us to determine the edge-node incidence matrix for the SC lattice of the present example as follows (see Fig.3.3)

$$\hat{C} = \begin{pmatrix} 1 & -1 & 0 & 0 & 0 & 0 & 0 \\ 1 & 0 & -1 & 0 & 0 & 0 & 0 \\ 1 & 0 & 0 & -1 & 0 & 0 & 0 \\ 1 & 0 & 0 & 0 & -1 & 0 & 0 \\ 1 & 0 & 0 & 0 & 0 & -1 & 0 \\ 1 & 0 & 0 & 0 & 0 & 0 & -1 \end{pmatrix}. \tag{3.12}$$

If we are interested in extracting $\Delta \boldsymbol{r}_{ij}$ from the incidence matrix, we first have to extract the j^{th} line of $\hat{C}$ by multiplying from the left side with the j^{th} edge vector

$$l_j \cdot \hat{C} = \delta_{j\gamma} C_{\gamma\alpha} \tag{3.13}$$

which gives us a linear combination of vertex vectors. To convert these vertex vectors in real space coordinates we define a matrix $\hat{R}$ that maps the vertex vectors onto real space coordinates. For a SC lattice, such a matrix has the form

$$\hat{R} = \begin{pmatrix} 0 & 0 & 0 \\ 1 & 0 & 0 \\ -1 & 0 & 0 \\ 0 & 1 & 0 \\ 0 & -1 & 0 \\ 0 & 0 & 1 \\ 0 & 0 & -1 \end{pmatrix}. \tag{3.14}$$

and $\Delta \boldsymbol{r}_{ij}$ can be expressed as

$$\Delta \boldsymbol{r}_{ij} = (l_j \cdot \hat{C}) \cdot \hat{R} = (\delta_{j\gamma} C_{\gamma\alpha}) R_{\alpha B}. \tag{3.15}$$

Assuming we are interested in computing $\Delta \boldsymbol{r}_{12}$. According to eq.(3.15), we have

$$\Delta \boldsymbol{r}_{12} = (l_2 C_{2\alpha}) R_{\alpha B} = \begin{pmatrix} 1 & 0 & -1 & 0 & 0 & 0 & 0 \end{pmatrix} \cdot \begin{pmatrix} 0 & 0 & 0 \\ 1 & 0 & 0 \\ -1 & 0 & 0 \\ 0 & 1 & 0 \\ 0 & -1 & 0 \\ 0 & 0 & 1 \\ 0 & 0 & -1 \end{pmatrix} = \begin{pmatrix} 1 & 0 & 0 \end{pmatrix}. \tag{3.16}$$

If we want to compute $\Delta \boldsymbol{r}_{13}$, using eq.(3.15) we would have

$$\Delta \boldsymbol{r}_{13} = (l_3 C_{3\alpha}) R_{\alpha B} = \begin{pmatrix} -1 & 0 & 0 \end{pmatrix}. \tag{3.17}$$

Using this notation, we can express (3.8) as

$$\Xi_{AB} = \frac{1}{2} \sum_{k,k'} R_{A\alpha} C_{\alpha\beta} \delta_{\beta k} J_k \delta_{kk'} \delta_{k'\gamma} C_{\gamma\rho} R_{\rho B} \tag{3.18}$$

$$= \frac{1}{2} [\hat{R}^T \cdot \hat{C}^T \cdot \hat{J} \cdot \hat{C} \cdot \hat{R}]. \tag{3.19}$$

where we have introduced the matrix $\hat{J} = J_k \delta_{kk'}$ for dimensional reasons. In the case

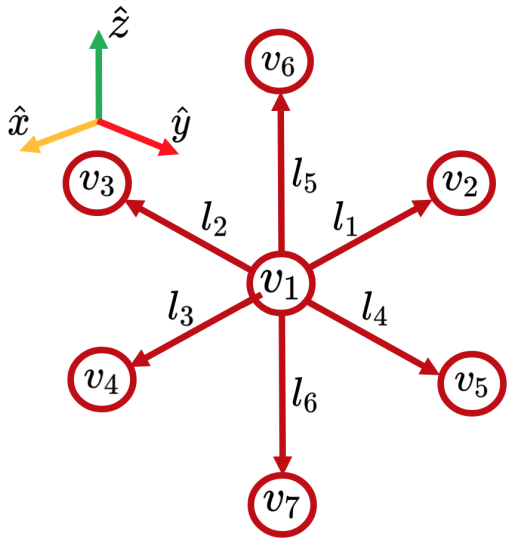

Fig. 3.3 Simple cubic (SC) nearest neighbors cluster represented as a directed graph

of a SC lattice, we can use the previously defined matrices $\hat{R},\hat{C}$ and, assuming (for simplicity) that $J_k = J$ is constant and independent of k, we obtain the known result [93]

$$\Xi_{AB} = J\delta_{AB}. \tag{3.20}$$

Where Ξ_{AB} has the units of an energy density. This approach is indeed versatile in that it can be easily adapted to situations where the crystal structure is not as trivial as the SC lattice, as well as cases where the exchange coefficient is not constant. We discuss some of these instances in 6.3.2.

3.1.1 The Dzyaloshinskii-Moriya Interaction

As discussed in Sec.2.4.1, the Dzyaloshinskii-Moriya interaction (DMI) in a microscopic discrete form can be summarized as an energy contribution of the form

$$E_{DMI} = \sum_{\langle i,j \rangle} \boldsymbol{D}_{ij} \cdot (\boldsymbol{S}_i \times \boldsymbol{S}_j), \tag{3.21}$$

where $\boldsymbol{D}_{ij}$ is a vector quantifying the strength and chirality of DMI and $\boldsymbol{S}_i$ represents the the unit vector of spin moment at atomic site $\boldsymbol{r}_i$. In the micromagnetic limit, where the magnetization can be approximated by a smooth, slowly varying magnetic field $\boldsymbol{m}(\boldsymbol{r})$, the DMI energy of (3.21) can be translated to [95]

$$E_{DMI} = \int_V \sum_A \boldsymbol{d}_A \cdot (\boldsymbol{m} \times \partial_A \boldsymbol{m})\, d^3\boldsymbol{r}. \tag{3.22}$$

Here ∂_A is the spatial derivative in the direction $\hat{e}_A$ and $\boldsymbol{d}_A$ is the micromagnetic DMI vector which can be related to the atomic parameter $\boldsymbol{D}_{ij}$ via the relation [95]

$$\boldsymbol{d}_A = \frac{1}{V} \sum_{j \in N.N \boldsymbol{r}_0} \left[\boldsymbol{r}_0 - \boldsymbol{r}_j\right]_A \boldsymbol{D}_{0j}, \tag{3.23}$$

where V is the volume of the magnetic part of the unit cell. While the form of eq.(3.21) is more general and can describe a broader range of magnetic orderings (e.g. short range spin canting in antiferromagnets), the micromagnetic limit of eq.(3.22) is sufficient to study the statics and dynamics of so called "magnetic soft modes" such as smoothly varying domain walls and topological structures such as skyrmion. Much like in eq.(3.8), the sum over nearest neighbours in the magnetic

Point Group ($n > 2$)	DMI energy density $\mathscr{E}_{DMI}$
C_{nv}	$\mathscr{E}_{DMI} = D(\mathscr{L}_{zx}^{(x)} - \mathscr{L}_{zy}^{(y)})$
D_n	$\mathscr{E}_{DMI} = D(\mathscr{L}_{xz}^{(y)} - \mathscr{L}_{yz}^{(x)}) + D'\mathscr{L}_{xy}^{(z)}$
D_{2d}	$\mathscr{E}_{DMI} = D(\mathscr{L}_{yz}^{(x)} + \mathscr{L}_{xz}^{(y)})$
C_n	$\mathscr{E}_{DMI} = D(\mathscr{L}_{xz}^{(x)} - \mathscr{L}_{yz}^{(y)}) + D'(\mathscr{L}_{xz}^{(y)} - \mathscr{L}_{yz}^{(x)}) + D''\mathscr{L}_{xy}^{(z}$
S_4	$\mathscr{E}_{DMI} = D(\mathscr{L}_{xz}^{(x)} - \mathscr{L}_{yz}^{(y)}) + D'(\mathscr{L}_{yz}^{(x)} + \mathscr{L}_{xz}^{(y)})$
T, O	$\mathscr{E}_{DMI} = D(\mathscr{L}_{zy}^{(x)} + \mathscr{L}_{xz}^{(y)} + \mathscr{L}_{yx}^{(z)})$

Table 3.1 The form of micromagnetic Dzyaloshinskii-Moriya energy density $\mathscr{E}_{DMI}$ for all 11 non-centrosymmetric point groups

unit cell implies that the symmetry properties of the material play a fundamental role in determining the shape of this form of interaction.

In the microscopic limit, the allowed directions of $\boldsymbol{D}_{ij}$ are restricted by the Moriya rules (see 2.4.1 or [67]), while in the micromagnetic limit of (3.22), the allowed forms of $\boldsymbol{d}_A$ are restricted by the von Neumann principle of crystallography [96]. The allowed forms of micromagnetic DMI energy are related to the different crystallographic point groups as reported in Table.3.1 [97, 98], where $\mathscr{L}_{AB}^{(C)} = m_B(\partial_C m_A) - m_A(\partial_C m_B)$ are the so called Lifshitz invariants and the indices A, B, C run over arbitrary Cartesian coordinated x, y, z.

3.2 Magnetic Anisotropy

Magnetic anisotropy is a property of magnetic materials that determines the energy of a magnet based on the direction of magnetization with respect to the crystal axes: it's at the basis of many fundamental phenomena in magnetic materials such hysteresis and coercivity. One of the significant sources of anisotropy in magnetic materials is magnetocrystalline anisotropy, which arises from the interaction of magnetic moments and the crystal field via spin orbit coupling (see sec.2.3.1). Another critical source of magnetic anisotropy is the long-range dipolar interaction of atomic magnetic moments.

The dependence of energy on the magnetization direction is encoded by anisotropy constants and the most general case may be described by a function $\mathscr{E}_{anis} = Kf(\boldsymbol{m}, \hat{\boldsymbol{n}})$ where f is a dimensionless function, $\hat{\boldsymbol{n}}$ represents a direction unit vector and K has the unit of an energy density J/m^3. In principle, any set of angular functions complying with the crystal symmetry of the material can represent a suitable basis, with group theory used to determine the allowed terms. While spherical harmonics $Y_{l,m}$ seem a natural choice as an orthogonal basis, simple trigonometric functions are often more useful in practice. For a cubic material (point group T) one finds

$$\mathscr{E}_T = K_1(\alpha_1^2\alpha_2^2 + \alpha_2^2\alpha_3^2 + \alpha_3^2\alpha_1^2) + K_2(\alpha_1^2\alpha_2^2\alpha_3^2) + K_3(\alpha_1^2\alpha_2^2\alpha_3^2)^2 + \cdots, \quad (3.24)$$

where α_i represent the direction cosines of the magnetization with the three axes. A hexagonal symmetry (point group C_{6v}) yields

$$\mathscr{E}_{C_{6v}} = K_1 \sin^2\theta + K_2 \sin^4\theta + \cdots, \quad (3.25)$$

where θ represents the polar angle between the magnetization $\boldsymbol{m}$ and the c-axis. The order of the magnetic anisotropy can be even higher (sixth order and beyond shown in Fig.3.4), however experimental observations [8] demonstrate a sharp decrease of magnitude upon increasing order. In many cases, the use of a second order uniaxial energy

$$\mathscr{E}_{anis} = K_u \sin^2\theta \quad (3.26)$$

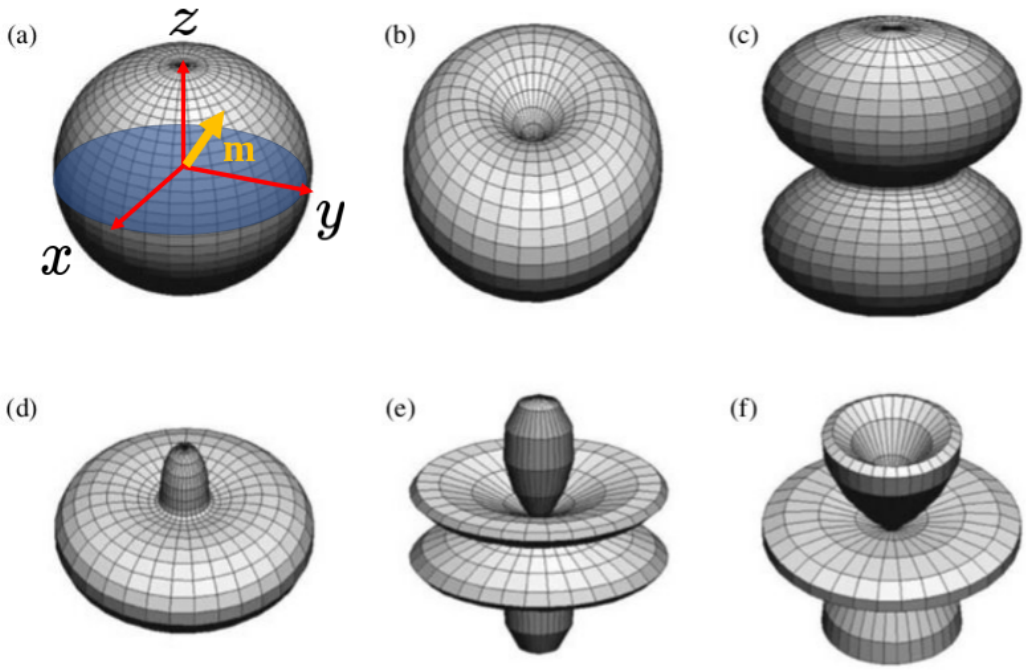

Fig. 3.4 Magnetic anisotropy energy landscapes: (a) isotropic (b) *easy-axis* anisotropy along z (c) *easy-plane* anisotropy in the $x-y$ plane (d) *easy-cone* anisotropy (e-f) sixth order anisotropy energy landscapes. Readapted from [8].

is enough to describe the main features of the statics and dynamics of the studied systems.

The physical interpretation of (3.26) depends on the sign of K_u: if $K_u < 0$ the energy density is minimized by $\theta = \pi/2$ and the magnetization is constrained to the basal plane (*easy-plane* anisotropy), while if $K_u > 0$ we have two possible minima, $\theta = \{\pi, 0\}$, implying that the easy axis is parallel to the symmetry axis of the material (*easy-axis* anisotropy). The strength of anisotropy may be described in terms of energy density (K_u) or in terms of a so-called "anisotropy field" $H_a = \frac{2K_u}{\mu_0 M_s}$, the latter being of particular use as it allows for a very quick comparison with other competing fields (such as applied fields or the coercivity H_c).

The Zeeman Energy

The Zeeman energy is related to the interaction of the magnetic moments and an external magnetic field $\boldsymbol{H}_{ext}$. The energy is proportional to the dot product of the local magnetization and the external magnetic field and has form

$$E_Z = -\int_V M_s \mu_0 \boldsymbol{m}(\boldsymbol{r}) \cdot \boldsymbol{H}_{ext}\, d^3\boldsymbol{r}. \tag{3.27}$$

It has a fairly simple structure and tries to align the magnetization vector in the direction of the applied field $\boldsymbol{H}_{ext}$.

Magnetostatic energy

Magnetostatic energy, also known as dipolar energy, represents the mutual Zeeman-type interaction arising between all magnetic moments of a magnetic body through their stray field. Due to its non local character, it is indeed the most difficult energy contribution to handle in micromagnetism with only very few cases being treatable analytically. Due to the non-uniformity of the generated effective field, it is a contribution of fundamental importance for the stabilization of magnetization patterns such as magnetic domains in large magnetic samples.

To visualize how this interaction may enter the energy functional, we write down the Zeeman energy of a single magnetic moment $\boldsymbol{m}_i = \boldsymbol{m}(\boldsymbol{r}_i)$ exposed to the stray

field $\boldsymbol{H}_d$ in a volume element ΔV

$$E_i = -\mu_0 \boldsymbol{m}_i \cdot (\boldsymbol{H}_d - \boldsymbol{\lambda}), \tag{3.28}$$

where $\boldsymbol{H}_d$ is the stray field generated by all the other magnetic moments and $\boldsymbol{\lambda}$ is a small correction given by neglecting the contribution of $\boldsymbol{m}_i$ itself (this term is ignored in the following). The total energy is given by the sum of all these contributions with the factor $1/2$ appearing to avoid double counting

$$E_d = -\frac{\mu_0}{2} \sum_i \boldsymbol{m}_i \cdot \boldsymbol{H}_d \tag{3.29}$$

$$= -\frac{\mu_0}{2} \sum_i \frac{\boldsymbol{m}_i}{\Delta V} \cdot \boldsymbol{H}_d \Delta V. \tag{3.30}$$

Performing the continuum limit (i.e $\lim_{\Delta V \to 0} E_d$) we can write the demagnetization energy as

$$E_d = -\frac{\mu_0}{2} \int_V \boldsymbol{M} \cdot \boldsymbol{H}_d \, d^3\boldsymbol{r}. \tag{3.31}$$

The stray field can be obtained by solving the Maxwell equations of magnetostatics [99]

$$\begin{cases} \nabla \times \boldsymbol{H}_d = 0, & \\ & \forall\, \boldsymbol{r} \in \mathbb{R}^3 \\ \nabla \cdot (\underbrace{\mu_0 \boldsymbol{H}_d + \boldsymbol{M}}_{=\boldsymbol{B}}) = 0 & \end{cases} \tag{3.32}$$

We emphasize that these Maxwell equations are valid in the whole space $\mathbb{R}^3$ and not only in the volume of the magnetic sample V. From eq.(3.32), we know that $\boldsymbol{H}$ is a gradient field, therefore

$$\boldsymbol{H_d} = -\nabla\Phi \Rightarrow \nabla^2\Phi = \rho_m = \nabla \cdot \boldsymbol{M}, \tag{3.33}$$

which shows that the magnetization $\boldsymbol{M}$ is the source of the stray field $\boldsymbol{H}_d$. The above is a Poisson equation for which we have to consider particular boundary conditions. We assume continuity and $\rho_m = 0$ outside the sample, allowing us to decompose the

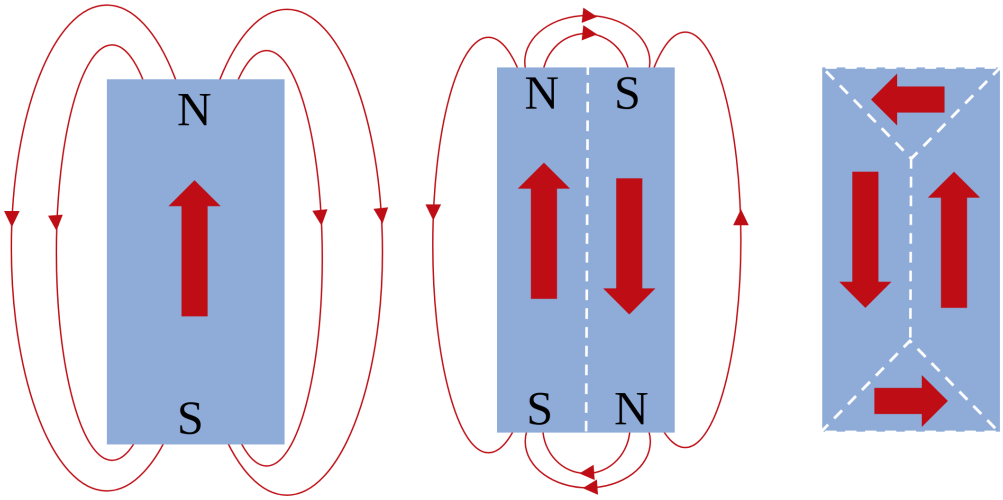

Fig. 3.5 Schematic representation of how the division in magnetic domains is a means to minimize the presence of magnetic surface and volume charges. The demagnetizing field stabilizes configurations displaying flux closure.

solution $\Phi(\boldsymbol{r})$ of the Poisson equation 3.33 in a volume and surface contribution

$$\Phi(\boldsymbol{r}) = -\frac{1}{4\pi}\int_{\mathbb{R}^3}\frac{\nabla\cdot\boldsymbol{M}(\boldsymbol{r}')}{|\,\boldsymbol{r}-\boldsymbol{r}'\,|}d^3\boldsymbol{r}' \tag{3.34}$$

$$= -\frac{1}{4\pi}\left(\int_V \frac{\rho_m(\boldsymbol{r}')}{|\,\boldsymbol{r}-\boldsymbol{r}'\,|}d^3\boldsymbol{r}' + \oint_{\partial V}\frac{\overbrace{\hat{\boldsymbol{n}}\cdot\boldsymbol{M}(\boldsymbol{r}')}^{\sigma_m(\boldsymbol{r}')}}{|\,\boldsymbol{r}-\boldsymbol{r}'\,|}d\Sigma'\right), \tag{3.35}$$

where ∂V represents the surface of the magnetic sample and $\hat{\boldsymbol{n}}$ the normal vector to the surface element $d\Sigma'$. From this equation we see how the contribution of the stray field aims at reducing ρ_m and σ_m which implicitly means that having surface and volume charges has an intrinsic energetic cost that the demagnetization field tries to minimize: magnetization configurations with vanishing magnetostatic energy are those that achieve flux closure (see Fig.3.5).

Demagnetizing factors

The calculation of the demagnetization field is in general a very hard problem to solve because of the long range nature of the dipolar interaction. For certain geometries however, it is possible to calculate the surface charges generated by a uniform

magnetization. In the case of a uniformly magnetized ellipsoid, the demagnetizing field only depends on the shape of the sample and can be expressed as [99]

$$\boldsymbol{H}_d = -M_s \overleftrightarrow{N}\, \boldsymbol{m} \tag{3.36}$$

where $\overleftrightarrow{N}$ is the demagnetizing tensor, which only depends on the geometry of the system. In this case the ellipsoid axes $\overleftrightarrow{N}$ can be diagonalized to

$$\overleftrightarrow{N} = \begin{pmatrix} N_x & 0 & 0 \\ 0 & N_y & 0 \\ 0 & 0 & N_z \end{pmatrix}, \tag{3.37}$$

and has to obey the constraint $\sum_{i\in\{x,y,z\}}^{3} N_i = 1$ [99]. The calculation of the demagnetizing factors can become quite cumbersome for certain geometries. We remark how in the case of a magnetic thin film, which is of particular interest for the contents of this dissertation, the demagnetizing factors can be computed analytically via a quite involved formula [100] that we will not show here. As a consequence of the presence of magnetostatic energy and the demagnetization field, the magnetization aligns along directions that generate less magnetic charges (see eq.3.35), leading to an anisotropic contribution linked to the shape of the sample, hence called "shape anisotropy term".

3.3 The micromagnetic energy functional and the variational principle

The total free energy of the system can now be written as the sum of the individual contributions and has the form $E[\boldsymbol{m}, \nabla \boldsymbol{m}]$ which is the object of variational considerations to obtain equilibrium configurations as a function of the different micromagnetic parameters

$$E[\boldsymbol{m}, \nabla \boldsymbol{m}] = \int_V \left[\mathscr{E}_{\text{exch}}(\boldsymbol{r}) + \mathscr{E}_{\text{DMI}}(\boldsymbol{r}) + \mathscr{E}_{\text{anis}}(\boldsymbol{r}) + \mathscr{E}_{\text{dmg}}(\boldsymbol{r}) + \mathscr{E}_{\text{Z}}(\boldsymbol{r}) \right] d^3\boldsymbol{r} \quad (3.38)$$

$$= \int_V \left[\sum_{A,B} \Xi_{AB} (\partial_A \boldsymbol{m}) \cdot (\partial_B \boldsymbol{m}) + \sum_A \boldsymbol{d}_A \cdot (\boldsymbol{m} \times \partial_A \boldsymbol{m}) \right. \quad (3.39)$$

$$\left. + f(\boldsymbol{m}, \hat{\boldsymbol{n}}) - \frac{\mu_0}{2} M_s \boldsymbol{m} \cdot \boldsymbol{H}_d - \mu_0 M_s \boldsymbol{m} \cdot \boldsymbol{H}_{ext} \right] d^3\boldsymbol{r}, \quad (3.40)$$

where we have considered contributions from exchange interaction Ξ_{AB}, DMI $\boldsymbol{d}_A$, magnetocrystalline anisotropy $f(\boldsymbol{m}, \hat{\boldsymbol{n}})$, magnetostatic interactions $\boldsymbol{H}_d$ and external field $\boldsymbol{H}_{ext}$. We remark how the energy functional of eq.(3.40) is extremely general and is often found in a simplified form relative to the particular system of study. For a cubic lattice with no DMI, the exchange stiffness tensor has diagonal form $\Xi_{AB} = A\delta_{AB}$ and the energy functional can be cast in the simplified form

$$E[\boldsymbol{m}, \nabla \boldsymbol{m}] = \int_V \left[\mathscr{E}_{\text{exch}}(\boldsymbol{r}) + \mathscr{E}_{\text{anis}}(\boldsymbol{r}) + \mathscr{E}_{\text{dmg}}(\boldsymbol{r}) + \mathscr{E}_{\text{Z}}(\boldsymbol{r}) \right] d^3\boldsymbol{r} \quad (3.41)$$

$$= \int_V \left[A |\nabla \boldsymbol{m}|^2 + f(\boldsymbol{m}, \hat{\boldsymbol{n}}) - \frac{\mu_0}{2} M_s \boldsymbol{m} \cdot \boldsymbol{H}_d - \mu_0 M_s \boldsymbol{m} \cdot \boldsymbol{H}_{ext} \right] d^3\boldsymbol{r}, \quad (3.42)$$

where $A|\boldsymbol{\nabla m}|^2 = A \sum_{AB} (\partial_A m_B)^2$. In the following we derive the variational principle for the simplified functional of eq.(3.42), treating the DMI separately in 3.3.1. Assuming we are at a sufficiently low temperature $T \ll T_C$ (where T_C represents the Curie temperature) as to keep the magnetization per unit volume constant, each energy minimum has to satisfy the variational condition $\delta E[\delta \boldsymbol{m}] = 0$ under the constraint of $|\boldsymbol{m}(\boldsymbol{r})| = 1 \; \forall \; \boldsymbol{r} \in V$. The variation of the energy functional

of eq.(3.42) is

$$\delta E[\delta\mathbf{m}(\mathbf{r})] = \int_V \left(2A\nabla\mathbf{m}\cdot\nabla\delta\mathbf{m} + \frac{\partial f}{\partial\mathbf{m}}\delta\mathbf{m} - \mu_0 M_s \mathbf{H}_M\cdot\delta\mathbf{m} - \mu_0 M_s \mathbf{H}_a\cdot\delta\mathbf{m}\right) d^3\boldsymbol{r}, \tag{3.43}$$

by using the identity $\nabla\cdot(\phi\boldsymbol{v}) = \phi\ (\nabla\cdot\boldsymbol{v}) + \boldsymbol{v}\cdot(\nabla\phi)$, eq.(3.43) becomes

$$\delta E[\delta\mathbf{m}(\mathbf{r})] = -\int_V \left(2A\nabla\cdot(\nabla\mathbf{m}) - \frac{\partial f}{\partial\mathbf{m}} + \mu_0 M_s\mathbf{H}_M + \mu_0 M_s\mathbf{H}_a\right)\cdot\delta\mathbf{m}\, d^3\boldsymbol{r} \tag{3.44}$$

$$+ 2\oint_{S=\partial V} A\left(\frac{\partial\mathbf{m}}{\partial n}\cdot\delta\mathbf{m}\right) d^2\boldsymbol{a} \tag{3.45}$$

$$= -\int_V (\mu_0 M_s\mathbf{H}_{\text{eff}}\cdot\delta\mathbf{m})\, d^3\boldsymbol{r} + 2\oint_{S=\partial V} A\left(\frac{\partial\mathbf{m}}{\partial n}\cdot\delta\mathbf{m}\right) d^2\boldsymbol{r}. \tag{3.46}$$

The first integral is performed over the volume of the sample while the second one is performed over surfaces. We also highlight how $\frac{\partial\mathbf{m}}{\partial n}$ represents the directional derivative along the surface normal $\hat{\boldsymbol{n}}$. Finally, $\boldsymbol{H}_{\text{eff}}$ is called the effective field and is defined as

$$\boldsymbol{H}_{\text{eff}} = -\frac{1}{\mu_0 M_s}\frac{\delta\mathscr{E}[\boldsymbol{m}]}{\delta\boldsymbol{m}} = -\frac{1}{\mu_0 M_s}\left(\nabla\frac{\partial\mathscr{E}}{\partial(\nabla\boldsymbol{m})} - \frac{\partial\mathscr{E}}{\partial(\boldsymbol{m})}\right), \tag{3.47}$$

where $\mathscr{E}(\boldsymbol{m})$ represents the micromagnetic energy density, i.e. the integrand of eq.(3.42). At this point we can exploit the normalization constraint on $\boldsymbol{m}$, which requires any variation $\delta\boldsymbol{m}$ to be perpendicular to $\boldsymbol{m}$ and implies $\delta\boldsymbol{m} = \boldsymbol{m}\times\delta\boldsymbol{\theta}$. We can rewrite eq.(3.46) as

$$\delta E([\delta\mathbf{m}(\mathbf{r}))] = -\int_V \mu_0 M_s\,(\mathbf{H}_{\text{eff}}\times\mathbf{m})\cdot\delta\boldsymbol{\theta}\ d^3\boldsymbol{r} + 2\oint_{S=\partial V} A\left(\frac{\partial\mathbf{m}}{\partial n}\times\mathbf{m}\right)\cdot\delta\boldsymbol{\theta}\ d^2\boldsymbol{r}. \tag{3.48}$$

The variational principle states that the minimizing configuration must satisfy the condition $\delta E[\boldsymbol{m}] = 0$ for any arbitrary variation $\delta\boldsymbol{\theta}$, therefore eq.(3.48) yields the following equations for the equilibrium magnetization (known as Brown's equations)

$$\mathbf{m}\times\mathbf{H}_{\text{eff}} = 0 \qquad \forall\,\mathbf{r}\ \in V, \tag{3.49}$$

$$\mathbf{m}\times\frac{\partial\mathbf{m}}{\partial n} = 0 \qquad \forall\,\mathbf{r}\in S. \tag{3.50}$$

The important message of the conditions expressed in eq.(3.49) is that the equilibrium magnetization has to lie parallel to the local effective field $\boldsymbol{H}_{\text{eff}}(\boldsymbol{r})$ in the bulk of the material. The second equation is essentially a boundary condition on the surface of the magnetized body. Notice that, since we impose a constant length of the magnetization $\boldsymbol{m}$, it's derivative has to be perpendicular to $\boldsymbol{m}$ itself, which allows to express the boundary condition in the simplified form

$$\frac{\partial \boldsymbol{m}}{\partial n} = 0 \; \forall \; \mathbf{r} \in S \tag{3.51}$$

3.3.1 Variational principle for the DMI term

In the following we derive the additional equilibrium conditions for the chiral energy term (DMI energy). As a first step, we observe the chiral energy term

$$E_{DMI}[\boldsymbol{m}, \nabla \boldsymbol{m}] = \int_V \sum_A \boldsymbol{d}_A \cdot (\boldsymbol{m} \times \partial_A \boldsymbol{m}) \; d\boldsymbol{r}^3 \tag{3.52}$$

can be rewritten as

$$E_{DMI}[\boldsymbol{m}, \nabla \boldsymbol{m}] = \int_V \boldsymbol{m} \cdot (\hat{\boldsymbol{Q}} \nabla \times \boldsymbol{m}) \; d^3\boldsymbol{r}, \tag{3.53}$$

where $\hat{\boldsymbol{Q}}\nabla = Q_{AB}\partial_B = \sum_A Q_{AB} \dfrac{\partial}{\partial x_B} \hat{e}_B$. We now proceed and derive the boundary conditions from the extremal requirement of the functional $\delta E_{DMI}[\delta \boldsymbol{m}, \delta \nabla \boldsymbol{m}] = 0$. The derivation is as follows:

$$\delta E_{DMI}[\delta \boldsymbol{m}, \delta \nabla \boldsymbol{m}] = 0 \tag{3.54}$$

$$\Rightarrow \int_V d^3\boldsymbol{r} \left[\delta \boldsymbol{m} \cdot (\hat{\boldsymbol{Q}} \nabla \times \boldsymbol{m}) + \boldsymbol{m} \cdot (\hat{\boldsymbol{Q}} \nabla \times \delta \boldsymbol{m}) \right] = 0 \tag{3.55}$$

The first term of the sum represents a part of the effective field term while the second, as we will show, results in the boundary conditions and has to be treated with some care. First of all, we notice that the equality

$$\nabla \cdot (\boldsymbol{m} \times \delta \boldsymbol{m}) = \delta \boldsymbol{m} \cdot (\nabla \times \boldsymbol{m}) - \boldsymbol{m} \cdot (\nabla \times \delta \boldsymbol{m}) \tag{3.56}$$

Also holds for $\tilde{\nabla} := \hat{\boldsymbol{Q}}\nabla$ because $\hat{\boldsymbol{Q}}$ acts linearly on the partial derivatives. We can therefore write the second member of (3.55) as

$$\int_V \boldsymbol{m} \cdot (\hat{\boldsymbol{Q}}\nabla \times \delta\boldsymbol{m})\, d^3\boldsymbol{r} = \int_V [\delta\boldsymbol{m} \cdot (\tilde{\nabla} \times \boldsymbol{m}) - \tilde{\nabla} \cdot (\boldsymbol{m} \times \delta\boldsymbol{m})]\, d^3\boldsymbol{r}. \tag{3.57}$$

At a first glance it appears as if we cannot apply the divergence theorem on the term $\int_V \tilde{\nabla} \cdot (\boldsymbol{m} \times \delta\boldsymbol{m})\, d^3\boldsymbol{r}$, however we can transpose $\hat{\boldsymbol{Q}}$ and let it act on $(\boldsymbol{m} \times \delta\boldsymbol{m})$ in the integral.

$$\int_V \nabla \cdot \hat{\boldsymbol{Q}}^T (\boldsymbol{m} \times \delta\boldsymbol{m})\, d^3\boldsymbol{r} \tag{3.58}$$

We can now use the divergence theorem to convert the volume integral in a surface integral

$$\int_V \nabla \cdot \hat{\boldsymbol{Q}}^T (\boldsymbol{m} \times \delta\boldsymbol{m})\, d^3\boldsymbol{r} = \oint_{S=\partial V} \hat{\boldsymbol{n}} \cdot \left[\hat{\boldsymbol{Q}}^T (\boldsymbol{m} \times \delta\boldsymbol{m})\right] d^2\boldsymbol{r} \tag{3.59}$$

Where $\hat{\boldsymbol{n}}$ represents the normal vector to the infinitesimal surface element $d^2\boldsymbol{r}$. We can again shift the action of the $\hat{\boldsymbol{Q}}^T$ matrix on the $\hat{\boldsymbol{n}}$ vector and use the cyclic property of the scalar triple product to obtain

$$\Rightarrow \oint_{S=\partial V} \delta\boldsymbol{m} \cdot (\hat{\boldsymbol{Q}}^T \hat{\boldsymbol{n}} \times \boldsymbol{m})\, d^2\boldsymbol{r} \tag{3.60}$$

The boundary term coming from ordinary isotropic exchange has the usual form, so the combined terms yield

$$\oint_{S=\partial V} \delta\boldsymbol{m} \cdot \left[2A\frac{\partial \boldsymbol{m}}{\partial n} + (\hat{\boldsymbol{Q}}^T \hat{\boldsymbol{n}} \times \boldsymbol{m})\right] d^2\boldsymbol{r} \tag{3.61}$$

The total variational derivative (which here only considers ferromagnetic exchange and DMI) therefore becomes:

$$\delta E = \int_V \delta\boldsymbol{m} \cdot \underbrace{\left[2A|\nabla\boldsymbol{m}|^2 + 2(\hat{\boldsymbol{Q}}\nabla \times \boldsymbol{m})\right]}_{:=\boldsymbol{H}_{\text{eff}}} d^3\boldsymbol{r} - \oint_{S=\partial V} \delta\boldsymbol{m} \cdot [2A\frac{\partial \boldsymbol{m}}{\partial n} + (\hat{\boldsymbol{Q}}\hat{\boldsymbol{n}} \times \boldsymbol{m})] d^2\boldsymbol{r} \tag{3.62}$$

$$= \int_V \delta\boldsymbol{\theta} \cdot (\boldsymbol{m} \times \boldsymbol{H}_{\text{eff}})\, d^3\boldsymbol{r} + \oint_{S=\partial V} \delta\boldsymbol{\theta} \cdot \left[2A\frac{\partial \boldsymbol{m}}{\partial n} \times \boldsymbol{m} + (\hat{\boldsymbol{Q}}\hat{\boldsymbol{n}} \times \boldsymbol{m}) \times \boldsymbol{m}\right] d^2\boldsymbol{r} \tag{3.63}$$

where, once again, we defined the variation of the magnetization as $\delta \boldsymbol{m} = \boldsymbol{m} \times \delta \boldsymbol{\theta}$. Eq.(3.63) allows us to define some new boundary conditions that must be satisfied by the equilibrium magnetization configuration $\boldsymbol{m}(\boldsymbol{r})$.

$$\boldsymbol{m} \times \boldsymbol{H}_{\text{eff}} = 0 \qquad \forall\, \boldsymbol{r} \in V, \tag{3.64}$$

$$\left[2A \frac{\partial \boldsymbol{m}}{\partial n} + (\hat{\boldsymbol{Q}}^T \hat{\boldsymbol{n}} \times \boldsymbol{m}) \right] \times \boldsymbol{m} = 0 \qquad \forall\, \boldsymbol{r} \in S. \tag{3.65}$$

Since the vector field in the square brackets of eq.(3.65) is required to be orthogonal to $\boldsymbol{m}(\boldsymbol{r})$ $\forall\ \boldsymbol{r} \in S$, we can only achieve such configuration on the surface of the magnetic body if

$$\left[2A \frac{\partial \boldsymbol{m}}{\partial n} + (\hat{\boldsymbol{Q}}^T \hat{\boldsymbol{n}} \times \boldsymbol{m}) \right] = 0 \ , \ \forall\, \boldsymbol{r} \in S. \tag{3.66}$$

3.4 Magnetism in lower dimensions: interfacial effects

3.4.1 Magnetic ordering in low dimensional magnetic systems

The interesting feature a of a ferromagnetic body is the spontaneous appearance of long range order below a critical temperature (the Curie Temperature) T_C. In the following we provide a short and intuitive explanation regarding the behavior of the ordering temperature as a function of the thickness of the magnetic body. One famous argument is based on the mean field approach proposed by Pierre Weiss. Weiss considered the atomic magnetic moments in the solid subject two an internal magnetic field of the form

$$\boldsymbol{H}_I = n_W \boldsymbol{M}_s + \boldsymbol{H}, \tag{3.67}$$

where $\boldsymbol{H}$ is the Zeeman field and $n_W \boldsymbol{M}_s$ is the so called "molecular field", i.e. the mean field perceived by a magnetic moment as a consequence of the presence all the other ones surrounding it. To bridge the gap between notions of ordering temperature and this mean field approach, we need to find a way to relate the molecular field to Heisenberg exchange described in 2.1.1

$$\mathscr{H} = -\frac{1}{2} \sum_{i,j} J_{ij} \boldsymbol{S}_i \cdot \boldsymbol{S}_j, \tag{3.68}$$

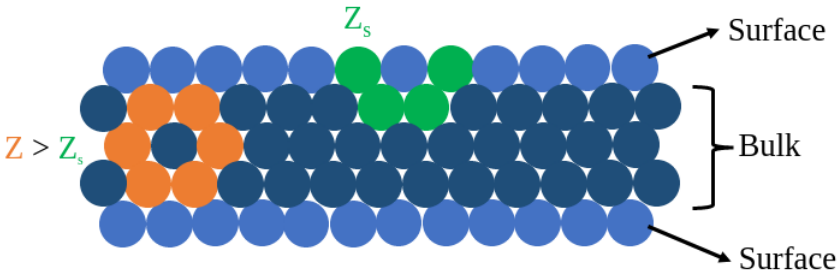

Fig. 3.6 Schematic representation of a thin film system. As can be seen the coordination number is decreased in the surface layers

where J_{ij} is the Heisenberg exchange parameter derived in 3.1 and $\boldsymbol{S}_i, \boldsymbol{S}_j$ are dimensionless spins located at sites i, j with magnitude S bound by $S \in [-J, J]$ associated with total magnetic moment $\mu_J = g_J J \mu_B$. we emphasize here that we are using a semi-classical approach, and therefore the Hamiltonian in (3.68) does not represent a quantum-mechanical operator. We can relate the molecular field n_W to the Heisenberg exchange parameter J_{ij} via [45]

$$J_{ij} = \frac{\mu_0 \mu_B n_W n g_J^2}{2Z}, \tag{3.69}$$

where Z is the number of nearest neighbors and n is the volume density of magnetic sites. Based on this assumption, the ordering temperature T_C can be derived via standard methods of statistical mechanics [53], yielding

$$T_C = \frac{2ZJ_{ij}J(J+1)}{3k_B} \propto Z. \tag{3.70}$$

This simple equation highlights a fundamental point, namely that the ordering temperature is proportional to the number of nearest neighbors which varies when considering a bulk or a thin film system. If we consider a magnetic thin film composed of N layers, the average number of nearest neighbors $Z_N < Z$ per definition, implying a lower ordering temperature T_C in eq.(3.70). If we define the average of nearest neighbors in the layered system

$$Z_N = Z + \frac{2(Z_s - Z)}{N}, \tag{3.71}$$

where Z_s is the number of nearest neighbors on the 2 boundary layers (see Fig.3.6), we see that the critical temperature scales with $T_C \propto N^{-1}$, i.e with the inverse of

the thickness. A more rigorous treatment [101] discovers a critical behavior for the thickness dependent critical temperature $T_C \propto t^{-\lambda}$, with $\lambda = 1.27 \pm 0.20$ representing the critical exponent.

3.4.2 Magnetic anisotropy in low dimensions

Dipolar anisotropy

As introduced in 3.2, the intricacies of magnetostatic energy (i.e. dipolar interactions) in magnetic samples can be formulated compactly via the demagnetization tensor $\overleftrightarrow{N}$ if we assume a uniformly magnetized sample. While the assumption of uniform magnetization can be rather outlandish when considering large bulk systems, it becomes more reasonable when considering low dimensional magnetic systems such as thin films. We have seen how, after proper diagonalization of the demagnetization tensor, the demagnetization field can be expressed as

$$\boldsymbol{H}_d = -M_s \overleftrightarrow{N} \boldsymbol{m}, \tag{3.72}$$

where the demagnetization coefficients have to satisfy the constraint $N_x + N_y + N_z = 1$. For thin films, $N_x = N_y = 0 \Rightarrow N_z = 1$ which implies the demagnetization field becomes $\boldsymbol{H}_d = -M_s \hat{e}_z$. The demagnetisation component of the micromagnetic energy $\mathscr{E}_{dmg} = K_d m_z^2(\boldsymbol{r})$ is minimized by $m_z(\boldsymbol{r}) = 0$, i.e. a magnetization pointing in the plane perpendicular to the $\hat{e}_z$ direction. For more general cases where one of the dimensions is much smaller than the other 2 we can extrapolate a general trend that sees the magnetization pointing in the direction with the lowest demagnetizing factor. We remark however, that the stated rule of thumb is only valid when no applied fields or strong magneto-crystalline anisotropy are present in the system.

Interface magnetic anisotropy

An anisotropy contribution of particular interest in magnetic multilayers and thin films is surface and interface anisotropy. As discussed and derived in 2.3.1, in $3d$ systems the Bruno model [49, 50] successfully links the appearance of finite magneto-crystalline anisotropy with the anisotropy of orbital magnetic moment via

$$\Delta E \propto \xi \Delta \mu_L, \tag{3.73}$$

where ξ represents the strength of the spin-orbit coupling term in the Hamiltonian $\mathscr{H}_{SO} = -\xi \hat{\boldsymbol{S}} \cdot \hat{\boldsymbol{L}}$ and $\Delta\mu_L$ represents the difference of orbital magnetic moment between easy and hard axis. In cubic bulk $3d$ metals ΔE is small because because electronic eigenfunctions in a cubic crystal field environment have nearly zero orbital magnetic moment [102] and therefore $\Delta\mu_L$ are typically of the order of $10^{-4}\mu_B$ per atom (which roughly translates to $K \approx 10^4 J/m^3$). In the vicinity of a surface however, the crystal field symmetry changes because of the different bonding environment and the orbital magnetic moment difference $\Delta\mu_B$ can increase up to 3 orders of magnitude. Both the direction and the strength of this effect however, obey the rules of crystal field theory [102] and therefore entirely depend on the indexing of the surface. A symmetry breaking surface is therefore a necessary but not sufficient condition to yield a strong interface anisotropy: as an example, only the bcc (011) surface supports a strong second order in plane anisotropy [8], while the corresponding (001) and (111) only display 4^{th} and 6^{th} order in plane anisotropies respectively. Most notably however, since bulk cubic anisotropies are usually 2 orders of magnitude weaker than surface anisotropies we notice how these can easily dominate the bulk anisotropy given a sufficiently large ratio of surface and bulk atoms (i.e a sufficiently thin sample). The competition of a variety of bulk and surface anisotropies may give rise to a spin reorientation transition as a function of sample thickness and temperature. This behavior can be described by the phenomenological expression of the total anisotropy as

$$K_{tot} = \frac{K_s}{t} + K_0, \tag{3.74}$$

where t is the film thickness, K_s is the surface anisotropy and K_0 encapsulates the bulk magneto-crystalline and magnetostatic (shape) anisotropy. The most substantial consequence of surface magnetic anisotropy, also having deep consequences for technological development, arises when $K_s < 0$ (i.e. surface anisotropy has an easy axis out of the thin film plane) and $K_0 > 0$ (i.e. bulk anisotropy has an easy plane anisotropy in the plane of the film): in that case, a sample thickness $t = t_C = \frac{|K_s|}{K_0}$ will trigger a spontaneous perpendicular magnetic anisotropy (PMA).

3.4.3 The interfacial Dzyaloshinskii-Moriya interaction

The discovery of DMI in thin magnetic multilayers with PMA has sparked significant scientific interest in the possibility of stabilizing novel magnetization patterns [103,

7, 104, 105] having the potential to expand the functionalities of memory storage devices in new and unexpected ways. One area where the discovery of DMI is particularly significant is in the context of ultrathin FM systems displaying PMA in contact with HM because the intrinsic broken inversion symmetry coupled with a strong SOC provided by the HM constitutes an ideal environment for DMI. One type of unconventional magnetic state that has been attributed solely to magnetic compounds with broken inversion symmetry is axisymmetric solitonic patterns, such as vortices or skyrmions [97, 106, 104, 107] Both of these states are stabilized by specific DMI arising in chiral magnets due to their crystallographic handedness.

The micromagnetics of chiral modulations

Topologically protected objects or states, such as quantum Hall states and chiral edge modes of topological insulators, have garnered significant interest from both the fundamental and applied research communities. In the realm of applied magnetism, the study of topological objects such as solitons and vortices has attracted significant attentions, due to the potential for small size, easy current-driven motion, and topological stability. The community is actively investigating new device concepts proposing integrated circuits based on magnetic skyrmions, but to transform them in a viable option for practical electronics such as magnetic memories and logic circuits, a profound understanding of the fundamental physics of skyrmions and the development of suitable material platforms for their stable realization are of paramount importance.

To understand why the DMI is essential in stabilizing new topological magnetization textures, we will briefly show how to derive energy minimizing magnetization configurations of the micromagnetic energy functional. As a model we consider a semi-infinite thin slab of thickness L along the $\hat{z}$-axis with PMA and an out-of-plane applied external field $\boldsymbol{H}_Z = H_Z\hat{\boldsymbol{n}}$. The energy density of such a system can be inferred by restricting the integrand of eq.(3.40) to 2-dimensions

$$\mathscr{E}(\boldsymbol{m},\nabla\boldsymbol{m}) = A|\nabla\boldsymbol{m}|^2 + \mathscr{E}_{DMI}(\boldsymbol{m}) - K_u(\boldsymbol{m}\cdot\hat{\boldsymbol{n}})^2 - \mu_0 M_s H_Z \boldsymbol{m}\cdot\hat{\boldsymbol{n}} - \frac{\mu_0 M_s}{2}\boldsymbol{m}\cdot\boldsymbol{H}_d, \tag{3.75}$$

Where A is the exchange stiffness, K_u is the uniaxial anisotropy constant, $\boldsymbol{H}_Z$ is the external applied magnetic field and $\boldsymbol{H}_d$ is the demagentization field. We parameterize

the reduced magnetization $\boldsymbol{m} = \boldsymbol{M}/M_s$ in spherical coordinates

$$\boldsymbol{m} = (\cos\phi\sin\theta, \sin\phi\sin\theta, \cos\theta)^T. \tag{3.76}$$

The DMI energy density is represented by the term $\mathscr{E}_{DMI}(\boldsymbol{m})$ and is a function of the Lifshitz-invariants defined in Table.3.1. To find the magnetization configurations $\boldsymbol{m}(\boldsymbol{r})$ that minimize the energy functional (3.75) we have to solve the Euler equations

$$2A|\nabla\boldsymbol{m}|^2 + \varepsilon_{DMI,V} = 0 \qquad \forall\, \boldsymbol{r} \in V, \tag{3.77}$$

$$2A\frac{\partial\boldsymbol{m}}{\partial n} + \varepsilon_{DMI,S} = 0 \qquad \forall\, \boldsymbol{r} \in S, \tag{3.78}$$

where $\varepsilon_{DMI,V}$ and $\varepsilon_{DMI,S}$ represent the DMI contributions to the Euler equations related respectively to the volume (V) and the surface of the magnetic body (S). The specific form of these terms depends on the crystallographic point group and the associated Lifshitz invariant combination repored in Table.3.1. To solve the problem completely we must not forget that associated Maxwell equations

$$\nabla\times\boldsymbol{H}_d = 0\ ,\ \nabla\cdot(\boldsymbol{H}_d + \mu_0 M_s\boldsymbol{m}) = 0, \tag{3.79}$$

must also be accounted for. The added complication introduced by the magnetostatic field $\boldsymbol{H}_d$ can be partially overcome by noticing how in chiral magnetic materials, DMI dominates over higher order dipolar interactions, allowing us to resort to the demagnetization ellipsoid approximation discussed in 3.2. In the $C_{nv}-$case, which is a point group symmetry group very well suited to describe HM/FM thin film heterostructures, the stray field can be included by redefining the anisotropy constants as follows

$$K_u \to K_u + K_d\ ,\ K_d = \mu_0 M_s^2/2. \tag{3.80}$$

To simplify the notation and exploiting the fact that we expect rotationally symmetric solutions, we introduce cylindrical coordinates for the spatial variable $\boldsymbol{r} = (\rho\cos(\psi), \rho\sin(\psi), z)^T$. We consider magnetization patterns anti-parallel to the applied field for $\rho = 0$ and approaching parallel orientation as $\rho \to \infty$. The magnetization is now parameterized as

$$\boldsymbol{m}(\theta(\boldsymbol{r}), \phi(\boldsymbol{r})) \to \boldsymbol{m}(\theta(\rho,\psi), \phi(\rho,\psi)) \tag{3.81}$$

and the energy functional (3.75) becomes

$$\mathscr{E}(\rho,\theta) = A\left[(\partial_\rho\theta)^2 + \frac{1}{\rho^2}(\partial_\psi\theta)^2 + \sin^2\theta\left((\partial_\rho\phi)^2 + \frac{1}{\rho^2}(\partial_\psi\phi)^2\right)\right] + \mathscr{E}_{DMI} - K\cos^2\theta - \mu_0 M_s H_Z\cos\theta - \mu_0 M_s \mathbf{m}\cdot\mathbf{H}_d/2. \quad (3.82)$$

Since the DMI energy is dependent on the crystal structure, different crystal symmetries yield different ground state magnetization configurations. A list of the Lifshitz invariants with transformed coordinates is reported in Appendix A.1 of ref.[107]. The configurations of $\boldsymbol{m}$ solving (3.77)-(3.79) are rotationally symmetric by construction and parametrized by

$$\theta = \theta(\rho)\ ,\ \phi = \phi(\psi)\ ,\ \boldsymbol{H}_d = \boldsymbol{H}_d(\rho). \quad (3.83)$$

The solutions $\theta(\rho)$ can be obtained by minimizing the $\psi-$integrated energy density

$$\mathscr{F} = 2\pi\int_0^\infty [\mathscr{E}(\rho,\theta) - \mathscr{E}_0]\rho d\rho, \quad (3.84)$$

where $\mathscr{E}_0$ is the energy density of a homogeneously magnetized state in the direction of the applied field and the anisotropy $\mathscr{E}_0 = -K - \mu_0 M_s H_Z$. Minimizing (3.84) with the boundary values

$$\theta(\rho\to 0) = \pi\ ,\ \theta(\rho\to\infty) = 0, \quad (3.85)$$

yields the solution [1].

$$\theta(\rho) \propto \frac{e^{-R(A,D,D',D'',K)\rho}}{\sqrt{\rho}}, \quad (3.86)$$

Where R is a parameter dependent on the material parameters A, K and the general form of DMI present in the system [107]. The solutions $\phi(\psi)$ can subsequently by derived by minimizing the functional (3.75) with the solution (3.85) [97], yielding the results of Table.3.2 The structures parameterized by the solutions of Table.3.2 are displayed in Fig.3.7 for different representative cases.

[1] In the original paper [97], the authors did not derive this form of the solution but instead proposed a trial function $\psi(\rho) = \pi(1-\rho/\rho_0)$ that, while in principle wrong, provided the correct boundary conditions and allowed the correct prediction of the form of $\phi(\psi)$

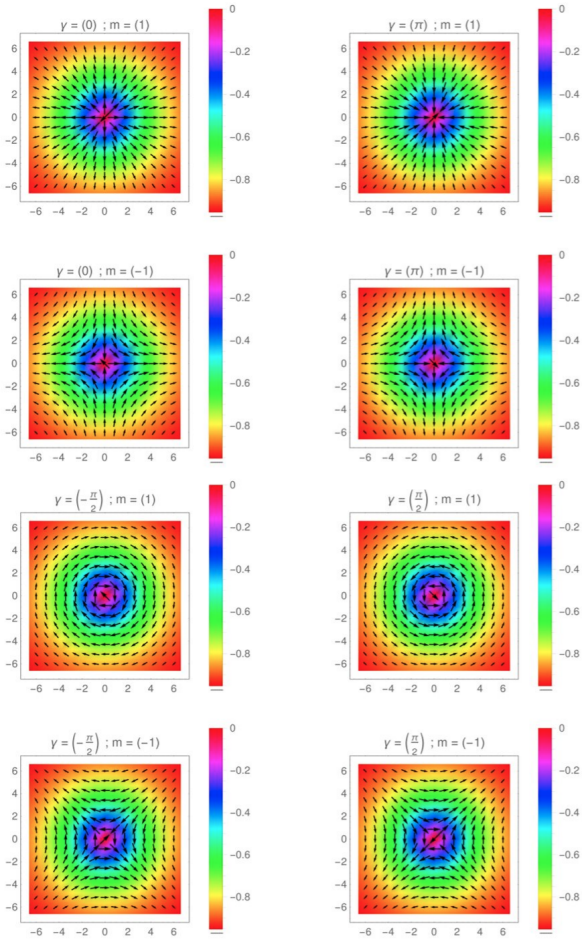

Fig. 3.7 Projection of the magnetization vector $\boldsymbol{m}$ on the basal plane of chiral skyrmions and antiskyrmions in non-centrosymmetric ferromagnets. The m and γ parameters correspond to the ones reported in Tab.3.2.

Point Group ($n > 2$)	$\phi(\psi)$
C_{nv}	$\phi = \psi$
D_n	$\phi = \psi + \frac{\pi}{2}$
D_{2d}	$\phi = -\psi + \frac{\pi}{2}$
C_n	$\phi = \psi + \arctan\left(\frac{D}{D'}\right)$
S_4	$\phi = -\psi + \arctan\left(\frac{D}{D'}\right)$
T, O	$\phi = \psi + \frac{\pi}{2}$

Table 3.2 $\phi(\psi) = m\psi + \gamma$ solutions for the 11 different non-centrosymmetric crystallographic point groups. D and D' refer to the DMI forms reported in Table.3.1

3.4.4 Characteristic scales in micromagnetism

As discussed in subsection.3.3, the ground state of the system is given by the magnetic configuration $\boldsymbol{m}(\boldsymbol{r})$ that minimizes the micromagnetic energy functional (while complying with the system specific boundary conditions). It is a general situation in physics that, given competing effects in determining the ground state of a system, characteristic quantities such as energy scales, length scales or even dimensionless numbers emerge which allow us to recognize some general trends even before minimizing the energy functional.

In the present context, these scales are built out of combinations of the micromagnetic parameters such as: A exchange stiffness, M_s saturation magnetization, applied fields $|\boldsymbol{H}|$ and anisotropy constants such as magnetocrystalline K_u and shape anisotropy K_d. Characteristic length scales are of special importance in micromagnetism as they determine the size below which certain features appear. As an example, let's assume a situation where the competing energy contributions come from A and K_u which have units, respectively, of J/m and J/m^3. The only way to combine these quantities yielding a length scale in $\Delta = \sqrt{A/K_u}$ which is called the anisotropy exchange length and is a direct measure domain wall width in systems where the magnetization changes (the rate of change being limited by the exchange interaction) between 2 domains whose direction is set by uniaxial anisotropy K_u.

In a situation where the competition is between exchange interaction A and magnetostatic energy manifest through shape anisotropy $K_d = \mu_0 M_s^2/2$, the emergent length scale has the form $\Delta_d = \sqrt{A/K_d}$ which is called dipolar exchange length which ranges from $\Delta_d \approx 1$ nm in hard magnetic materials (large K_d) to several hundred nm in the case of soft magnetic materials (small K_d). As an example for

dimensionless quantities, we report the so called quality factor $Q_f = K_u/K_d$ which encodes the competition between magnetocrystalline- and shape-anisotropy. In thin-film systems with out-of-plane magnetocrystalline anisotropy, the occurrence and types of domains are determined by the quality factor.

3.5 The Landau-Lifshitz Gilbert equation

We have so far explored which are the conditions that the magnetization $\boldsymbol{m}(\boldsymbol{r})$ has to satisfy as to reach a stable energy minimum, but have no knowledge as to how this minimum can be reached: we have discussed the statics of the system but not the dynamics. The precession of a magnetic moment $\boldsymbol{M}$ in the presence of an effective magnetic field $\boldsymbol{H}_{\text{eff}}$ is classically presented as a consequence of the gyromagnetic relation which links magnetism and mechanics via $\boldsymbol{M} = \gamma \boldsymbol{L}$, where $\boldsymbol{L}$ represents the angular momentum of the electron and γ is the gyromagnetic ratio. In the general case, where the electron is considered as a particle having both orbital and spin angular momentum, the value of the gyromagnetic ratio is given by $\gamma = g\frac{q}{2m_e}$, where g represents the Landée factor, q is the electron charge and m_e is the electron mass.

The simple application of Newton's second law $\dot{\boldsymbol{L}} = \boldsymbol{M} \times \boldsymbol{H}_{\text{eff}}$ immediately allows us to recover the precession equation $\dot{\boldsymbol{M}} = \gamma \boldsymbol{M} \times \boldsymbol{H}_{\text{eff}}$. This equation, while indeed elegant, does not account for dissipation effects and therefore is in conflict with the empirical evidence that the magnetization in magnetic material can be oriented in the direction of an applied magnetic field and does not precess indefinitely. To fix this shortcoming, Landau and Lifshitz proposed an equation for the dynamics of the magnetization that empirically takes in account the effects of dissipation:

$$\dot{\boldsymbol{M}} = \gamma \boldsymbol{M} \times \boldsymbol{H}_{\text{eff}} + \alpha \boldsymbol{M} \times (\boldsymbol{M} \times \boldsymbol{H}_{\text{eff}}), \tag{3.87}$$

where α is a phenomenological damping coefficient. At the core of the derivation for this equation of motion is the assumption that the magnetization remains of fixed absolute value during the dynamics, while around 20 years later, T.L Gilbert derived an equivalent equation via a more rigorous mathematical treatment that made use of the classical Lagrangian formalism with the addition of a dissipation function accounting for the damping effects. In the following we provide a systematic derivation of the Landau-Lifshitz-Gilbert equation that starts from the formulation

of a Lagrangian and a Rayleigh dissipation function. We follow the approach of Wegrowe and Ciornei [108] as it provides a modern take on this old problem and allows for an interesting discussion of the inertial terms that are becoming increasingly relevant for Terahertz (THz) dynamics.

We follow a mechanical analogy that identifies the magnetization vector as a rigid stick of length M_s and direction $\boldsymbol{m}$, i.e. $\boldsymbol{M} = M_s\boldsymbol{m}$. We parameterize the rotation around the vertical axis with the angular velocity $\dot{\phi}$ and the rotation around the symmetry axis with the angular velocity $\dot{\psi}$ (see Fig.3.8). The relation between angular momentum $\boldsymbol{L}$ and angular velocity $\boldsymbol{\Omega}$ is given by $\boldsymbol{L} = \overleftrightarrow{I}\,\boldsymbol{\Omega}$, where $\overleftrightarrow{I}$ is the inertial tensor. In the body-fixed frame $\{\hat{e}_1, \hat{e}_2, \hat{e}_3\}$, the inertial tensor can be diagonalized revealing the principal moments of inertia:

$$\overleftrightarrow{I} = \begin{pmatrix} I_1 & 0 & 0 \\ 0 & (I_2 = I_1) & 0 \\ 6 & 0 & I_3 \end{pmatrix}, \tag{3.88}$$

where we have used the magnetization vector is symmetric with respect to rotations around the $\hat{e}_3$-axis to set $(I_2 = I_1)$. In the body fixed frame, the angular velocity as a function of the Euler angles $\{\theta, \phi, \psi)$ is given by

$$\boldsymbol{\Omega} = \begin{pmatrix} \Omega_1 \\ \Omega_2 \\ \Omega_3 \end{pmatrix} = \begin{pmatrix} \dot{\phi}\sin\theta\sin\psi + \dot{\theta}\cos\psi \\ \dot{\phi}\sin\theta\cos\psi + \dot{\theta}\sin\psi \\ \dot{\phi}\cos\theta + \dot{\psi} \end{pmatrix}. \tag{3.89}$$

Since in this formalism the magnetization can be thought of as a rigid stick, one of the Euler angles is unnecessary (rotating along the proper axis of the magnetization vector has no effect on the energy of the system). Depending on the convention, we can neglect one of the angles: we choose $\psi = 0$, whence

$$\boldsymbol{\Omega} = \begin{pmatrix} \dot{\theta} \\ \dot{\phi}\sin\theta \\ \dot{\phi}\cos\theta \end{pmatrix}, \tag{3.90}$$

and the kinetic equation for a vector $\boldsymbol{M}$ of fixed length M_s reads

$$\frac{d\boldsymbol{M}}{dt} = \boldsymbol{\Omega} \times \boldsymbol{M}. \tag{3.91}$$

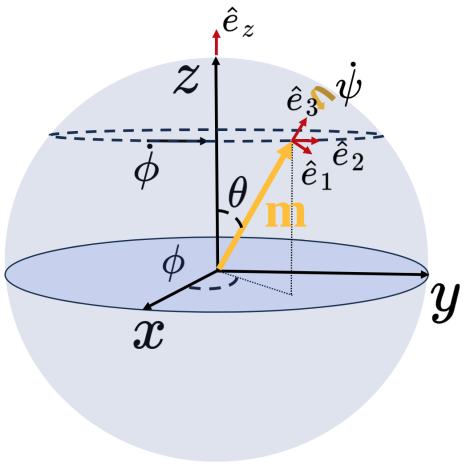

Fig. 3.8 Illustration of the mechanical analogy of a spinning top of fixed length M_s pointing in the direction $\boldsymbol{m}$ precessing around the z-axis. The coordinates of the vector in the space-fixed reference frame are parameterized by the angles (θ, ϕ, ψ) and the body fixed frame $\{\hat{e}_1, \hat{e}_2, \hat{e}_3\}$
rotates with angular velocity $\dot{\psi}$ and precesses around the z-axis with angular velocity $\dot{\phi}$.

By cross-multiplying (3.91) from the left and making use of the identity $\mathbf{A} \times (\mathbf{B} \times \mathbf{C}) = (\mathbf{A} \cdot \mathbf{C})\mathbf{B} - (\mathbf{A} \cdot \mathbf{B})\mathbf{C}$, while choosing the space-fixed reference frame such that the magnetization is parallel to the $\hat{e}_3$ axis, i.e $\boldsymbol{M} = M_s \hat{e}_3$, we can write eq.(3.91) as

$$\boldsymbol{\Omega} = \frac{\boldsymbol{M}}{M_s} \times \frac{d\boldsymbol{M}}{dt} + \Omega_3 \hat{e}_3. \tag{3.92}$$

The knowledge of the angular velocity allows us to write the kinetic part of the Lagrangian function $\mathscr{L}$ describing the dynamics of the spinning top

$$\mathscr{L} = \frac{1}{2}(\overleftrightarrow{I}\,\boldsymbol{\Omega})\boldsymbol{\Omega} - V(\theta, \phi), \tag{3.93}$$

where $V(\theta, \phi)$ represents the ferromagnetic potential that defines the effective field $\boldsymbol{H}_{\text{eff}}$ via $\boldsymbol{H}_{\text{eff}} = -\boldsymbol{\nabla} V(\theta, \phi)$ and creates the connection with the different micromagnetic energy terms discussed in 3.3. In order to account for the dissipation effects that ultimately lead to the relaxation of the magnetization in the direction of the effective fields, we must add a dissipation function

$$\mathscr{F} = \frac{\alpha}{2}\left(\frac{d\boldsymbol{M}}{dt}\right)^2 = \frac{\alpha}{2} M_s^2 (\Omega_1^2 + \Omega_2^2), \tag{3.94}$$

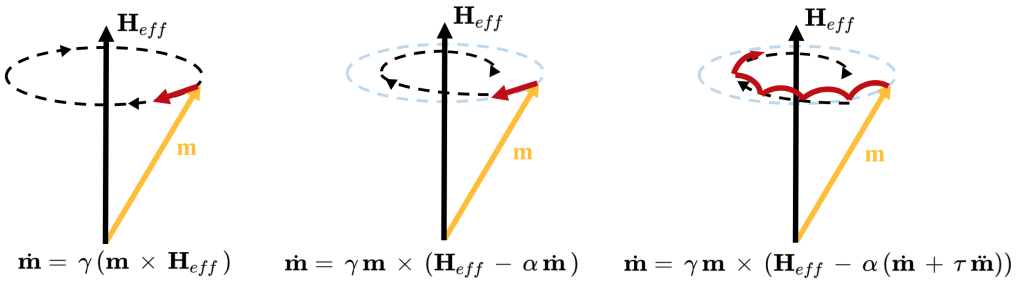

Fig. 3.9 Schematic representation of the precessional trajectory of the magnetization $\boldsymbol{m}$ around the effective field H_{eff} for the case (a) undamped precession (b) damped precession with Gilbert's assumption (eq.(3.102)) (c) damped precession with additional nutation motion as a consequence of inertial terms present in eq.(3.103)

where the coefficient α is strictly positive. The choice of a dissipation function $\propto \left(\frac{d\boldsymbol{M}}{dt}\right)^2$ is done in order to ensure the relaxation of the magnetization toward the effective field direction in finite time. We can now proceed and compute the Euler-Lagrange-Rayleigh equations as a function of the generalized coordinates $q_i \in \{\phi, \theta, \psi\}$

$$\frac{d}{dt}\left(\frac{\partial \mathscr{L}}{\partial \dot{q}_i}\right) - \frac{\partial \mathscr{L}}{\partial q_i} + \frac{\partial \mathscr{F}}{\partial \dot{q}_i} = 0 \tag{3.95}$$

Plugging in what we have leads to the differential equations in terms of Euler angles

$$\frac{d}{dt}(I_1\dot{\theta}) - I_1\dot{\phi}^2 \sin\theta\cos\theta + I_3\dot{\phi}\sin\theta(\dot{\phi}\cos\theta + \dot{\psi}) = -\partial_\theta \mathscr{F} - \partial_\theta V \tag{3.96}$$

$$\frac{d}{dt}(I_1\dot{\phi}\sin^2\theta + I_3(\dot{\phi}\cos\theta + \dot{\psi})\cos\theta) = -\partial_\psi \mathscr{F} - \partial_\psi V \tag{3.97}$$

$$\frac{d}{dt}(I_3(\dot{\phi}\cos\theta + \dot{\psi})) = 0 \tag{3.98}$$

We notice how for the moment these equations does not correspond to the LLG equation (3.87) because of the presence of many non-linear terms of the form $\dot{\phi}^2, \ddot{\phi}\cdots$. Gilbert realised that the issue can be circumvented [109] by making the

assumption $I_1 = I_2 = 0$ which in turn simplifies the equations to

$$\frac{M_s}{\gamma}\dot{\phi}\sin\theta + \partial_\theta \mathscr{F} + \partial_\theta V = 0 \tag{3.99}$$

$$\frac{d}{dt}\frac{M_s}{\gamma} + \partial_\phi \mathscr{F} + \partial_\phi V = 0 \tag{3.100}$$

$$\frac{d}{dt}\frac{M_s}{\gamma} = 0. \tag{3.101}$$

Noticing that in the rotating frame the effective field can be written as $H_{\text{eff},1} = -\frac{1}{\sin\theta}\partial_\phi V$, $H_{\text{eff},2} = \partial_\theta V$ can be cast in the familiar form

$$\dot{\boldsymbol{M}} = \gamma \boldsymbol{M} \times \left(\boldsymbol{H}_{\text{eff}} - \alpha \dot{\boldsymbol{M}}\right). \tag{3.102}$$

At this point, a brief discussion about Gilbert's assumption on the inertial tensor $I_1 = I_2 = 0$ should be made. If we stick to the mechanical analogy, this assumption poses some problems because no physical object can possess such an inertial tensor. If however, we keep the full set of equations with the inertial terms (3.96)-(3.98) and use the the fact $\dot{\boldsymbol{\Omega}} \cdot \hat{e}_3 = 0$, the LLG equation can be written in the form

$$\dot{\boldsymbol{M}} = \gamma \boldsymbol{M} \times \left(\boldsymbol{H}_{\text{eff}} - \alpha \left(\dot{\boldsymbol{M}} + \tau \ddot{\boldsymbol{M}}\right)\right) \tag{3.103}$$

where we have introduced the relaxation time $\tau = \frac{I_1}{\alpha M_s^2}$ which is the typical nutation period around the effective field $\boldsymbol{H}_{\text{eff}}$. It is easy to observe that in the limit $\tau \to 0$, eq.(3.103) converges to the ordinary LLG equation, i.e. the condition $I_1 = I_2 = 0$ is replaced by the condition $I_1 \ll \alpha M_s^2$, a more physically consequential assumption. In summary, the actual LLG equation has the form of (3.103), however, as long as the frequencies we are studying are smaller than τ^{-1} (which for typical material parameters is in the THz range), we are allowed to use eq.(3.102).

3.6 Magnetic domain walls

Making use of theoretical approaches based on energy minimization of the energy functional in eq.(3.40) is possible to derive different stable magnetic structures. Recalling what the discussion of 3.4.4, the competition of exchange ,magnetostatic and magnetos crystalline anisotropy causes the ground state of the magnetic material

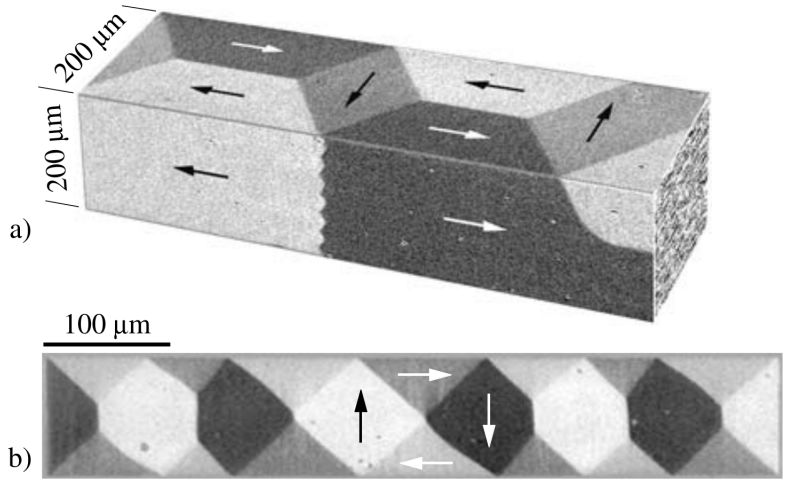

Fig. 3.10 Magnetic domains observed via Kerr microscopy. (a) Perspective view of the magnetic domains of an iron whisker. (b) Top view of the magnetic domains present in a NiFe thin film. Reproduced from [3].

to collapse towards a state displaying regions of different magnetization, called magnetic domains. The boundary regions between magnetic domains are called domain walls (DWs) and are of particular interest both from a scientific and from an applications point of view. In the following we study the structure of some simple DWs, showcasing the effects of the different micromagnetic energy contributions with special attention being devoted to the effect of DMI.

3.6.1 Collective coordinate models

In the context of magnetic DW motion, it is useful to reduce the complexity of the problem by introducing the so called collective coordinates q (representing the DW position), ϕ (internal DW magnetization angle) and Δ (DW width). In the following we show how to convert the solution of the LLG equation as a function of the magnetization field $\boldsymbol{m}(\boldsymbol{r})$ to a solution of the LLG equation as a function of $\{\phi(\boldsymbol{r}), q(\boldsymbol{r}), \Delta(\boldsymbol{r})\}$, allowing for an efficient way to relate the results of numerical simulations or experiments to analytical results. As a first step, we exploit the rotational invariance of the problem, by rewriting the LLG Eq.(3.102) in spherical coordinates. By rewriting $\boldsymbol{m} = (\sin\theta\cos\phi, \sin\theta\sin\phi, \cos\theta)^T$ (see Fig.3.8), eq.(3.102) becomes

$$\dot{\theta} + \alpha \sin\theta \dot{\phi} = -\frac{\gamma_0}{\mu_0 M_s \sin\theta} \frac{\delta \mathscr{E}}{\delta \phi}, \tag{3.104}$$

$$\alpha \dot{\theta} - \sin\theta \dot{\phi} = -\frac{\gamma_0}{\mu_0 M_s} \frac{\delta \mathscr{E}}{\delta \theta} \tag{3.105}$$

where $\mathscr{E}$ is the micromagnetic energy density of the system and is built from the contributions displayed in eq.(3.40). These contributions, which are functions of the magnetization $\boldsymbol{m}(\boldsymbol{r})$ and its gradients $\nabla \boldsymbol{m}(\boldsymbol{r})$ can be cast in spherical coordinates as follows

$$\mathscr{E}_{\text{exch}} = A(\nabla \mathbf{m})^2 = A\left[(\nabla\theta)^2 + \sin^2\theta (\nabla\phi)^2\right], \tag{3.106}$$

$$\mathscr{E}_{\text{anis}} = K_u \left[1 - (\mathbf{m}\cdot\hat{\mathbf{u}}_z)^2\right] = K_u \sin^2\theta, \tag{3.107}$$

$$\begin{aligned}
\mathscr{E}_{\text{dmg}} &= -\frac{1}{2}\mu_0 M_s^2 \mathbf{m}\cdot \overleftrightarrow{N}\, \mathbf{m} \\
&= -\frac{1}{2}\mu_0 M_s^2 \left(N_x m_x^2 + N_y m_y^2 + N_z m_z^2\right) \qquad (3.108) \\
&= -\frac{1}{2}\mu_0 M_s^2 \left[N_z + (N_x - N_z)\sin^2\theta + (N_y - N_x)\sin^2\theta \sin^2\phi\right], \qquad (3.109)
\end{aligned}$$

$$\mathscr{E}_{\text{DMI}} = D\left[\cos\phi \frac{\partial\theta}{\partial x} + \sin\phi \frac{\partial\theta}{\partial y} + \sin\theta\cos\theta \left(\sin\phi \frac{\partial\phi}{\partial x} - \cos\phi \frac{\partial\phi}{\partial y}\right)\right], \tag{3.110}$$

$$\mathscr{E}_{\text{Z}} = -\mu_0 M_s \left(H_x \sin\theta\cos\phi + H_y \sin\theta\sin\phi + H_z\cos\theta\right). \tag{3.111}$$

where we have assumed a uniaxial anisotropy contribution along the z-axis and have simplified the magnetostatic interaction to a local demagnetizing field $\boldsymbol{H}_{dmg} = \overleftrightarrow{N}\, \boldsymbol{m}(\boldsymbol{r})$. To simplify the notation, the magnetocrystalline anisotropy contribution $\mathscr{E}_{anis}$ and the demagnetization contribution $\mathscr{E}_{dmg}$ are usually combined

$$\mathscr{E}_{\text{anis}} + \mathscr{E}_{\text{dmg}} = \underbrace{\left[K_u + \frac{1}{2}\mu_0 M_s^2 (N_x - N_z)\right]}_{K_0} \sin^2\theta + \underbrace{\left[\frac{1}{2}\mu_0 M_s^2 (N_y - N_x)\right]}_{K} \sin^2\theta \sin^2\phi. \tag{3.112}$$

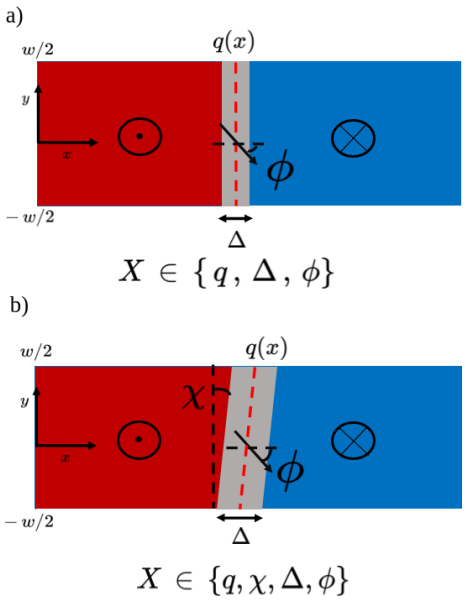

Fig. 3.11 (a) untilted DW configuration in semi-infinite nanowire geometry (infinite length along x and finite width w along y). The collective coordinates needed to treat the dynamics of such a system are reported on the bottom and are the DW position q, the internal DW magnetization angle ϕ and the DW width Δ. (b) tilted DW configuration in a semi-infinite nanowire geometry. An additional collective coordinate is needed to treat the dynamics of such a system, namely the canting angle χ,

3.6.2 The Bloch profile

At this point, we discuss some special cases for which the minimization procedure can be performed analytically which allow us to derive some important DW models. We make the following assumptions on the system

- We assume an infinitely long wire with 2 magnetic domains separated by a flat DW (see Fig.3.11-(a))
- We neglect any edge effects, i.e. we discard any term dependent on the derivatives in along the y-axis.
- We neglect DMI energy contributions.

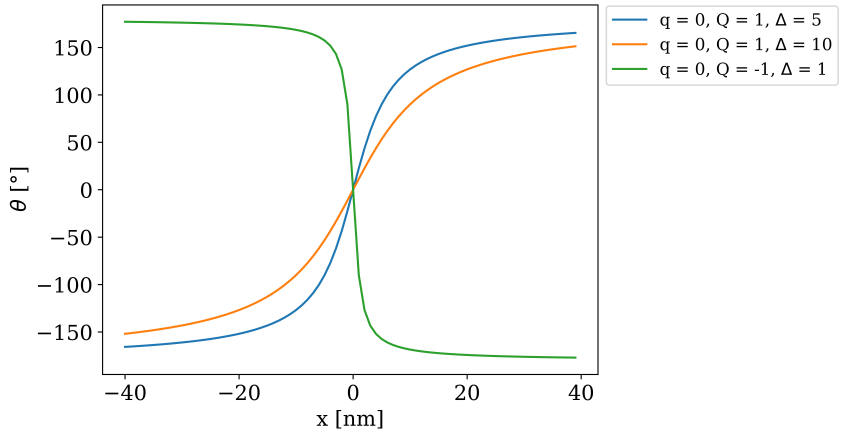

Fig. 3.12 Depiction of the Bloch profile $\theta(x)$ as reported in eq.(3.114) . We show the effect of different DW width (Δ) and an opposed Q value.

These assumptions allow us to combine the energy terms (3.106)-(3.111) as follows

$$\mathscr{E}_{1D} = A\left(\frac{\partial\theta}{\partial x}\right)^2 + \left(K_u + \frac{\mu_0 M_s^2}{2}\left(N_x\cos^2\phi + N_y\sin^2\phi - N_z\right)\right)\sin^2\theta + \frac{\mu_0 M_s^2}{2}N_z \tag{3.113}$$

The static solution of this differential equation is found by setting the energy density to a constant $\mathscr{E} = const.$. The solution $\theta(x)$ is then given by the so called "Bloch profile"

$$\tan\left(\frac{\theta}{2}\right) = \exp\left(Q\,\frac{x-q}{\Delta}\right), \tag{3.114}$$

where $Q = \pm 1$ is a parameter describing the DW configuration ($Q = 1 \Rightarrow$ down-up and $Q = -1 \Rightarrow$ up-down configurations) and

$$\Delta = \sqrt{\frac{A}{K_u + \frac{\mu_0 M_s^2}{2}\left(N_x\cos^2\phi + N_y\sin^2\phi - N_z\right)}} \tag{3.115}$$

corresponds to the DW width. We remark how this parameter can directly be related to the emergent length scale of this system discussed in 3.4.4, where the competing interactions determining the DW structure are indeed exchange and anisotropy. To derive the value of ϕ from eq.(3.113), we plug in the Bloch profile from eq.(3.114) in the energy density eq.(3.113) and integrate along the x-direction to obtain a DW

surface energy

$$\sigma_{DW} = \int_{-\infty}^{\infty} \mathscr{E}_{1D}\, dx = \frac{-2A}{\Delta} - 2\Delta\left(K_u + \frac{\mu M_s^2}{2}\left(N_x \cos^2\phi + N_y \sin^2\phi - N_z\right)\right) + \frac{\mu_0 M_s^2}{2} N_z L \tag{3.116}$$

where L corresponds to the sample width along the y-direction. We remark how, to perform the integration we employ the fact

$$\frac{\partial\theta(x)}{\partial x} = \frac{\sin\theta}{\Delta} \tag{3.117}$$

which can be used to easily compute integrals of the form

$$\int_{-\infty}^{\infty} \sin\theta\, dx = \int_{\theta(-\infty)=0}^{\theta(\infty)=\pi} \sin\theta \underbrace{\frac{dx}{d\theta}}_{\Delta/\sin\theta} d\theta = \pi\Delta \tag{3.118}$$

$$\int_{-\infty}^{\infty} \sin^2\theta\, dx = \int_0^{\pi} \Delta\sin\theta\, d\theta = 2\Delta. \tag{3.119}$$

At this point we can compute the static configurations of ϕ assuming an energy minimum via $\frac{\partial\sigma_{DW}}{\partial\phi} = 0$, while keeping in mind that the DW width Δ in eq.(3.116) also depends on the angle ϕ.

$$\frac{\partial\sigma_{DW}}{\partial\phi} = 0 \Rightarrow -\Delta\mu_0 M_s^2 (N_y - N_x)\sin 2\phi = 0 \Rightarrow \phi \in \left\{0, \frac{\pi}{2}, \pi, \frac{3\pi}{2}\right\}. \tag{3.120}$$

We can see how, even in the context of this very simplified model, we are able to extract some important information regarding magnetic DWs. Eq.(3.120) shows that there are 2 main classes of magnetic DWs that can be stabilized. If $\phi = 0\ ,\ \pi$ we have so called Néel DWs, which are characterized by a magnetization rotating along an axis parallel to the DW and thus have a magnetization in at DW-center pointing outside of the DW-plane (Fig.3.13-(a)). If on the other hand $\phi \in \{\pi/2\ ,\ 3\pi/2\}$ we have so called Bloch DWs, which are characterized by a magnetization rotating along an axis perpendicular to the DW and thus have a magnetization in at DW-center pointing inside of the DW-plane (Fig.3.13-(b)).

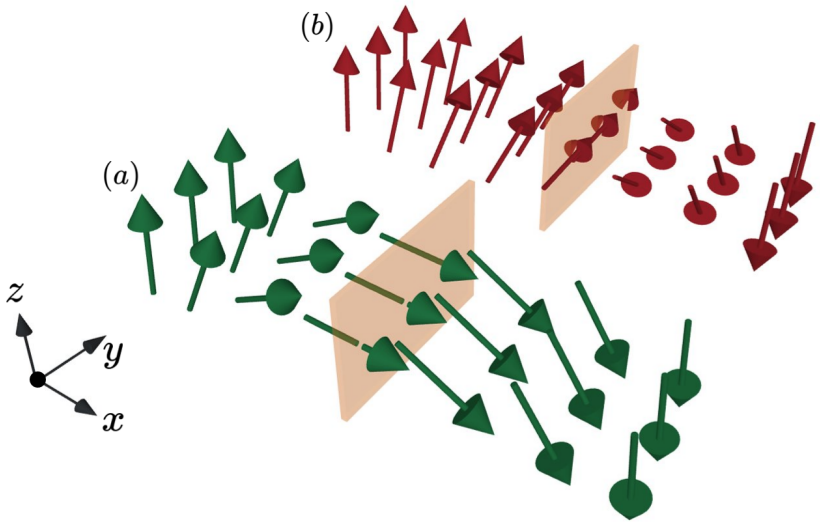

Fig. 3.13 (a) Néel DWs (b) Bloch DWs

3.6.3 Dynamical equations for the DW - the $q-\phi-\Delta$ model

Having established an effective Ansatz for the static magnetization profile in the 1D case (i.e. the Bloch profile of eq.(3.114)), we can now proceed and derive the dynamical equations for the CCM. To do so we employ the Lagrangian approach derived by Döring [93]. As mentioned in 3.5, the LLG equation in spherical coordinates can be from a Lagriangian density $\mathscr{L}$ of the form

$$\mathscr{L} = \mathscr{E}(\boldsymbol{m}) + \frac{\mu_0 M_s}{\gamma_0}\dot{\phi}\cos\theta \tag{3.121}$$

and an additional Rayleigh density function $\mathscr{F}$ to account for all dissipative processes

$$\mathscr{F} = \frac{\alpha\mu_0 M_s}{2\gamma_0}(\dot{\mathbf{m}})^2 = \frac{\alpha\mu_0 M_s}{2\gamma_0}\left(\dot{\theta}^2 + \sin^2\theta\dot{\phi}^2\right), \tag{3.122}$$

where $\mathscr{E}$ represents the energy density of the system built from the contributions of eqs.(3.106)-(3.111) and α is a phenomenological dimensionless parameter called damping parameter. The LLG equation can be obtained from the principle of least action suitably modified by the presence of dissipative phenomena [93], i.e. form

the Euler-Lagrange-Rayleigh equations

$$\frac{\delta \mathscr{L}}{\delta X} - \frac{d}{dt}\left(\frac{\partial \mathscr{L}}{\partial \dot{X}}\right) + \frac{\partial \mathscr{F}}{\partial \dot{X}} = 0, \tag{3.123}$$

where X represents a set of suitably chosen generalized coordinates. Since we are interested in narrowing down the problem to the dynamics of DWs, we can simplify the set of equations (3.123) by plugging in the Bloch Ansatz of eq.(3.114) in eqs. (3.121) and (3.122) and integrating out the x-variable as done in eq.(3.116). As an example we show how the this procedure looks for the energy density $\mathscr{E}$ of eq.(3.121). Summing all the energy contributions eq.(3.106)-(3.111) and integrating the x-variable as done in eq.(3.116) we can write a DW surface energy density σ_{DW}

$$\sigma_{DW} = \int_{-\infty}^{\infty} \left[\mathscr{E}_{exhc} + \mathscr{E}_{anis} + \mathscr{E}_{dmg} + \mathscr{E}_{DMI} + \mathscr{E}_{Z} \right] dx \tag{3.124}$$

$$\begin{aligned} &= \int_{-\infty}^{\infty} \Bigg[\frac{\sin^2\theta}{\Delta^2} + K_0 \sin^2\theta + K \sin^2\theta \sin^2\phi + QD\cos\phi \frac{\sin\theta}{\Delta} \\ &\quad - \mu_0 M_s (H_x \sin\theta\cos\phi + H_s \sin\theta \sin\phi + H_s \cos\theta) \Bigg] dx, \end{aligned} \tag{3.125}$$

we can perform the integration by using the 3 identities (3.117)-(3.119) and the fact that $Q^2 = 1$ to obtain the expression

$$\begin{aligned} \sigma_{DW} =& \frac{2A}{\Delta} + 2\Delta(K_0 + K\sin^2\phi) + \pi QD\cos\phi - \mu_0 M_s \pi\Delta(H_x\cos\phi + H_y\sin\phi) \\ &- 2Q\mu_0 M_s q H_z. \end{aligned} \tag{3.126}$$

This change of variables reduces the complexity of the problem significantly and now allows to derive the dynamics of the problem by writing the Euler-Lagrange-Rayleigh equations for each of the DW coordinates $X = \{q, \phi, \Delta\}$

$$\dot{\Delta} = \frac{12\gamma_0}{\mu_0 M_s \alpha \pi^2}\left[\frac{A}{\Delta} - \Delta(K_0 + K\sin^2\phi) + \mu_0 M_s \Delta \frac{\pi}{2}(H_x\cos\phi + H_y\sin\phi)\right], \quad (3.127)$$

$$\dot{q} = \frac{\Delta\gamma_0}{1+\alpha^2}\left[\alpha Q H_z + Q H_K \frac{\sin 2\phi}{2} - \frac{\pi}{2} H_{DMI}\sin\phi - Q\frac{\pi}{2}(H_y\cos\phi - H_z\sin\phi)\right], \quad (3.128)$$

$$\dot{\phi} = \frac{\gamma_0}{1+\alpha^2}\left[H_z - \alpha\left(H_K\frac{\sin 2\phi}{2} - Q\frac{\pi}{2}H_{DMI}\sin\phi - \frac{\pi}{2}(H_y\cos\phi - H_x\sin\phi)\right)\right], \quad (3.129)$$

where $H_K := \frac{2K_u}{\mu_0 M_s}$ and $H_{DMI} := \frac{D}{\mu_0 M_s \Delta}$. Eqs. (3.127)-(3.129) completely describe the dynamics of the DW coordinates q, ϕ, Δ as a function of an applied external field $\boldsymbol{H}_{ext}$.

3.6.4 Static configurations in the $q - \phi - \Delta$ model with chiral interactions

In the absence of applied external fields ($H_{x,y,z} = 0$), the static configurations of the DW can be studied by analyzing the partial derivatives of the DW surface energy density shown in eq.(6.94) which becomes

$$\sigma_{DW} = \frac{2A}{\Delta} + 2\Delta(K_0 + K\sin^2\phi) + \pi Q D\cos\phi. \quad (3.130)$$

and therefore yields the following partial static configurations for the collective coordinates:

$$\left.\frac{\partial\sigma_{DW}}{\partial\Delta}\right|_{\Delta=\Delta_0} = 0 \Rightarrow \Delta_0 = \sqrt{\frac{A}{K_0 + K\sin^2\phi}} \quad (3.131)$$

$$\left.\frac{\partial\sigma_{DW}}{\partial\phi}\right|_{\phi=\phi_0} = 0 \Rightarrow \phi_0 = \begin{cases} 0 & |\pi D| > |4\Delta K|\ ,\ QD < 0 \\ \pi & |\pi D| > |4\Delta K|\ ,\ QD > 0 \\ \cos^{-1}\left(\frac{\pi QD}{4\Delta K}\right) & |\pi D| < |4\Delta K| \end{cases} \quad (3.132)$$

The validity of the result depends on several factors such as the accuracy of the Bloch profile as an Ansatz to write the DW energy density. In the following we show a case in which another Ansatz has to be used because of the simultaneous presence of chiral interactions and IP applied fields. This combination causes the emergence of DW tilting [9] and therefore an additional coordinate describing the tilting angle χ has to be taken into account.

Dynamical equations for the DW - the $q-\phi-\chi-\Delta$ model

As known from experimental observation [110],theoretical predictions and numerical modeling [9], the presence of chiral interactions is known to produce an additional canting of the DW in the presence of IP applied magnetic fields (see Fig.3.11-(b) and Fig-3.14). The canting of the DW is of dynamical nature, and therefore in order to correctly describe the equations of motion of such a structure in the presence of chiral interactions, a slightly more sophisticated Ansatz for the DW profile has to be formulated in comparison to the Bloch profile of eq.(3.114). We extend the Bloch profile by an additional collective coordinate χ, namely the DW tilting angle

$$\tan\frac{\theta}{2}=\exp\left(Q\frac{(x-q)\cos\chi+y\sin\chi}{\Delta}\right). \tag{3.133}$$

To derive the dynamical equations for the collective coordinates which are now $\{q,\phi,\chi,\Delta\}$ we must again write the Lagrangian density $\mathscr{L}$ and the Rayleigh dissipation density function $\mathscr{F}$. Some algebra shows

$$\mathscr{L}=\overbrace{\frac{A}{\Delta}\sin^2\theta}^{\text{Exch.}}+\overbrace{\frac{D}{\Delta^2}\cos(\phi-\chi)\sin\theta}^{\text{DMI}}+\overbrace{K_U\sin^2\theta}^{\text{Anis.}} \tag{3.134}$$

$$+\overbrace{\frac{\mu_0}{2}M_s^2\left(N_x\sin^2\theta\cos^2(\phi-\chi)+N_y\sin^2\theta\sin^2(\phi-\chi)\right)}^{\text{dmg}} \tag{3.135}$$

$$\overbrace{-\mu_0 M_s\left[(H_x\cos\phi+H_y\sin\phi)\sin\theta+H_z\cos\theta\right]}^{\text{Zeeman}}+\overbrace{\frac{M_s}{\gamma}\phi\cos\theta}^{\text{Precessional}} \tag{3.136}$$

$$\mathscr{F}=\frac{\alpha M_s}{2\gamma}\left[\left(-\dot{q}\frac{\cos\chi}{\Delta}+\dot{\chi}\frac{y-\Delta\sin\chi\ln(\tan(\theta/2))}{\Delta\cos\chi}-\frac{\dot{\Delta}}{\Delta}\frac{(x-q)\cos\chi+y\sin\chi}{\Delta}\right)^2\sin^2\theta. \tag{3.137}$$

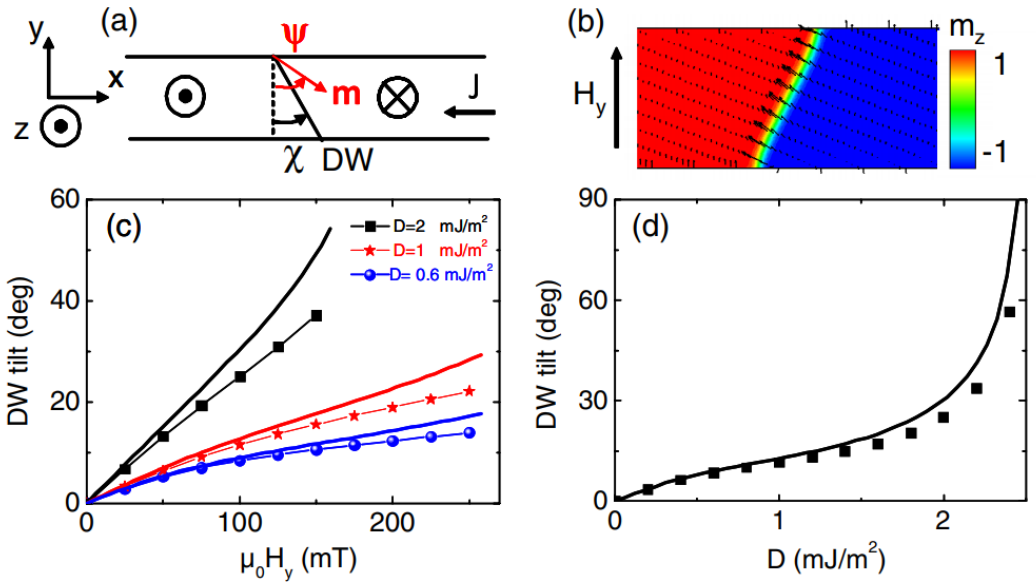

Fig. 3.14 (a) Schematic of the tilted DW. (b) Micromagnetic configuration of a 100 nm wide track with DM D = 2 mJ/m^2 and a transverse magnetic field $H_y = 100$ mT. (c) DW tilt angle χ as a function of H_y for several values of D and (d) as a function of D for $H_y = 100$ mT. Dots are the results of micromagnetic simulations, whereas the continuous lines are the results of the collective coordinates model. Reproduced from [9]

We can again, perform the integration along the length of the nanowire similarly to what was done in eq.(3.126) keeping in mind that the newly introduced Ansatz of eq.(3.133) modifies the identities (3.117)-(3.119) as follows

$$\frac{\partial\theta}{\partial x} = \frac{\sin\theta}{\Delta}\cos\chi \ , \ \frac{\partial\theta}{\partial y} = \frac{\sin\theta}{\Delta}\sin\chi \tag{3.138}$$

$$\frac{\partial\theta}{\partial t} = \Bigg(-\dot{q}\cos\chi + \frac{\dot{\chi}}{\cos\chi}\big(y - \Delta\sin\chi\ln\big(\tan\big(\theta/2\big)\big)\big) - \frac{\dot{\Delta}}{\Delta}\big((x-q)\cos\chi + y\sin\chi\big)\Bigg)\frac{\sin\theta}{\Delta} + \dot{\phi}^2\sin^2\theta \tag{3.139}$$

We can therefore obtain the Lagrangian DW density $\mathscr{L}_x = \int_{-\infty}^{\infty} \mathscr{L}\, dx$ and the Rayleigh DW dissipation density $\mathscr{F}_x = \int_{-\infty}^{\infty} \mathscr{F}\, dx$

$$\begin{aligned}\mathscr{L}_x =& \frac{2A}{\Delta^2}\cos\chi + \pi\frac{D}{\Delta^2}\cos(\phi-\chi) + 2\frac{M_s}{\gamma}\dot{\phi}\,(q - y\tan\chi) \\ &+ \frac{2\Delta}{\cos\chi}\left[K_U + \frac{\mu_0}{2}M_s^2\left(N_x\cos^2(\phi-\chi) + N_y\sin^2(\phi-\chi) - N_x\right)\right] \\ &- \pi\mu_0 M_s\left[H_x\cos\phi + H_y\sin\phi + 2H_z\,(q - y\tan\chi)\right] \end{aligned} \tag{3.140}$$

$$\begin{aligned}\mathscr{F}_x =& \frac{\alpha M_s}{\gamma}\left[\frac{\dot{q}^2}{\Delta}\cos\chi + \frac{\pi^2}{12}\frac{\dot{\Delta}^2}{\Delta\cos\chi} + \frac{\dot{\chi}^2\Delta}{\cos\chi}\left(\left(\frac{y}{\Delta\cos\chi}\right)^2 + \frac{\pi^2}{12}\tan^2\chi\right)\right. \\ &\left. + \dot{\phi}^2\frac{\dot{\Delta}}{\cos\chi} - 2y\frac{\dot{q}}{\Delta}\frac{\dot{\chi}}{\cos\chi} + \frac{\pi^2}{6}\dot{\Delta}\frac{\dot{\chi}}{\cos\chi}\tan\chi\right] \end{aligned} \tag{3.141}$$

at this point we have written the Lagrangian density and the Rayleigh dissipation density function in the most general case. Several equations of motion can be derived from the Euler-Lagrange-Rayleigh equation depending on the combination of collective coordinates physically relevant to the problem. One situation of particular relevance in experimental settings [9] considers the dynamics of the DW width parameter Δ much faster than the dynamics of ϕ, χ, q, implying that the DW reaches equilibrium width much faster than ϕ, χ, q. A rather simple yet powerful assumption applying in many cases of interest, is that the Δ parameter is assumed to follow the dynamics of the other collective coordinates adiabatically and therefore it can be treated as a parameter rather than a dynamic variable. This allows to derive the set of dynamical equations by performing the partial derivatives in eq.(3.123) with respect to the collective coordinates $\{q, \phi, \chi\}$ [9]

$$\dot{\phi} + \frac{\alpha\cos\chi}{\Delta}\dot{q} = \gamma_0 H_z, \tag{3.142}$$

$$-\frac{q\cos\chi}{\Delta} + \alpha\psi = \frac{\gamma_0 H_k}{2}\sin 2(\phi-\chi) + \frac{\pi D\gamma_0}{2\mu_0 M_s\Delta}\sin(\psi-\chi) \tag{3.143}$$

$$\begin{aligned}-\dot{\chi}\frac{\alpha\mu_0 M_s\Delta\pi^2}{6\gamma_0}&\left(\tan^2\chi + \left(\frac{w}{\pi\Delta}\right)^2\frac{1}{\cos^2\chi}\right) \\ &= \sigma_{DW}\tan\chi + \pi D\cos(\phi-\chi) + \mu_0 H_s M_s\Delta\sin 2(\phi-\chi)\end{aligned} \tag{3.144}$$

where w is the width of the sample (see Fig.3.11 and Fig.3.14) and σ_{DW} is the DW surface energy density

$$\sigma_{DW} = 4\sqrt{AK} + \pi D \sin(\psi - \chi) + \mu_0 H_k M_s \Delta \sin^2(\psi - \chi) + \pi \Delta M_s H_y \cos\psi \quad (3.145)$$

3.6.5 Field driven DW motion

By observing equation (3.142) we can immediately see that the application of a field perpendicular to the plane where the DW exists can induce a finite velocity of the structure , i.e. $\dot{q} \neq 0$. This can be understood intuitively by noticing how the Zeeman term stabilizes magnetic configurations aligned to it: since we are studying magnetic domains, the application of a field in the z-direction is going to shrink one of the domains and expand the other. In the CCM-picture, this can only mean that the boundary between the regions (i.e. the DW) is moving. DWs can be moved by several other means, i.e. spin-orbit torques [111, 112], spin-transfer torques [113, 114] and even strain gradients [115]. DW motion is at the heart of many concepts for novel memory storage architectures [116–118], therefore understanding how to manipulate this process is of high relevance also for the field of application. One of the fundamental limitations of field driven DW motion is the so called Walker-breakdown phenomenon, which sets an upper limit to its maximum attainable velocity.

In the following, we show how this threshold emerges from the equation of motion 3.142 and how the presence of chiral interactions can partially improve DW velocity in magnetic thin film systems. In the following, we only explore field driven DW motion and for the time being, limit ourselves to the discussion of the $q - \phi$ model. For simplicity, we impose $\dot{\Delta} = 0$ and $K/K_0 \ll 1$ allowing us to fix $\Delta = \Delta_0 = \sqrt{\frac{A}{K_0}}$. The assumption $K/K_0 \ll 1$ is justified in many thin film heterostructures where the magnetocrystalline anisotropy dominates the magnetostatic contribution. We also highlight how, if the geometry imposes a demagnetizing tensor with $N_x \approx N_y$, the assumption $K/K_0 \ll 1$ can be valid also in the absence of a pure magnetocrystalline predominance of anisotropy contributions. The description of DW dynamic can be further simplified by specifying the scope of our observations to the so called stationary regime, where the DW propagates through the material while keeping its internal magnetization angle ϕ fixed (i.e. $\dot{\phi} = 0$). The relevant equation to solve is

now

$$\Rightarrow H_z = \alpha\left(H_K\frac{\sin 2\phi}{2} - \frac{\pi}{2}H_{DMI}\sin\phi\right). \tag{3.146}$$

In the absence of chiral interactions ($H_{DMI} = 0$), the equation is solved by

$$\phi_0 = \arcsin\left(\frac{1}{2}\frac{2H_z}{\alpha H_K}\right). \tag{3.147}$$

which represents the dynamical equilibrium angle, determined by the competing interactions of the Zeeman- H_z and the anisotropy-field H_K. There is a caveat though: since the domain of the arcsin function is $[-1,1]$, the dynamical equilibrium angle ϕ_0 is only defined as long as the condition

$$|H_z| \leq \left|\frac{\alpha}{2}H_K\right| \tag{3.148}$$

is met. While eq.(3.148) holds true, the DW moves at a constant speed given by

$$\dot{q} = \frac{\Delta\gamma_0}{\alpha}H_z. \tag{3.149}$$

The limiting field of eq.(3.148) is called the Walker Breakdown field (H_W). After Walker breakdown is reached, the DW enters the so called "precessional motion regime" in which the anisotropy is not strong enough to counteract the torque of the external field H_z. The DW indeed still moves, but the magnetisation inside of it rotates according to the precessional dynamic described by the LLG equation (3.102), thereby drastically reducing its overall speed (See Fig.3.15).

Chiral interactions as Walker breakdown enhancers

DW Walker breakdown indeed sets a strong natural barrier for the maximum attainable operational speed of hypothetical DW based magnetic memory devices. Finding ways to enhance Walker breakdown is therefore an important challenge, still being tackled today [115, 119]. From the material engineering perspective, the choice of magnetic materials displaying chiral magnetic interactions can indeed improve the WB threshold significantly. As an example we study the simple case of eq.3.128, but now assume that $H_{DMI} \gg H_k$, which modifies the solution of the dynamical

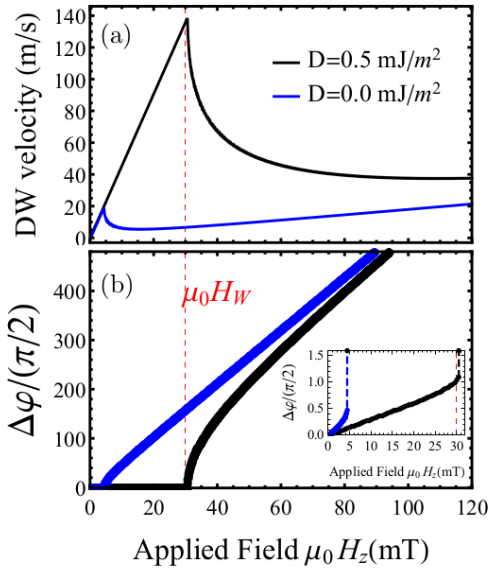

Fig. 3.15 (a) DW velocity as a function of the applied field in the presence (D = 0.5 mJ/m^2) and absence ((D = 0 mJ/m^2) of DMI. A clear shift in the Walker (red dashed line) field is visible for the case with present DMI. After Walker breakdown is achieved, the DW velocity drops down significantly (b) DW internal magnetisation angle $\Delta\phi$ as a function of applied field H_z in the presence (D = 0.5 mJ/m^2) and absence ((D = 0 mJ/m^2) of DMI. The dynamical equilibrium angle ϕ_0 is constant for higher values of the applied field in the case where DMI is present in the system. After H_w is reached, the DW motion starts precessing. Reproduced by [10].

equilibrium angle as follows:

$$\phi_0 = \arcsin\left(\frac{1}{2}\frac{2H_z}{\pi\alpha H_{DMI}}\right), \tag{3.150}$$

which in turn changes the Walker Breakdown to

$$|H_z| \leq \left|\frac{\alpha\pi}{2}H_{DMI}\right|. \tag{3.151}$$

Despite looking very similar to eq.(3.148), the significant advantage of this expression is the fact that, depending on the material choice, the DMI effective field H_{DMI} can be much larger than the magenetocrystalline anisotropy field H_K, implying that precessional motion ensues later. In Fig.3.15, we can clearly see how the inclusion of DMI (iDMI in this case) has the effect of increasing H_W (Fig.3.15-(a)), while at the same time keeping the dynamical equilibrium angle fixed (Fig.3.15-(b)).

As a side note, we remark how the presented explanation of the WB enhancement is performed by only considering iDMI, which is indeed one of the more common forms of DMI present is multilayered systems. Recent studies have however explored the effect of bDMI (which is represented by energy terms of the form presented in [119]) on the WB enhancement. The main difference in that case resides in the fact that the bDMI tends to induce an effective field that stabilizes Bloch DWs rather that Néel DWs. It can be shown that the dynamical equation previously used (eq.3.128) simply changes to [119]

$$H_z = \alpha\left(H_K\frac{\sin 2\phi}{2} - \frac{\pi}{2}H_{bDMI}\cos\phi\right), \tag{3.152}$$

where the preference for Bloch configurations from this new DMI term is encoded in the angular dependence in the cos rather than the sin. In the large DMI limit, keeping the assumption $K_0/K \ll 1$ we obtain a linear enhancement

$$|H_z| \leq \left|\frac{\alpha\pi H_{bDMI}}{2}\right|, \quad K_0/K \ll 1. \tag{3.153}$$

Chapter 4

The geometrization of micromagnetic exchange

As previously mentioned, the DMI is commonly introduced in micromagnetism through the continuum limit of the exchange energy term (see 3.1). It can be however shown, that the presence of chiral interactions is intricately linked to the geometric properties of micromagnetism as a continuum theory.

Similar to the manner in which gravity arises from the curvature of space-time in general relativity, the emergence of chiral interactions in ferromagnets can be attributed to the intricate interplay of non-trivial spin-parallel transport within the framework of the Heisenberg model [120].

In the following we develop a compact introduction to parallel transport and gauge covariant derivatives, highlighting how these concepts can be applied to micromagnetism yielding some interesting consequences and providing a seldom explored, yet modern point of view of the theory of magnetic interactions in the continuum. We deliberately avoid delving in the deep mathematical implications and instead opt for a more intuitive approach which is then expanded and developed in the results section 6.3.3.

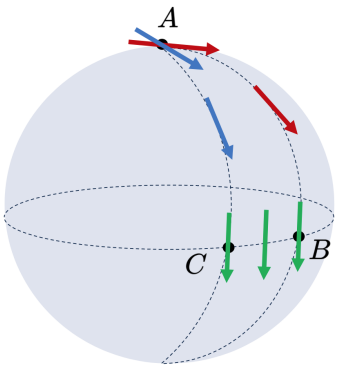

Fig. 4.1 parallel transport of a vector on a curved surface along the path $A \to B \to C \to A$

4.1 A simple example of non trivial parallel transport

The Heisenberg model necessary to describe micromagnetic exchange, at its core, revolves around the concept of the scalar product which simply provides a mathematical tool for comparing vectors located at different points in space: it is therefore implied that, in cases where parallel transport is not trivial, some extra care has to be taken when describing magnetic exchange interaction.

While the comparison of 2 vectors is straight forward in ordinary "flat" space (just carry 2 vectors on top of each other), things get more complicated as soon as we try and imagine slightly more interesting manifolds. The classical example here is the $\mathscr{S}^2$ sphere immersed in $\mathbb{R}^3$ (see fig.4.1). We can imagine ourselves sitting at the north pole of a sphere facing the horizon (point A), the notion of transporting a vector along this surface is not trivial anymore: if we move along the surface with the objective of pointing always in the direction of the horizon, after we reach the equator of the sphere (point B), the vector we are holding in our hand looks very different from the one we started with. Even more interesting is the case of a closed path on the surface that transports us back to the north pole (path A $\to$ B$\to$ C$\to$ A). We immediately see how the vector now has rotated by an angle. To try and translate the notion of parallel transport in mathematical terms, suppose we define a vector field on $\mathbb{R}^3$ (a simple manifold)

$$\boldsymbol{v}(\boldsymbol{r}) = v_i(\boldsymbol{r})\hat{e}^i, \boldsymbol{r} \in \mathbb{R}^3 \tag{4.1}$$

and would now like to compare the value of the field at 2 different but infinitesimally close locations of the manifold $\boldsymbol{r}$ and $\boldsymbol{r}+d\boldsymbol{r}$. According to the rules of differential calculus for vector fields, at point $\boldsymbol{r}+d\boldsymbol{r}$ we have

$$\boldsymbol{v}(\boldsymbol{r}+d\boldsymbol{r}) = \boldsymbol{v}(\boldsymbol{r}) + \left.\frac{\partial \boldsymbol{v}}{\partial x_i}\right|_{\boldsymbol{v}} dr^i + \mathscr{O}(d\boldsymbol{r}^2) \tag{4.2}$$

$$\Rightarrow \boldsymbol{v}(\boldsymbol{r}+d\boldsymbol{r}) - \boldsymbol{v}(\boldsymbol{r}) = \left.\frac{\partial \boldsymbol{v}}{\partial x_i}\right|_{\boldsymbol{r}} dr^i \tag{4.3}$$

Eq.(4.3) tells us that the notion of parallel transport is directly related to the concept of partial derivative. The condition $\left.\frac{\partial \boldsymbol{r}}{\partial x_i}\right|_{\boldsymbol{r}} = 0$ is implicitly establishing that for two vectors $\boldsymbol{v}(\boldsymbol{r}+d\boldsymbol{r}), \boldsymbol{v}(\boldsymbol{r})$ to be identical , the partial derivative along the path connecting them has to vanish.

If we now restrict the existence of the vector field the sphere $\mathscr{S}^2$, the situation is more complicated because the basis in which the vector field is expressed now also depends on the location

$$\boldsymbol{v}(\boldsymbol{r}) = v_i(\boldsymbol{r})\hat{e}^i(\boldsymbol{r}), \boldsymbol{r} \in \mathscr{S}^2, \tag{4.4}$$

therefore the Taylor expansion yields additional terms that have to be considered,

$$\Rightarrow \boldsymbol{v}(\boldsymbol{r}+d\boldsymbol{r}) - \boldsymbol{v}(\boldsymbol{r}) = \underbrace{\left[\left.\frac{\partial v_j}{\partial x_i}\right|_{\boldsymbol{r}} dr^i\right] \hat{e}^j(\boldsymbol{r}) + v_j \left[\left.\frac{\partial \hat{e}^j(\boldsymbol{r})}{\partial x_i}\right|_{\boldsymbol{r}} dr^i\right]}_{\text{par. trasp.}=0} \tag{4.5}$$

The condition for parallel transport is now different, as evident from the right hand side of eq.(4.5). In the following we discuss how redefining parallel transport in physical theories is not a mere consequence of the real space curvature (we do not need to rethink parallel transport only if we describe physics on a sphere or a cylinder) but has much more fundamental and far reaching consequences.

4.2 Global symmetries vs. local symmetries

The need to redefine the concept of parallel transport in a theory is not necessarily tied to the fact we are describing something happening on a curved surface in real

space. In the following we show how parallel transport is actually linked to a very fundamental aspect of the theory itself, namely symmetry.

In the realm of physics, systems are mathematically described using Lagrangians or Hamiltonians, which often involve an excess of degrees of freedom: for example, consider a physical problem where the choice of origin is entirely arbitrary or one in which the orientation of the axis is arbitrary. Any transformation that preserves the the system's Lagrangian is referred to as a "symmetry" and any collection of symmetries forms a mathematical structure known as a group.

Symmetry transformations can be classified into two categories: global symmetries and local symmetries. A global symmetry is such that it acts identically on the fields at all space-time points x. As an example, let $\phi(x)$ be a scalar field, then a global symmetry is such that

$$\phi(x) \rightarrow \phi'(x) = e^{i\theta}\phi(x) \; \forall \, x.$$

A local symmetry, on the other hand, is such that it acts differently on the fields at different spacetime points.

$$\phi(x) \rightarrow \phi'(x) = e^{i\theta(x)}\phi(x) \; \forall \, x.$$

Requiring a Lagrangian to satisfy local vs. global symmetries has some extremely deep consequences as we are going to demonstrate that it involves 2 different notions of parallel transport. As an example relating closely to micromagnetism, we discuss the illustrative case of a Lagrangian in which we promote the $SU(N)$ symmetry from global to local. Let $\mathbf{\Phi} = (\phi_1, \phi_2, \cdots, \phi_N)$ represent a collection of N different free complex scalar fields of the same mass m. The Lagrangian of such fields can be written as

$$\mathscr{L} = \partial_\mu \phi_j^* \partial^\mu \phi^j - m^2 \phi_j^* \phi^j. \tag{4.6}$$

Let us now introduce the U matrices, which we take from the group of unitary $N \times N$ matrices which form a group called $U(N)$. We notice how the Lagrangian density is invariant under a global symmetry transformation of the form

$$\phi^{j\prime}(x) = U_k^j \phi^k(x) \; , \; \phi^{*j\prime}(x) = (U^\dagger)_j^k \phi_k^*(x), \tag{4.7}$$

or in the more compact notation where we collect the field in a vector of the form $\mathbf{\Phi} = (\phi_1, \phi_2, \cdots, \phi_N)$,

$$\Phi'(x) = U\Phi(x),\ \Phi^{\dagger\prime}(x) = \Phi^\dagger(x)U^\dagger. \tag{4.8}$$

Now we come to the crucial step, namely promoting the global symmetry of the Lagrangian to a local symmetry. To do so, we simply have to rewrite the transformation eq.(4.8), assuming that now the matrices $U \to U(x)$ are allowed to depend on the point in space-time x.

$$\Phi'(x) = U(x)\Phi(x),\ \Phi^{\dagger\prime}(x) = \Phi^\dagger(x)U^\dagger(x) \tag{4.9}$$

$$U(x) \neq U(x')\ ,\ \forall\, x \neq x'. \tag{4.10}$$

While the mass term of the Lagrangian (4.6) is indeed still invariant under the newly introduced local transformations, the kinetic term depending on the partial derivatives of the fields is not invariant with respect to these new transformations. It is easy to check that the partial derivatives of the $U(x)$ matrices yield extra terms upon applying the transformation (4.9). The theory so as it stands, is therefore not invariant under local transformations. Now we come the crucial point: we observe that to restore the lost invariance, we need to redefine the partial differential operators as follows

$$\partial_\mu \to \mathscr{D}_\mu \tag{4.11}$$

$$\mathscr{L} = (\mathscr{D}_\mu\Phi^\dagger)(\mathscr{D}^\mu\Phi) - m^2\Phi^\dagger\Phi \tag{4.12}$$

where the new covariant derivatives $\mathscr{D}_i$ have to satisfy the following conditions

$$(\mathscr{D}_\mu\Phi(x))' = U(x)\mathscr{D}_\mu\Phi(x), \quad (\mathscr{D}_\mu\Phi^\dagger(x))' = \big(\mathscr{D}_\mu\Phi^\dagger(x)\big)U^\dagger(x). \tag{4.13}$$

To achieve such property of the $\mathscr{D}_\mu$, we have to introduce the matrix valued connection $\mathscr{A}_\mu(x)$ (often referred to as gauge field) which is required to transform as

$$\mathscr{A}'_\mu(x) = U(x)\mathscr{A}_\mu(x)U^{-1}(x) + i(\partial_\mu U(x))U^{-1}(x), \tag{4.14}$$

when the fields transform according to the local transformation (4.9). With the new, matrix valued connection we can finally specify the form of the covariant derivatives

$$\mathscr{D}_\mu \Phi(x) = \partial_\mu \Phi(x) + i\mathscr{A}_\mu(x)\Phi(x), \tag{4.15}$$

$$\mathscr{D}_\mu \Phi^\dagger(x) = \partial_\mu \Phi^\dagger(x) - i\Phi^\dagger(x)\mathscr{A}_\mu^\dagger(x) \tag{4.16}$$

Equipped with the newly defined covariant derivatives (4.15),(4.16) and the transformation law for the gauge field under local symmetry transformation (4.14), we can rewrite the Lagrangian in a locally invariant form

$$\begin{cases} \mathscr{L} = (\mathscr{D}_\mu \Phi^\dagger)(\mathscr{D}^\mu \Phi) - m^2 \Phi^\dagger \Phi \\ \mathscr{D}_\mu \Phi(x) = \partial_\mu \Phi(x) + i\mathscr{A}_\mu(x)\Phi(x), \\ \mathscr{D}_\mu \Phi^\dagger(x) = \partial_\mu \Phi^\dagger(x) - i\Phi^\dagger(x)\mathscr{A}_\mu^\dagger(x) \\ \mathscr{A}_\mu(x) \to \mathscr{A}'_\mu(x) = U(x)\mathscr{A}_\mu(x)U^{-1}(x) + i(\partial_\mu U(x))U^{-1}(x) \end{cases} \tag{4.17}$$

The requirement of the redefinition of the partial derivative and the introduction of the covariant derivative is indeed a consequence of our requirement to promote the symmetry of our theory from global to local. In 6.3.3 we explore the application of this formalism to our continuum theory of interest, namely micromagnetism. In our context the object of which we require invariance is indeed the micromagnetic energy functional, while the group transformation that we promote from local to global is the group of 3D rotations, namely elements of the $SO(3)$ group.

4.2.1 Local vs. global symmetries for magnetic interactions

What is the relevant symmetry in micromagnetism and why would we want to promote it from local to global? In other words, what creates the need to redefine parallel transport in the context of magnetic interactions?

Let us start dissecting the problem at its core, by recalling the essence and central role of the SOC in interacting many electron systems. As elucidated in 2.1.1 (anti-) ferromagnetic interactions in interacting many electron systems arise as a consequence of delicate interplay between Coulomb repulsion, Pauli exclusion and kinetic energy. DMI appears as a consequence of the introduction of SOC in the

Hamiltonians of interest, therefore it seems likely that the key missing ingredient hides behind the symmetry properties of interacting spin-orbit Hamiltonians.

Let us spend a couple of words to give a hint as to what the relation between SOC and symmetry of the electronic Hamiltonian is: the Pauli equation, which describes the behavior of spin-$1/2$ particles (such as electrons) in the presence of external electromagnetic fields exhibits a rich symmetry under local $U(1) \times SU(2)$ transformations [121]. The $U(1)$ symmetry transformations act on the spatial part of the electronic wave function, while the $SU(2)$ symmetry transformations act on the spin part of the wave function. While the local $U(1)$ symmetry is related to the relativistic properties associated to the interaction of the electron charge and the electromagnetic fields, the local $SU(2)$ symmetry is tied to the interaction of the spin degree of freedom with the same fields.

The important fact to highlight here however, is that the presence of SOC tacitly implies that parallel transport is no longer trivial because it is making our theory invariant with respect to local $SU(2)$ transformations as opposed to global $SU(2)$ symmetry.

In the context of effective spin-models such as the ones explored in 2.1.1 and 2.4.1, however, the energy of our systems is not extracted from electronic wave spinor wave functions, but rather from spin vectors $\boldsymbol{S} = (S^x, S^y, S^z)$ in a Cartesian reference frame and their relative orientation. It turns out that the local $SU(2)$ invariance of the Pauli equation becomes a local $SO(3)$ invariance of the Hamiltonian in the effective spin model.

4.3 Non trivial parallel transport and Heisenberg exchange

At this point a short recapitulation is in order: we state that in the absence of SOC, the equations describing the behavior of electrons are invariant with respect to global $SU(2)$ transformations. On the level of effective spin models, this means that parallel transport is trivial and we recover the ordinary Heisenberg model of eq.(3.68). If SOC is present, we need to employ a theory that on the level of the electronic spinor wave function is invariant under local $SU(2)$ transformations: on the level

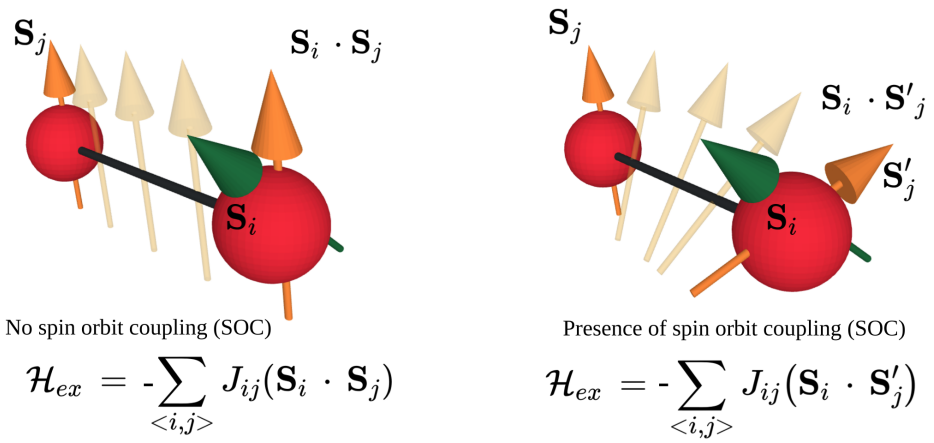

Fig. 4.2 Diagrammatic representation the concept of parallel transport in the Heisenberg model while in the presence and absence of SOC.

of effective spin model, this translates to a theory requiring local $SO(3)$ invariance where parallel transport is no longer trivial.

To add a layer of intuition to the thus far presented explanation of local vs. global symmetry in the theory of magnetic interactions, let us illustrate the consequences of non-trivial parallel transport in the Heisenberg model

$$\mathscr{H} = -J \sum_{<i,j>} \mathbf{S}_i \cdot \mathbf{S}_j = -J \sum_{<i,j>} \mathbf{S}(\boldsymbol{r}_i) \cdot \mathbf{S}(\boldsymbol{r}_j) \tag{4.18}$$

where the the classical spin vectors $\mathbf{S}(\boldsymbol{r}_i)$ fulfill normalization $|\mathbf{S}(\boldsymbol{r}_i)|^2 = 1 \ \forall \ i$. According to the thus far conducted line of reasoning, if we assume the presence of SOC (therefore local $SO(3)$ symmetry), the notion of dot product is ill defined as it tries to compare vectors located at different points of the lattice (Fig.4.2). To generalize the Heisenberg exchange with non trivial parallel transport, we can write

$$\mathscr{H} = \frac{-J}{2} \sum_{<i,j>} \mathbf{S}(\boldsymbol{r}_i) \cdot \mathbf{S}'(\boldsymbol{r}_j) \tag{4.19}$$

where $\mathbf{S}'(\boldsymbol{r}_j)$ represents the parallel transported version of $\boldsymbol{S}_j$ at the location of $\boldsymbol{S}_i$. Since we consider $\boldsymbol{S}$ as spin vectors, rotations that keep the length of the vectors unchanged are elements of the $SO(3)$ group, which can be represented as 3×3

orthogonal matrices with determinant $+1$. $\boldsymbol{S}'_j$ can therefore be rewritten as

$$\boldsymbol{S}'(\boldsymbol{r}_j) = \boldsymbol{G}(\boldsymbol{r}_i - \boldsymbol{r}_j)\boldsymbol{S}_j = G^{\alpha}_{\beta}(\boldsymbol{r}_i - \boldsymbol{r}_j)S^{\beta}(\boldsymbol{r}_j) \tag{4.20}$$

where $\boldsymbol{G}(\boldsymbol{r}_i - \boldsymbol{r}_j) \in SO(3)$ depends on the position of the spin vectors $\boldsymbol{r}_i, \boldsymbol{r}_j$. This subtlety allows us to uplift the ill-defined form of the dot product of the ordinary Heisenberg model and automatically yields the generalized Heisenberg Hamiltonian described in 2.4.1

$$\mathscr{H} = \sum_{<i,j>} S_{\alpha}(\boldsymbol{r}_i)G^{\alpha}_{\beta}(\boldsymbol{r}_i - \boldsymbol{r}_j)S^{\beta}(\boldsymbol{r}_j) \tag{4.21}$$

To finally make contact with the interaction terms derived by Moriya [67], we can resort to the Rodriguez formula to decompose an arbitrary $SO(3)$ matrix as follows [122]

$$G^{\alpha}_{\beta}(\hat{n}, \Psi) = \underbrace{\delta^{\alpha}_{\beta}\cos\Psi}_{\text{diagonal}} - \underbrace{\varepsilon^{\alpha\gamma}_{\beta}n_{\gamma}\sin(\Psi)}_{\text{antisymmetric}} + \underbrace{n_{\beta}n^{\alpha}(1-\cos\Psi)}_{\text{symmetric}} \tag{4.22}$$

Where $\hat{n}$ represents the axis of rotation and Ψ the angle. These 2 parameters of course also depend on the positions $\boldsymbol{r}_i, \boldsymbol{r}_j$, but impy their dependency in the following to lighten the notation. If we substitute (4.22) in (4.21), we immediately see how the different components of the matrix $G^{\alpha}_{\beta}(\boldsymbol{r}_i - \boldsymbol{r}_j)$ contribute to the interactions

$$\begin{aligned}\mathscr{H} = J \sum_{<i,j>} &\underbrace{\left[S_{\alpha}(\boldsymbol{r}_i)\delta^{\beta}_{\alpha}S_{\beta}(\boldsymbol{r}_j)\cos\Psi\right]}_{\text{Isotropic exchange}} - \underbrace{\left[n_{\gamma}\sin\Psi S_{\alpha}(\boldsymbol{r}_i)\varepsilon^{\alpha\gamma}_{\beta}S^{\beta}(\boldsymbol{r}_j))\right]}_{\text{DMI}} \\ &+ \underbrace{\left[n^{\alpha}n_{\beta}(1-\cos\Psi)S_{\alpha}(\boldsymbol{r}_i)S^{\beta}(\boldsymbol{r}_j)\right]}_{\text{Kitaev exchange}}\end{aligned} \tag{4.23}$$

$$= \sum_{<i,j>} J_{ij}\boldsymbol{S}(\boldsymbol{r}_i)\cdot\boldsymbol{S}(\boldsymbol{r}_j) + \boldsymbol{D}_{ij}\cdot\left[\boldsymbol{S}(\boldsymbol{r}_i)\times\boldsymbol{S}(\boldsymbol{r}_j)\right] + \boldsymbol{S}^{T}(\boldsymbol{r}_i)\overset{\leftrightarrow}{\Gamma}_{ij}\boldsymbol{S}(\boldsymbol{r}_j), \tag{4.24}$$

where we have defined $J_{ij} = J\cos\Psi$, $\boldsymbol{D}_{ij} = \hat{n}\sin\Psi$ and $\overset{\leftrightarrow}{\Gamma}_{ij} = \hat{n}\otimes\hat{n}(1-\cos\Psi)$. As a consistency check, we see how in the absence of SOC, parallel transport becomes trivial again and the rotation angle $\Psi = 0$ giving us the normal isotropic Heisenberg model. In conclusion we have shown how writing a locally invariant $SO(3)$ theory of Heisenberg exchange automatically yields the terms of Dzyaloshinskii-Moriya

interaction and Kitaev exchange (also known as 2 site anisotropy). In 6.3.3 we expand on this concept to micromagnetism, showing how the same procedure can be applied to the micromagnetic energy functional of eq.(3.40) yielding precisely the analogous of DMI and Kitaev exchange terms in the continuum. We also highlight how this approach applied to micromagnetism has the merit of allowing to treat chiral interactions in a particularly efficient matrix notation that allows to extract a lot of information about chiral interactions at a glance.

Chapter 5

Computational Methods

Having laid the theoretical foundations for magnetism both at the atomic and micrometer-scale, it is apparent that the analytical solution of realistic systems is impossible in all but the simplest cases. Magnetism is indeed a field where numerical simulations are heavily employed to produce theoretical predictions or motivate experimental findings. In this dissertation we have produced contributions both at the atomistic level and at the micromagnetic level, mandating us to introduce the foundational principles of some of the more common computational methods employed to solve problems at these 2 different length scales.

5.1 The basics of density functional theory

Paul Dirac's famous quote of 1920 states "the fundamental laws necessary for the mathematical treatment of a large part of physics and the whole of chemistry are completely known has held true to this day. However, the difficulty lies in the fact that the application of these laws often results in equations that are too complex to solve." This challenge is particularly evident in the field of solid-state physics, where the framework of the theory is straightforward to establish, but obtaining the actual solutions has proven to be an ongoing and exciting puzzle for over a century.

A major breakthrough in this field occurred when John Hohnberg and Walter Kohn laid the foundations of density functional theory (DFT) published 2 seminal papers [123, 124] that essentially constitute the bedrock of modern computational

material science. DFT is a powerful tool that allows researchers to predict the properties of materials from first principles, without the need for experimental data. It achieves this by approximating the behavior of the electrons in the system, which govern the material properties of interest.

In this chapter, we provide an introduction to the basics of DFT and focus on computing the magnetic properties of materials from first principles. Our approach begins with the many-body electronic Hamiltonian and the Born-Oppenheimer approximation to eliminate nuclear motion. We then shift our focus to solving the ground state problem of the many-body Schrödinger equation, which involves the Hohenberg-Kohn theorems and the Kohn-Sham equations.

Finally, we introduce spin-orbit coupling, which is a relativistic effect that couples the spin and orbital angular momentum of the electrons in the system and show how DFT can be used to calculate magnetic exchange parameters.

5.1.1 The many-body Schrödinger equation

Our starting point is a very general system composed of N electrons and M nuclei. For the time being, we only assume that these objects are very small and thus follow the rules of quantum mechanics. We also assume that they are very large $\mathscr{O} \sim 10^{23}$ in number since they are related to realistic materials. All the physical properties of this many body system can be inferred from the solutions of the time dependent Schrödinger equation

$$i\hbar\partial_t \Psi(\boldsymbol{r}_1 \cdots \boldsymbol{r}_N, \boldsymbol{R}_1 \cdots \boldsymbol{R}_M; t) = \mathscr{H}_{tot} \Psi(\boldsymbol{r}_1 \cdots \boldsymbol{R}_N, \boldsymbol{R}_1 \cdots \boldsymbol{r}_M; t), \tag{5.1}$$

where Ψ represents the wave function of the N electrons labelled by $\boldsymbol{r}_i$ $(i = 1 \cdots N)$ and M nuclei labelled by $\boldsymbol{R}_j$ $(j = 1 \cdots M)$. $\mathscr{H}_{tot}$ represents the electron-nuclei

Hamiltonian and in the absence of external fields has the form

$$\mathscr{H}_{tot} = \underbrace{-\sum_i^M \frac{\hbar^2}{2M_i}\nabla^2_{R_i}}_{\text{Kinetic energy: ions}} + \underbrace{\frac{1}{2}\sum_{i\neq j}\frac{Z_i Z_j e^2}{|\boldsymbol{R}_i - \boldsymbol{R}_j|}}_{\text{Coulomb repulsion: ions}} - \underbrace{\sum_i^N \frac{\hbar^2}{2m_i}\nabla^2_{r_i}}_{\text{Kinetic energy: electrons}}$$
$$+ \underbrace{\frac{1}{2}\sum_{i\neq j}\frac{e^2}{|\boldsymbol{r}_i - \boldsymbol{r}_j|}}_{\text{Coulomb repulsion: electrons}} - \underbrace{\sum_{i,j}^{N,M}\frac{Z_i e^2}{|\boldsymbol{R}_i - \boldsymbol{r}_j|}}_{\text{Coulomb attraction: electrons-ions}}, \tag{5.2}$$

where M_i represents the mass of the ions and m_i the masses of the electrons. Since the Hamiltonian (5.2) does not depend on time, we can factor out the time dependence in the wave function

$$\Psi(\boldsymbol{r}_1 \cdots \boldsymbol{r}_N, \boldsymbol{R}_1 \cdots \boldsymbol{R}_M; t) = \Psi(\boldsymbol{r}_1 \cdots \boldsymbol{r}_N, \boldsymbol{R}_1 \cdots \boldsymbol{R}_M) f(t). \tag{5.3}$$

Plugging in this Ansatz in the time dependent Schrödinger equation (5.1), yields the eigenvalue problem

$$\mathscr{H}_{tot}\Psi(\boldsymbol{r}_1 \cdots \boldsymbol{r}_N, \boldsymbol{R}_1 \cdots \boldsymbol{R}_M) = E\Psi(\boldsymbol{r}_1 \cdots \boldsymbol{r}_N, \boldsymbol{R}_1 \cdots \boldsymbol{R}_M) \tag{5.4}$$

$$f(t) = \exp\left(\frac{E}{i\hbar}t\right) \tag{5.5}$$

5.1.2 The Born Oppenheimer approximation

The Hamiltonian of eq.(5.2), while completely general, is far too intricate to solve the associated eigenvalue problem. We can start to simplify things by arguing that the electrons and the nuclei have radically different time scales in which they reach their respective ground states since the mass of an electron is roughly ~ 2000 smaller that that of a nucleus. This means that, in the reference frame of an electron, the motion of the nuclei appears essentially suppressed. Therefore the electrons reach their ground state much faster than the nuclei making the nuclei specific part of the Hamiltonian approximately constant and thus negligible. Discarding the pure ionic contribution to the Hamiltonian turns out to be correct in many situations and yields

the simpler form

$$\mathscr{H}_{BO} = \underbrace{-\frac{\hbar^2}{2m}\sum_{i}^{n}\nabla_{r_i}^2}_{:=T} + \underbrace{-\sum_{i,j}^{N,M}\frac{Z_i e^2}{|\boldsymbol{R}_i - \boldsymbol{r}_j|}}_{:=V} + \underbrace{\frac{1}{2}\sum_{i\neq j}^{N}\frac{e^2}{|\boldsymbol{r}_i - \boldsymbol{r}_j|}}_{:=U}. \tag{5.6}$$

This procedure is known as the Born-Oppenheimer approximation and allows to rewrite the Eigenvalue problem of eq.(5.5) as

$$\mathscr{H}_{BO}\Psi(\boldsymbol{r}_1 \cdots \boldsymbol{r}_N) = E\Psi(\boldsymbol{r}_1 \cdots \boldsymbol{r}_N). \tag{5.7}$$

Despite having greatly reduced the number of variables by transforming the wave function from

$$\Psi(\boldsymbol{r}_1 \cdots \boldsymbol{r}_N, \boldsymbol{R}_1 \cdots \boldsymbol{R}_M) : \mathbb{R}^{3N+3M} \to \mathbb{C} \tag{5.8}$$

$$\Psi(\boldsymbol{r}_1 \cdots \boldsymbol{r}_N) : \mathbb{R}^{3N} \to \mathbb{C}, \tag{5.9}$$

The eigenvalue problem is still far too large to solve numerically even with today's most advanced supercomputers. As a reference, one simple nichel atom ($N = 28$) located on 10 discrete grid points would require us to store $10^{3\times 28}$ complex numbers with float-precision (i.e. 16 bytes per number). This simple system requires 16×10^{75} Gb of storage capacity. To put this absurd number in perspective, the total amount of information contained on the internet today is estimated to be $\sim 5 \times 10^9$ Gb.

5.1.3 Density Functional Theory

DFT is a formalism used to study the behavior of interacting electronic systems. It has emerged as an incredibly powerful tool that allows researchers to accurately predict the properties of molecules and materials at the atomic level because it lends itself to a quite straight forward numerical implementation. The basic idea behind DFT is to reduce the interacting Hamiltonians of electronic systems to effective one-particle problems. This is achieved by building a theory of interacting electrons using the electronic density instead of many body wave functions as the central object of inquiry. DFT is in fact based on the idea that the ground state electron density $n_0(\boldsymbol{r})$ contains all the information needed to describe the behavior of the

system.

$$n_0(\boldsymbol{r}) = N \int d^3\boldsymbol{r} \cdots d^3\boldsymbol{r}_N \, |\Psi_0(\boldsymbol{r}_1 \cdots \boldsymbol{r}_N)|^2, \tag{5.10}$$

where Ψ_0 represents the fully anti-symmetrized electronic wave function. We immediately notice that the electron density n_0 contains much less information than the full wave function. Hohenberg and Kohn demonstrated that the ground state energy is a unique functional of the electronic ground state wave function $E_0 = E[n_0(\boldsymbol{r})]$. If the spectrum is non degenerate, there is only one wave function corresponding to the electron density $n_0(\boldsymbol{r}) \leftrightarrow \Psi_0$ meaning that, in principle, we can avoid working with the highly complicated wave function and only perform computations with the much simpler electron density.

5.1.4 The Hohenberg-Kohn Theorems

The Hohenberg-Kohn theorems, formulated in 1964, establish the fundamental basis of DFT. The theorems state that the ground-state electron density uniquely determines the external potential and energy of a many-electron system. This means that the complex interacting Hamiltonians of electronic systems can be reduced to effective one-particle problems by modeling the electronic density. We start by declaring the theorems

- The ground state density $n(\boldsymbol{r})$ of a many-electron system determines uniquely the external one-body potential $V(\boldsymbol{r})$ (up to a spatial constant), and vice versa.
- The density $n_0(\boldsymbol{r})$ minimizing the total energy is the exact ground-state density.

We now provide the (incredibly) short proof by contradiction: we start by taking a system of interacting electrons in an external potential

$$\mathscr{H} = T + U + V = \sum_i^N \frac{p_i}{2m} + \sum_{i \neq j} U(\boldsymbol{r}_i - \boldsymbol{r}_j) + \sum_i^N V_{ext}(\boldsymbol{r}_i) \tag{5.11}$$

We assume that the spectrum is non degenerate

$$\Rightarrow E_0 = \langle \Psi_0 | H | \Psi_0 \rangle = \langle \Psi_0 | T + U | \Psi_0 \rangle + \int d^3\boldsymbol{r} V_{ext}(\boldsymbol{r}) n_0(\boldsymbol{r}). \tag{5.12}$$

Suppose now we had a different ground state wave-function leading to the same electron density, i.e

$$n_0(\boldsymbol{r}) = N \int d^3\boldsymbol{r}_1 \cdots d^3\boldsymbol{r}_N |\Psi_0|^2 = N \int d^d r_1 \cdots d^3\boldsymbol{r}_N |\Psi_1|^2 \tag{5.13}$$

Since both Ψ_0 and Ψ_1 are ground states, but the spectrum is assumed to be non degenerate, they have to belong to different Hamiltonians. Since for fixed N the interaction and kinetic energy the between the Hamiltonians has to be identical, the only allowed parameter to change is the external potential V_{ext}

$$H = T + U + V\,; H' = T + U + V' \tag{5.14}$$

$$\Rightarrow E_0 = \langle \Psi_0 | H | \Psi_0 \rangle < \tag{5.15}$$

$$< \langle \Psi_1 | H | \Psi_1 \rangle = \langle \Psi_1 | H' + V - V' | \Psi_1 \rangle \tag{5.16}$$

$$= E_1 + \int d^3\boldsymbol{r}\ (V(\boldsymbol{r}) - V'(\boldsymbol{r}))n_0(\boldsymbol{r}) \tag{5.17}$$

or the other way around

$$\Rightarrow E_1 = \langle \Psi_1 | H' | \Psi_1 \rangle < \tag{5.18}$$

$$< \langle \Psi_0 | H' | \Psi_0 \rangle = \langle \Psi_1 | H + V' - V | \Psi_1 \rangle \tag{5.19}$$

$$= E_0 - \int d^d x (V(\boldsymbol{r}) - V'(\boldsymbol{r}))n_0(\boldsymbol{r}) \tag{5.20}$$

$$E_0 - E_1 < E_0 - E_1 \Rightarrow\Leftarrow \tag{5.21}$$

It follows that the assumption on the wave functions Ψ_1 , Ψ_0 having the same electron density $n_0(\boldsymbol{r})$ must be wrong. We can therefore safely assume that the ground state electron density is a unique minimum of the energy functional $E[n(\boldsymbol{r})]$ under the condition that $\int d^3\boldsymbol{r} n(\boldsymbol{r}) = N$. In summary, we have shown that the ground state density is uniquely related to the studied system and corresponds to the variational minimum of the energy.

5.1.5 The Kohn-Sham equations

From the Hohenberg-Kohn theorems, 2 important corollaries emerge

- There exists a one-to-one relation between the one body potential V and the ground state energy density $n_0(\boldsymbol{r})$

- Since the ground state wave function Ψ_0 is uniquely related to the ground state density n_0, so is the expectation value of each observable $\langle \hat{O} \rangle = \langle \Psi_0 | \hat{O} | \Psi_0 \rangle$.

We remark how, until now, no approximations have been done (safe for the elementary Born-Oppenheimer approximation). The drawback of this exact approach is that the relation between $n_0(\boldsymbol{r})$ and $V(\boldsymbol{r})$ is not known and constitutes possibly one of the most challenging and important problems of computational material science. The knowledge of this exact relation (which should in principle exist), would allow for the exact calculation of all electronic properties of all solids. In order to perform some calculation with the developed formalism we must introduce some approximations. The original formulation of DFT dates back to 1965 and rests its foundation upon considering an auxiliary system on N non interacting electrons, where all the complexity of the interactions has been packed in an arbitrarily complicated (and unknown) potential. Such an auxiliary system can be described by a one particle Hamiltonian

$$\mathscr{H}\Phi_q(\boldsymbol{r}) = \left(-\frac{\nabla}{2} + V_{KS}(\boldsymbol{r})\right)\Phi_q(\boldsymbol{r}) = \varepsilon_q \Phi_q(\boldsymbol{r}), \tag{5.22}$$

Where, $V_{KS}(\boldsymbol{r})$ represents the so called Kohn-Sham potential, i.e. a space dependent potential that has the same effect on the single electrons as the effect of correlations and exchange in the interacting system. The power of this auxiliary system is that, if we manage to build V_{KS} such that $n_q(\boldsymbol{r}) = n_0(\boldsymbol{r})$, we can effectively solve the interactive system using a non-interactive one. With this approach, the energy functional of this auxiliary system can be written as

$$E_{KS}[n(\boldsymbol{r})] = T_{KS}[n(\boldsymbol{r})] + E_{ext}[n(\boldsymbol{r})] + E_{Ha}[n(\boldsymbol{r})] + E_{XC}[n(\boldsymbol{r})] \tag{5.23}$$

where

- The Kohn-Sham (non-interacting) kinetic energy $T_{KS}[n(\boldsymbol{r})]$ has the form

$$T_{KS}[n(\boldsymbol{r})] = -\frac{1}{2}\int \sum_q f_q |\nabla \Phi_q|^2 \, d^3\boldsymbol{r} \tag{5.24}$$

  Where f_q represents the Fermionic electron occupation function.

- The energy of the external potential $E_{ext}[n(\boldsymbol{r})]$ has the form

$$E_{ext}[n(\boldsymbol{r})] = -\int \sum_{j}^{M} \frac{Z_j}{|\boldsymbol{r}-\boldsymbol{R}_j|}\, n(\boldsymbol{r})\, d^3\boldsymbol{r} \tag{5.25}$$

- The energy of the electron-electron Coulomb repulsion $E_{Ha}[n(\boldsymbol{r})]$ has the form

$$E_{Ha}[n(\boldsymbol{r})] = -\int \frac{n(\boldsymbol{r})n(\boldsymbol{r}')}{2|\boldsymbol{r}-\boldsymbol{r}'|}\, d^3\boldsymbol{r}' \tag{5.26}$$

- Finally the so called exchange correlation energy functional $E_{XC}[n(\boldsymbol{r})]$

$$E_{XC}[n(\boldsymbol{r})] = \int V_{XC}[n(\boldsymbol{r})]\, n(\boldsymbol{r})\, d^3\boldsymbol{r} \tag{5.27}$$

  This term accounts for all necessary many-body correlation effects and is the great unknown of DFT calculations. This term is crucial for magnetic properties in the solid state and many other material properties: much of the theoretical efforts of the last 60 years have been devoted in trying to find effective approximations of this term.

To find the minimum of the integro-differential eq.(5.23) we invoke the constrained variational principle (the integrated electron density must give us the total number of electrons N). The ground state density $n_{KS}(\boldsymbol{r})$ satisfies

$$\frac{\delta}{\delta\phi_{\mathrm{q}}(\boldsymbol{r})^{\dagger}}\left(E_{\mathrm{KS}}[n(\boldsymbol{r})] - \varepsilon_{\mathrm{q}}\left(\int n(\boldsymbol{r})d^3\boldsymbol{r} - N\right)\right) = 0, \tag{5.28}$$

where the normalization constraint is imposed by the presence of the Lagrange-multiplier ε_q. By performing the variational derivatives on the terms (5.24)-(5.27) we can write down the so called Kohn-Sham equations

$$\left(-\frac{1}{2}\nabla^2 + V_{\mathrm{ext}}(\boldsymbol{r}) + V_{\mathrm{Ha}}[n(\boldsymbol{r}),\boldsymbol{r}] + V_{\mathrm{XC}}[n(\boldsymbol{r}),\boldsymbol{r}]\right)\phi_{\mathrm{q}}(\boldsymbol{r}) = \varepsilon_{\mathrm{q}}\phi_{\mathrm{q}}(\boldsymbol{r}). \tag{5.29}$$

This equation however, cannot be solved with ordinary methods since the differential operator also depends on the eigenvector of the problem. This type of problems is part of a broader class of problems dubbed self-consistent eigenvalue problems and can be solved numerically with a so called "self-consistency loop". A conceptual

algorithm to solve the self consistent problem of eq.(5.29) would proceed as follows (see Fig.5.1):

1 We initialize the algorithm by providing a starting guess for the electron density $n(\boldsymbol{r})$

2 We build the effective potential V_{KS} with this initial guess and solve the eigenvalue equation (5.29). The output of this calculation is a new set of eigenfunctions $\{\Phi_q\}$ from which we can calculate an electronic density $n_1(\boldsymbol{r})$.

3 If the newly obtained density differs from the original one by a value smaller than some user defined threshold, we have reached convergence.

4 If the newly obtained density does not differ from the original one by a factor smaller than some user define threshold t, we build the effective potential V_{KS} with this new density and solve (5.29) again to obtain a new density $n_2(\boldsymbol{r})$. This procedure is repeated until the computed density differs from the previous iteration of the loop by a value smaller that the user defined tolerance.

At this point an important disclaimer is in order: the eigenfunctions $\{\Phi_q\}$ (called Kohn-Sham orbitals) and eigenvalues $\{\varepsilon_q\}$ derived from solving the Kohn-Sham equation eq.(5.29) pertain to an auxiliary physical system and do not necessarily relate to the real interacting system one wishes to simulate. Strictly speaking, only the density derived from the set of eigenfunctions $\{\Phi_q\}$ translates to the electron density of the real system. Luckily, for many applications (even in the case of magnetic systems), the Kohn-Sham orbitals serve as a good enough approximation for the calculation of the quantities of interest.

Relativistic DFT: the road to magnetism in computational material science

It is widely known that the magnetic properties of solid state systems originate from finite spin angular momentum in the valence band of materials. Unfortunately, the Hamiltonian of eq. (5.1) does not take in account the spin degree of freedom of electrons and therefore would fail to many of the magnetic properties discussed in the previous sections of this dissertation. Luckily for us, the hitherto developed formalism can easily be re-adapted to the use of the Dirac Hamiltonian, which is fully relativistic and therefore able to capture spin and spin-orbit related phenomena

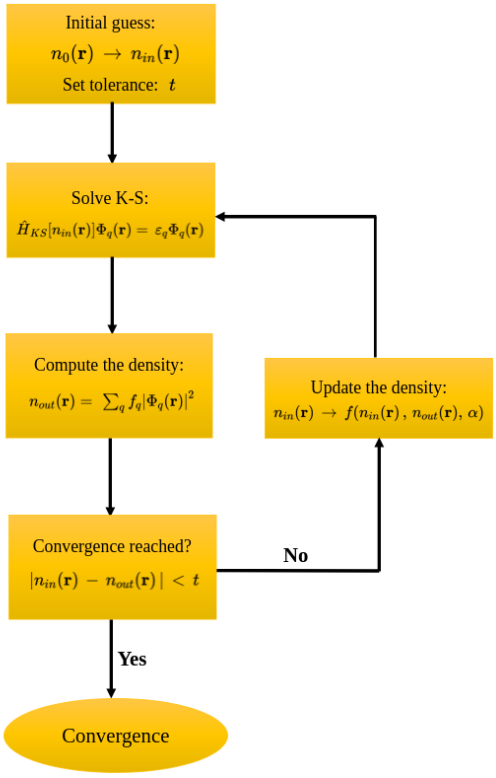

Fig. 5.1 Conceptual diagram showing the essential steps of the self-consistent calculation (scf), which is at the heart of all main DFT codes.

such as magnetism. The Dirac Hamiltonian in the above formulated KS-formalism reads [125, 126]:

$$\mathscr{H}_{\mathrm{DKS}}(\boldsymbol{r}) = \begin{pmatrix} \boldsymbol{\sigma}\cdot\boldsymbol{B}_{\mathrm{XC}}(\boldsymbol{r}) + mc^2\boldsymbol{I}_2 & c\boldsymbol{\sigma}\cdot\hat{\boldsymbol{p}} \\ c\boldsymbol{\sigma}\cdot\hat{\boldsymbol{p}} & -\boldsymbol{\sigma}\cdot\boldsymbol{B}_{\mathrm{XC}}(\boldsymbol{r}) - mc^2\boldsymbol{I}_2 \end{pmatrix} + (V_{\mathrm{ext}}(\boldsymbol{r}) + V_{\mathrm{Ha}}[n(\boldsymbol{r}),\boldsymbol{r}] + V_{\mathrm{XC}}[n(\boldsymbol{r}),\boldsymbol{r}])\,\boldsymbol{I}_4, \tag{5.30}$$

where $\boldsymbol{\sigma} = (\sigma_1,\sigma_2,\sigma_3)^T$ is the vector of Pauli matrices, $\boldsymbol{B}_{XC}(\boldsymbol{r})$ is he so-called exchange correlation field, $\hat{\boldsymbol{p}} = -i\hbar\boldsymbol{\nabla}$ is the quantum-mechanical momentum operator and $\boldsymbol{I}_4$ is the 4×4 identity matrix. The eigenvalue equation (5.29) (now dubbed Dirac-Kohn-Sham equation) has an analogous form

$$\mathscr{H}_{\mathrm{DKS}}(\boldsymbol{r})\Psi_q(\boldsymbol{r}) = \varepsilon_q\Psi_q(\boldsymbol{r}), \tag{5.31}$$

but we need to be wary of the fact that now the wave function $\Psi_q(\boldsymbol{r})$ is a 4-component object and that, as a consequence, the density also become a 4-component object

$$n(\boldsymbol{r}) \to \boldsymbol{n}(\boldsymbol{r}) = \begin{pmatrix} n(\boldsymbol{r}) \\ \boldsymbol{m}(\boldsymbol{r}) \end{pmatrix}, \tag{5.32}$$

where

$$n(\boldsymbol{r}) = \sum_q f_q\Psi_q(\boldsymbol{r})^\dagger\Psi_q(\boldsymbol{r}) \tag{5.33}$$

$$m_i(\boldsymbol{r}) = \sum_q f_q\Psi_q(\boldsymbol{r})^\dagger\sigma_i\Psi_q(\boldsymbol{r}). \tag{5.34}$$

Where f_q represents the Fermionic electron occupation function and σ_i represents the i^{th} Pauli matrix. These additional densities define the exchange correlation field $\boldsymbol{B}_{XC}(\boldsymbol{r})$ of eq.(5.30) in analogy to how the ordinary density $n(\boldsymbol{r})$ defines the exchange correlation potential V_{XC} in the non relativistic limit of eq.(5.29)

$$\boldsymbol{B}_{XC}(\boldsymbol{r}) = \frac{\delta E_{XC}[n(\boldsymbol{r}),\boldsymbol{m}(\boldsymbol{r})]}{\delta\boldsymbol{m}(\boldsymbol{r}))} \tag{5.35}$$

As discussed in 2.3.1 and 2.4.1, the appearance of magneto-crystalline anisotropy and Dzyaloshinskii-Moriya interactions in magnetic systems is due to spin-orbit coupling, an essential ingredient of the relativistic treatment outlined here. Full-

blown relativistic DFT calculations can however be extremely time consuming and perturbational approaches such as scalar relativistic approximations with explicit inclusion of spin-orbit coupling terms can help reduce the computational costs severely [127, 128]. In this thesis we employ the scalar relativistic approximation with spin orbit coupling as implemented by the FLEUR code [129, 130].

5.1.6 Ab initio methodology for magnetic exchange parameters

A detailed description of the implementation methods and solutions of the relativistic KS equations introduced above is far beyond our scope in this dissertation. Here we assume that the self consistent energy of solid state system with finite magnetic moment can be computed and show how the results of DFT calculations can be used to extract magnetic exchange parameters.

The starting point of our derivation is a general quadratic exchange spin Hamiltonian with single ion anisotropy

$$\mathscr{H} = \sum_{i \neq j} \boldsymbol{S}_i \cdot J_{ij} \cdot \boldsymbol{S}_j + \sum_i \boldsymbol{S}_i \cdot A_{ii} \cdot \boldsymbol{S}_i. \tag{5.36}$$

As extensively discussed in 2.1.1, the first term represents the magnetic exchange interaction between atomic sites sites i and j, while the second term represent the on-site anisotropy. As discussed in 2.1.1, we deal with classical 3×1 spin vectors of the form $\boldsymbol{S}_i = (S_x^i, S_y^i, S_z^i)$.

Exchange parameter J_{ij}

In order to determine the exchange interaction between neighboring sites 1 and 2, we have to compute all 9 elements of the matrix

$$J_{12} = \begin{pmatrix} J_{12}^{xx} & J_{12}^{xy} & J_{12}^{xz} \\ J_{12}^{yx} & J_{12}^{yy} & J_{12}^{yz} \\ J_{12}^{zx} & J_{12}^{zy} & J_{12}^{zz} \end{pmatrix}. \tag{5.37}$$

Having isolated our atoms of interest at atomic sites 1 and 2, we can rewrite the summation of (5.36)

$$\begin{aligned}\mathscr{H} = \sum_{i\neq j}\Big[& S_i^x \cdot J_{ij}^{xx} \cdot S_j^x + S_i^x \cdot J_{ij}^{xy} \cdot S_j^y + S_i^x \cdot J_{ij}^{xz} \cdot S_j^z \\ & + S_i^y \cdot J_{ij}^{yx} \cdot S_j^x + S_i^y \cdot J_{ij}^{yy} \cdot S_j^y + S_i^y \cdot J_{ij}^{yz} \cdot S_j^z \\ & + S_i^z \cdot J_{ij}^{zx} \cdot S_j^x + S_i^z \cdot J_{ij}^{zy} \cdot S_j^y + S_i^z \cdot J_{ij}^{zz} \cdot S_j^z \Big]. \end{aligned} \tag{5.38}$$

as

$$\begin{aligned}\mathscr{H} = & \boldsymbol{S}_1 \cdot J_{12} \cdot \boldsymbol{S}_2 + \sum_{j\neq 2} \boldsymbol{S}_1 \cdot J_{1j} \cdot \boldsymbol{S_j} + \sum_{i\neq 1} \boldsymbol{S_i} \cdot J_{i2} \cdot \boldsymbol{S}_2 \\ & + \sum_{i\neq 1, j\neq 2} \boldsymbol{S_i} \cdot J_{ij} \cdot \boldsymbol{S_j} + \boldsymbol{S}_1 \cdot A_{11} \cdot \boldsymbol{S}_1 + \boldsymbol{S}_2 \cdot A_{22} \cdot \boldsymbol{S}_2 \\ & + \sum_{i\neq 1,2} \boldsymbol{S_i} \cdot A_{ii} \cdot \boldsymbol{S_i}. \end{aligned} \tag{5.39}$$

The sum is written in such a way as to emphasize the interaction of the selected spins ($\boldsymbol{S}_1$ and $\boldsymbol{S}_2$) and the interaction of the selected spins with the "bath" of spins surrounding them. The strategy to isolate a particular exchange matrix element here is to select a set of states for $\boldsymbol{S}_1$ and $\boldsymbol{S}_2$ and compute 4 self consistent energies, combining them in order to eliminate the interaction of the selected spins and the spin bath surrounding them. Following ref.[131] , we show how to explicitly compute the matrix element J_{12}^{xz} and then provide a general recipe in order to extend the procedure to arbitrary matrix elements $J_{12}^{\alpha\beta}$. If one chooses 4 relative spin orientations of $\boldsymbol{S}_1$ and $\boldsymbol{S}_2$ as follows:

$$\text{State 1} : \boldsymbol{S}_1 = (+S,0,0), \quad \boldsymbol{S}_2 = (0,0,+S), \tag{5.40}$$

$$\text{State 2} : \boldsymbol{S}_1 = (+S,0,0), \quad \boldsymbol{S}_2 = (0,0,-S), \tag{5.41}$$

$$\text{State 3} : \boldsymbol{S}_1 = (-S,0,0), \quad \boldsymbol{S}_2 = (0,0,+S), \tag{5.42}$$

$$\text{State 4} : \boldsymbol{S}_1 = (-S,0,0), \quad \boldsymbol{S}_2 = (0,0,-S), \tag{5.43}$$

and chooses all other spins $\boldsymbol{S}_{i\neq 1,2} = (0,\pm S,0)$ composing the spin bath to lie perpendicularly to $\boldsymbol{S}_1$ and $\boldsymbol{S}_2$ (see Fig.5.2), the 4 self consistent energies obtained from DFT calculations can be mapped on the Hamiltonian (5.39) as follows

$$
\begin{aligned}
E_1 &= S\cdot J_{12}^{xz}\cdot S+\sum_{j\neq 2} S\cdot J_{1j}^{xy}\cdot S+\sum_{i\neq 1} S\cdot J_{i2}^{yz}\cdot S \\
&+\sum_{i\neq 1,j\neq 2} S\cdot J_{ij}^{yy}\cdot S+S\cdot A_{11}^{xx}\cdot S+S\cdot A_{22}^{zz}\cdot S \\
&+\sum_{i\neq 1,2} S\cdot A_{ii}^{yy}\cdot S, \qquad (5.44)\\
E_2 &= -S\cdot J_{12}^{xz}\cdot S+\sum_{j\neq 2} S\cdot J_{1j}^{xy}\cdot S-\sum_{i\neq 1} S\cdot J_{i2}^{yz}\cdot S \\
&+\sum_{i\neq 1,j\neq 2} S\cdot J_{ij}^{yy}\cdot S+S\cdot A_{11}^{xx}\cdot S+S\cdot A_{22}^{zz}\cdot S \\
&+\sum_{i\neq 1,2} S\cdot A_{ii}^{yy}\cdot S, \qquad (5.45)
\end{aligned}
$$

$$
\begin{aligned}
E_3 &= -S\cdot J_{12}^{xz}\cdot S-\sum_{j\neq 2} S\cdot J_{1j}^{xy}\cdot S+\sum_{i\neq 1} S\cdot J_{i2}^{yz}\cdot S \\
&+\sum_{i\neq 1,j\neq 2} S\cdot J_{ij}^{yy}\cdot S+S\cdot A_{11}^{xx}\cdot S+S\cdot A_{22}^{zz}\cdot S \qquad (5.46)\\
&+\sum_{i\neq 1,2} S\cdot A_{ii}^{yy}\cdot S,\\
E_4 &= S\cdot J_{12}^{xz}\cdot S-\sum_{j\neq 2} S\cdot J_{1j}^{xy}\cdot S-\sum_{i\neq 1} S\cdot J_{i2}^{yz}\cdot S \\
&+\sum_{i\neq 1,j\neq 2} S\cdot J_{ij}^{yy}\cdot S+S\cdot A_{11}^{xx}\cdot S+S\cdot A_{22}^{zz}\cdot S \\
&+\sum_{i\neq 1,2} S\cdot A_{ii}^{yy}\cdot S. \qquad (5.47)
\end{aligned}
$$

The strategy now is to combine the energies $E_1 \cdots E_4$ in such a way that we cancel out the interaction of the isolated spins and the spin bath surrounding them. This can be achieved by combining them as follows

$$
\begin{aligned}
E_1+E_4-E_2-E_3 &= 4S^2 J_{12}^{xz} \qquad (5.48)\\
\Rightarrow J_{12}^{xz} &= \frac{E_1+E_4-E_2-E_3}{4S^2}. \qquad (5.49)
\end{aligned}
$$

This approach can be extended to all other exchange matrix elements, following this recipe:

1 Assume one is interested in computing the exchange matrix element $J_{12}^{\alpha\beta}$

2 After having selected the reference spins $\boldsymbol{S}_1$ and $\boldsymbol{S}_2$, the 4 states to extract the desired exchange matrix element have to be chosen according to the following scheme

$$\text{State 1} : \boldsymbol{S_1} = +S\hat{e}_\alpha, \quad \boldsymbol{S}_2 = +S\hat{e}_\beta, \tag{5.50}$$
$$\text{State 2} : \boldsymbol{S}_1 = +S\hat{e}_\alpha, \quad \boldsymbol{S}_2 = -S\hat{e}_\beta, \tag{5.51}$$
$$\text{State 3} : \boldsymbol{S}_1 = -S\hat{e}_\alpha, \quad \boldsymbol{S}_2 = +S\hat{e}_\beta, \tag{5.52}$$
$$\text{State 4} : \boldsymbol{S_1} = -S\hat{e}_\alpha, \quad \boldsymbol{S}_2 = -S\hat{e}_\beta, \tag{5.53}$$

all other spins in the spin bath have to be chosen perpendicular to the 2 selected spins $S_{k\neq 1,2} \cdot S_{i=1,2} = 0 \; \forall \; k$.

3 Once the energies $E_1 \cdots E_4$ associated with the 4 states mentioned in the previous step have been computed, we can extract the matrix element via

$$J_{12}^{\alpha\beta} = \frac{E_1 + E_4 - E_2 - E_3}{4S^2}.$$

Once the desired exchange parameters have been computed, they can be combined to evaluate the different components of the exchange. For example, we can combine them to obtain the DMI vector components by expressing the antisymmetric part of the exchange matrix

$$D_{12}^x = \frac{1}{2}(J_{12}^{yz} - J_{12}^{zy}) \tag{5.54}$$
$$D_{12}^y = \frac{1}{2}(J_{12}^{xy} - J_{12}^{yx}) \tag{5.55}$$
$$D_{12}^z = \frac{1}{2}(J_{12}^{xy} - J_{12}^{yx}) \tag{5.56}$$

Of course, the symmetry of the crystal imposes some constraints on the symmetry properties of the exchange matrix, e.g. in the case of a centrosymmetric crystal we cannot have an antisymmetric component of the exchange matrix because the

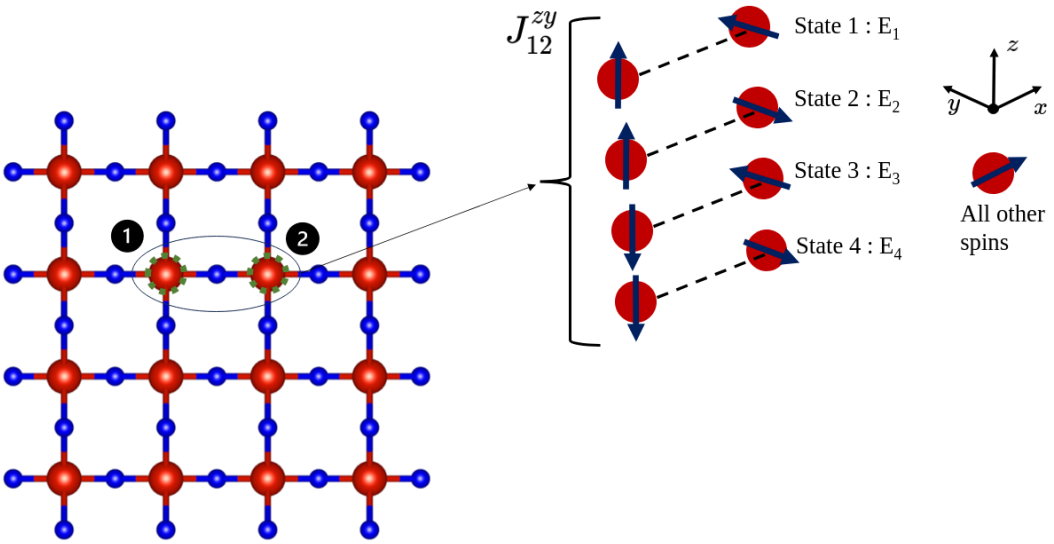

Fig. 5.2 Exemplary case of the 4 state method for the calculation of the J_{12}^{zy} coefficient of the exchange matrix of eq.(6.19)

Moriya rules [67] do not allow for the presence of DMI in such systems. A schematic representation of the 4 states necessary to compute J_{12}^{zy} is provided in Fig.5.2.

Single-ion anisotropy

The strategy to compute the matrix elements of single-ion anisotropy (we choose site $i = 1$ without loss of generality)

$$A_1 = \begin{pmatrix} A_1^{xx} & A_1^{xy} & A_1^{xz} \\ A_1^{yx} & A_1^{yy} & A_1^{yz} \\ A_1^{zx} & A_1^{zy} & A_1^{zz} \end{pmatrix} \tag{5.57}$$

are fairly similar to the ones detailed for the exchange matrix elements, with the significant difference that the matrix does not possess antisymmetric parts and that the procedure to compute diagonal and off-diagonal elements is slightly different. Since the procedure is very similar to the one detailed above, we state the recipe necessary to compute the required matrix element of (5.57) and refer or [131] for the detailed computations. If we are interested in computing the off-diagonal elements

$A_1^{\alpha\beta}$, $\alpha \neq \beta$ one should choose the 4 states of $\boldsymbol{S}_1$ according to

$$\text{State 1} : \boldsymbol{S_1} = \frac{\sqrt{2}S}{2}(\hat{e}_\alpha + \hat{e}_\beta), \tag{5.58}$$

$$\text{State 2} : \boldsymbol{S}_1 = \frac{\sqrt{2}S}{2}(\hat{e}_\alpha - \hat{e}_\beta), \tag{5.59}$$

$$\text{State 3} : \boldsymbol{S}_1 = \frac{\sqrt{2}S}{2}(-\hat{e}_\alpha + \hat{e}_\beta), \tag{5.60}$$

$$\text{State 4} : \boldsymbol{S}_1 - \frac{\sqrt{2}S}{2}(\hat{e}_\alpha + \hat{e}_\beta). \tag{5.61}$$

All the other spins composing the spin bath have to be chosen to lie outside of the plane spanned by $\hat{e}_\alpha$ and $\hat{e}_\beta$, i.e. parallel to $\hat{e}_\alpha \times \hat{e}_\beta$. Once the energy of the 4 states has been computed self-consistently, the anisotropy coefficient can be computed via

$$A_1^{\alpha\beta} = \frac{E_1 + E_4 - E_2 - E_3}{4S^2}. \tag{5.62}$$

In the case of the diagonal elements of (5.57), the fixed length of the spin vector $|\boldsymbol{S}_i|^2 = \sum_\alpha (S_i^\alpha)^2$ allows to rewrite the diagonal part of the single-ion anisotropy component of (5.36) as

$$\mathscr{H}_{\text{SIA}}^{\text{dia}} = S_1^x A_1^{xx} S_1^x + S_1^y A_1^{yy} S_1^y + S_1^z A_1^{zz} S_1^z \tag{5.63}$$

$$= A_1^{xx} S_1^2 + \left(A_{11}^{yy} - A_1^{xx}\right)\left(S_1^y\right)^2 \tag{5.64}$$

$$+ \left(A_1^{zz} - A_1^{xx}\right)\left(S_1^z\right)^2. \tag{5.65}$$

which shows that the terms $A_1^{yy} - A_1^{xx}$ and $A_1^{zz} - A_1^{xx}$ already contain all the information of the diagonal part of the SIA part of the Hamiltonian, allowing us to reduce the number of simulations. The general recipe to compute these 2 combinations is as follows: if we are interested in computing the SIA parameter $A_1^{\alpha\alpha} - A_1^{\beta\beta}$, we have to chose the 4 reference states to isolate from the bath as follows

$$\text{State 1} : \boldsymbol{S_1} = S\hat{e}_\alpha, \tag{5.66}$$

$$\text{State 2} : \boldsymbol{S}_1 = -S\hat{e}_\alpha, \tag{5.67}$$

$$\text{State 3} : \boldsymbol{S}_1 = S\hat{e}_\beta, \tag{5.68}$$

$$\text{State 4} : \boldsymbol{S}_1 - S\hat{e}_\beta. \tag{5.69}$$

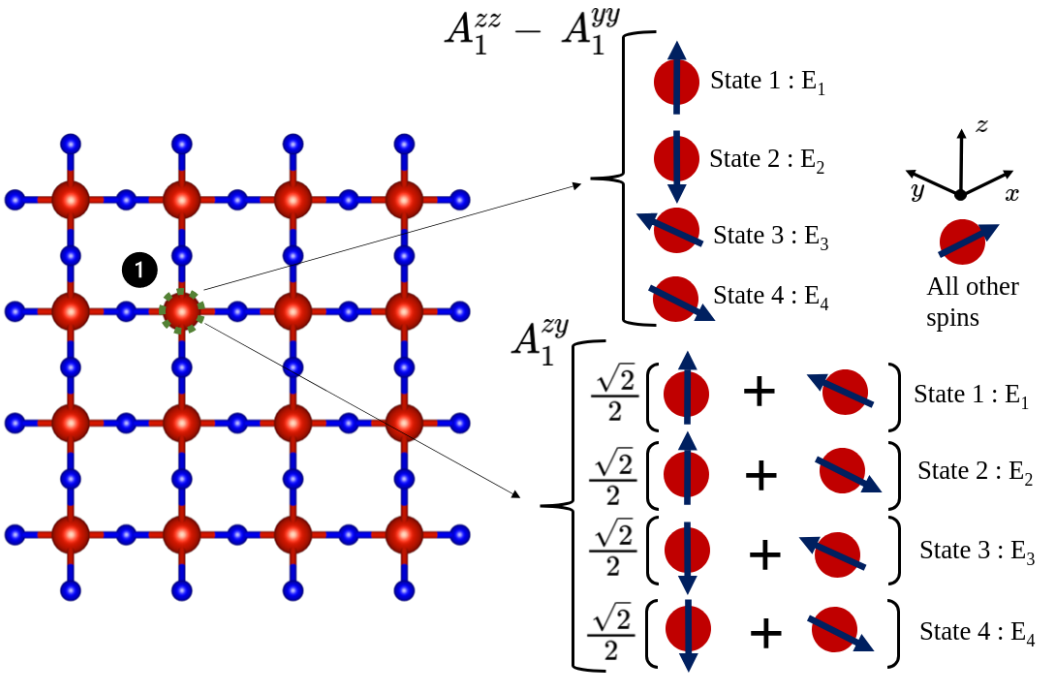

Fig. 5.3 Exemplary case of the 4 state method for the calculation of the A_1^{zy} and the $A_1^{zz} - A_1^{yy}$ coefficients of the single ion anisotropy matrix of eq.(5.57)

Once more all the other spins composing the spin bath have to be chosen to lie outside of the plane spanned by $\hat{e}_\alpha$ and $\hat{e}_\beta$. Once the energy of the 4 states has been computed self-consistently, the anisotropy coefficient can be computed via (beware the different ordering of the energy terms)

$$A_1^{\alpha\alpha} - A_1^{\beta\beta} = \frac{E_1 + E_2 - E_3 - E_4}{4S^2} \tag{5.70}$$

A schematic representation of the 4 states necessary to compute A_1^{zy} and is provided in Fig.5.2.

5.2 Numerical principles for micromagnetic solvers

As discussed in 3.5, the power of the micromagnetic approach lies in allowing us to explore the dynamics of large magnetic samples via the solution of the LLG equation. Unfortunately, due to the non-local long range nature of the physical interactions being described, the partial differential equations arising are analytically solvable in

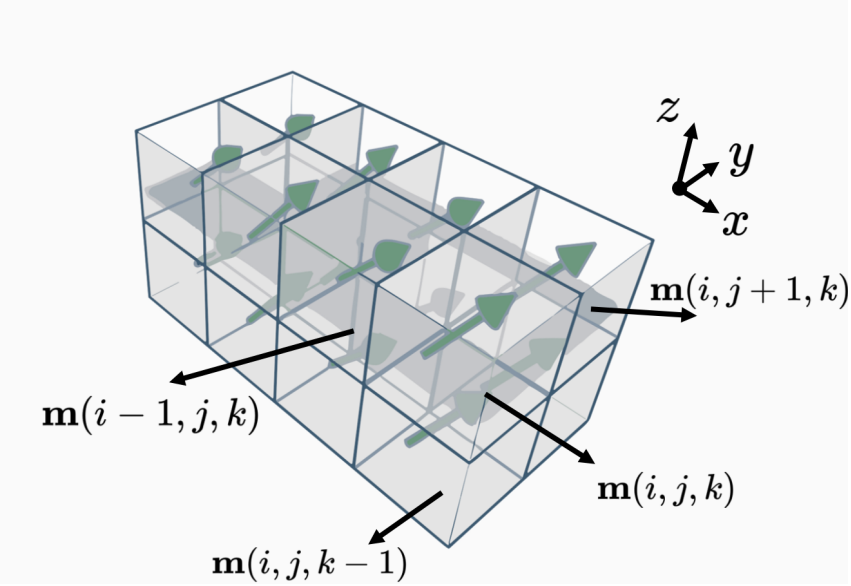

Fig. 5.4 Schematic representation of the material discretization used for micromagnetic simulations

but a handful of selected cases; the full blown solution of the LLG is only accessible via numerical treatment. In the following we very briefly go over the main principles employed by one of the more popular open source micromagnetic solvers available used in this dissertation: MuMax3 [14] .

5.2.1 Discretizing the magnetization field

The first step toward the numerical solution of the LLG equation is the discretization of the magnetization field $\boldsymbol{m}(\boldsymbol{r}) \rightarrow \boldsymbol{m}(i,j,k)$, whereby the continuous field $\boldsymbol{m}(\boldsymbol{r})$ is transformed into an array $\{\boldsymbol{m}_1, \boldsymbol{m}_2, \cdots, \boldsymbol{m}_i, , \cdots \boldsymbol{m}_N\}$ where N is the total number of cells. The total number of cells is given by the produce of number of cells in each spatial dimension $N = N_x \times N_y \times N_z$. Within the cell, magnetization is considered as a constant vector of length M_s and the number of cells in each spatial dimension is a simulation parameter controlled by the choice of cell size ($\Delta_{x,y,z}$) and sample dimensions ($L_{x,y,z}$):

$$N_{x,y,z} = \frac{L_{x,y,z}}{\Delta_{x,y,z}}. \tag{5.71}$$

The cell size is therefore the upper bound to the magnetization volume that displays a uniform value. As discussed in 3.4.4 the length scales that emerge in micromagnetism

are a natural guide to the cell sizes one should consider. In general the dominating length scales in micromagnetic simulations are determined by exchange and magneto-crystalline anisotropy, therefore a good choice is

$$\Delta_{x,y,z} \leq \min(l_{ex}, l_w), \tag{5.72}$$

where

$$l_w = \sqrt{\frac{A}{K_u}} \tag{5.73}$$

is the length scale emerging from the competition of exchange and magneto-crystalline anisotropy and

$$l_{ex} = \sqrt{\frac{2A}{\mu_0 M_s^2}} \tag{5.74}$$

is the characteristic length scale emerging from the competition of exchange and magnetostatic contributions in the micromagnetic energz functional. If we were to chose a cell size $\Delta_{x,y,z} > \min(l_{ex}, l_w)$, we would not be able to distinguish the features arising from the competition of exchange and anisotropy energies e.g. magnetic domain walls. We should remark that the effective field $\boldsymbol{H}_{\text{eff}}$ and the LLG equations are also a function of space

$$\dot{\boldsymbol{M}} = \gamma \boldsymbol{M} \times \left(\boldsymbol{H}_{\text{eff}} - \alpha \dot{\boldsymbol{M}} \right). \tag{5.75}$$

and therefore must also be discretized in order to be solved with numerical methods. Taking in account the discretized form of the effective field we can write an LLG equation fit for numerical solvers:

$$\frac{d\boldsymbol{m}(i,j,k)}{dt} = -\gamma_0(\boldsymbol{m}(i,j,k) \times \boldsymbol{H}_{\text{eff}}(i,j,k)) - \gamma_0 \alpha(\boldsymbol{m}(i,j,k) \times (\boldsymbol{m}(i,j,k) \times \boldsymbol{H}_{\text{eff}}(i,j,k))) \tag{5.76}$$

In the following we discuss how to discretize the different terms of the effective field discussed in 3.3

5.2.2 Finite difference version of the effective field terms

Micromagnetic exchange

The effective field component related to micromagnetic exchange has the form

$$\boldsymbol{H}_{\text{eff}}^{(exch.)}(\boldsymbol{r}) = \frac{2A}{\mu_0 M_s}\nabla^2 \boldsymbol{m}(\boldsymbol{r}). \tag{5.77}$$

The discretized form of this vector field can be expressed by

$$\boldsymbol{H}_{\text{eff}}^{(exch.)}(\boldsymbol{r}) \rightarrow \boldsymbol{H}_{\text{eff}}^{(exch.)}(i,j,k) = \frac{2A}{\mu_0 M_s} \sum_{<l,m,n>} \frac{\boldsymbol{m}(l,m,n) - \boldsymbol{m}(i,j,k)}{\Delta_{l,m,n}^2}, \tag{5.78}$$

where the indices $< l,m,n >$ run over the nearest neighbours of the the cell identified by (i,j,k) (see Fig.5.4).

Chiral interactions

Chiral interactions have a similar structure to the effective field relative to micromagnetic exchange, but only host fist order derivatives as visible from the table of Lifshitz invariants (Table 3.1). The partial derivatives $\partial_{x,y,z}$ can easily be translated in discrete terms as follows

$$\partial_x \boldsymbol{m}(i,j,k) = \frac{\boldsymbol{m}(i+1,j,k) - \boldsymbol{m}(i-1,j,k)}{2\Delta_x}, \tag{5.79}$$

$$\partial_y \boldsymbol{m}(i,j,k) = \frac{\boldsymbol{m}(i,j+1,k) - \boldsymbol{m}(i,j+1,k)}{2\Delta_y}, \tag{5.80}$$

$$\partial_z \boldsymbol{m}(i,j,k) = \frac{\boldsymbol{m}(i,j,k+1) - \boldsymbol{m}(i,j,k-1)}{2\Delta_z}. \tag{5.81}$$

According to these definitions, we can therefore write the i^{th} component of the effective field coming from DMI as

$$(\boldsymbol{H}_{\text{eff}}^{(DMI)})_i = (2\hat{\boldsymbol{Q}}\nabla \times \boldsymbol{m})_i = 2Q_{\alpha\beta}\partial_\beta m_\gamma \varepsilon_{\alpha\gamma i} \tag{5.82}$$

$$\begin{aligned} &= 2Q_{\alpha x}\frac{m_\gamma(i+1,j,k) - m_\gamma(i-1,j,k)}{2\Delta_x}\varepsilon_{x\gamma i} \\ &+ 2Q_{\alpha y}\frac{m_\gamma(i,j+1,k) - m_\gamma(i,j-1,k)}{2\Delta_y}\varepsilon_{y\gamma\sigma} \\ &+ 2Q_{\alpha z}\frac{m_\gamma(i,j,k+1) - m_\gamma(i,j,k-1)}{2\Delta_z}\varepsilon_{z\gamma i} \end{aligned} \tag{5.83}$$

where we recall that $Q_{\alpha\beta}$ represents the components of the spiralization tensor (or DMI tensor). In Appendix **III** we show how we implemented a DMI tensor of the form

$$\hat{\boldsymbol{Q}} = \begin{pmatrix} D_1 & D_2 & 0 \\ D_2 & -D_1 & 0 \\ 0 & 0 & 0 \end{pmatrix} \tag{5.84}$$

in the MuMax3 code as an exemplary case.

Magnetocrystalline anisotropy

The magnetocrystalline anisotropy term is local as it does not depend on partial derivatives of the magnetization field: this makes it trivial to handle in a discretized form

$$\boldsymbol{H}_{\text{eff}}^{(an.)} = \frac{2K_u}{\mu_0 M_s}[\hat{\boldsymbol{n}}_u \cdot \boldsymbol{m}(i,j,k)]\hat{\boldsymbol{n}}_u, \tag{5.85}$$

where $\hat{\boldsymbol{n}}_u$ represents the uniaxial anisotropy easy axis.

Magnetostatic energy

The effective field component coming from the magnetostatic interaction is indeed the most computationally intensive to treat as it entails long range interactions. The effective field component associated to the magnetostatic energy has the form

$$\boldsymbol{H}_{\text{eff}}^{(dmg.)}(\boldsymbol{r}) = -\frac{1}{4\pi}\int_V \underbrace{\nabla \cdot \boldsymbol{M}_s(\boldsymbol{r}')}_{\rho_M(\boldsymbol{r}')}\frac{\boldsymbol{r}-\boldsymbol{r}'}{|\boldsymbol{r}-\boldsymbol{r}'|^3}d^3\boldsymbol{r}' + \frac{1}{4\pi}\oint_{\partial V=S}\underbrace{\hat{\boldsymbol{n}} \cdot \boldsymbol{M}_s(\boldsymbol{r}')}_{\sigma_M(\boldsymbol{r}')}\frac{\boldsymbol{r}-\boldsymbol{r}'}{|\boldsymbol{r}-\boldsymbol{r}'|^3}d^2\boldsymbol{r}'. \tag{5.86}$$

We now change our notation somewhat to make the discretization procedure more easy to follow: instead of identifying a cell with the three indices (i, j, k) as before, we identify it with a singe indexed vector $\boldsymbol{r}_j$. In this notation $\boldsymbol{M}(\boldsymbol{r}_j)$ indicates the averaged magnetization inside the cell located at $\boldsymbol{r}_j$. With this new notation we can write the demagnetizing field as

$$\boldsymbol{H}_{\text{eff}}^{(dmg.)}(\boldsymbol{r}_i) = -\frac{1}{4\pi}\sum_j \int_{V_j} \rho_M(\boldsymbol{r}'_j)\frac{\boldsymbol{r}_j - \boldsymbol{r}'_j}{|\boldsymbol{r}_j - \boldsymbol{r}'_j|^3} d^3\boldsymbol{r}'_j + \frac{1}{4\pi}\sum_j \oint_{\partial V_j = S_j} \sigma_M(\boldsymbol{r}'_j)\frac{\boldsymbol{r}_j - \boldsymbol{r}'_j}{|\boldsymbol{r}_j - \boldsymbol{r}'_j|^3} \tag{5.87}$$

where we have used the fact that inside V_j the magnetization is constant and therefore $\rho_M(\boldsymbol{r}_j) = 0\ \forall \boldsymbol{r}_j \in V_j$. The assumption of constant magnetization inside the individual volumes V_j allows us to use the demagnetization tensor approximation discussed in 3.2. We write the demagnetizing field in discrete form as

$$\boldsymbol{H}_{\text{eff}}^{dmg.}(\boldsymbol{r}_i) = \sum_j \overleftrightarrow{N}(\boldsymbol{r}_i - \boldsymbol{r}_j)\boldsymbol{M}(\boldsymbol{r}_i), \tag{5.88}$$

where $\overleftrightarrow{N}(\boldsymbol{r}_i - \boldsymbol{r}_j)$ is the demagnetizing tensor which in this case depends on the cell dimensions and on the distance from the other cells [100]. The actual calculation of the demagnetizing field in MuMax3 is performed in reciprocal space, as the use of Fast-Fourier-Transform FFT allows to reduce the operation count from $\mathcal{O}(N^2)$ to $\mathcal{O}(N \log N)$.

Chapter 6

Results

After having laid the theoretical and numerical foundations for magnetic interface phenomena and their interplay with some aspects of the electric field, we proceed and discuss the main results obtained in this Dissertation. In 6.1 and 6.2 we explore some facets of the intricate reversibility patterns displayed by magneto-ionic manipulations of MCAE. In particular, 6.1 deals with the experimental evidence of multiple magneto-ionic regimes in Ta/$Co_{20}Fe_{60}B_{20}$/HfO_2 multilayers, while in 6.2 we investigate the displayed patterns on a microscopic scale with the aid of atomistic simulations. In 6.3 and 6.4 we shift our focus on electric field manipulation of chiral interactions such as DMI. In 6.3 we present a theoretical study in which we demonstrate how, by building a gauge covariant micromagnetic theory, we are able to correctly predict all manners of possible different chiral interaction allowed by non centrosymmetric point groups. We pose particular attention at the interplay between an electric field low-dimensional forms of DMI. In 6.4 we apply our formalism to the field of magnetic domain wall motion and characterization: we uncover several interesting unexplored phenomena such a non-linear enhancement of DW velocity in the presence of some particular forms of DMI, as well as discussing how domain wall canting in the presence and absence of transverse IP magnetic fields is affected. We conclude this section with a discussion of the possible new avenues that the research of these 3 years has opened.

6.1 Multiple magneto-ionic regimes in $Ta/Co_{20}Fe_{60}B_{20}/HfO_2$

In Ta/(Co,Fe)B/HfO_2 stacks, a gate voltage drives, in a nonvolatile way, the system from an underoxidized state exhibiting in-plane anisotropy (IPA) to an optimum oxidation level resulting in perpendicular anisotropy (PMA) and further into an overoxidized state with IPA. The IPA $\rightarrow$ PMA regime is found to be significantly faster than the PMA $\rightarrow$ IPA regime, whereas only the latter shows full reversibility under the same gate voltages. The effective damping parameter also shows a marked dependence with gate voltage in the IPA $\rightarrow$ PMA regime, going from 0.029 to 0.012, and only a modest increase to 0.014 in the PMA $\rightarrow$ IPA regime. The existence of two magneto-ionic regimes has been linked to a difference in the chemical environment of the anchoring points of oxygen species added to underoxidized or overoxidized layers. Our results show that multiple magneto-ionic regimes can exist in a single device and that their characterization is of great importance for the design of high-performance spintronics devices.

Acknowledgement: The content of this Section is readapted from the publication Pachat, R., Ourdani, D., van der Jagt, J. W., Syskaki, M.-A., Di Pietro, A., Roussigné, Y., Ono, S., Gabor, M. S., Chérif, M., Durin, G., Langer, J., Belmeguenai, M., Ravelosona, D., & Diez, L. H. (2021). Multiple Magnetoionic Regimes in $Ta/Co_{20}Fe_{60}/B_{20}/HfO_2$ In Physical Review Applied (Vol. 15, Issue 6). American Physical Society (APS). https://doi.org/10.1103/physrevapplied.15.064055 [132] in a paper in which I contributed as a **co-author**. Please use this paper for citations.

6.1.1 Introduction

Controlling magnetic properties using an electric field has garnered significant attention due to its potential implications for applications with reduced power consumption. The tuning of magnetic anisotropy through charge accumulation effects has been successfully demonstrated in various systems [133–135]. However, a primary challenge associated with this mechanism is its volatility, as well as the strong locality of the effect.

As discussed in 2.3.4, magneto-ionic manipulation of magnetic properties has emerged as a promising alternative: despite much efforts still needed to improve aspects such as operation speed and cyclability, this technique offers a more uniform and extended effect over the volume of the magnetic film in addition to the required non-volatility. It should be stressed however, that the non-volatile nature of magneto-ionic manipulation is advantageous as long as the device can reliably exhibit reversibility, ensuring consistent and predictable magnetic behavior. Unfortunately, the factors influencing the reversibility of magnetization manipulation remain unclear, prompting extensive investigations into the diverse reversibility behaviors exhibited by different oxide-based systems [62].

In the following we show how the complexity of the reversibility issue can display an additional degree of freedom. The present study conducted on a series of $Ta/Co_{20}Fe_{60}B_{20}/HfO_2$ multilayers in fact reveals that both reversible and irreversible behaviors can be displayed. The study identifies two magneto-ionic regimes in the device, with access to each regime dependent on the duration of the applied gate voltage. These findings underscore the intricate nature of magneto-ionic reversibility and highlight the need for further research to elucidate the underlying mechanisms and optimize device performance.

6.1.2 Experimental setup

In this study, the magnetic materials employed are amorphous Ta(5 nm)/CoFeB(1 nm)/HfO2(3 nm) films, grown using a magnetron sputtering technique. The choice of these materials ensures a suitable magnetic system for investigating the effects of magneto-ionic manipulation. To apply the gate voltage, an ionic liquid (IL) is utilized instead of a solid-state gating method. Specifically, the IL employed in this study is [EMI][TFSI], which has been demonstrated to generate an electric field of sufficient strength to induce ionic motion in various materials [136]. The effective thickness of the IL is estimated by considering only the distance over which electric double layers are formed at the electrode edges, resulting in an estimated thickness of approximately 1 nm [137].

A counter electrode composed by a 100-nm thick indium tin oxide (ITO) layer deposited onto a glass substrate is positioned on top of the IL, enabling the application of the gate voltage over an area of approximately 0.25 cm^2. Hysteresis loops for the

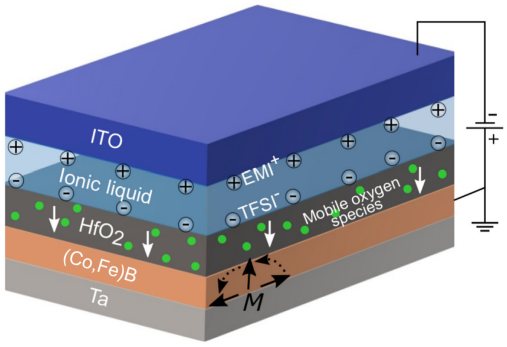

Fig. 6.1 Graphic representation of the magneto-ionic stack covered with the ionic liquid $[EMI]^+[TFSI]^-$ and the counter electrode made of ITO

OOP component of the magnetization, are measured using the anomalous Hall effect employing a bias current of 400 μA. A scheme of the setup is presented in Fig.6.1.

6.1.3 Magneto-ionic Regimes I and II

In the initial state, prior to exposure to the gate voltage, the sample exhibits an in-plane (IP) magnetic anisotropy (IPA) (Fig.6.2-(a)). Upon application of a negative gate voltage, a first magneto-ionic regime is identified and a transition from IPA to perpendicular magnetic anisotropy (PMA) is observed (Fig.6.2-(b,c)). By further increasing the gate voltage, a second magneto-ionic regime is identified, where the system undergoes another spin reorientation transition (SRT), driving it from PMA back to IPA (Fig.6.2-(d)). Throughout the experiment, a gate voltage of $G_V = -2$ V is applied continuously for a total duration of $t = 1380s$.

It is well established that there exist optimal oxidation windows for ferromagnetic materials, within which the promotion of PMA is observed [138]. Additionally, HfO_2 has been recognized as an oxide in which the predominant ionic mobility contribution, upon the application of a gate voltage, stems from oxygen ions [139]. Therefore, it is likely that the manipulation of magnetic anisotropy observed in the experimental data is driven by the mobility of oxygen ions and their interaction with the ferromagnetic interface.

When comparing the two observed magneto-ionic regimes, several notable differences emerge. Firstly, the SRT occurs at a faster rate in regime I compared to regime II (see Fig.6.3-(a)) suggesting that the continued application of the gate voltage

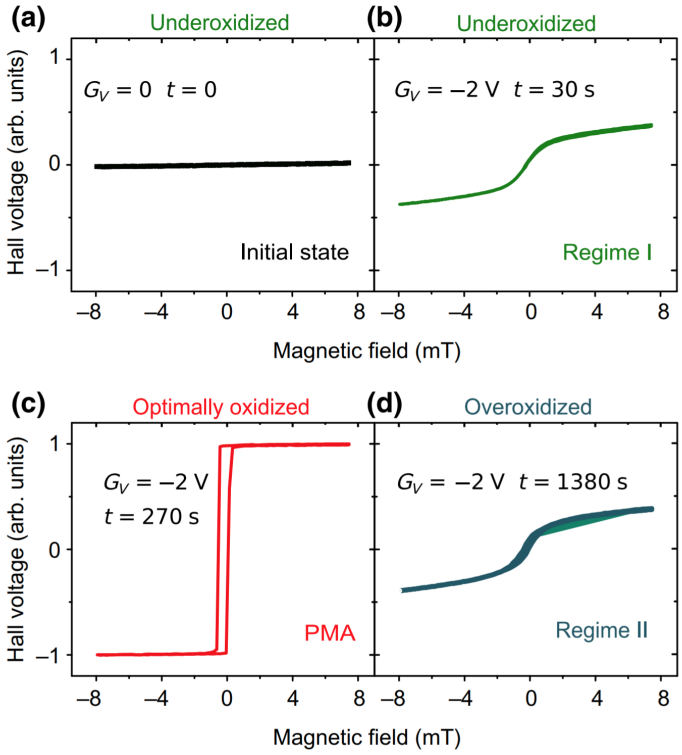

Fig. 6.2 Hall voltage response to the progressive oxidation induced upon exposure to a gate voltage G_V = -2 V. Different exposure times t drive the system from the initial state (IPA-(a)) through regime I (b) into PMA (c) and back to IPA through regime II (d).

causes alterations of the chemical environment that differ between the regimes. In particular, it is speculated that the continued application of the gate voltage might cause the new oxygen species approaching the FM surface to be more difficult to bond, therefore leading to variations in the energy barrier , leading to an altered disposition of the surface to bind new oxygen species.

Another interesting observation is the reduced SRT speed observed in samples that have been annealed at 180 °C. The goal of the annealing process is to reduce the presence of trapped moisture in the samples while avoiding sample crystallization to gauge the relative importance of stoichiometric oxygen of the HfO_2 and the additional oxygen coming from atmospheric interaction. As can be seen from Fig.6.3-(a), the speed of the magneto-ionic manipulation in these annealed samples is significantly reduced therefore hinting at the fact that atmospheric oxygen indeed plays a central role in the switching process.

Regimes I and II do not only display different speeds in the SRT process, but also a fundamental difference regarding reversibility. The reversibility of the SRT has been tested in Reg. I and II with gate voltages going from -2 V to + 4 V. The effects of the application of +4 V for 10 min up to 60 minutes are shown in Fig.6.4-(a). As can be seen, only minor changes to the hysteresis loop are observable, indicating that the induced magnetization state cannot be reverted to the initial IP configuration. Regime II shows a different behavior when exposed to the positive bias voltage if $G_V = +4$ V. In Fig.6.4-(b) we can indeed observe a fully reversible transition between IPA and PMA. Fig. 6.4-(c) shows the remanence variation over 10 cycles of alternating gate voltage sign. It is interesting to notice that the transition PMA $\rightarrow$ IPA in the first cycle is obtained after an application of -2V for t =1200 s while for all subsequent cycles, the gate voltage application time is reduced to 240s. This observation indicates that the magneto-ionic process most likely undergoes an "activation" phase in which the diffusion of the oxygen ions is likely to require the overcoming of some additional energy barrier. To summarize, Regime I displays a faster dynamic than Regime II (Fig.6.4-(b)) under the application of G_V = -2 V and an irreversible SRT upon application of G_V = +4 V. Regime II on the contrary displays a full reversibility and a slower dynamic.

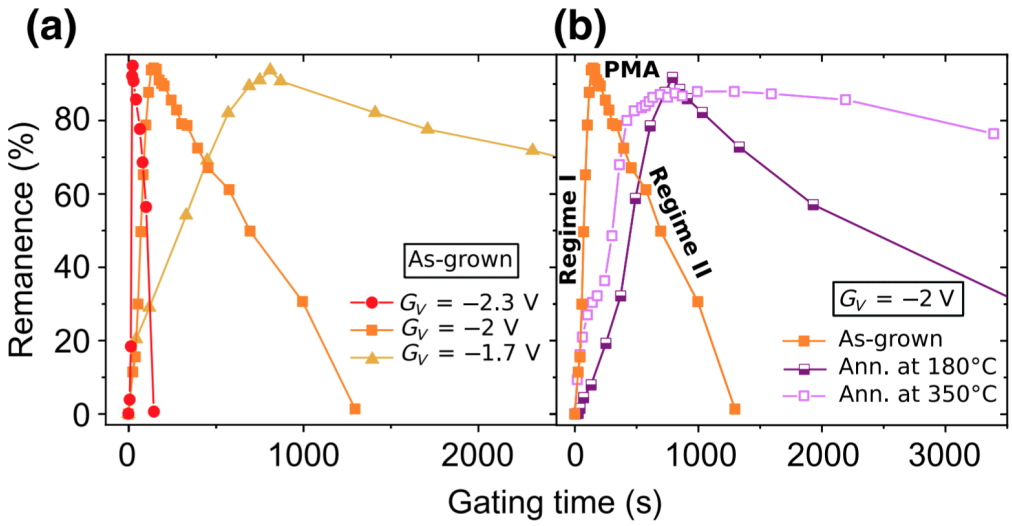

Fig. 6.3 Remanence as a function of gating time in (a) non-annealed (as-grown) samples under G_V = -2.3 V (circles), G_V = -2 V (squares) and G_V = -1.7 V (triangles). (b) Remanence as a function of gating time in samples annealed at 180 °C (half open square) and 350 °C (open squares) under G_V = -2 V.

6.1.4 Discussion

The magneto-ionic mechanisms underlying regimes I and II are illustrated in Fig.6.5. In the presence of a negative gate voltage ($G_V < 0$), mobile oxygen species within the HfO_2 layer (depicted as bright green dots in Fig.6.1) migrate towards the CoFeB layer and, after the gate voltage is switched off, these species remain bound to the FM surface (Fig.6.5-(a)), thereby inducing a gradual transition from in-plane anisotropy (IPA) to perpendicular magnetic anisotropy (PMA). An optimal gate voltage application time is observed, after which PMA is achieved (end of regime I).

If the negative gate voltage ($G_V < 0$) continues to be applied, the magneto-ionic manipulation of anisotropy progresses to regime II, in which the newly incorporated oxygen species contribute to the PMA-to-IPA transition (Fig.6.5-(b)). Since regime II begins with an optimally oxidized CoFeB surface, the continued application of the gate voltage is likely to result in the binding of oxygen species to sites distinct from those occupied by the oxygens in regime I. Furthermore, a longer duration of gate voltage application increases the likelihood of oxygen species penetrating deeper into the CoFeB layer [5, 63] (see Fig.6.5-(c)).

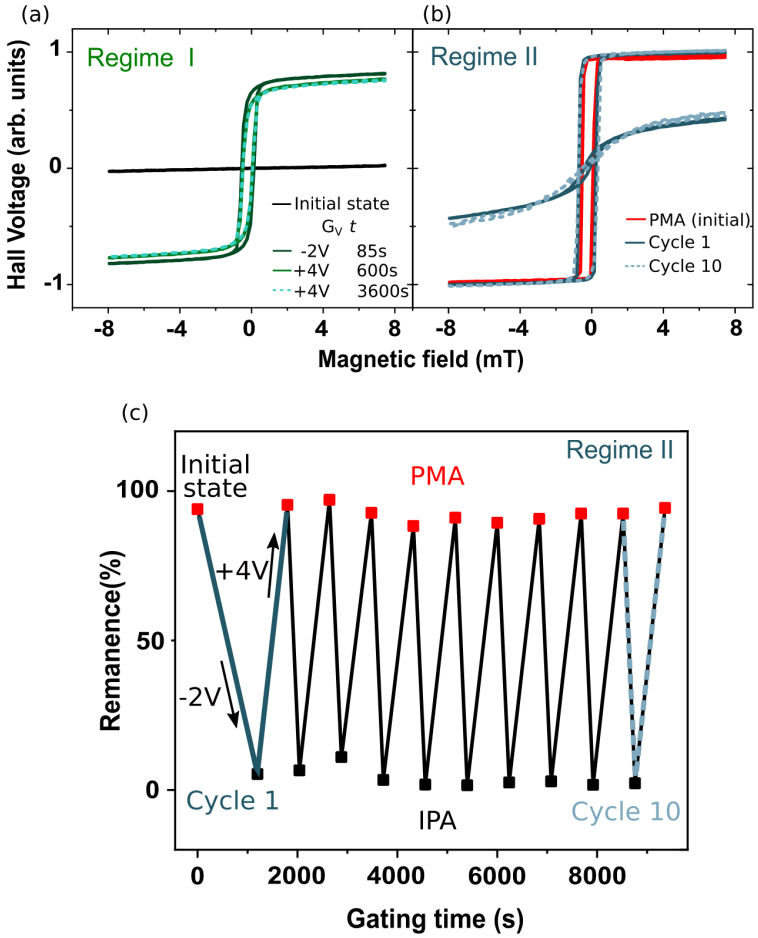

Fig. 6.4 (a) Hysteresis loops for the (irreversible) IPA $\rightarrow$ PMA transition under the application of $G_V = +4V$ in the first magneto-ionic regime. (b) First hysteresis loops for the PMA $\rightarrow$ IPA transition (solid line) and subsequent 10 cycles (dotted lines) in regime II. (c) Magnetic remanence as a function of the cycle number in regime II.

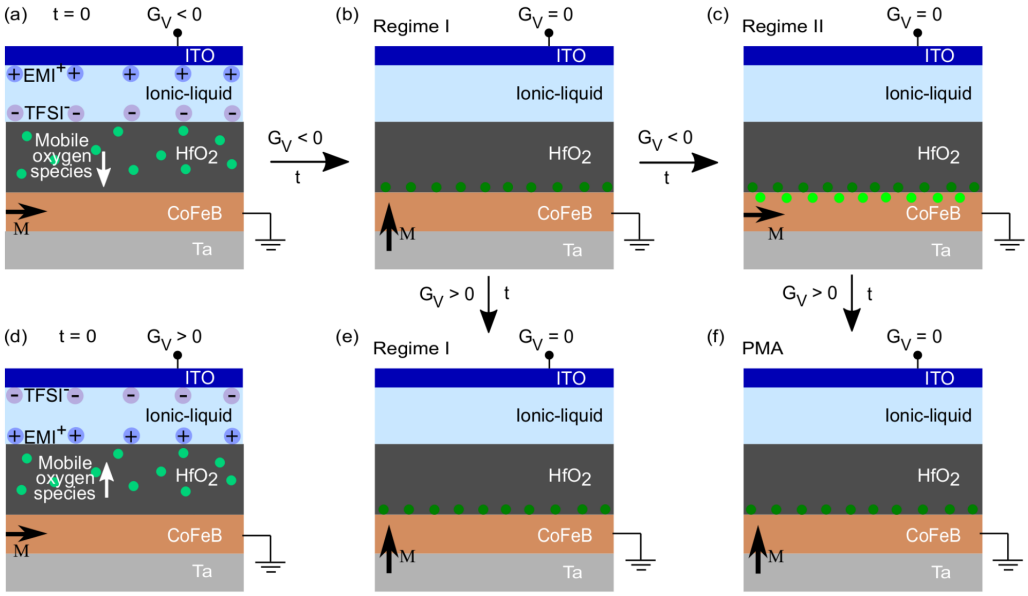

Fig. 6.5 Proposed magneto-ionic mechanism for regimes I and II. (a) When $G_V < 0$, oxygen species migrate towards the ferromagnetic (CoFeB) layer. After a certain amount of time, PMA is achieved, indicating that some optimum in surface coverage has been achieved. (b) If $G_V < 0$ keeps being applied, oxygen species continue to be incorporated in the CoFeB layer, resulting in a gradual return to the IPA (Regime II), shown in (c). (d) If the voltage sign is reversed $G_V > 0$, mobile oxygen species can migrate back to the top electrode. For the same applied voltage G_V there is no reversibility in regime I ((b) towards (e)) while full reversibility is achieved in regime II ((c) toward (f)).

Under sufficiently high positive gate voltages ($G_V > 0$), it is anticipated that mobile oxygen species will migrate back to the top electrode (Fig.6.5-(d)). However, it is important to note that the reversibility of the anisotropy manipulation is highly suppressed for oxygen species incorporated in regime I under the same positive gate voltage (see Fig.6.5-(b) transitioning to Fig.6.5-(e)), while full reversibility is observed in regime II (see Fig.6.5-(c) transitioning to Fig.6.5-(f)).

The fundamental difference in the reversibility of anisotropy manipulation is attributed to disparities in the binding sites and associated anchoring strength of the oxygen species bound to the CoFeB surface during the two regimes. This distinction in binding behavior gives rise to varying degrees of reversibility, emphasizing the role of binding mechanisms in governing the observed magneto-ionic effects. The literature explores the surface and bulk components of the magneto-ionic effect in various systems, notably Pt/Co/GdOx and Pt/Co/HfO_2 [140, 63]. In these systems, complete irreversibility of anisotropy manipulation has been observed as a

consequence of deep oxygen anchoring in the magnetic layer. The present system however seems to show a different behavior, since our investigation reveals that in regime I, irreversibility is suppressed even at low oxygen content, thus excluding the possibility of deep oxygen anchoring in the CoFeB layer.

This claim gains further support by considering the total reversibility observed in regime II after prolonged application of negative voltage, further challenging the prevailing notion that irreversibility in magneto-ionic manipulation necessitates profound oxygen anchoring.

The complex nature of oxidation processes in FM materials has been addressed in studies exploring the incorporation of oxygen species from the gas phase into crystalline Co and Fe samples. Notably, in Co, a distinct change in slope is observed in the oxygen intake process, indicative of a two-step mechanism. This has been linked to an initial formation of a CoO layer (up to a specific surface area coverage threshold), followed by the subsequent formation of Co_3O_4 species at elevated temperatures [141]. A similar behavior has been observed in Fe samples at room temperature, where the oxygen sticking coefficient is reported to decrease sharply up to a value of 0.5, after which a slower decrease is observed following an inflexion point [142, 143].

In this case, the oxygen incorporation mechanism is speculated to gradually develop from simple oxygen absorption to the the nucleation and expansion of an FeO layer. Further oxygen incorporation, now happening in the presence of FeO, appears to be significantly slowed down and leading to the formation of a Fe_2O_3/Fe_3O_4 three dimensional oxide structure.

We underline the fact that the system under investigation exhibits an amorphous nature, which may blur the distinction between different oxide phases. Nevertheless, prior studies have demonstrated the strong impact of varying Fe percentages in $Co_{20}Fe_{60}B_{20}$ films on the manipulation of interfacial anisotropy [144]. The amorphous nature of the studied magnetic compound therefore does not seem to undermine the core assumption of the magneto-ionic mechanism in place, which views a multi-step oxidation process of the interface as the driver of reversibility/irreversibility in this system.

Regime I therefore likely corresponds to the initial absorption of oxygen and the subsequent formation of a FeO layer, entailing a change in the valence state of Fe from Fe^0 to Fe^{2+}. The development of full two-dimensional FeO layer may be

associated with the attainment of an optimal oxidation state related to perpendicular magnetic anisotropy (PMA). The continued supply of oxygen species beyond this point, once a 2D FeO layer is established, should yield a less efficient absorption process, thus leading to a decelerated dynamic of anisotropy manipulation, clearly observed in regime II.

In regime II, the continued incorporation of oxygen leads to the formation of a Fe_3O_4 oxide phase, characterized by a mixture of Fe^{2+} and Fe^{3+} valence states. We propose that the gradual addition of oxygen promotes the generation of an increasing proportion of Fe^{3+} states relative to Fe^{2+}: this gradual increase in Fe^{3+} states is expected to be reversible due to the low energy barrier for the inverse process, allowing for the observed reversibility of anisotropy manipulation in regime II.

It should be noted however, that a complete conversion to Fe^{3+} valence states, would result in a significantly high energy barrier for the inverse process, thus suppressing reversibility of anisotropy changes once again. This observation is in alignment with the experimental observation of a fully irreversible IPA state when a strong negative voltage of G_V= -3 V is applied for $t = 120$s.

6.1.5 Conclusions

In conclusion, we have shown the existence of two distinct non-volatile magneto-ionic regimes in Ta/CoFeB/HfO_2 stacks where oxygen species migrate under negative/positive gate voltages toward/away from the CoFeB layer. This voltage driven ionic motion induces first an IPA $\rightarrow$ PMA transition in regime I corresponding to a transition from an underoxidized to an optimally oxidized state. In regime II, a PMA$\rightarrow$ IPA transition occurs and it is correlated to a transition from optimally oxidized to overoxidized state. Regime I shows much faster dynamics and highly suppressed reversibility for positive gate voltages with respect to regime II. The existence of regimes I and II is proposed to be the result of a difference in the binding strength of the migrated oxygen species, that can be correlated with different binding sites on the surface and inside the CoFeB layer, respectively. The results presented here reveal the complexity of magneto-ionics and the importance of a deep understanding of the ionic mechanisms involved in order to design robust and reliable devices for spintronics applications.

6.2 Ab-initio study of magneto-ionic mechanisms in ferromagnet/oxide multilayers

The application of gate voltages in heavy metal/ferromagnet/Oxide multilayer stacks has been identified as one possible candidate to manipulate their anisotropy at will. However, this method has proven to show a wide variety of behaviours in terms of reversibility, depending on the nature of the metal/oxide interface and its degree of oxidation. In order to shed light on the microscopic mechanism governing the complex magneto-ionic behaviour in Ta/CoFeB/HfO_2, we perform ab-initio simulations on various setups comprising Fe/O, Fe/HfO_2 interfaces with different oxygen atom interfacial geometries. After the determination of the more stable interfacial configurations, we calculate the magneto-crystalline anisotropy energy on the different unit cell configurations and formulate a possible mechanism that well describes the recent experimental observations in Ta/CoFeB/HfO_2.

Acknowledgement: The content of this Sections is published in "Di Pietro, A., Pachat, R., Qiao, L., Herrera-Diez, L., van der Jagt, J. W., Picozzi, S., Ravelosona, D., Ren, W., & Durin, G. (2023). Ab initio study of magneto-ionic mechanisms in ferromagnet/oxide multilayers. In Physical Review B (Vol. 107, Issue 17). American Physical Society (APS). https://doi.org/10.1103/physrevb.107.174413" [145]. Please use this paper for citations.

6.2.1 Introduction

The ever-increasing demand for memory storage in the modern IT industry has made the need for new energy efficient storage alternatives all the more important. Voltage control of magnetic anisotropy (VCMA) [146] has gained scientific interest as one of the prime candidates to develop ultra-low energy memory storage devices [147, 52, 59, 6] and is usually studied in two different variants: the first one aims at modifying magnetic properties of thin films by pure charge accumulation/depletion effects induced by voltage application [84, 148, 59, 56]. The second variant makes use of voltage–induced ionic motion in heavy metal (HM)/ferromagnet (FM)/Oxide (Ox) thin film multilayers to carefully tune the oxygen/ferromagnet chemical and electrostatic interaction, enabling the control of magnetic anisotropy [54, 38, 52]. The main advantage of ionic manipulation in comparison to pure charge accumula-

tion/depletion techniques is the non-volatility of the magnetization switching, while the trade off is a more complex reversibility mechanism combining ion mobility and chemical composition at the FM/Ox interface.

The work of Fassatoui et al. [62] clearly shows how the application of gate voltages causes a reversible magnetization switching in Pt/Co/AlOx as well as in Pt/Co/TbOx. At the same time, applying a gate voltage in Pt/Co/MgOx has the effect of irreversibly pushing the anisotropy easy axis out-of-plane. This discrepancy has been attributed to the result of the different character of the ionic mobility of the oxides: TbOx and AlOx have the common property of being oxides with a predominantly oxygen based ionic mobility [62, 149], while MgOx is known to have Mg as the principal ionic carrier under the application of gate voltages [150]. CoFeB/Oxide multilayer structures are of great technological interest as they have shown promise for the design of non-volatile, high-density memory storage devices thanks to their high tunneling mangeto-resistance (TMR), low damping and perpendicular magnetic anisotropy (PMA) [151–153]. A recent work from Pachat et. al [154] highlighted a more complex magneto-ionic behavior in Ta/CoFeB/HfO_2 multilayers. The application of a gate voltage to the as-grown material with in-plane anisotropy (IPA) initially causes a non-volatile, irreversible spin-reorientation transition (SRT) to a perpendicular anisotropy state (PMA). Further application of the gate voltage causes the transition to a fully reversible regime. This 2-step process is in contrast with the picture presented in [62] because ionic mobility in HfO_2 is attributed to oxygen [139]. To formulate a hypothesis on the mechanism governing these different reversibility behaviors in Ta/CoFeB/HfO_2, we perform ab-initio simulations using density functional theory (DFT) to determine the structural and magnetic properties of two FM/Oxide interfaces.

The work is structured as follows: In Sec. 6.2.2, we provide the computational details of our simulations and a brief overview of the theoretical framework used to describe magnetic anisotropy in FM/Oxide interfaces. In Sec. 6.2.3 we analyze the structural properties of two different FM/Oxide interfaces, displaying either interstitial or frontal oxygen positioning (see Fig. 6.6 and Fig. 6.8-(c)). After having determined the optimal oxygen configurations of these setups, we compute the magnetic anisotropy energy of the Fe/HfO_2 unit cells. We also explore the role of ionic mobility in determining the magnetic anisotropy properties of Fe/HfO_2 interfaces and highlight how the energy costs involved in ionic mobility is different depending on the site occupied. In Sec. 6.2.4, we discuss the results and compare

them to the experimental data [154] and theoretical predictions [148, 5] in order to formulate a hypothesis for the appearance of different magneto-ionic regimes in CoFeB/HfO_2 multilayers. Finally, in Sec. 6.2.5 we provide a summary of the findings and outline new possible systems to analyze to further probe our hypothesis.

6.2.2 Methods and computational details

Structural relaxations

We perform structural relaxation using density functional theory and applying the full-potential linearized augmented plane wave (FLAPW) method [155], as implemented in the FLEUR code [129, 130]. In particular, we rely on the generalized gradient approximation for the exchange-correlation potential, as implemented by the Perdew–Burke-Ernzerhof (PBE) functional [156].

Since the simulation of amorphous systems such as CoFeB is extremely challenging for ab-initio methods, we reduced the ferromagnetic component of the system to the Fe atoms only. This approximation is justified on the basis of the composition of the $Co_{20}Fe_{60}B_{20}$/HfO_2 stacks studied in the literature, which are iron rich [154]. Furthermore, this approximation for CoFeB in ab-initio simulations is commonly used in the literature [157]. We designed 5 different unit cells comprising: an Fe/O interface (structures (I) and (II) in Fig. 6.6) composed of 5 magnetic layers (ML) of Fe sandwiched between 2 mono-atomic layers of oxygen on each side, an Fe/HfO_2 system (structures (III) and (IV) in Fig. 6.6) composed of 5 ML of Fe atoms sandwiched between 2 ML of HfO_2 on each side. Finally, to account for oxygen coming from atmospheric interaction with the sample, we designed an Fe/HfO_2 system displaying both frontal and interstitial oxygen atoms [158] . This system is composed of 5 ML of Fe atoms sandwiched between 2 ML of HfO_2 on each side with an additional O-layer located in the interstitial site of 2 Fe atoms (Fig. 6.8-(c)). We refer to this kind of system as "mixed interface" throughout the work. The in-plane lattice constant of the system is fixed to the value of body-centered cubic (BCC) Fe, i.e $a_{Fe} = 2.87$ Å. To perform structural relaxation, we selected a cutoff value for the plane wave basis of $K_{max} = 4.5\, a_B^{-1}$. We select the following values for the Muffin-Tin sphere radius of the atoms: $R_{MT}(\mathrm{Fe}) = 2.18\, a_B$, $R_{MT}(\mathrm{Hf}) = 2.54\, a_B$, $R_{MT}(\mathrm{O}) = 1.19\, a_B$ and a k-point mesh of dimensions $10 \times 10 \times 1$. These parameters allow us to obtain self consistent energies converged to at least 0.009 eV/Atom. To determine the

optimal interfacial configurations of oxygen atoms, structural relaxation performed until the forces are smaller than 0.01 eV/Å.

Magneto-crystalline anisotropy energy (MCAE)

The ab-initio calculation of the MCAE [159] is performed according to the following procedure [160, 158, 84]: after having determined the more stable interfacial geometries via the structural relaxation as outlined in 6.2.2, spin orbit coupling (SOC) is treated in second variation [161] in the Kohn-Sham Hamiltonian and the MCAE is computed by comparing sums of one-electron energies via the magnetic force theorem [127, 128]. This method is widely used and has been validated for transition metal interfaces [162].

The measurement of magneto-crystalline anisotropy requires an increased precision compared to structural relaxation: we therefore increase the size of the k-point mesh to $22 \times 22 \times 1$. Both with and without spin-orbit coupling, the plane wave cutoff is kept at $K_{max} = 4.5\, a_B^{-1}$. With these parameters, we are able to obtain self consistent energies converged to at least 0.01 meV/Atom[1].We remark how this contribution to the total magnetic anisotropy of the system is solely due to SOC and therefore neglects the contributions coming from dipole-dipole interactions (i.e. shape anisotropy effects). We neglect these terms in our discussion as the SOC in the presented system is lower than what can be found in actual multilayers (we do not add a heavy metal layer at the bottom of our unit cell) and their inclusion could unnecessarily hide the effects of oxygen on the anisotropy of the system.

Theoretical background

The origins of oxygen enabled anisotropy manipulation in FM/Oxide interfaces have been discussed extensively in the literature [5, 158]. The underlying theoretical frameworks have been developed by Bruno [49] and Van Der Laan [50], which successfully linked a finite anisotropy in the orbital magnetic moment to an anisotropy contribution in the total energy in the presence of spin-orbit coupling. These theoret-

[1] Some of the presented results, especially concerning equilibrium geometries, were benchmarked with the Vienna Ab-initio Simulation Package (VASP) [163, 164]. The used simulation parameters were: Energy cutoff of 500 eV and k_{mesh}-size $11 \times 11 \times 1$. The total energy convergence threshold was set to 10^{-6} eV and the structural relaxation convergence was set to a maximum force on each atom lower than 0.02 eV/Å.

ical frameworks predict a heavy dependence of the anisotropy energy on the exact shape and hybridization of the 3d orbitals.

In this framework, oxygen atoms, when posed at a specific distance, can have dramatic effects in the disruption of the otherwise almost isotropic magnetic moment distribution of the 3d orbitals of transition metal ferromagnets [158]. In particular, the 3d-electrons of Fe tend to hybridize very effectively with the oxygen $2p_z$ orbitals. Therefore, depending on the relative position of Fe and O, the orbital character of majority 3d-orbitals will change. If, for instance, we imagine an oxygen atom sitting on top of an Fe atom, the atomic orbitals that are more likely to hybridize have out-of-plane (OOP) character [165] $\{3d_{z^2}, 3d_{xz}, 3d_{yz}\}$. This results in a larger portion of occupied atomic orbitals with in-plane character, i.e $\{3d_{x^2-y^2}, 3d_{xy}\}$ orbitals. The orbital moment of the Fe atom will therefore point OOP and the anisotropy easy axis will follow it [158] according to the approximate analytic relation[49, 50]

$$\Delta E_{SO} = \xi_{SO} \frac{\Delta\mu}{4\mu_B}, \tag{6.1}$$

where ΔE_{SO} represents the anisotropy energy , $\Delta\mu$ the orbital moment anisotropy and ξ_{SO} the material–dependent spin-orbit coupling constant. We emphasize how this is an approximate relation that reproduces the results semi-quantitatively but correctly reproduces the sign the MCAE [166]. On the other hand, if the oxygen atom is located in the same plane of the Fe atom, hybridization is going to involve orbitals with in-plane (IP) character $\{3d_{x^2-y^2}, 3d_{xy}\}$. Fe atoms now retain a larger proportion of 3d-orbitals with $\{3d_{z^2}, 3d_{xz}, 3d_{yz}\}$ orbital character which reverses the trend and shifts the orbital moment and the anisotropy easy axis in-plane. Despite the thinness of the FM layers, one should always consider that the contributions to magnetic anisotropy are not limited to the first layer, but in fact often involve the second layer and possibly beyond (as in the case of Fe/MgO MTJs [84]).

In addition, the appearance of magnetic anisotropy is still constrained by the symmetries of the crystal field that is coupled to the spin of the electrons via SOC. This implies that different lattice geometries have different angular dependencies of the anisotropy energy [49]. Layered systems with cubic structure (SC, FCC or BCC) and interfaces in the (001) direction (*i.e.* the ones we are concerned with) are

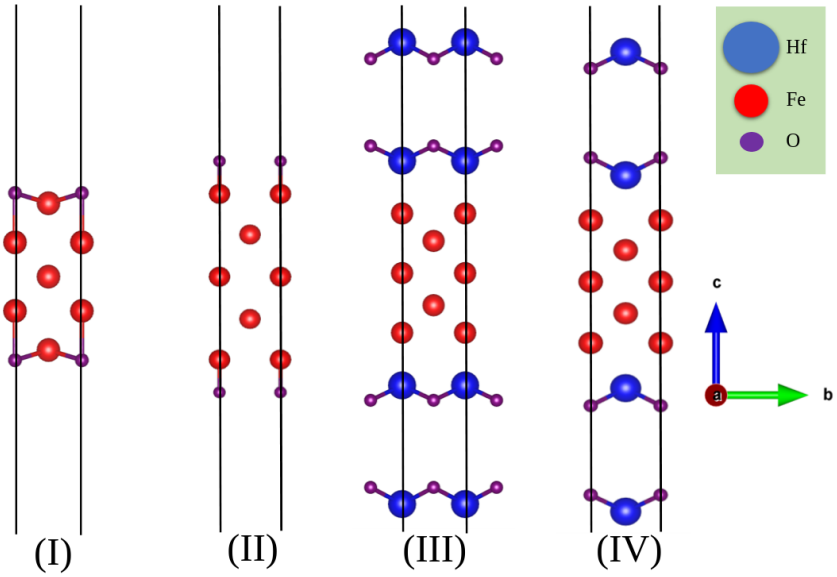

Fig. 6.6 Sketch of the different interfacial configurations. Unit cells (I) and (II) represent Fe/O interfaces while unit cells (III) and (IV) represent the Fe/HfO_2 interfaces.

$E_{(II)}$ - $E_{(I)}$	$E_{(III)}$ - $E_{(IV)}$
6.4 eV/Cell	2.1 eV/Cell

Table 6.1 Total energy difference between the relaxed structures of Fig.6.6

predicted to have the uniaxial relation

$$\Delta E_{SO} = K_0 + K_1 \sin^2 \theta \tag{6.2}$$

where θ is the spin quantization axis angle with respect to the $\hat{z}-$axis and K_0, K_1 represent material dependent constants of anisotropy. An in-plane magnetic anisotropy (IPA) correspond to the minimum of ΔE_{SO} for $\theta = \frac{\pi}{2}$, while perpendicular magnetic anisotropy (PMA) correspond to the minimum of ΔE_{SO} for $\theta = 0$. This is the fitting function that we are going to use in all our MCAE calculations presented in Section 6.2.3. We define our convention for MCAE as follows:

$$MCAE = \Delta E_{SO} = E(\theta = 0) - E(\theta = \pi/2) \tag{6.3}$$

6.2.3 Results

Pure interfaces

As a first step, we perform structural relaxation on 4 different unit cells where we suppose that no interaction with atmospheric oxygen has taken effect (we refer to these as “pure interfaces"). As can be seen by the plotted energies (Fig. 6.6), the optimal oxygen configurations change depending on the system considered: a pure Fe/O interface (structures (I) and (II) of (Fig. 6.6)) favours oxygen atoms to be located in the interstitial site with respect to Fe atoms. This preference appears to be reverted in the case of HfO_2, where a frontal *i.e.* top positioning of oxygen atoms with respect to the Fe atoms seems to be strongly favoured. After having determined the optimal configurations for the different unit cells, we proceed and include spin-orbit coupling to compute their magnetic anisotropy energy. In this case we focus specifically on the Fe/HfO_2 interface. By observing Fig. 6.7 we notice how the more stable frontally aligned oxygen setup, (structure (IV) of (Fig. 6.6)) displays IP magnetic anisotropy (Fig. 6.7-(a)), whereas an interstitial oxygen configuration (structure (III) of (Fig. 6.6)) yields PMA (Fig. 6.7-(d)). At this point, we introduce vertical ionic displacements (with respect to equilibrium configurations) on the interfacial oxygen atoms and recalculate the magnetic anisotropy. For simplicity, in all this analysis the Hf atoms are kept fixed. We notice that, by shifting the frontal oxygen atom in order to reduce the O-Fe distance by $\approx 2\ a_B$, we are able to achieve PMA (Fig. 6.7-(b)). As a side note, we remark how shifting the interstitial oxygen atom of structure (III) in Fig. 6.6 has the effect of recovering IP magnetic anisotropy (Fig. 6.7-(e)).

Mixed Fe/HfO_2 interface

The application of a gate voltage is known to cause the oxidation of the FM surface. We model this effect by designing an Fe/HfO_2 unit cell displaying both interstitial and frontal oxygen alignment at the interface (see Fig. 6.8-(c)). By analyzing the effect on the magnetic anisotropy of different oxygen species mobility, we can get some hints on the microscopic mechanism governing magneto-ionic regimes in an experimental, more disordered scenario.

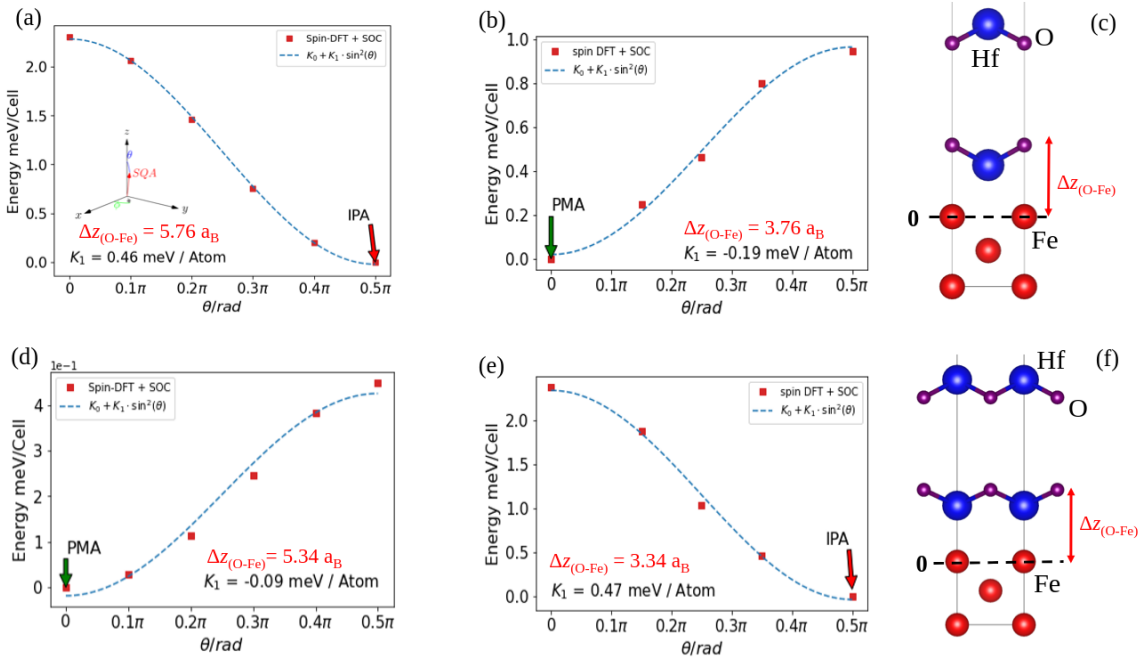

Fig. 6.7 Magneto-crystalline anisotropy energy (MCAE) comparison of the pure Fe/HfO_2 interface (structures (III) and (IV)). The θ angle of the spin quantization axis (SQA) from eq.(6.2) is shown in the inset of (a). (a,b) MCAE for the ground state of the Fe/HfO_2 unit cell with frontal O-Fe distance of (a) $\Delta z_{\text{(O-Fe)}} = 5.76$ a$_B$ (equilibrium) and (b) $\Delta z_{\text{(O-Fe)}} = 3.76$ a$_B$ (shifted). $\Delta z_{\text{(O-Fe)}}$ represents the interplanar distance of the interstitial oxygen species from the Fe surface respectively (marked with the dashed line) (c) Fe/HfO_2 unit cell with frontal oxygen positioning. (d,e) Ground state of the Fe/HfO_2 unit cell with interstitial interplanar O-Fe distance of (d) $\Delta z_{\text{(O-Fe)}} = 5.34$ a$_B$ (equilibrium) and (e) $\Delta z_{\text{(O-Fe)}} = 3.34$ a$_B$ (shifted). (f) Fe/HfO_2 unit cell with interstitial oxygen positioning. The K_1 represents the value of the MCAE and is given by $E(\theta = 0) - E(\theta = \pi/2)$.

As can be seen in Fig. 6.8-(a), the relaxed structure with both frontal and interstitial oxygen displays OOP magnetic anisotropy. If we shift the frontal oxygens (while keeping the interstitial species still) by a nominal distance of 1.16 a$_B$, we notice little effect on magnetic anisotropy (Fig. 6.8-(b) and Fig. 6.9-(a)). If on the other hand, we shift the interstitial oxygen atom 1.96 a_B from the FM surface, we notice how the MCAE becomes sensitive to frontal oxygen shifts and displays switching for a frontal shift of 0.74 a$_B$ (Fig. 6.9-(b)). Despite having checked the effect of oxygen shifts on anisotropy manipulation in this mixed surface setup, we expect the ionic mobility behavior of these two oxygen species to be different given their different environment. By observing Fig. 6.10-(a), we can see that the energy cost of a frontal shift is lower than the energy cost of an interstitial shift, in accordance with our

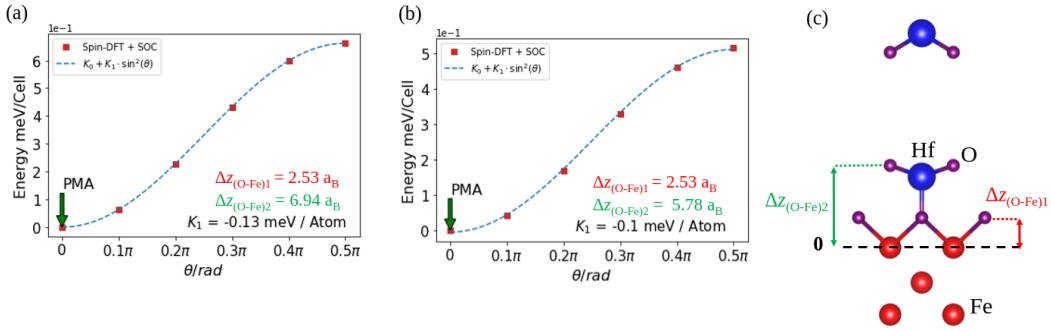

Fig. 6.8 Magneto-crystalline anisotropy energy (MCAE) (θ from eq.(6.2)) in the Fe/HfO_2 setup shown with shifted oxygen species at the interface. (a) MCAE of the mixed surface in its ground state. (b) MCAE of the mixed surface with a frontal O-Fe distance of 5.78 a_B . (c) Side view of the Fe/HfO_2 unit cell with the mixed setup. The $\Delta z_{(\text{O-Fe})1}$ and $\Delta z_{(\text{O-Fe})2}$ denote the interplanar distance of the frontal and interstitial oxygen species from the Fe surface respectively (marked with the dashed line).

expectations. The energy costs are obtained by comparing the energy of identical unit cells that differ only by the position of the frontal/interstitial oxygen atom [167].

We point out how the disruption of PMA can also be obtained by only pushing the interstitial oxygens deeper in the ferromagnetic layer (Fig. 6.10-(c)) [158]. From Fig. 6.10-(c) we can however observe that once PMA is destroyed by this type of oxygen incorporation, it cannot be restored by moving the frontal oxygen atoms closer to the surface. This observation is also in agreement with the experiments [154], where samples that were exposed to a negative gate voltage for long times (for a reference of the field direction, see Fig. 6.11) did not display any reversibility of the voltage induced SRT.

6.2.4 Discussion

Considering the results presented above, we propose the following hypothesis for the appearance of different magneto-ionic regimes in Ta/HfO_2/CoFeB. We once more highlight how we are assuming that the SRT caused by magneto-ionic effects in these systems is largely due to the MCAE changes (i.e. the part of magnetic anisotropy due to spin-orbit coupling [49]). We do not discuss the effects of shape anisotropy in the present study as oxygen migration effects are expected to cause the most significant changes to magnetic anisotropy via the hybridization and SOC

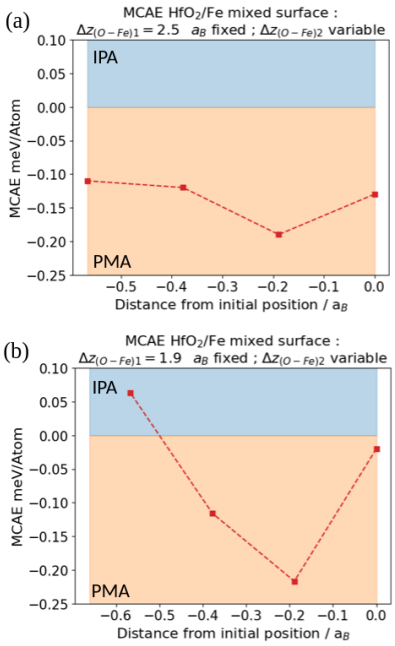

Fig. 6.9 Magneto-crystalline anisotropy energy (MCAE) as a function of the frontal and interstitial oxygen atoms interplanar distance as depicted in Fig.6.8-(c). (a) Effect of frontal oxygen shifts ($\Delta z_{(\text{O-Fe})2}$ variable) while the interstitial oxygen is kept fixed at a distance $\Delta z_{(\text{O-Fe})2} = 2.53\,a_B$ from the FM surface.(b) Effect of frontal oxygen shifts ($\Delta z_{(\text{O-Fe})2}$ variable) while the interstitial oxygen is kept fixed at a distance $\Delta z_{(\text{O-Fe})2} = 1.96\,a_B$ from the FM surface. The initial interplanar distance of the frontal oxygen atoms is $\Delta z_{(\text{O-Fe})2} = 6.94\ a_B$ in both (a) and (b)

effects described in Sec 6.2.2[49]. As can be seen from Fig. 6.7-(a) and Fig. 6.6, the pure Fe/HfO_2 surface with frontally aligned oxygens appears to be both the more stable structure and the one displaying IP magnetic anisotropy (Fig. 6.11-(a)). This is in accordance with the experimental observation, where samples in the as-grown form displayed IP magnetic anisotropy [154]. As observed in [154], the application of a negative gate voltage across Ta/CoFeB/HfO_2 results in an irreversible SRT from IPA to PMA caused by the diffusion of oxygen species towards the CoFeB layer. We model this irreversible switching with the relaxed Fe/HfO_2 surface with both frontal and interstitial oxygens ((Fig. 6.8-(c)).

We hypothesize that in this first regime the frontal oxygen atoms are too far away to contribute to the anisotropy manipulation (Fig. 6.8-(b)). In contrast, the oxygens diffusing towards the surface and occupying the interstitial sites have a strong impact on the anisotropy of the system and induce PMA (Fig. 6.8-(a)). We therefore suggest

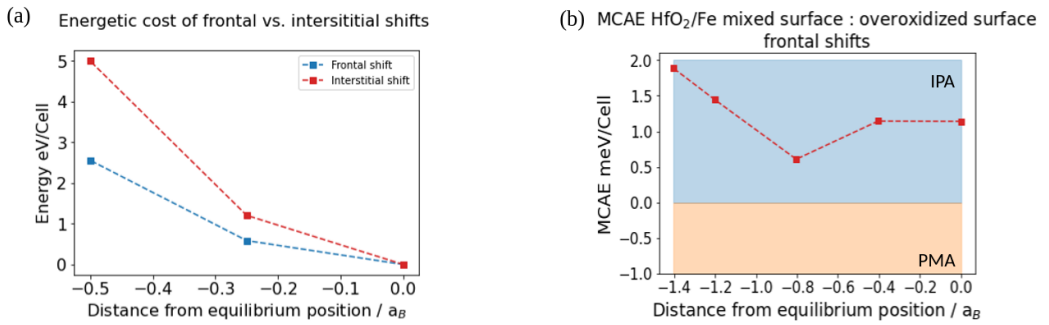

Fig. 6.10 (a) Energetic cost of shifting interstitial and frontal oxygen atoms in the mixed interface setup displayed in panel (c) of Fig. 6.8. The starting positions are $\Delta z_{(\text{O-Fe})1} = 2.53$ a_B for the interstitial oxygen atom and $\Delta z_{(O-Fe)2} = 6.94$ a_B for the frontal oxygen atoms (i.e. the setup of panel (a) in Fig. 6.8) (b) MCAE at different frontal oxygen positions $\Delta z_{(\text{O-Fe})2}$ represented in panel (d) of Fig. 6.8. The starting positions are $\Delta z_{(O-Fe)1} = -0.08$ a_B for the interstitial oxygen atom and $\Delta z_{(\text{O-Fe})2} = 6.94$ a_B for the frontal oxygen atoms (i.e the setup of panel (c) in Fig. 6.8). Positive values on the y-axis indicate that the system has IP magnetic anisotropy.

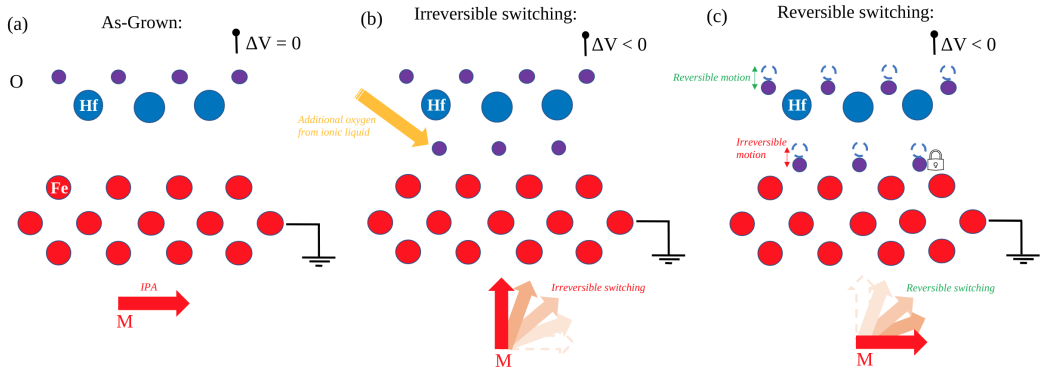

Fig. 6.11 Hypothesis for the mechanism governing the different magneto-ionic regimes in CoFeB/HfO_2 multilayers. (a) Ground state of the system. (b) Irreversible magnetization switching via interstitial sites occupied by migrating oxygen species. (c) Reversible magnetization switching via frontal oxygen shifts. The bottom cartoon in all three panels represents the magnetization direction and the switching process.

that the initial irreversible anisotropy change in Ta/CoFeB/HfO_2 could be due to the irreversible occupation of the interstitial interface sites (Fig. 6.11-(b)). Once PMA is achieved, experimental observation [154] shows that the application of the gate voltage beyond the PMA state has the effect of pushing the magnetic anisotropy easy axis in-plane, albeit in a reversible way.

Our results suggest that this switch to a reversible behavior beyond PMA could be explained by the following: the continued application of the gate voltage has the effect of mobilizing frontal and interstitial oxygen species. As can be seen on Fig. 6.8-(b), the MCAE is not sensitive to the frontal oxygen shifts at first. If on the other hand we shift the interstitial oxygen closer to the Fe surface by $0.57\,a_B$, we notice how the MCAE becomes sensitive to the shift of the frontal oxygen atoms and can be switched (Fig. 6.9-(b)). Furthermore, from Fig.6.10-(a), we know that mobilizing the interstitial oxygen atoms is more difficult than mobilizing the frontal ones: this could be to due the stronger bonding of the interstitial oxygen species with the superficial Fe atoms. This observation suggests that the reversibility of the anisotropy switching beyond the initial PMA could be largely attributed to frontal oxygen shifts (Fig. 6.11-(c)). As shown in Fig. 6.8-(b), the transition PMA $\rightarrow$ IPA can also be achieved by shifting the interstitial oxygens deeper inside the ferromagnetic layer. We do not attribute the reversible manipulation of anisotropy beyond initial PMA to these oxygen species because, once the anisotropy is shifted in-plane by means of the interstitial oxygen species pushed deeper in the sample, it is impossible to manipulate the magnetic anisotropy of the system by shifting the frontal oxygen species closer to the Fe surface (as displayed in Fig. 6.10-(c)).

6.2.5 Conclusion

In this work we performed an ab-initio analysis of the interplay between oxygen ionic mobility and anisotropy manipulation in two FM/Oxide interfaces in order to formulate a hypothesis for the appearance of magneto-ionic regimes in Ta/CoFeB/HfO_2 stacks [154]. We found out that the different nature of the oxide at the interface plays an important role in determining the optimal interfacial oxygen geometry. In particular, we discovered how the pure Fe/HfO_2 interface displays a preferential frontal oxygen alignment which corresponds to an IP magnetic anisotropy. We observed how frontal oxygen mobility can induce PMA [59].

The inclusion of oxygen species in additional interstitial sites was investigated in order to determine their role in the appearance of magneto-ionic regimes [154]. We have shown how in these so called mixed surfaces, the ionic mobility of frontal oxygen species is energetically more favorable than the mobility of interstitial ones. We have also shown how the interplay of mobility between these two different oxygen species can change the magnetic anisotropy of the sample. We conclude that the irreversibility of the transition between IPA (under-oxidised) and PMA (optimally oxidised) could be mainly due to the interaction of the interstitial oxygen of the mixed surface and that the reversibility of the second regime is due to the mobility of the frontal oxygen species of the pure and mixed surface (Fig. 6.11).

We point out how the Ta/CoFeB/HfO_2 multilayer in [154] is composed by amorphous materials that do not display the ordered structure of our unit cells. In spite of this difference, we find qualitative agreement between our results and the ones reported in [154] and are therefore led to believe that anisotropy manipulation in these kinds of systems may be a consequence of relative FM/oxygen positioning localized at the interface.

To further probe the validity of the hypothesis, one could analyze the relative range of magneto-ionic regimes in Ta/CoFeB/HfO_2 samples with different degrees of atmospheric oxygen interaction. We predict that the extreme case where there has been little to no exposure to atmospheric oxygen should result in a purely reversible system. In addition, a comparison between crystalline and policrystalline structures could provide hints on the role played by the amorphous nature of the materials. Understanding in closer detail the interplay between ionic mobility and magnetic property tuning could prove very useful for the optimization of highly energy efficient read/write mechanisms for next-generation memory storage devices.

6.3 Gauge theory applied to magnetic lattices

Micromagnetic exchange is usually derived by performing the continuum limit of the Heisenberg model on a cubic lattice, where the exchange integrals are assumed to be identical for all nearest neighbors. This limitation normally imposes the use of a microscopic theory to explain the appearance of higher order magnetic interactions such as the Dzyaloshinskii-Moriya interaction (DMI). In this paper we combine graph- and gauge field- theory to simultaneously account for the symmetries of the crystal, the effect of spin-orbit coupling and their interplay on a micromagnetic level. We obtain a micromagnetic theory accounting for the crystal symmetry constraints at all orders in exchange and show how to successfully predict the form of micromagnetic DMI in all 32 point groups.

Acknowledgement: The content of this Section is published in "Di Pietro, A., Ansalone, P., Basso, V., Magni, A., Durin, G. (2022). Gauge theory applied to magnetic lattices. In Europhysics Letters (Vol. 140, Issue 4, p. 46003). IOP Publishing. https://doi.org/10.1209/0295-5075/aca0ba". [13]. Please use this paper for citations.

6.3.1 Introduction

The Heisenberg model [168–170] is a low energy limit of the more general Hubbard model [44, 95] and it allows to translate the complexity of quantum mechanical exchange in a geometrical framework where the degrees of freedom are localized magnetic moments. Understanding the Heisenberg model beyond ordinary ferromagnetic/antiferromagnetc exchange is of central scientific relevance as higher order interactions are at the core of most of the exotic physical phenomena that could be harnessed in future spintronics devices [171, 172, 105, 173].

As an example, the Dzyaloshinskii-Moriya interaction (DMI) [67, 68] is known to stabilize skyrmionic/antiskyrmionic structures [71, 70] which hold promise as information carriers in novel spintronic memory devices. At the same time, micromagnetic solvers [14] that can then be employed to simulate the magnetization dynamics on the micro-scale rely on continuum formulations making the generalization of the Heisenberg model and it's higher order extensions to the continuum [94] of central importance. On the microscopic scale the inclusion of higher order

interactions in the Heisenberg model can be done by considering the low energy limit of increasingly complicated multi-band Hubbard models [95]. On a micromagnetic level, the traditional approach relies on phenomenological thermodynamic arguments and spin wave expansions of the micromagnetic energy functional [106, 174, 175], but disregards the underlying Heisenberg model in favor of a pure field theoretical approach. The generalized expression of the micromagnetic energy functional that one finds in the literature is [95, 176, 107]

$$E_{ex}[\mathbf{m}, \nabla\mathbf{m}] = \int_{\Omega_V} \left\{ A \mid \nabla\mathbf{m} \mid^2 + \hat{\boldsymbol{Q}}\mathscr{M}(\boldsymbol{m}) \right\} d^3\boldsymbol{r}, \tag{6.4}$$

where $\hat{\boldsymbol{Q}}\mathscr{M}(\boldsymbol{m}) = \sum_{A,C} \hat{\boldsymbol{Q}}_{AC}\mathscr{M}_{AC}$ constitutes the DMI energy of the system [177] and is represented as the contraction of the DMI tensor $\hat{\boldsymbol{Q}}_{AC}$ and the chirality $\mathscr{M}(\boldsymbol{m}) = \nabla\boldsymbol{m} \times \boldsymbol{m}$ of the material. The above mentioned approaches, while extremely powerful, are phenomenological in nature and neglect the fact that higher order interactions are intimately related lower order ones as they come from the low energy limit of a more general energy functional [67]. A formulation of the continuum limit that rigorously and organically keeps track of the coordination of the magnetic atoms on the lattice and higher order interactions is still missing. In this work we propose an alternative procedure to the continuum limit of the Heisenberg model [178] that employs graph theory to systematically account for lattices of arbitrary point group symmetry and local $SO(3)$ gauge invariance of the micromagnetic energy functional to account for the appearance of higher order interactions [179–181]. The outcome is a continuum limit that naturally represents the exchange interaction energy in the most general form at all orders, both in the bulk and in thin film geometries

$$E_{ex} = \int_{\Omega_V} \left\{ \Xi_{AC}\, \partial^A m^B \partial^C m_B - Q_{Al}\mathscr{M}^{lA} \right\} d^3\boldsymbol{r} \tag{6.5}$$

where Ξ_{AC} is the anisotropic symmetric exchange tensor and Q_{Al} is the DMI tensor. The structure of the paper is as follows: in the first Section, we reformulate the continuum limit of exchange using graph theory and we rewrite exchange in a form that keeps track of the lattice beyond the simple cubic case. In the second Section we require local $SO(3)$ gauge invariance to account for the appearance of the DMI tensor [182]. The Neumann principle of crystallography allows us to derive the non-vanishing components of the anisotropic exchange and micromagnetic DMI for all 32 crystallographic point groups. In the last Section we discuss our result and

validate our predictions by comparing them with the existing literature and several experimental systems. In the Appendix we review the Taylor expansion on discrete lattices and some key concepts of graph theory.

6.3.2 Continuum limit of Heisenberg exchange on arbitrary lattices

We start by writing the Heisenberg exchange interaction in the usual way

$$\mathscr{H} = -\sum_{<i,j>} J_{ij} \boldsymbol{S}_i \cdot \boldsymbol{S}_j \tag{6.6}$$

here $J\left(\boldsymbol{r}_{ij}\right) = J_{ij}$ are the coupling coefficients coming from the exchange integral, a function of the distance $\boldsymbol{r}_{ij}$ from atom i to atom j. We can split the energy sum in the contribution coming from each individual Wigner-Seitz (WS) cell of the lattice labelled R_k (see Fig.6.12-b). The advantages of this decomposition are twofold: firstly, the WS cell construction is based in the Voronoi tassellation [11], i.e. on the location of nearest neighbours. Secondly, the WS cell (a primitive cell) for a given lattice point inherits the full point group symmetry of the lattice by constructions [43]

$$\mathscr{H} = -\sum_{k=1}^{N} \sum_{<\alpha,\beta>\in R_k} J_{\alpha\beta}\, \boldsymbol{S}_\alpha \cdot \boldsymbol{S}_\beta \, \Delta V \tag{6.7}$$

here R_k represents the set of nearest neighbors used for the construction of the k-th WS cell [183, 43]. We define $\mathscr{E}_k$ as the energy density cost due to spin misalignment per WS cell with volume ΔV

$$\mathscr{E}_k = -\sum_{<\alpha,\beta>\in R_k} J_{\alpha\beta}\, \boldsymbol{S}_\alpha \cdot \boldsymbol{S}_\beta \tag{6.8}$$

we assume that $\boldsymbol{s}_\alpha$ and $\boldsymbol{s}_\beta$ are nearly parallel when nearest neighbours and have fixed length $|\boldsymbol{S}|^2 = 1$ (see Fig.6.12-b), allowing us to write the exchange term as

$$\mathscr{E}_k = -\sum_{<\alpha,\beta>\in R_k} J_{\alpha\beta} |\boldsymbol{S}|^2 \cos\theta_{\alpha\beta} \ , \ \theta_{\alpha\beta} \ll 1 \tag{6.9}$$

$$\approx -\sum_{<\alpha,\beta>\in R_k} J_{\alpha\beta}\, \delta^{\alpha\beta} - J_{\alpha\beta} |\boldsymbol{S}_\alpha - \boldsymbol{S}_\beta|^2. \tag{6.10}$$

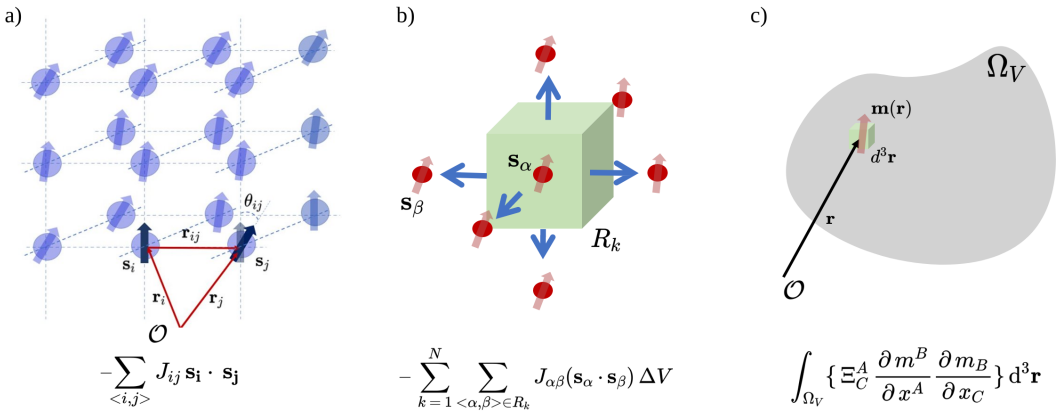

Fig. 6.12 a) Heisenberg model on a cubic lattice. We indicate the lattice sites with indices i, j b) Decomposition of the cubic lattice in nearest neighbour clusters using the Voronoi tassellation [11]. In this decomposed lattice we use the k index to identify the cell and α, β indices to indicate the nearest neighbors. c) Continuum limit performed on the cell from b). The cell index k becomes continuous $d^3\boldsymbol{r}$ and the atomic moments become a continuous function of space $\boldsymbol{m}(\boldsymbol{r})$.

Since we are treating the ferromagnetic case (i.e $J_{\alpha\beta}$ symmetric positive semi-definite) we can rewrite the exchange matrix as $J_{\alpha\beta} = G_{\alpha n}G_{n\beta} = \hat{G}^T\hat{G}$. We neglect the first term of (6.10) as it's simply a constant and we can rewrite the exchange energy as

$$\mathscr{E}_k = \sum_{<\alpha,\beta>\in R_k} G_{\alpha n}G_{n\beta}\,|\boldsymbol{S}_\alpha - \boldsymbol{S}_\beta|^2 \tag{6.11}$$

since for small $\theta_{\alpha\beta} \approx |\boldsymbol{S}_\alpha - \boldsymbol{S}_\beta|$, we assume that $\boldsymbol{s}_i$ can be fitted to a continuous function, i.e. $\boldsymbol{S}_i \to \boldsymbol{m}(\boldsymbol{r} - \boldsymbol{r}_i)$ of position in the lattice. Let us write down the general expression for the Taylor expansion of the magnetization vector field for small $\Delta\boldsymbol{r}$

$$\boldsymbol{m}(\boldsymbol{r}+\Delta\boldsymbol{r}) \approx \boldsymbol{m}(\boldsymbol{r}) + d\boldsymbol{m}(\boldsymbol{r};\Delta\boldsymbol{r}) + \mathscr{O}\left(|\Delta\boldsymbol{r}|^2\right) \tag{6.12}$$

where $d\boldsymbol{m}(\boldsymbol{r};\Delta\boldsymbol{r})$ represents the directional derivative of the vector valued function $\boldsymbol{m}(\boldsymbol{r})$ along the vector $\Delta\boldsymbol{r}$, i.e.

$$dm_i(\boldsymbol{r};\Delta\boldsymbol{r}) = \nabla m_i \cdot \Delta\boldsymbol{r} = \partial_j m_i \Delta r_j. \tag{6.13}$$

We now formally define a nearest-neighbour cluster of atoms as a directed graph - (see Fig.6.13 for an example of the cubic lattice) introducing the edge-node incidence

matrix C_{ij} [184] defined as

$$C_{ij} = \begin{cases} +1 \text{ if edge } l_j \text{ leaves vertex } v_i \\ -1 \text{ if edge } l_j \text{ enters vertex } v_i \\ 0 \text{ otherwise} \end{cases} . \tag{6.14}$$

It can be shown [184] that the incidence matrix of a graph is the natural matrix representation of the discrete differential. Let us now denote the edges of the directed graph representing the lattice as $\boldsymbol{l}^i$ (see Fig.6.13), we can generalize eq. (6.13) to

$$dm_i(\boldsymbol{r};\Delta\boldsymbol{r}) = (\nabla_k m_i) C_{kj} \boldsymbol{l}^j \tag{6.15}$$

and finally write the components of the expansion (6.12) as

$$\boldsymbol{m}(\boldsymbol{r}+\boldsymbol{r}_i) \approx \boldsymbol{m}(\boldsymbol{r}) + C_{i\alpha} \boldsymbol{l}^\alpha \cdot \boldsymbol{\nabla}\boldsymbol{m}(\boldsymbol{r}) \tag{6.16}$$

where $C_{i\alpha}$ represents the incidence matrix of the directed graph describing the nearest neighbor cluster of magnetic atoms (see 6.3.2 for the case of a simple cubic lattice), $\boldsymbol{l}^\alpha = l_A^\alpha \hat{e}^A$ represents the edge vectors of the directed graph and $\boldsymbol{\nabla} = \hat{e}^A \frac{\partial}{\partial x^A}$. With this generalized notation we can write the exchange term of eq.(6.10) as

$$\mathscr{E}(\boldsymbol{r}) = \sum_{<\alpha,\beta>} \left[G_{\alpha n} C_\gamma^\alpha l_A^\gamma \frac{\partial m^B}{\partial x^A} \right] \left[G_{n\beta} C_\beta^\rho l_C^\rho \frac{\partial m_B}{\partial x^C} \right]. \tag{6.17}$$

We remark how by transforming the magnetization in a continuous function of space, we automatically promote the energy per cell to a continuous function of space as well, i.e. $\mathscr{E}_k \to \mathscr{E}(\boldsymbol{r})$. This also applies to the volume R_k of eq.(6.11) which is now promoted to an infinitesimal volume element $d^3\boldsymbol{r}$. We store all the information related to the symmetry of the lattice and the exchange J_{ij} in the (symmetric) anisotropic exchange tensor Ξ^{AC}.

$$\Xi_{AC} := \sum_{<\alpha,\beta>} G_{\alpha n} C_\gamma^\alpha l_A^\gamma G_{n\beta} C_\beta^\rho l_C^\rho. \tag{6.18}$$

The total exchange energy is now obtained by integrating $\mathscr{E}(\boldsymbol{r})$ over the whole volume

$$E_{ex}[\boldsymbol{m}, \nabla\boldsymbol{m}] = \int_{\Omega_V} \Xi_{AC} \frac{\partial m_B}{\partial x^C} \frac{\partial m^B}{\partial x^A} \, \mathrm{d}^3\boldsymbol{r}. \tag{6.19}$$

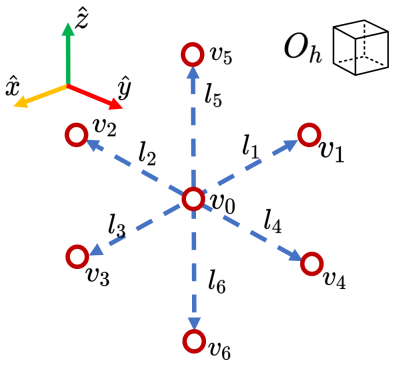

Fig. 6.13 Directed graph representing the nearest neighbors (n.n) on the cubic lattice. The vertices are represented by v_i and the edges by l_i.

In the case of a cubic lattice all the exchange integrals $J_{ij} = J$ are constant and we have $\Xi_{AC} = -2J\delta_{AC}$. We refer to the Supplementary material for the detailed calculation of the simple cubic case and the C_{6v} case.

Exact calculation of Ξ_{AC} for the simple cubic lattice

In the following we provide a step-by-step calculation of the Ξ_{AC} tensor according to the definition

$$\Xi_{AC} := \underbrace{\Big(\sum_i G_{in} C^i_\gamma\Big)}_{\tilde{C}^n_\gamma} (\boldsymbol{l}^\gamma)_A \underbrace{\Big(\sum_j G_{nj} C^\rho_j\Big)}_{\tilde{C}^\rho_n} (\boldsymbol{l}^\rho)_C. \tag{6.20}$$

As a first step we compute the incidence matrix of the oriented graph representing the nearest neighbors of the simple cubic lattice (Fig.6.13).

$$C_{ij} := \hat{C} = \begin{pmatrix} 1 & -1 & 0 & 0 & 0 & 0 & 0 \\ 1 & 0 & -1 & 0 & 0 & 0 & 0 \\ 1 & 0 & 0 & -1 & 0 & 0 & 0 \\ 1 & 0 & 0 & 0 & -1 & 0 & 0 \\ 1 & 0 & 0 & 0 & 0 & -1 & 0 \\ 1 & 0 & 0 & 0 & 0 & 0 & -1 \end{pmatrix}. \tag{6.21}$$

We can write the matrix denoting the edges of the graph $(\boldsymbol{l}^{\gamma})^{A}$ as

$$\hat{R} := (\boldsymbol{l}^{\gamma})_{A} = \begin{pmatrix} 1 & 0 & 0 \\ 0 & 1 & 0 \\ -1 & 0 & 0 \\ 0 & -1 & 0 \\ 0 & 0 & 1 \\ 0 & 0 & -1 \end{pmatrix} \tag{6.22}$$

The $\tilde{C}$ matrix can be interpreted as a weighted directed graph, where the weight on each edge of the graph is determined by the magnitude of the exchange integral J_{ij}. If we assume that the strength of the interaction is a function of the inter-site distance, we have $J_{ij} = J$ and $\tilde{C}$ acquires the simplified form

$$\hat{\tilde{C}} = \omega \cdot \hat{C}\,,\ \omega^{2} = J. \tag{6.23}$$

We can now write the the expression $\tilde{g}^{AC}$ in matrix form

$$\begin{aligned} \Xi_{AC} &:= \underbrace{\Big(\sum_{i} G_{in} C^{i}_{\gamma}\Big)}_{\tilde{C}^{n}_{\gamma}} (\boldsymbol{l}^{\gamma})_{A} \underbrace{\Big(\sum_{j} G_{nj} C^{\rho}_{j}\Big)}_{\tilde{C}^{\rho}_{n}} (\boldsymbol{l}^{\rho})_{C} && (6.24) \\ &= (\boldsymbol{l}_{\rho})_{C} \tilde{C}^{\rho}_{n} \tilde{C}^{n}_{\gamma} (\boldsymbol{l}^{\gamma})_{A} && (6.25) \\ &= J(\hat{R}^{T} \cdot \hat{C} \cdot \hat{C}^{T} \cdot \hat{R}) && (6.26) \end{aligned}$$

with these definitions we can proceed and compute the Ξ_{AC} tensor

$$\Xi_{AC} = -2J\delta_{AC}. \tag{6.27}$$

Effect of the basis choice on the DMI tensor

The choice of the basis can have an effect on the form of the DMI tensor and should therefore be treated carefully. As an example we show the case of C_{6v} symmetry. The edge-node incidence matrix is given by

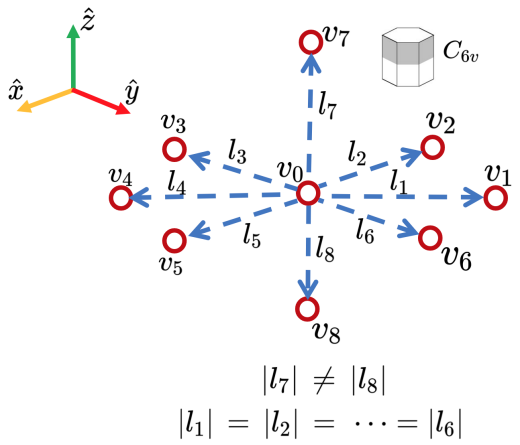

Fig. 6.14 Directed graph representing the nearest neighbors (n.n) on a C_{6v}. The vertices are represented by v_i and the edges by l_i.

$$\hat{C} = \begin{pmatrix} 1 & -1 & 0 & 0 & 0 & 0 & 0 & 0 & 0 \\ 1 & 0 & -1 & 0 & 0 & 0 & 0 & 0 & 0 \\ 1 & 0 & 0 & -1 & 0 & 0 & 0 & 0 & 0 \\ 1 & 0 & 0 & 0 & -1 & 0 & 0 & 0 & 0 \\ 1 & 0 & 0 & 0 & 0 & -1 & 0 & 0 & 0 \\ 1 & 0 & 0 & 0 & 0 & 0 & -1 & 0 & 0 \\ 1 & 0 & 0 & 0 & 0 & 0 & 0 & -1 & 0 \\ 1 & 0 & 0 & 0 & 0 & 0 & 0 & 0 & -1 \end{pmatrix}. \tag{6.28}$$

At this point we can write down the crystal vectors in 2 different bases depicted in Fig.6.15

$$\hat{R}_{\hat{a},\hat{b},\hat{z}} = \begin{pmatrix} 1 & 0 & 0 \\ 0 & 1 & 0 \\ -1 & 1 & 0 \\ -1 & 0 & 0 \\ 0 & -1 & 0 \\ 1 & -1 & 0 \\ 0 & 0 & c \\ 0 & 0 & -\tilde{c} \end{pmatrix} \quad \hat{R}_{\hat{x},\hat{y},\hat{z}} = \begin{pmatrix} 1 & 0 & 0 \\ \frac{1}{2} & \frac{\sqrt{3}}{2} & 0 \\ -\frac{1}{2} & \frac{\sqrt{3}}{2} & 0 \\ -1 & 0 & 0 \\ -\frac{1}{2} & -\frac{\sqrt{3}}{2} & 0 \\ \frac{1}{2} & -\frac{\sqrt{3}}{2} & 0 \\ 0 & 0 & c \\ 0 & 0 & -\tilde{c} \end{pmatrix} \tag{6.29}$$

where c and $\tilde{c}$ represent the distance of nearest neighbors in the $\pm z$ direction. The

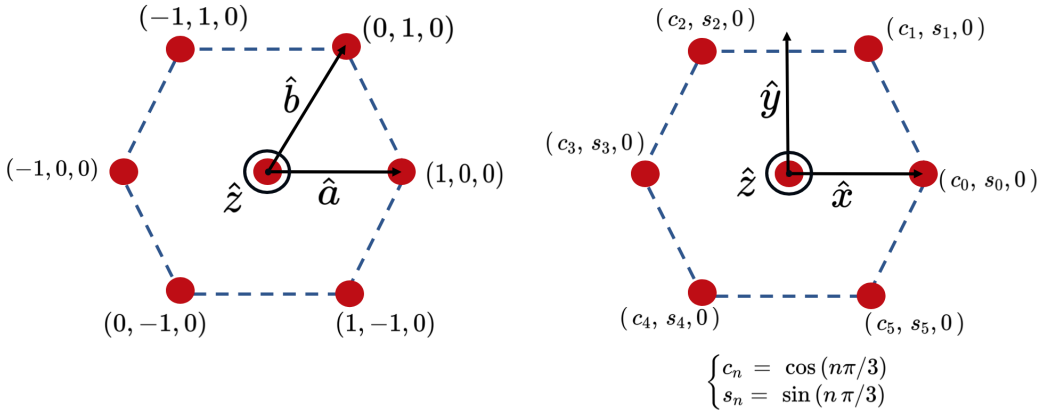

Fig. 6.15 2 different basis choices to represent the lattice vectors in the C_{6v} geometry. We only depict the basis choice in the C_6 plane as along the z-axis the choice is trivial.

different choice of basis yields different Ξ_{AC} tensors

$$\hat{\boldsymbol{\Xi}}_{\hat{a},\hat{b},\hat{z}} = \begin{pmatrix} -4J & 2J & 0 \\ 2J & -4J & 0 \\ 0 & 0 & -2(c-\tilde{c})^2 J \end{pmatrix} \tag{6.30}$$

$$\hat{\boldsymbol{\Xi}}_{\hat{x},\hat{y},\hat{z}} = \begin{pmatrix} -3J & 0 & 0 \\ 0 & -3J & 0 \\ 0 & 0 & -2(c-\tilde{c})^2 J \end{pmatrix}. \tag{6.31}$$

This of course has implications for the shape of the DMI tensor

$$\hat{\boldsymbol{Q}}_{C_{6v},\hat{a},\hat{b},\hat{z}} = \begin{pmatrix} Q_{11} & 2Q_{11} & 0 \\ -2Q_{11} & -Q_{11} & 0 \\ 0 & 0 & 0 \end{pmatrix} \tag{6.32}$$

$$\hat{\boldsymbol{Q}}_{C_{6v},\hat{x},\hat{y},\hat{z}} = \begin{pmatrix} 0 & Q_{12} & 0 \\ -Q_{12} & 0 & 0 \\ 0 & 0 & 0 \end{pmatrix}. \tag{6.33}$$

This discrepancy can be reconciled by recalling the definition of the DMI tensor obtained in the main text of the article, namely

$$Q_{Al} = \Xi_{AC} \partial^C \psi_l \tag{6.34}$$

from which we have

$$(\Xi)^{-1}_{AC} Q_{Al} = \partial^C \psi_l. \tag{6.35}$$

We notice how the two DMI tensor shapes can be connected one to another via

$$\hat{\boldsymbol{\Xi}}^{-1}_{\hat{a},\hat{b},\hat{z}} \hat{\boldsymbol{Q}}_{C_{6v},\hat{a},\hat{b},\hat{z}} = \hat{\boldsymbol{\Xi}}^{-1}_{\hat{x},\hat{y},\hat{z}} \hat{\boldsymbol{Q}}_{C_{6v},\hat{x},\hat{y},\hat{z}} \tag{6.36}$$

To avoid any confusion, we always chose the reference frame and the generators reported in [12].

6.3.3 Gauge covariant derivatives and the DMI tensor

As discussed in [179, 182, 120], the appearance of DMI in a continuum theory of magnetic interactions is a direct consequence of promoting the global $SO(3)$ symmetry of the micromagnetic energy functional to a local symmetry. The requirement of invariance with respect to a local rotation of the magnetic moment requires the inclusion of a non-Abelian Gauge degree of freedom encoded in the modification of the ordinary differential operator $\partial_i := \frac{\partial}{\partial x^i}$. Formally speaking, let $\mathscr{R}(\boldsymbol{x})$ be an element of SO(3) acting on 3-component vectors such as the local magnetization according to $\boldsymbol{m}' = \mathscr{R}(\boldsymbol{x})\boldsymbol{m}$. Enforcing invariance of the exchange energy density of eq.(6.19) requires us to redefine the differential operator via the covariant derivative $\mathscr{D}$ and the gauge field $\mathscr{A}$ in the following way [179]:

$$\partial^i m^j \to \mathscr{D}^i m^j = \partial^i m^j - (\mathscr{A}^i)_k m^l \varepsilon_{kl}{}^j \tag{6.37}$$

$\mathscr{A}_k$ designates the k-th component of the non-Abelian gauge potential that transforms according to the rule

$$\mathscr{A}'_k = \mathscr{R}^T \mathscr{A}_k \mathscr{R} + \mathscr{R}^T \partial_k \mathscr{R} \tag{6.38}$$

where the rotation matrices $\mathscr{R}$ can be represented via

$$\mathscr{R}(\boldsymbol{x}) = \exp(i\phi(\boldsymbol{x})\,\hat{n}\cdot\boldsymbol{J}) \tag{6.39}$$

where $\phi(\boldsymbol{x})$ is a space dependent rotation angle, $\hat{n}$ in a rotation axis and the generators of SO(3) are encoded in a vector $\boldsymbol{J}$ such that $[J_\rho, J_\sigma] = i\varepsilon_{\rho\sigma}{}^{\nu} J_\nu$. If we limit ourselves

to the pure gauge case [182], we can restrict the gauge transformations to

$$\mathscr{A}'_k = \mathscr{R}^T \partial_k \mathscr{R} \tag{6.40}$$

And obtain the gauge covariant derivative of the form:

$$\mathscr{D}^i m^j = \partial^i m^j - \partial^i \psi^l \, m^k \varepsilon_{ljk} \tag{6.41}$$

where ψ_l quantifies the rotation of a vector around the axis $\hat{n}_l$. Inserting this definition in eq.(6.17) yields the following expression for the energy density

$$\mathscr{E}(\boldsymbol{r}) = \sum_{<\alpha,\beta>} \left[G_{\alpha n} C^{\alpha}_{\gamma} l^{\gamma}_{A} \mathscr{D}^A m^B \right] \left[G_{n\beta} C^{\rho}_{\beta} l^{\rho}_{C} \mathscr{D}^C m_B \right] \tag{6.42}$$

and the following expression for the integrated total energy

$$E_{ex}[\boldsymbol{m}, \nabla \boldsymbol{m}] = \int_{\Omega_V} d^3\boldsymbol{r} \, \{ \Xi_{AC} \, \mathscr{D}^A m^B \mathscr{D}^C m_B \} \tag{6.43}$$

$$\begin{aligned} &= \int_{\Omega_V} d^3\boldsymbol{r} \big\{ \, \Xi_{AC} \, \partial^A m^B \partial^C m_B - \\ &- \Xi_{AC} \, \partial^C \psi^l \varepsilon_{lkB} \underbrace{\left[(\partial^A m^B) m^k - m^B (\partial^A m^k) \right]}_{\mathscr{L}^{ABk}} \\ &+ \Xi_{AC} \, \partial^A \psi^l m^k \varepsilon_{lkB} \partial^C \psi^r m^s \varepsilon_{rsB} \big\} \end{aligned} \tag{6.44}$$

where Ξ_{AC} is defined in eq.(6.18). We highlight how $\mathscr{L}_A{}^{Bk}$ represents the usual Lifshitz invariant terms of DMI. We remark how this treatment of micromagnetic interactions also gives rise to a factor of intrinsic anisotropy $\Xi_{AC} \, \partial^A \psi^l m^k \varepsilon_{lkB} \partial^C \psi^r m^s \varepsilon_{rsB}$ which represents an anisotropic term [120] normally neglected in the literature. If we concentrate on terms of order $\mathscr{O}(\nabla \boldsymbol{\psi})$ we can rewrite the exchange in eq.(6.19) as

$$E_{ex} = \int_{\Omega_V} d^3\boldsymbol{r} \big\{ \, \Xi_{AC} \, \partial^A m^B \partial^C m_B - \Gamma^A_{kB} \mathscr{L}_A{}^{Bk} \, \big\} + \mathscr{O}((\nabla \boldsymbol{\psi})^2) \tag{6.45}$$

where we have introduced the compact notation

$$\Gamma^k_{AB} := \Xi_{AC} \, \partial^C \psi^l \varepsilon^k_{lB}. \tag{6.46}$$

We highlight how symmetric anisotropic exchange is contracted in the prefactors Γ^{k}_{AB} of the DMI Lifshitz invariant, showing how the two orders of interactions cannot be treated separately in accordance with the original microscopic treatment of [67]. We can now apply the Neumann principle of crystallography [185] to the Γ^{A}_{kB} prefactors of the Lifshitz invariants in eq.(6.46) to reveal their independent components. Let $\mathscr{R}^{(\alpha)}$ be the 3-dimensional representation of the point group symmetry associated with the crystal system we are considering (α represents the index numbering the generators of the group). The Neumann principle [185] imposes

$$\Gamma^{i}{}_{jk} = \left(\mathscr{R}^{(\alpha)}\right)^{i}_{i'}\left(\mathscr{R}^{(\alpha)}\right)^{j'}_{j}\left(\mathscr{R}^{(\alpha)}\right)^{k'}_{k}\Gamma^{i'}{}_{j'k'}\ ,\ \forall\ \alpha. \tag{6.47}$$

We can now extract the non-vanishing components of the DMI tensor $Q_{Al} := \Xi_{AC}\,\partial^{C}\psi_{l}$ by contracting $\Gamma^{k}{}_{AB}$ with the Levi-Civita tensor $\varepsilon_{l}{}^{Bk}$ and using standard identity $\varepsilon_{ijk}\varepsilon_{ljk} = 2\delta_{il}$ which yields

$$Q_{Al} = -\frac{1}{2}\Gamma^{k}_{AB}\varepsilon_{lk}{}^{B}. \tag{6.48}$$

This formula now allows to systematically predict the shape of the DMI tensor for

Symmetric exchange components $\hat{\boldsymbol{\Xi}}$		
$\left.\begin{matrix}C_1\\C_i\end{matrix}\right\}$ $\begin{pmatrix}\Xi_{11}&\Xi_{12}&\Xi_{13}\\\Xi_{12}&\Xi_{22}&\Xi_{23}\\\Xi_{13}&\Xi_{23}&\Xi_{33}\end{pmatrix}$	$\left.\begin{matrix}D_2\,,C_{2v}\,,D_{2h}\,,\\C_4,\,S_4,\,C_{4h}\,,\\D_4\,,C_{4v}\,,D_{2d}\,,\\D_{4h}\,,C_3\,,S_6,\\D_3\,,C_{3v}\,,D_{3d}\,,\\C_6,\,C_{3h}\,,C_{6h}\,,\\D_6\ \,,C_{6v}\,,D_{3h}\,,\\D_{6h}\end{matrix}\right\}$ $\begin{pmatrix}\Xi_{11}&0&0\\0&\Xi_{11}&0\\0&0&\Xi_{33}\end{pmatrix}$	$\left.\begin{matrix}T\,,T_h\,,\\O\,,T_d\,,\\O_h\end{matrix}\right\}$ $\begin{pmatrix}\Xi_{11}&0&0\\0&\Xi_{11}&0\\0&0&\Xi_{11}\end{pmatrix}$
$\left.\begin{matrix}C_2\\C_s\\C_{2h}\end{matrix}\right\}$ $\begin{pmatrix}\Xi_{11}&\Xi_{12}&0\\\Xi_{12}&\Xi_{11}&0\\0&0&\Xi_{11}\end{pmatrix}$		

Fig. 6.16 Symmetric exchange components $\hat{\boldsymbol{\Xi}}_{ij} := \Xi_{ij}$ from eq.(6.18) as a function of all 32 non-centrosymmetric crystallographic point groups as imposed by the Neumann principle (6.47). The generators are expressed in the basis used in [12].

all 32 crystallographic point groups. Using the generators for the crystallographic point groups contained in [186] we arrive at DMI tensors Q_{Al} of the form shown in Fig.6.17. With this we get the final form of the exchange energy functional of eq.(6.64)

Non-centrosymmetric Point Group PG (= without inversion center)		
Polar non-chiral PG	Non-polar Non-chiral PG	Enantiomorphic PG = Chiral PG
(C_s): $\begin{pmatrix} 0 & 0 & Q_{13} \\ 0 & 0 & Q_{23} \\ Q_{31} & Q_{32} & 0 \end{pmatrix}$	(S_4): $\begin{pmatrix} Q_{11} & Q_{12} & 0 \\ Q_{12} & -Q_{11} & 0 \\ 0 & 0 & 0 \end{pmatrix}$	(C_1): $\begin{pmatrix} Q_{11} & Q_{12} & Q_{13} \\ Q_{21} & Q_{22} & Q_{23} \\ Q_{31} & Q_{32} & Q_{33} \end{pmatrix}$ (D_4) (D_3) $\begin{pmatrix} Q_{11} & 0 & 0 \\ 0 & Q_{11} & 0 \\ 0 & 0 & Q_{33} \end{pmatrix}$
(C_{2v}): $\begin{pmatrix} 0 & Q_{12} & 0 \\ Q_{21} & 0 & 0 \\ 0 & 0 & 0 \end{pmatrix}$	(D_{2d}): $\begin{pmatrix} Q_{11} & 0 & 0 \\ 0 & -Q_{11} & 0 \\ 0 & 0 & 0 \end{pmatrix}$	(C_2): $\begin{pmatrix} Q_{11} & Q_{12} & 0 \\ Q_{21} & Q_{22} & 0 \\ 0 & 0 & Q_{33} \end{pmatrix}$ (C_4) (C_6) (C) $\begin{pmatrix} Q_{11} & Q_{12} & 0 \\ -Q_{12} & Q_{11} & 0 \\ 0 & 0 & Q_{33} \end{pmatrix}$
(C_{3v}) (C_{4v}) (C_{6v}) $\begin{pmatrix} 0 & Q_{12} & 0 \\ -Q_{12} & 0 & 0 \\ 0 & 0 & 0 \end{pmatrix}$	(C_{3h}) (D_{3h}) (T_d) $\begin{pmatrix} 0 & 0 & 0 \\ 0 & 0 & 0 \\ 0 & 0 & 0 \end{pmatrix}$	(D_2): $\begin{pmatrix} Q_{11} & 0 & 0 \\ 0 & Q_{22} & 0 \\ 0 & 0 & Q_{33} \end{pmatrix}$ (O) (D_6) (T) $\begin{pmatrix} Q_{11} & 0 & 0 \\ 0 & Q_{11} & 0 \\ 0 & 0 & Q_{11} \end{pmatrix}$

Fig. 6.17 DMI tensor components $(\hat{\boldsymbol{Q}})_{ij} := Q_{ij}$ from eq.(6.48) as a function of all 21 non-centrosymmetric crystallographic point groups as imposed by the Neumann principle of eq.(6.47). The 11 centrosymmetric point groups have a vanishing DMI tensor and are not shown. The generators are expressed in the basis used in [12].

$$E_{ex} = \int_{\Omega_V} \left\{ \Xi_{AC}\, \partial^A m^B \partial^C m_B - Q_{Al} \mathscr{M}^{lA} \right\} d^3\boldsymbol{r} \tag{6.49}$$

where the chirality is given by $\mathscr{M}^{lA} = \varepsilon^{l}_{kB} \mathscr{L}^{ABk}$. We remark how the Neumann principle can also be applied to the $\hat{\boldsymbol{\Xi}}$ tensor from eq.(6.18)

$$\Xi_{ij} = \left(\mathscr{R}^{(\alpha)}\right)^{i'}_{i} \left(\mathscr{R}^{(\alpha)}\right)^{j'}_{j} \Xi_{i'j'} \tag{6.50}$$

revealing the non vanishing components of symmetric exchange shown in Fig.6.16

6.3.4 DMI tensor decomposition and ground state selection criterion

We now proceed to describe some of the physical consequences of the symmetry properties of the DMI tensor written in the form of eq.(6.48) [182]. First of all we note that the DMI tensor of eq.(6.48), much like any rank-2 tensor, can be decomposed as a sum of symmetric and skew-symmetric components

$$\hat{\boldsymbol{Q}} = \underbrace{\frac{1}{2}(\hat{\boldsymbol{Q}} - \hat{\boldsymbol{Q}}^T)}_{\hat{\boldsymbol{Q}}_A} + \underbrace{\frac{1}{2}(\hat{\boldsymbol{Q}}^T + \hat{\boldsymbol{Q}})}_{\hat{\boldsymbol{Q}}_S}. \tag{6.51}$$

A purely anti-symmetric DMI tensor yields Lifshitz invariant terms of the form

$$\mathscr{E}_{A;DMI} = -2\boldsymbol{D} \cdot [\boldsymbol{m}(\nabla \cdot \boldsymbol{m}) - (\nabla \cdot \boldsymbol{m})\boldsymbol{m}] \tag{6.52}$$

where one expresses the anti-symmetric tensor as $(Q_A)_{ij} = D_k \varepsilon_{kij}$. This term corresponds to the continuum limit of the familiar microscopic interfacial DMI term [71, 81]

$$\mathscr{H}_{DMI} = \sum_{<i,j>} \boldsymbol{D}_{ij} \cdot (\boldsymbol{s}_i \times \boldsymbol{s}_j) \tag{6.53}$$

where $\boldsymbol{s}_i$ represents a magnetic moment located at lattice site i and $\boldsymbol{D}_{ij}$ is the DMI contribution to the Heisenberg Hamiltonian. Lifshitz invariant terms of the form eq.(6.52) correspond to the surface DMI term appearing in magnetic thin films [10]. The symmetric component of the DMI tensor yields an energy contribution of the form

$$\mathscr{E}_{S;DMI} = -\boldsymbol{m} \cdot (\hat{\boldsymbol{Q}}_S \nabla \times \boldsymbol{m}) \tag{6.54}$$

Where $\hat{\boldsymbol{Q}}_S \nabla = (Q_S)_{ij} \partial_j$. The special case of a purely diagonal matrix yields an energy term of the form

$$\mathscr{E}_{S;DMI} = -2(Q_S)_{ii} (\boldsymbol{m} \cdot \partial_i \boldsymbol{m})_i \tag{6.55}$$

which, in the case of a single independent component $Q_{ii} = D \; \forall \; i$ yields

$$\mathscr{E}_{S;DMI} = -2D\, \boldsymbol{m} \cdot (\nabla \times \boldsymbol{m}). \tag{6.56}$$

This energy contribution corresponds to a bulk DMI term responsible for stabilizing bulk chiral structures [177, 70, 182]. As discussed in [177], the shape of the DMI tensor is a decisive factor in determining the appearance of skyrmionic or antiskyrmionic structures in the ground state of magnetic materials. The main result of [177] is the identification of the determinant of the DMI tensor as the relevant quantity predicting the stability of skyrmions or anti-skyrmions as follows:

$$\det(\hat{\boldsymbol{Q}}) \begin{cases} < 0 & \text{Anti-skyrmions stabilized} \\ > 0 & \text{Skyrmions stabilized} \\ = 0 & \text{Coexistence} \end{cases} . \tag{6.57}$$

We can now apply this rule to the set of DMI tensors shown in Fig.6.17 and discuss if the predicted ground state structure are compatible with experimental results discussed in the literature.

6.3.5 Discussion

The structure of eq.(6.48) automatically implies that all centrosymmetric crystallographic point groups exclude the possibility to have DMI. Furthermore, we notice how the above discussed method also correctly predicts the absence of DMI on some non-centrosymmetric crystal systems such as T_d, C_{3h}, D_{3h} which is in accordance with the literature [176]. We can now proceed and discuss an example of a non vanishing DMI tensor: MnSi is a magnetic material which has attracted a lot of attention as it is one of the first materials in which the the presence of helical magnetic order was detected. As known from the literature, at low temperatures MnSi can be modelled using the extended classical Heisenberg model [187] and the system is known to crystallize in a B20 structure [188]. If we isolate the magnetic atoms of this material, i.e. the Mn atoms, the resulting sublattice displays T point group symmetry [104]. From Fig.6.17. we can see how the T point group symmetry allows the material to have a purely diagonal DMI tensor which can be linked to the presence of bulk DMI, a form compatible with the appearance of bulk chiral magnetism [70, 182, 188].

$$\hat{\boldsymbol{Q}}_T = \begin{pmatrix} Q_{11} & 0 & 0 \\ 0 & Q_{11} & 0 \\ 0 & 0 & Q_{11} \end{pmatrix} \tag{6.58}$$

$$\Rightarrow \mathscr{E}_{S;DMI} = -2Q_{11}\,\boldsymbol{m}\cdot(\nabla\times\boldsymbol{m}). \tag{6.59}$$

If we want to consider only thin film geometries in which the growth direction lies parallel to the $\hat{z}$-axis, we simply have to consider the top left submatrix

$$\hat{\boldsymbol{Q}}_T[1,2;1,2] = \begin{pmatrix} Q_{11} & 0 \\ 0 & Q_{11} \end{pmatrix} \tag{6.60}$$

and the determinant of this submatrix is strictly positive. Recalling the selection criterion of eq.(6.57) [177], we know that a strictly positive determinant of the DMI tensor stabilizes skyrmions given the presence of a sufficiently high external Field

[104]. Further examples of applicability of the present formalism concern Heusler Alloys [189–191]. Despite the full Heusler structure displaying cubic symmetry (and therefore no DMI), recent studies have shown how altering the Mn concentration in inverse tetragonal Mn-based Heusler compounds such as Mn_xPtSn can lower the symmetry of the material as much as reaching D_{2d} [192] in thin film geometries. Observing the DMI tensor of the D_{2d} symmetry group from Fig.6.17, we notice it has a symmetric trace less form:

$$\hat{\boldsymbol{Q}}_{D_{2d}} = \begin{pmatrix} 0 & Q_{12} & 0 \\ Q_{12} & 0 & 0 \\ 0 & 0 & 0 \end{pmatrix}. \tag{6.61}$$

Much like in the case of MnSi, restricting the DMI tensor to a thin film geometry in which the growth direction lies parallel to the $\hat{z}$-axis yields

$$\hat{\boldsymbol{Q}}_{D_{2d}}[1,2;1,2] = \begin{pmatrix} 0 & Q_{12} \\ Q_{12} & 0 \end{pmatrix}. \tag{6.62}$$

We immediately notice how $\det(\hat{\boldsymbol{Q}}_{D_{2d}}[1,2;1,2]) = -Q_{12}^2 < 0$. Again, according to eq.(6.57) this DMI tensor can only stabilize antiskyrmions (given a sufficiently high external field). It has in fact been experimentally shown that Mn_xPtSn thin films can only support anti-skyrmions structures [190]. As a final case of interest, we consider heavy metal/ferromagnet (HM/FM) multilayers such as Pt(111)/Co which have been under intense scientific investigation for the development of energy efficient magnetic memory storage devices [81, 193]. In such systems, one of the effects of the inclusion/exclusion of the Pt layer is that of reducing the point group symmetry of the Co layer from D_{6h} to C_{3v} which, in terms of DMI tensors from Fig.6.17 means

$$\hat{\boldsymbol{Q}}_{D_{6h}} = \begin{pmatrix} 0 & 0 & 0 \\ 0 & 0 & 0 \\ 0 & 0 & 0 \end{pmatrix} \rightarrow \hat{\boldsymbol{Q}}_{C_{6v}} = \begin{pmatrix} 0 & Q_{12} & 0 \\ -Q_{12} & 0 & 0 \\ 0 & 0 & 0 \end{pmatrix}. \tag{6.63}$$

This immediately highlights how the broken inversion symmetry can cause the emergence of DMI interaction at Pt/Co(111) interfaces. At the same time, we notice how $\det(\hat{\boldsymbol{Q}}_{C_{6v}}) > 0$ and therefore only skyrmions can be stabilized in systems displaying this symmetry [81]. As an aside, we also remark how the applications of strain

gradients [194] and electric fields [180] to materials displaying chiral interactions can alter the properties of the DMI tensor. In particular, strong electric fields can lead to the change of the antisymmetric components of the DMI tensor [179] and could therefore constitute a way to manipulate skyrmions and antiskyrmions in an energy efficient way.

6.3.6 Conclusions

In this work we presented a new perspective on the continuum limit of the classical Heisenberg model to derive the micromagnetic exchange energy functional. Our approach systematically keeps track of the crystal symmetries of the system and reveals the importance of the interplay between symmetric anisotropic exchange and DMI. We show a rigorous treatment of higher order interactions when promoting the symmetry of the Hamiltonian from global to local via the introduction of gauge covariant derivatives [179, 182]. As an example, we show how the symmetry constraints imposed by the lattice can be implemented rigorously via the Neumann principle of crystallography, revealing the independent components of the DMI tensor for all 32 crystallographic point groups. We point out how the determinant of the DMI tensor can be used as a tool to predict the stabilization of skyrmions and antiskyrmions [177] and we observe how several experimental results behave in accordance with our theoretical predictions.

6.4 Domain wall statics and dynamics in the presence of arbitrary Dzyaloshinskii-Moriya interaction tensors

The influence of different Dzyaloshinskii-Moriya interaction (DMI) tensor components on the static and dynamic properties of domain walls (DWs) in magnetic nanowires is investigated using one dimensional collective coordinates models and micromagnetic simulations. It is shown how the different contributions of the DMI can be compactly treated by separating the symmetric traceless, antisymmetric and diagonal components of the DMI tensor. First, we investigate the effect of all different DMI components on the static DW tilting in the presence and absence of in plane (IP) fields. We discuss the possibilities and limitations of this measurement approach for arbitrary DMI tensors. Secondly, the interplay of different DMI tensor components and their effect on the field driven dynamics of the DWs are studied and reveal a non-trivial effect of the Walker breakdown field of the material. It is shown how DMI tensors combining diagonal and off-diagonal elements can lead to a non-linear enhancement of the Walker field, in contrast with the linear enhancement obtainable in the usual cases (interface DMI or bulk DMI).

Acknowledgement: The content of this Section is published in A. Di Pietro, F. García-Sánchez, and G. Durin, "Domain wall statics and dynamics in nanowires with arbitrary Dzyaloshinskii-Moriya tensors," Phys. Rev. B, vol. 108, no. 17, p. 174427, Nov. 2023, doi: 10.1103/PhysRevB.108.174427. [145]. Please use this paper for citations.

Recent years have seen an increased interest in the study of magnetic domain wall (DW) dynamics in perpendicularly magnetized nanowires as these are at the core of many emerging spintronic device concepts in memory storage [117, 116], sensing [195, 196] and logic [197–199]. To this day, many challenges still need to be addressed in order to make such technologies viable for the industry. Among the challenges to be faced is the phenomenon of Walker breakdown [200] field which sets a strong upper limit to the velocity a DW can be efficiently moved through a nanowire.

It is a well established fact that magnetic DWs can be moved through a magnetic nanowire either via applied magnetic fields or spin transfer torque induced by spin polarized currents [201, 112]. For small enough values of the driving force, the shape anisotropy of the material (which in thin film geometries favours Bloch walls) is able to counter act the torque on the magnetization that would cause precessional motion [202]. In the steady state regime, the DW is able to move rigidly and its peak velocity displays a linear dependence from the driving force. As the driving force increases, the competing torque becomes too strong and cannot be compensated by the effective field inside the DW: once that threshold, called Walker Breakdown (WB) field, is reached, the domain wall begins the so called precessional motion regime [10, 202], in which the peak velocity of the DW drastically reduces.

Several strategies have been tried to counteract this phenomenon and increase the maximum attainable DW velocity [115, 203]. For instance, the choice of materials displaying chiral interactions such as the Dzyaloshinskii-Moriya interaction (DMI) [67, 68] in perpendicularly magnetized nanowires is known to greatly enhance the domain wall Walker breakdown [10] because of the effective field component providing an additional restoring torque for the moving DW. While the effects of interface DMI (iDMI) are well known and understood, the effects of different, more exotic types of DMI [97, 107, 204] found in lower symmetry magnetic crystals are, to our knowledge, not studied in detail. The study of the possible effects induced by these additional DMI forms is becoming increasingly relevant as new deposition techniques are making the production of thin films with the required low symmetries a reality [205, 192, 206]. In the following we propose a micromagnetic study to analyze the DW statics and dynamics with additional terms accounting for arbitrary DMI tensors in magnetic nanowires.

The paper is organized as follows: in Section 6.4.1 we describe the energy contributions of our system and show how to compactly treat more exotic DMI tensors by decomposing them in antisymmetric, symmetric traceless and diagonal contributions. In Section 6.4.2, we introduce the collective coordinate models (CCMs) and derive the DW energy density for arbitrary DMI tensors both in the $q-\chi-\phi$ model [9] and the $q-\phi$ model [207, 10]. In Sections 6.4.3 and 6.4.4 we show how the derived energy densities correctly predict the DW tilting both with an without applied in-plane (IP) fields. In Section 6.4.5, we explore the applicability of the canting angle method to measure forms of the DM tensor going beyond the iDMI discussed in ref.[9]. Finally, in Section 6.4.6 we derive the dynamical

equations for the DW in the $q-\phi$ model and show how the presence of certain combinations of DMI tensor components can lead to non-trivial changes in the DW Walker breakdown field. The derived analytical results are compared throughout with Micromagnetic simulations performed with the MuMax3 [14] software. We conclude by summarizing our results and providing an outlook for future investigations in Section 6.4.7.

6.4.1 Energy density in the presence of arbitrary DMI tensors

We consider a magnetic ultrathin film of volume Ω_V grown on a substrate and a capping layer of a different material so that the symmetry is broken along the normal to the plane. In addition to the usual energy terms, we add a contribution relative to an arbitrary DMI tensor yielding a total density of the form [177, 13]

$$E = \int_{\Omega_V} \Big\{ A|\boldsymbol{\nabla m}|^2 - Q_{ij}\mathscr{M}^{ji} - \frac{1}{2}\mu_0 M_s \boldsymbol{m}\cdot\boldsymbol{H}_d \\ -K_u(\boldsymbol{m}\cdot\hat{\boldsymbol{u}}_z)^2 - \mu_0 M_s \boldsymbol{m}\cdot\boldsymbol{H}_z \Big\} d^3\boldsymbol{r} \tag{6.64}$$

where $\boldsymbol{m}(x,t) = \boldsymbol{M}(x,t)/M_s$ is the normalized magnetization vector, A is the symmetric exchange coefficient (in this case a constant), $\boldsymbol{H}_d$ is the magnetostatic field, $\boldsymbol{H}_z$ is the Zeeman field and K_u is the uniaxial anisotropy constant with the easy axis directed along z. Finally, Q_{ij} represents the DMI tensor and $\mathscr{M}_{ji} = \sum_k \varepsilon_{ik}(m_z\partial_j m_k - m_k\partial_j m_z)$ is the chirality of the magnetic configuration [177]. We remark how both the chirality $\mathscr{M}_{ji}$ and the DMI tensor Q_{ij} treated here are already restricted to a 2 dimensional system, i.e. $\mathscr{M}_{ji}, Q_{ij} \in \mathbb{R}^{2\times 2}$ and are reported in Fig.6.18.

In the following we briefly outline some of the consequences of the symmetry properties of the DMI tensor. First of all, we remark that the DMI tensor, much like any other rank-2 tensor, can be decomposed in a sum of symmetric traceless, antisymmetric and diagonal components as follows

$$\hat{\boldsymbol{Q}} = \underbrace{\begin{pmatrix} 0 & D_a \\ -D_a & 0 \end{pmatrix}}_{\text{Antisymmetric}} + \underbrace{\begin{pmatrix} D_b & D_s \\ D_s & -D_b \end{pmatrix}}_{\text{Symmetric-traceless}} + \underbrace{\begin{pmatrix} D_t & 0 \\ 0 & D_t \end{pmatrix}}_{\text{Diagonal}}. \tag{6.65}$$

A purely anti-symmetric DMI tensor $(Q_A)_{ij} = \sum_k D_k \varepsilon_{kij}$ yields Lifshitz invariant energy density terms of the form

$$\mathscr{E}_{A;DMI} = -2\boldsymbol{D} \cdot [\boldsymbol{m}(\nabla \cdot \boldsymbol{m}) - (\nabla \cdot \boldsymbol{m})\boldsymbol{m}], \tag{6.66}$$

which correspond to the interface DMI (iDMI) term often studied in the literature [10, 90]. The symmetric component of the DMI tensor, on the other hand, yields an energy contribution of the form

$$\mathscr{E}_{S;DMI} = -\boldsymbol{m} \cdot (\hat{\boldsymbol{Q}}_S \nabla \times \boldsymbol{m}), \tag{6.67}$$

where $\hat{\boldsymbol{Q}}_S \nabla = \sum_j (Q_S)_{ij} \partial_j$. A DMI of this form is related to the so called "anisotropic DMI" in the discrete microscopic treatment [208–210]. The special case of a purely diagonal matrix yields an energy term of the form

$$\mathscr{E}_{S;DMI} = -2(Q_S)_{ii}(\boldsymbol{m} \cdot \partial_i \boldsymbol{m})_i \tag{6.68}$$

which, in the case of a single independent component $Q_{ii} = D$ yields

$$\mathscr{E}_{S;DMI} = -2D\,\boldsymbol{m} \cdot (\nabla \times \boldsymbol{m}). \tag{6.69}$$

This energy contribution corresponds to a bulk DMI (bDMI) term responsible for stabilizing bulk chiral structures [70]. We emphasize that, since the micromagnetic DMI tensor is related to the microscopic DMI vector via the following expression [177]

$$Q_{ij} = \frac{1}{V} \sum_{\boldsymbol{r}_b \in N.N\, \boldsymbol{r}_a} \left[\boldsymbol{r}_a - \boldsymbol{r}_b\right]_i D_{ab,j}, \tag{6.70}$$

where Q_{ij} corresponds to the micromagnetic DMI tensor and $D_{ab,j}$ represents the j-th component of the microscopic DMI vector on bond $a-b$, V represents the volume of the unit cell and the sum runs over all nearest neighbors of the reference atom a. As can be seen, even though $\boldsymbol{D}_{ab}$ comes from the antisymmetric components of the exchange tensor $\overset{\leftrightarrow}{J}_{ab}$ in

$$\mathscr{H} = \sum_{<i,j>} \boldsymbol{S}_i \overset{\leftrightarrow}{J}_{ij} \boldsymbol{S}_j, \tag{6.71}$$

the corresponding micromagnetic DMI tensor $\hat{\boldsymbol{Q}}$ is not constrained to being antisymmetric.

Non-centrosymmetric Point Groups PG (without inversion center)		
Polar non-chiral PG	Non-polar, non-chiral PG	Enantiomorphic PG = Chiral PG
$C_s : \begin{pmatrix} 0 & 0 \\ 0 & 0 \end{pmatrix}$	$S_4 : \begin{pmatrix} D_b & D_s \\ D_s & -D_b \end{pmatrix}$	$\left.\begin{matrix} C_1 \\ C_2 \end{matrix}\right\} \begin{pmatrix} D_{11} & D_{12} \\ D_{21} & D_{22} \end{pmatrix}$ $D_2 : \begin{pmatrix} D_{11} & 0 \\ 0 & D_{22} \end{pmatrix}$
$C_{2v} : \begin{pmatrix} 0 & D_{12} \\ D_{21} & 0 \end{pmatrix}$	$D_{2d} : \begin{pmatrix} D_b & 0 \\ 0 & -D_b \end{pmatrix}$	$\left.\begin{matrix} D_4 \\ D_3 \\ D_6 \\ O \\ T \end{matrix}\right\} \begin{pmatrix} D_t & 0 \\ 0 & D_t \end{pmatrix}$ $\left.\begin{matrix} C_4 \\ C_6 \\ C \end{matrix}\right\} \begin{pmatrix} D_t & D_a \\ -D_a & D_t \end{pmatrix}$
$\left.\begin{matrix} C_{3v} \\ C_{4v} \\ C_{6v} \end{matrix}\right\} \begin{pmatrix} 0 & D_a \\ -D_a & 0 \end{pmatrix}$	$\left.\begin{matrix} C_{3h} \\ D_{3h} \\ T_d \end{matrix}\right\} \begin{pmatrix} 0 & 0 \\ 0 & 0 \end{pmatrix}$	

Fig. 6.18 DMI tensor components for all 21 non-centrosymmetric crystallographic point groups as imposed by the Neumann principle [13]. The 11 centrosymmetric point groups have a vanishing DMI tensor and are not shown. The components D_a, D_s, D_b, D_t are the ones shown in the decomposition of eq.(6.65), while terms of the form D_{ij} are combinations of D_a, D_s, D_b, D_t.

6.4.2 Collective coordinate models with arbitrary DMI

Since the contributions of the iDMI terms (i.e. the D_a part of eq.(6.65)) and bDMI (i.e. the D_t part of eq.(6.65)) to ordinary collective coordinate models (CCMs) are known [9, 119], to account for the complete DMI tensor we just have to compute the energy density terms relative to the symmetric D_s and traceless D_b components. To this end, we consider a DMI tensor compatible with the S_4 point group symmetry which has the form

$$\hat{\boldsymbol{Q}}_{S_4} = \begin{pmatrix} D_b & D_s \\ D_s & -D_b \end{pmatrix}. \tag{6.72}$$

Plugging this DMI tensor in eq.(6.64) and writing the magnetization in spherical coordinates $\boldsymbol{m} = \boldsymbol{M}/M_s = \big(\sin\theta\cos\varphi, \sin\theta\sin\varphi, \cos\theta\big)^T$ we can write the S_4 DMI energy density as follows

$$\begin{aligned} \mathscr{E}_{DMI,S_4} = D_b(\sin\varphi\ \partial_x\theta + \cos\varphi\ \partial_y\theta) + \\ D_s(\sin\varphi\ \partial_y\theta - \cos\varphi\ \partial_x\theta). \end{aligned} \tag{6.73}$$

To derive the CCM we must now substitute θ and ϕ with the Ansatz for the tilted DW [9]

$$\tan\left(\frac{\theta(q,\chi)}{2}\right) = \exp\left(P\frac{(x-q)\cos\chi + y\sin\chi}{\Delta}\right) \tag{6.74}$$

$$\varphi(t) = \phi(t), \tag{6.75}$$

where q represents the DW position along the x-axis, χ represents the DW tilting angle, Δ the DW width and $P = \pm 1$ represents the sense of rotation of angle θ (i.e. $P = \pm 1 \Rightarrow m_z(-\infty) = \pm 1$ and $m_z(+\infty) = \mp 1$). For a schematic of the system and the angles, refer to Fig.6.19-(a). Noticing that the Ansatz of eq.(6.74) allows us to compactly compute the derivatives of eq.(6.73) as

$$\partial_x\theta = P\frac{\sin\theta\cos\chi}{\Delta} \tag{6.76}$$

$$\partial_y\theta = P\frac{\sin\theta\sin\chi}{\Delta} \tag{6.77}$$

we can write the energy density $\mathscr{E}_{DMI,S_4}$ of eq.(6.73) as

$$\mathscr{E}_{DMI,S_4} = P\frac{\sin\theta}{\Delta}\left[D_b\sin(\phi+\chi) - D_s\cos(\phi+\chi)\right]. \tag{6.78}$$

To obtain the DW surface energy, we integrate out the x-degree of freedom of eq.(6.78)

$$\begin{aligned}\sigma_{DW,S_4} &= \int_{-\infty}^{+\infty}\mathscr{E}_{DMI,S_4}\,\mathrm{d}x \\ &= \pi P\left[D_b\sin(\phi+\chi) - D_s\cos(\phi+\chi)\right].\end{aligned} \tag{6.79}$$

We can now add this DW energy component to the other energy terms already used in [9] to obtain a generalized DW energy density as a function of all the DMI tensor components

$$\begin{aligned}\sigma_{DW}(\phi,\chi) =& 2\frac{A}{\Delta} + \pi P\left[D_a\cos(\phi-\chi) - D_s\cos(\phi+\chi) - D_t\sin(\phi-\chi) + D_b\sin(\phi+\chi)\right] + \\ & 2\Delta(K_0 + K\sin^2(\phi-\chi)) - \pi\Delta M_s(H_y\sin\phi + H_x\cos\phi),\end{aligned} \tag{6.80}$$

with $K_0 = K_u + \frac{M_s \mu_0}{2}(N_x - N_z)$ and $K = \frac{M_s \mu_0}{2}(N_y - N_x)$ being the effective and shape anisotropy constants, respectively. N_x, N_y, N_z are the demagnetizing factors which depend on the geometry of the sample [211, 100]. If the phenomenon of DW tilting is not to be considered, the properties of the DW can be studied by considering the more simple $q - \phi$ model [207, 10] which can be obtained by setting $\chi = H_x = H_y = 0$ in eq.(6.80),

$$\sigma_{DW}(\phi) = 2\frac{A}{\Delta} + \pi P\left[(D_a - D_s)\cos(\phi) + (D_b - D_t)\sin(\phi)\right] + 2\Delta(K_0 + K\sin^2(\phi)) \tag{6.81}$$

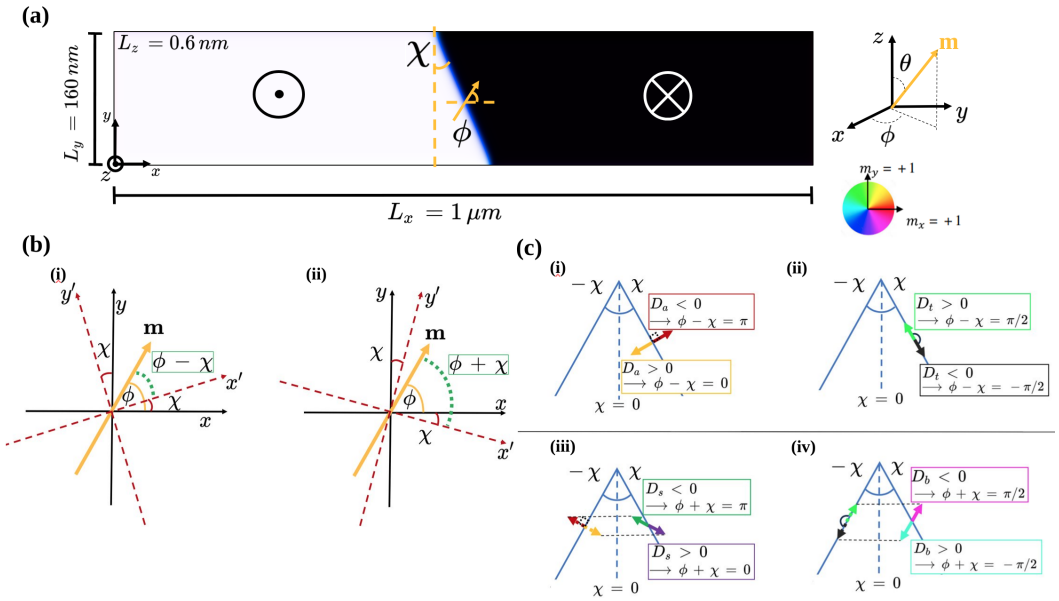

Fig. 6.19 (a) Scheme of the system used in the micromagnetic simulations. We show the dimensions $L_x = 1\ \mu$m , $L_y = 160$ nm and $L_z = 0.6$ nm as well as the internal DW angle ϕ and the DW tilt angle χ. (b) ϕ and χ angles in the case of $\chi > 0$ (i.) ϕ and χ angles in the case of $\chi > 0$ (ii.) (c) Schematic representation of the internal DW angle (the colored arrows in the middle of the domain wall indicate the orientation of the magnetization in the $x - y$ plane) stabilized by the presence of the different DMI tensor components of eq.(6.80) in the presence of an applied IP field

6.4.3 In plane field driven DW titling in the presence of arbitrary DMI tensors

It is a well established fact, that the presence of iDMI induces a tilt in the DW profile [9, 212] under the application of an external in-plane (IP) transverse field. The origin of this phenomenon is explained by considering the relative energy balance of the DW in presence of chiral interactions and Zeeman fields. In the absence of applied IP fields, the DW reaches an internal equilibrium angle dictated by the relative strength of DMI and demagnetizing contributions.

If we apply an external IP field along the positive y-direction, the DW magnetization is going to feel the added competing interaction requiring it to align along the direction of the external field. At the same time, the iDMI produces an effective field component that stabilizes Néel walls. To try and accommodate both torques, the DW tilts by an angle χ increasing the DW energy by a factor $1/\cos\chi$. In the following we try and extend what is known about DW tilting in the presence of iDMI to the case of arbitrary DMI tensors (see Fig.6.18). As a first step, we analyze the new DMI energy terms of the $\chi = 0$ case

$$\sigma_{DMI} = \pi\big[(D_a - D_s)\cos(\phi) + (D_b - D_t)\sin(\phi)\big] \tag{6.82}$$

and of the $\chi \neq 0$ case

$$\begin{aligned}\sigma_{DMI} = \pi\big[&D_a\cos(\phi-\chi) - D_s\cos(\phi+\chi)\\ &-D_t\sin(\phi-\chi) + D_b\sin(\phi+\chi)\big],\end{aligned} \tag{6.83}$$

where we have set $P = 1$ for convenience. In the untilted case $\chi = 0$, eq.(6.82) suggests that the different DMI tensor components all simply induce either Néel or Bloch wall stabilizing effective fields, however this intuitive picture is only valid as long as no tilting is observable. If tilting is present (eq.(6.83)) in the system, we need to take in account the fact that the D_s and D_b components minimize the energy of the DW as a function of $\phi + \chi$ as opposed to $\phi - \chi$.

As a first step to understand the implications of this difference, we discuss the equilibrium angles stabilized by all the different DMI tensor components of eq.(6.80). The values of the physical parameters used in the micromagnetic simulation for the statics and dynamics of the DW represent the values measured in

Pt/Co/AlOx nanowires [90]. We set the exchange constant $A = 10^{-11}$J/m, the saturation magnetization $M_s = 1.09$ MA/m, the effective anisotropy constant $K_0 = 1.25$ MJ/m^3, the damping coefficient $\alpha = 0.5$. The chosen nanowire dimensions are $L_x = 1$ μm , $L_y = 160$ nm and $L_z = 0.6$ nm (see Fig.6.19-(a) for the schematics of the setup). By observing the Fig.6.19-(b)-i., (assuming $\chi > 0$) we notice how $\phi - \chi$ represents the DW magnetization angle in the reference frame of the tilted DW. $\phi + \chi$ on the other hand, represents the DW magnetization in the reference frame of a mirrored image of the tilted DW, i.e. with a canting angle of $-\chi$ (see Fig.6.19-(b)-ii). As obtained from [119] and [9], the D_a and D_t components of the DM tensor stabilize, respectively, Néel and Bloch DWs in the reference frame of the tilted DW (see Fig.6.19-(c)-i. and -ii.).

On the other hand, the dependence from the $\phi + \chi$ angle of D_s and D_b components results in the stabilization of Néel or Bloch DWs in a reference located in a mirror image version of the DW itself (see Fig.6.19-(c)-iii. and -iv.). To emphasize how the effect of the D_s and D_b components can only be distinguished from the D_a and D_t contributions in the presence of DW tilting (i.e. $\chi \neq 0$), we analyze the equilibrium configurations obtained from the minimization of the untilted case and compare them with micromagnetic simulations performed with a version of the MuMax3 code [14] suitably modified to account for the new components of the DMI tensor of eq.(6.78).

By observing eq.(6.81), it is immediately apparent that in the case $\chi = 0$, the effect of D_s and D_a (or D_b and D_t) cannot be untangled as all these energy terms contribute to the stabilization of an untilted Néel- (D_s and D_a) or an untilted Bloch-wall (D_b and D_t). This effect is clearly visible in Fig.6.20-(a), where a DM tensor composed only of a D_a part stabilizes a Néel wall (Fig.6.20-(a)-ii.) while a DM tensor composed of a D_s part stabilized a Néel wall with opposite chirality (Fig.6.20-(a)-i.). In the presence of DW tilting (induced e.g. by the presence of an applied IP field along the y-axis), the different energy contributions become distinguishable as can be seen in Fig.6.20-(b)-i. and -ii., where the DW magnetization in the presence of $D_s = \pm 1.5$ mJ/m^2, $D_a = D_b = 0$ and an IP field of $H_y = 100$ mT points in a direction compatible with a Néel wall in a reference frame tilted in the opposite direction $-\chi$. (see the dotted line in Fig. 3(d-e)). In summary, all DMI-tensor contributions that depend on $\cos(\phi + \chi)$ (or $\sin(\phi + \chi)$), rather than $\cos(\phi - \chi)$ (or $\sin(\phi - \chi)$), generate a tilting of the DW in order to maintain a Néel (or Bloch) configuration, but use a fictitious DW tilted in the opposite direction (see the light blue dashed line in Fig.6.20-(d,e)) as a reference instead of the DW itself. The simultaneous presence

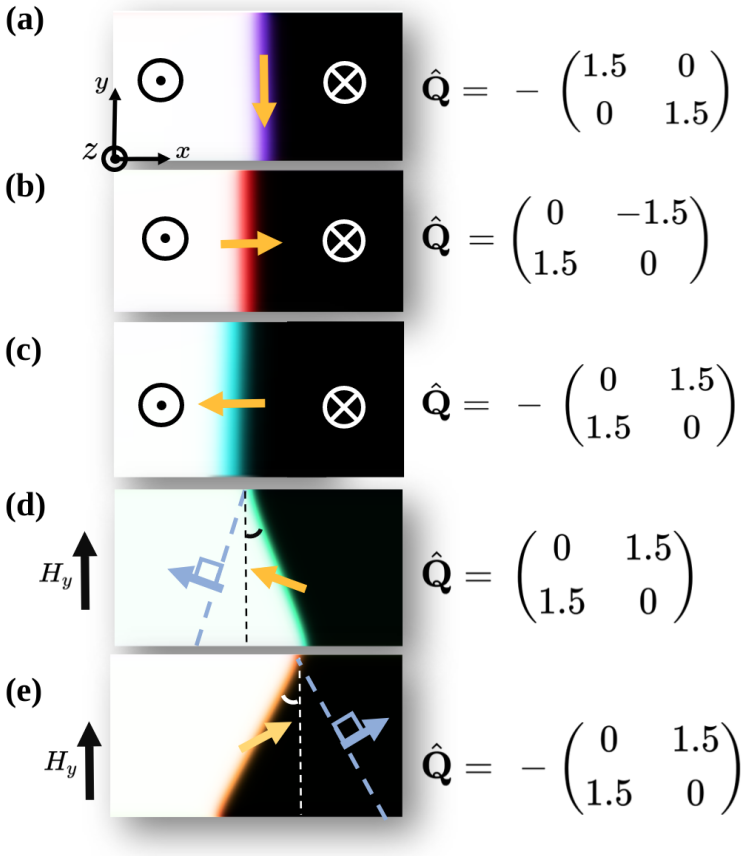

Fig. 6.20 a-c) Internal DW magnetization (the orange arrows in the middle of the domain wall indicate the orientation of the magnetization in the $x-y$ plane) angle stabilized by 3 different representative DMI tensors in the absence of an applied IP field (d-e) Internal DW magnetization angle stabilized by 2 different representative DMI tensors in the presence of an applied IP field. The mirrored image of the tilted domain wall in (d) and (e) is included for clarity. The DMI tensor components are expressed in mJ/m^2.

of all the different DMI contributions as well as their relative importance is more complex and is studied both numerically, via the minimization of eq.(6.80) and with micromagnetic simulations. In Fig.6.21-(a) we observe the tilting angle χ of the DW in the presence of a DMI tensor compatible with C_{2v} crystal symmetry [97], i.e.

$$\hat{\boldsymbol{Q}}_{C_{2v}} = \begin{pmatrix} 0 & D_{12} \\ D_{21} & 0 \end{pmatrix}. \tag{6.84}$$

By observing the value of χ for $D_{21} = 0$ we notice a vanishing of the DW tilting while a form of DMI ($D_{12} \neq 0$) is still present. This phenomenon can be understood using the intuitive picture of competing effective fields. As can be observed in the untilted

model of eq.(6.81), the term stabilizing Néel walls has the form $(D_a - D_s)\cos(\phi)$. In the C_{2v} case of eq.(6.84), we have $D_a = (D_{12} - D_{21})/2$ and $D_s = (D_{12} + D_{21})/2$ and therefore

$$\Rightarrow D_a - D_s = D_{21} \tag{6.85}$$

implying that the component of the DMI tensor that stabilizes Néel walls (and is responsible for tilting since it competes with the H_y torque) is the D_{21} component. In Fig.6.21-(b,c) on the other hand, we observe the behavior or the DW tilting angle χ in the presence of a DMI tensor compatible with S_4 crystal symmetry [97, 107] in 2 different cases. In Fig.6.21-(b) we have

$$\hat{\boldsymbol{Q}}_{S_4} = \begin{pmatrix} 0 & D_s \\ D_s & 0 \end{pmatrix}, \tag{6.86}$$

while in Fig.6.21-(c) we have

$$\hat{\boldsymbol{Q}}_{S_4} = \begin{pmatrix} D_b & D_s \\ D_s & -D_b \end{pmatrix}. \tag{6.87}$$

By comparing the 2 graphs we can observe how the presence of D_b terms emphasizes the canting effect. This can be understood by recalling how the D_b terms energetically favors the formation of Bloch walls. In the presence of a transverse field along the y-direction, the effective field coming from D_b acts constructively and exacerbates the canting one would normally observe without D_b. In Fig.6.21-(d,e) we explore the canting angle χ in the presence of a DMI tensor compatible with the point group symmetry T (or others [13]) i.e.

$$\hat{\boldsymbol{Q}}_{T} = \begin{pmatrix} D_t & 0 \\ 0 & D_t \end{pmatrix}. \tag{6.88}$$

In Fig.6.21-(d,e) we study the behavior of χ as a function of D_t in the presence of a transverse field along the y-direction (Fig.6.21-(d)) and in the presence of a transverse field along the x-direction (Fig.6.21-(e)). We observe how tilting is only present in the case of an applied transverse field applied along the x-direction. This can be explained observing eq.(6.80) where we notice that the DMI associated to D_t tends to stabilize Bloch walls (Fig.6.20-(c)-ii.): as a consequence a transverse H_x field tries to change the internal DW magnetization to a Néel configuration. Much

like in the case of the D_a and D_s (see Fig.6.19-(c)-i. and -iii.), the DW responds by tilting to try and accommodate both the Zeeman- and the D_t effective field.

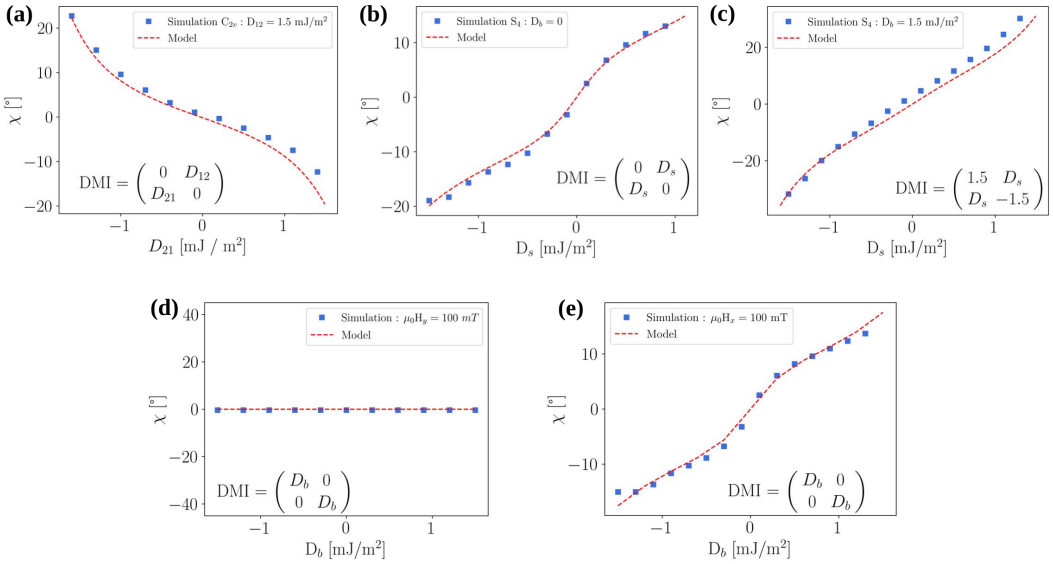

Fig. 6.21 Comparison of Micromagnetic simulations [14] and numerical minimization of the energy density of eq.(6.80) for (a) The tilting angle χ as a function of the D_{21} DMI tensor component of in the case of a C_{2v} symmetric DMI. (b) Tilting angle χ as a function of the D_s DMI tensor component of in the case of a S_4 symmetric DMI in the case of $D_b = 0$. (c) Tilting angle χ as a function of the D_s DMI tensor component of in the case of a S_4 symmetric DMI in the case of $D_b = 1.5$ mJ/m^2. (d) Tilting angle χ as a function of the D_b DMI tensor component of in the case of a T symmetric DMI with an IP applied field in the y-direction of magnitude $\mu_0 H_y = 100$ mT (e) Tilting angle χ as a function of the D_b DMI tensor component of in the case of a T symmetric DMI with an IP applied field in the x-direction of magnitude $\mu_0 H_x = 100$ mT.

6.4.4 Intrinsic DW tilting in the presence of D_b and D_s

As mentioned in the discussion of Sec.6.4.3, the appearance of DW tilting in perpendicularly magnetized nanowires is a consequence of the internal equilibrium of torques trying to orient the DW magnetization some preferred configuration. According to eq.(6.80), if the DMI tensor of the system displays both diagonal and off diagonal components, the conflict of Néel- and Bloch-wall stabilizing torques is expected to be present even in the absence of an applied IP field. By observing Fig.6.22-(c), we can in fact see how the presence of a DMI tensor compatible with the S_4 point group symmetry (see eq.(6.87)), DW tilting occurs even in the absence

of IP fields. In the thin film limit, considering a situation where the DMI strength dominates the demagnetizing field, the magnetization angle in the reference frame of the DW (i.e. $\phi+\chi$) can be easily derived by minimizing the simplified DW energy density

$$\sigma_{DW}(\phi,\chi) = 2\frac{A}{\Delta} + \pi\left[D_b\sin(\phi+\chi) - D_s\cos(\phi+\chi)\right], \tag{6.89}$$

which yields the simple solution (Fig.6.22-(a))

$$\phi+\chi = \arctan\left(-\frac{D_b}{D_s}\right). \tag{6.90}$$

To obtain an approximate solution for the tilting angle χ in the $D_s/D_b \ll 1$ limit as a function of the material parameters, we can follow the procedure outlined in ref.[9] making the analogy between the D_b DMI field and an applied field along the $y-$axis. As discussed in Section.6.4.1, DW tilting is the result of an energy balance between satisfying the internal constraints of the DW and the energy cost due to its surface area increase. We imagine a scenario where the initial state of the DW is a Néel configuration (large D_s hypothesis), i.e. $\sigma_0 = 2A/\Delta + \pi D_s + 2\Delta K_0$. The energy of the DW surface scales with $\sim 1/\cos\chi$, while the energy gain of the D_b DMI component in the DW scales approximately with $\sin\chi$. If we assume a small D_b contribution ($D_b/D_s \ll 1$), we can approximate the DW energy in the Néel configuration as fixed and the energy of the DW as

$$\sigma_{DW} \approx \frac{\sigma_0 - \pi D_b\sin\chi}{\cos\chi}, \tag{6.91}$$

which is minimized by

$$\sin\chi = \frac{\pi D_b}{\sigma_0} = \frac{\pi D_b}{2A/\Delta + \pi D_s + 2\Delta K_0}. \tag{6.92}$$

As we can see from Fig.6.22-(b), the above formula fits the simulations data reasonably well for small D_b, where the dependency of the tilting angle χ from the D_b component is approximately linear.

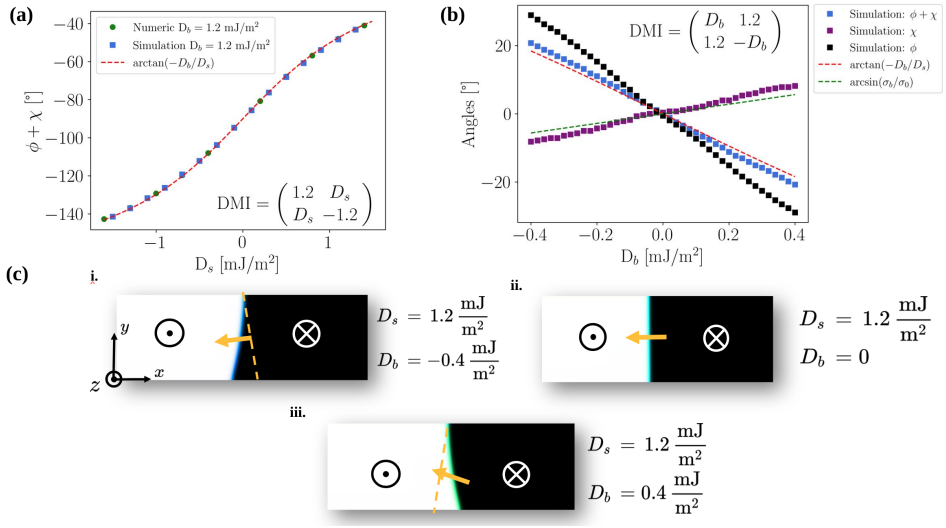

Fig. 6.22 (a) DW angle $\phi + \chi$ as a function of the off-diagonal DMI tensor components D_s in the S_4 symmetric case. (b) DW angles as a function of the diagonal DMI tensor components D_b ($D_b/D_s \ll 1$ limit) in the S_4 symmetric case. (c) intrinsic DW tilting in the presence of simultaneous presence of D_s and D_b for 3 representative cases.

6.4.5 Measuring D_a and D_s DMI contributions with IP fields

According to the discussion of Sec.6.4.3 and Fig.6.20, it might seem impossible to use the canting angle as a function of applied IP fields to measure D_a and D_s since in the untilted case of eq.(6.81), the D_s energy density component simply contributes to the stabilization of a Néel wall and can either collaborate or compete with the D_a contribution depending on the relative sign. We can in fact observe how in Fig.6.23-(a), the response of the tilting angle χ to an IP H_y field in the case of $D_s \neq 0$ is identical to the case $-D_a$ and cannot be distinguished. However, according to eq.(6.80), Fig.6.20-(b)-i. and -ii., even when the canting angle χ is identical, the equilibrium angle ϕ inside the DW in the presence of D_s is different when compared to a system with D_a. This implies that the simultaneous action of H_y and H_x IP fields should induce a different response of the DW canting angle χ in the nanowire. In Fig.6.23-(b), we show how the canting angle χ responds differently in the presence of D_a or D_s under the application of a rotating IP field of the form

$$\mu_0 \boldsymbol{H} = \mu_0 H_0 \begin{pmatrix} \cos(\omega t) \\ \sin(\omega t) \\ 0 \end{pmatrix}, \tag{6.93}$$

where $t \in [0, T]$, $\omega = 2\pi/T$ and $\mu_0 H_0 = 100mT$. We stress the fact that the variable t does not have the unit of a physical time, since in the simulation the canting angle χ in response to the applied field is recorded after the system has had time to relax and not after a fixed time interval. In the x-axis of Figs-6.23-(a,b) we refer to this variable as "steps". In Fig.6.23-(b) also shows how the form of these curves could in principle be fitted to Eq.(6.80) to extract the D_a, D_s coefficients, potentially allowing for the magneto-optical measurements of different DMI tensor components with the canting angle method. The fit is performed by calculating χ from a constrained minimization of the DW energy density of eq.(6.80) using H_x, H_y as variables and D_a and D_s as fitting parameters.

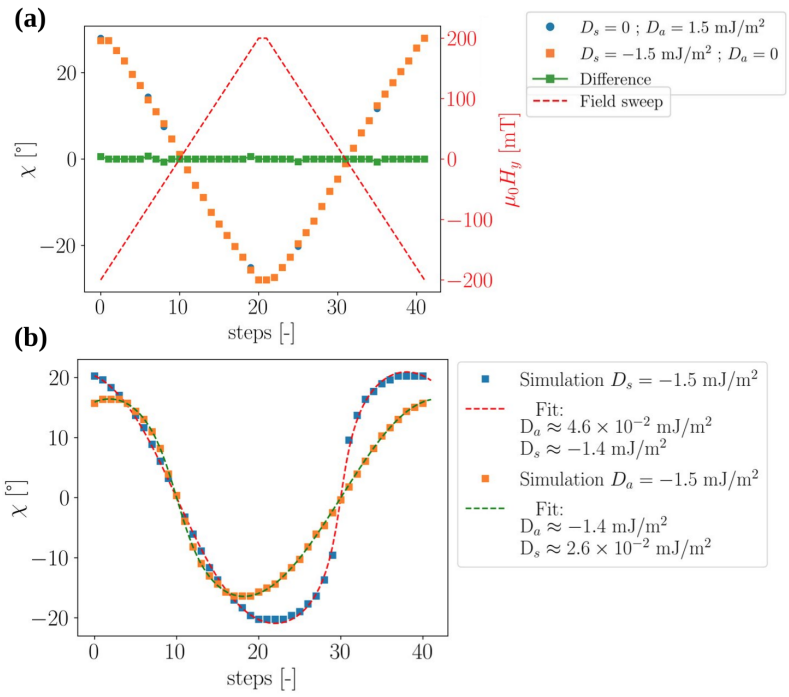

Fig. 6.23 (a) DW tilting angle χ response to an H_y field sweep from -200 mT to $+200$ mT in the case of pure D_a (blue dots) and pure D_s (orange squares) contributions to DMI. As can be seen the 2 responses overlap almost completely. (b) DW tilting angle χ response to a rotating IP field with H_y and H_x components (see eq.(6.93) in the case of pure D_a and pure D_s contributions to DMI. The dashed curves are obtained by fitting the energy minimum of eq.(6.80) onto the results obtained via micromagnetic simulations using D_a and D_s as the fitting parameters.

6.4.6 Domain-wall dynamics in the presence of arbitrary DMI tensors

After having studied the effects of the different components of the DMI tensor on the static configurations of magnetic domain walls in nanowires, we now focus on the effects on the dynamics. Given that in the field driven, steady state regime the magnetization angle in the reference frame of the DW is only dependent on the IP torques exerted by the driving field H_z, the anisotropy contributions H_k and the various components of the DMI tensor, we can avoid considering χ as a collective coordinate in the dynamical equations and work with the simpler $q-\phi$ model [9, 212] whose DW energy density $\sigma_{DW}(q,\phi)$ with the generalized chiral interaction tensor from eq.(6.65) can be written as

$$\begin{aligned}\sigma_{DW}(\phi) =& 2\frac{A}{\Delta} + \pi\big[(D_a - D_s)\cos(\phi) + (D_b - D_t)\sin(\phi)\big] + \\ & 2\Delta(K_0 + K\sin^2(\phi)) - \pi\Delta M_s(H_y\sin\phi + H_x\sin\phi).\end{aligned} \tag{6.94}$$

By explicitly writing the Lagrangian of the DW as $\mathscr{L} = \sigma_{DW} + (M_s/\gamma)\phi\dot{\theta}\sin\theta$ and the Rayleigh dissipation function to correctly account for damping effects $\mathscr{F} = (\alpha M_s/2\gamma)\,\dot{\boldsymbol{m}}$. We can derive the equations of motion from the Euler-Lagrange-Rayleigh equation [207],

$$\frac{\partial\mathscr{L}}{\partial X} - \frac{d}{dt}\left(\frac{\partial\mathscr{L}}{\partial\dot{X}}\right) + \frac{\partial\mathscr{F}}{\partial\dot{X}} = 0, \;\; X \in \{q,\phi,\Delta\}, \tag{6.95}$$

obtaining the following equations of motion

$$\dot{q} = \frac{\Delta\gamma_0}{1+\alpha^2}\left[\alpha H_z + H_K\frac{\sin 2\varphi}{2} - \frac{\pi}{2}\tilde{f}'_{\mathrm{DMI}}(\varphi) - \frac{\pi}{2}\left(H_y\cos\varphi - H_x\sin\varphi\right)\right], \tag{6.96}$$

$$\dot{\varphi} = \frac{\gamma_0}{1+\alpha^2}\left[H_z - \alpha\left(H_K\frac{\sin 2\varphi}{2} - \frac{\pi}{2}\tilde{f}'_{\mathrm{DMI}}(\varphi) - \frac{\pi}{2}\left(H_y\cos\varphi - H_x\sin\varphi\right)\right)\right], \tag{6.97}$$

$$\dot{\Delta} = \frac{12\gamma_0}{\mu_0 M_s\alpha\pi^2}\left[\frac{A}{\Delta} - \Delta\left(K_0 + K\sin^2\varphi\right) + \mu_0 M_s\Delta\frac{\pi}{2}\left(H_x\cos\varphi + H_y\sin\varphi\right)\right]. \tag{6.98}$$

Where we define

$$H_K = \frac{2K}{M_s\mu_0}\ ,\ \tilde{f}'_{DMI}(\phi) = \frac{1}{2\Delta M_s\mu_0}\frac{\partial f_{DMI}(\phi)}{\partial\phi} \tag{6.99}$$

and $f_{DMI}(\phi)$ represents the trigonometric function with all the different DMI contributions (antisymmetric D_a, symmetric D_s, traceless D_b and diagonal D_t)

$$f_{DMI}(\phi) = (D_a - D_s)\cos\phi + (D_t - D_b)\sin\phi. \tag{6.100}$$

If we assume an up-down initial configuration ($P = +1$) and an in plane (IP) field free stationary case (i.e $H_x = H_y = 0$), imposing the stationary conditions $\dot{\phi} = \dot{\Delta} = 0$ yields the conditions [200, 115] for rigid motion of the DW magnetization

$$H_z = \alpha\left(H_k\ \frac{\sin 2\phi}{2} - \frac{\pi}{2}\left((H_{DMI,a} - H_{DMI,s})\sin\phi + \ (H_{DMI,b} - H_{DMI,t})\cos\phi\right)\right), \tag{6.101}$$

where $H_{DMI,i\in\{a,s,b,t\}} = D_i/2\Delta\mu_0 M_s$ is the effective field strength associated to the different DMI components. In order to make the notation more compact, we define

$$\kappa := \frac{K}{K_0}\ ,\ \tilde{D}' := \frac{\pi(D_a - D_s)}{\mu_0 H_K M_s\Delta_0}\ ,\ \tilde{D}'' := \frac{\pi(D_t - D_b)}{H_K\mu_0 M_s\Delta_0} \tag{6.102}$$

where $\Delta_0 = \sqrt{\frac{A}{K_0 + K\sin^2\phi}}$ represents the equilibrium DW width that can be obtained by setting $\dot{\Delta} = 0$ in eq.(6.98). These definitions allow us to rewrite (6.101) in the form

$$H_z = \frac{\alpha H_k}{2}\left[(\tilde{D}''\cos\phi - \tilde{D}'\sin\phi)\frac{\sqrt{1+\kappa\sin^2\phi}}{\kappa} + \sin 2\phi\right]. \tag{6.103}$$

For fixed $\kappa, \tilde{D}'', \tilde{D}'$, the Walker field is identified as the largest H_z fulfilling eq.(6.103) and is obtained by maximising the right hand side of eq.(6.103) [119], i.e.

$$H_W := \frac{\alpha H_k}{2}\times \max_{\phi\in[0,2\pi)}\left[(\tilde{D}''\cos\phi - \tilde{D}'\sin\phi)\frac{\sqrt{1+\kappa\sin^2\phi}}{\kappa} + \sin 2\phi\right] \tag{6.104}$$

The maximization of (6.104) is not possible in closed analytical form, however one can treat the thin film limit, where the perpendicular magnetic anisotropy dominates over the shape anisotropy , i.e. $N_z \gg N_x$, N_y implying the condition $\kappa \ll 1$ on eq.(6.104). The asymptotic solution in that case has the following form

$$H_W \sim \begin{cases} \frac{\tilde{D}''\ |\tilde{D}''|+|\tilde{D}'|\ \tilde{D}'}{\kappa\sqrt{(\tilde{D}'')^2+(\tilde{D}')^2}} \text{ if } sign(\tilde{D}''\cdot\tilde{D}') = 1 \\ \frac{\tilde{D}''\ |\tilde{D}''|-|\tilde{D}'|\ \tilde{D}'}{\kappa\sqrt{(\tilde{D}'')^2+(\tilde{D}')^2}} \text{ if } sign(\tilde{D}''\cdot\tilde{D}') = -1 \end{cases} \quad (\text{as } \kappa \to 0). \tag{6.105}$$

We validate the assumption of $\kappa \ll 1$ approximation in our case by pointing out how the demagnetizing factors in the case of a slab geometry can be calculated analytically [100] and our geometry $L_x = 1$ μm, $L_y = 160$ nm and $L_z = 0.6$ nm yields the following values for the demagnetizing factors

$$N_x = 0.0013\ ,\ N_y = 0.0082\ ,\ N_z = 0.990. \tag{6.106}$$

We now proceed and discuss the obtained analytical result by comparing them with numerical simulations. By observing eq.(6.105), we first of all notice how in the limit of $\tilde{D}' \to 0$ (i.e. a DMI tensor with only elements on the diagonal) or the limit $\tilde{D}'' \to 0$ (i.e. a DMI tensor with only elements on the off-diagonal) the asymptotic

behavior of eq.(6.105) becomes

$$H_W(\tilde{D}' \to 0) \sim \tilde{D}''/\kappa \tag{6.107}$$

$$H_W(\tilde{D}'' \to 0) \sim \tilde{D}'/\kappa \tag{6.108}$$

$$\tag{6.109}$$

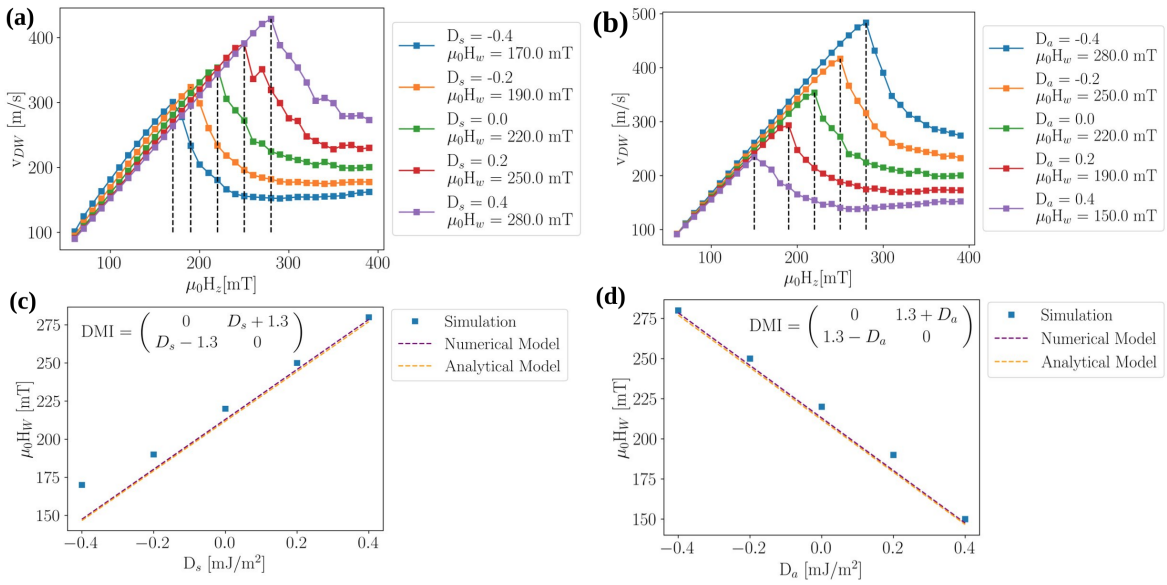

Fig. 6.24 Comparison of Micromagnetic simulations [14], numerical minimization (6.101) and analytical estimate (see eq.(6.105)) for the DW Walker breakdown H_W. (a) DW velocity v_{DW} as a function of an applied out-of-plane field H_z. The different curves show the velocity profile for different values of the symmetric component of a C_{2v} symmetric DMI tensor (see inset of (c)). (b) DW velocity v_{DW} as a function of an applied out-of-plane field H_z. The different curves show the velocity profile for different values of the anti symmetric component of a C_{2v} symmetric DMI tensor (see inset of (d)). (c) Comparison of simulation results, numerical maximization of eq.(6.103) and analytical estimate (see eq.(6.105)) of the Walker breakdown as a function of the symmetric component of a C_{2v} symmetric tensor. (d) Comparison of simulation results, numerical maximization of eq.(6.103) and analytical estimate (see eq.(6.105)) of the Walker breakdown as a function of the anti symmetric component of a C_{2v} symmetric tensor.

which shows a linear behavior compatible both with our numerical results (see Fig.6.24) and, in the $H_W(\tilde{D}' \to 0) \sim \tilde{D}''/\kappa$ case, with the results shown in [119]. We emphasize how these limiting cases show a linear dependence of the WB field only in the case of exclusive presence of diagonal or off-diagonal elements, but not both at the same time. By observing Fig.6.25-(a,b) we point out how the presence of both a diagonal and off-diagonal component of the DMI tensor results in a departure from

the linear behavior also described by eq.(6.107) and eq.(6.108) hinting at the fact that the components of the effective field counteracting precessional motion do not cooperate additively but in a non-linear way. Furthermore, we emphasize how this behavior of the WB field directly translates in the attainable peak DW velocity since, in the $\kappa \ll 1$ limit,

$$v_{max} \sim \frac{\Delta_0 \gamma_0 \alpha}{1+\alpha^2} H_W = \tag{6.110}$$

$$\frac{\Delta_0 \gamma_0 \alpha}{1+\alpha^2} \begin{cases} \frac{\tilde{D}'' \, |\tilde{D}''| + |\tilde{D}'| \, \tilde{D}'}{\kappa \sqrt{(\tilde{D}'')^2 + (\tilde{D}')^2}} \text{ if } sign(\tilde{D}'' \cdot \tilde{D}') = 1 \\ \frac{\tilde{D}'' \, |\tilde{D}''| - |\tilde{D}'| \, \tilde{D}'}{\kappa \sqrt{(\tilde{D}'')^2 + (\tilde{D}')^2}} \text{ if } sign(\tilde{D}'' \cdot \tilde{D}') = -1 \end{cases}$$

$$(\text{as } \kappa \to 0). \tag{6.111}$$

In Fig.6.25-(c) we report the peak velocities calculated with eq.(6.111) and show how with $D_s = 1.5$ mJ/m^2 and $D_b = -1.5$ mJ/m^2 even peak velocities as high as $v_{max} \approx 1200$ m/s are theoretically achievable. Furthermore, using experimentally measured [205] parameters for the S_4 symmetric Schreibersite compound $Fe_{1.9}Ni_{0.9}Pd_{0.2}P$ ($A = 8$ pJ/m , $K_u = 31$ kJ/m^3 , $M_s = 417$ kA/m) while keeping the nanowire dimensions unchanged, eq.(6.111) predicts how peak velocities $v_{max} \approx 1700$ m/s can be achieved even with much smaller DMI tensor components (i.e. $D_s = D_b = 0.2$ mJ/m^2).

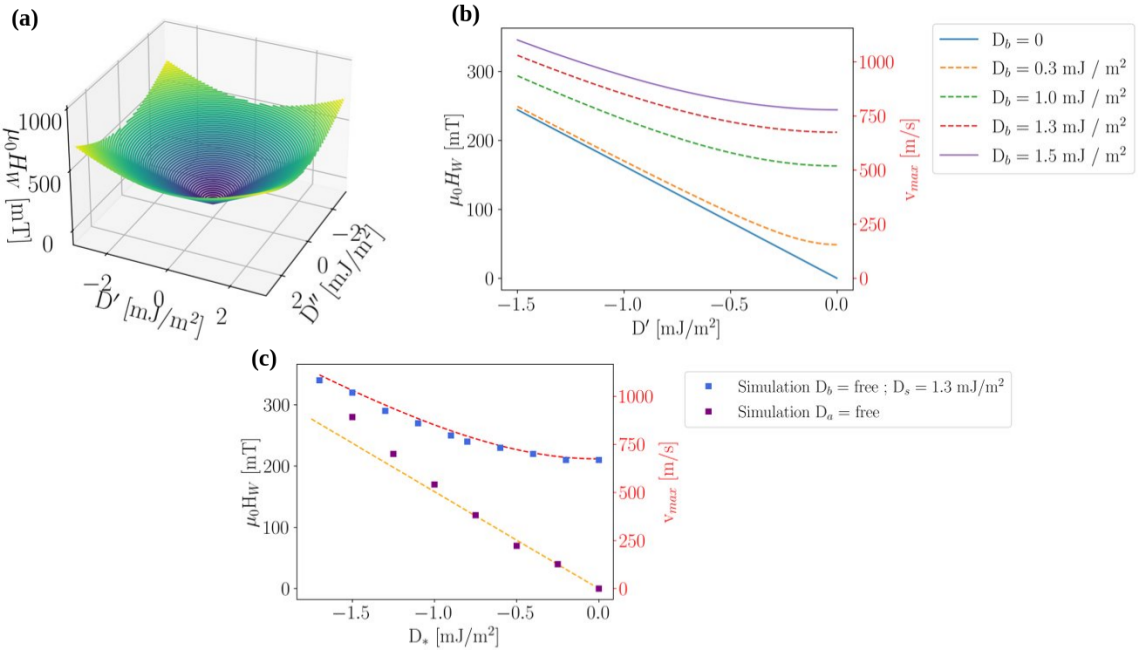

Fig. 6.25 (a) 3D plot of eq.(6.105) (b) Plot of the analytical formula for the WB field H_W as a function of the off-diagonal $\tilde{D}'$ component (see eq.(6.105)). The different curves represent the behavior of the WB field for different diagonal DMI D_b values. At $D_b = 0$ (i.e the blue curve) we recover the linear behavior. The peak velocities are reported on the second y-axis shown in red. (c) Comparison of WB field calculated from a micromagnetic simulation with a DMI tensor compatible with S_4 symmetry ($D_l = 1.3$ mJ/m^2 and free D_b) and the analytical estimate of eq.(6.105). The peak velocities are reported on the second y-axis shown in red.

6.4.7 Conclusion

In this work we modified to the existing CCM [207, 9, 212] to include and study the effects of arbitrary DMI tensors on the statics and dynamics of domain walls in magnetic nanowires. We discuss how the effects of a DMI tensors can be described by inspecting how its symmetric traceless (D_s, D_b), antisymmetric (D_a) and diagonal (D_t) components act on the effective field inside the DW. We first show how DW canting is well described by the energy density of the $q - \phi - \chi$ model (see Fig.6.21) and discuss how the canting angle method is able to distinguish diagonal (D_b,D_t) DMI contributions and off-diagonal DMI contributions (D_a, D_s). We also observe how measuring the response of the canting angle χ to the simultaneous application of an IP field with both H_x and H_y components could potentially be a means to magneto-optically measure symmetric (D_s) and antisymmetric (D_a) contributions

(see Fig.6.23) to DMI. Other IP field applications schemes could be studied to further enhance the resolution power of this technique. We then proceed and show how, in the presence of both D_s and D_b DMI components, DW tilting can be present even in the absence of IP fields. We derive a simple analytic formula for the canting angle χ as a function of D_b valid in the $D_s/D_b \ll 1$ limit (see Fig.6.22). We then study the effect of the different DMI tensor components on the the field driven dynamic properties of DWs in magnetic nanowires. We discover that the effects of the interplay of the Néel- and Bloch-Stabilizing DMI components on the magnitude of the WB field is not trivial and determines a departure from the simple linear dependency (Fig.6.25-(a)) in the case of pure interface- [10] of bulk-DMI [119]. We then derive an analytic formula describing the dependency the of the WB field on the different DMI tensor components (eq.(6.105)) in the thin film limit, comparing its predictions with micromagnetic simulations (Fig.6.25-(b)). The very high theoretically achievable DW velocities in the order km/s (Fig.6.25-(c)) is confirmed by simulation and could open the way to a new wave of experimental investigations in low-symmetry magnetic thin films. These results indeed hint at the fact that materials displaying these more exotic forms of DMI combining both Bloch and Néel stabilising effective fields, could be interesting candidates for novel DW motion based technology concepts.

Chapter 7

Summary of results and future outlook

7.1 Summary of results

In the following we provide a concise account of the main results obtained in these 3 years of research activity:

- **Multiple magneto-ionic regimes:** A combination of experimental efforts and ab-initio calculations allowed us to propose a microscopic mechanism for the different observed reversibility regimes in the magnetization switching in Ta/$Co_{20}Fe_{60}B_{20}$/HfO_2 multilayers. In these systems, the geometry of the oxygen-ferromagnet interaction seems to be of crucial importance for the reversibility characteristics of magneto-ionic switching.
- **Gauge field theory of chiral interactions in arbitrary crystals:** the use of gauge invariance, a tool borrowed from interacting field theories, led to the development of a formalism for compactly describing chiral interactions in micromagnetism taking in account arbitrary crystallographic point groups. This formalism was successfully translated into computational tools by adapting the open source micromagnetic code MuMax3 [14], enabling the study of magnetic domain wall behavior in crystals of arbitrary point groups under chiral interactions.

- **Collective coordinate models with arbitrary chiral interactions:** The previously developed formalism allowed us to expand existing collective coordinate models to describe domain wall motion in nanowires displaying arbitrary chiral interactions. We discovered a highly non-trivial behavior of magnetic domain wall canting angles and a nonlinear enhancement of the Walker breakdown field in the presence of certain types of chiral interactions.

- **Electric Field Effects on Magnetostatic Spin Waves:** In insulating materials, we have shown through a micromagnetic theoretical analysis of the electric field effect on the dispersion relation of magnetostatic surface waves, two main contributions emerge: a purely macroscopic relativistic one and a contribution that operates on the level of quantum mechanical magnetic exchange. We speculate that since the physical origin of these two is drastically different, the nature of the electric field itself must be carefully considered when analyzing experimental data. We remark how these result, despite being in line with the overall theme of the thesis, concern dynamical magnetization processes. In the interest of brevity and to keep the presentation of the results as tight as possible, we have decided not to include these result in the present version of the dissertation.

- **Observation of a phase transition triggered by the change of character of chiral interactions in response to oxygen positioning:** we were able to register (via DFT calculations) a change from anti-skyrmionic DMI to skyrmionic Dzyaloshinskii-Moriya interaction in response to the movement of oxygen atoms in the 2D magnet VO_2. Despite the observation of this transition, the microscopic mechanism governing it is still under investigation. Because of the open ended nature of these preliminary results, we have decided not to include them in the present version of the thesis.

7.2 Future outlook

The obtained results have opened up several avenues for future research. Foremost among these questions is the verification of whether the application of an electric field perpendicular to the plane of a thin film hosting anisotropic Dzyaloshinskii-Moriya interaction (DMI) could indeed induce a phase transition from an antiskyrmion to

a skyrmion phase. This predicted phenomenon holds significant implications for the control and manipulation of topological magnetic textures and warrants further investigation to confirm its occurrence and understand its underlying mechanisms.

Furthermore, the idea of symmetry breaking along the $\hat{z}$-axis to trigger a phase transition from antiskyrmion to skyrmion is not limited to the use of electric fields but also appears promising in the context of magneto-ionic manipulation of magnetic properties. The application of perpendicular electric fields has recently demonstrated the ability to induce a change in the sign of interfacial DMI (iDMI) [7], indicating that interfacial manipulations of this nature align with the predicted direction for symmetry breaking. Exploring the interplay between electric fields, magneto-ionic effects, and symmetry breaking in relation to DMI manipulation holds great potential for advancing our understanding of the underlying mechanisms and establishing practical techniques for controlling topological magnetic structures.

By addressing these open questions, future research can further explore the full potential of electric field and magneto-ionic manipulation principles for controlling magnetic properties and topological structures in magnetic thin films, paving the way for the development of next-generation spintronic devices with enhanced performance and reduced environmental impact.

The exploration of the 2-site anisotropy term, as discussed in the theory section, presents another intriguing avenue for future research. This interaction term has garnered increased attention with the development of 2D magnetism, as it can become relevant in such systems. The study of this term and its implications in 2D magnets offer a promising research direction to uncover new phenomena and understand the underlying physics.

In particular, in the context of 2D magnets displaying Kitaev exchange, the additional symmetry breaking along the $\hat{z}$-direction presents an unexplored research frontier, especialy when coupled with the possibility of stabilizing magnetic structures with non-vanishing topological properties analogous to the role of Dzyaloshinskii-Moriya interaction (DMI) in skyrmions and antiskyrmions [213]. The more delicate nature of this interaction increases the hope to induce visible effects of a more modest electric field compared to systems where the effects should emerge against much larger energy scales such as DMI and MCA.

Addressing the role and effects of the 2-site anisotropy term within the framework of micromagnetism also represents a research direction that has yet to be extensively

pursued. Exploring the interplay between this term and other magnetic interactions through theoretical modeling and numerical simulations can shed light on its impact on the stability and behavior of magnetic structures, including the possible emergence of non-trivial topological properties.

Publications

- Pachat, R., Ourdani, D., van der Jagt, J. W., Syskaki, M.-A., **Di Pietro, A.**, Roussigné, Y., Ono, S., Gabor, M. S., Chérif, M., Durin, G., Langer, J., Belmeguenai, M., Ravelosona, D., & Diez, L. H. (2021). Multiple Magnetoionic Regimes in Ta/$Co_{20}Fe_{60}$/B_{20}/HfO_2 In Physical Review Applied (Vol. 15, Issue 6). American Physical Society (APS).

- Pachat, R., Ourdani, D., Syskaki, M., Lamperti, A., Roy, S., Chen, S., **Di Pietro, A.**., Largeau, L., Juge, R., Massouras, M., Balan, C., van der Jagt, J. W., Agnus, G., Roussigné, Y., Gabor, M., Chérif, S. M., Durin, G., Ono, S., Langer, J., ... Herrera Diez, L. (2022). Magneto-Ionics in Annealed W/CoFeB/HfO 2 Thin Films. In Advanced Materials Interfaces (Vol. 9, Issue 36, p. 2200690). Wiley.

- **Di Pietro, A.**, Ansalone, P., Basso, V., Magni, A., Durin, G. (2022). Gauge theory applied to magnetic lattices. In Europhysics Letters (Vol. 140, Issue 4, p. 46003). IOP Publishing.

- **Di Pietro, A.**, Pachat, R., Qiao, L., Herrera-Diez, L., van der Jagt, J. W., Picozzi, S., Ravelosona, D., Ren, W., & Durin, G. (2023). Ab initio study of magneto-ionic mechanisms in ferromagnet/oxide multilayers. In Physical Review B (Vol. 107, Issue 17). American Physical Society (APS).

- Basso, V., Ansalone, P., **Di Pietro, A.**, 2023. Disentangling electric field effect on spin waves in ferromagnetic insulators. Physica B: Condensed Matter 671, 415422.

- **Di Pietro, A.**, García-Sánchez, F. & Durin, G. (2023). Domain wall statics and dynamics in nanowires with arbitrary Dzyaloshinskii-Moriya tensors. In Physical Reviw B (Vol. 107, Issue 17). American Physical Society (APS).

- Adrien A. D. Petrillo, A., D., A., Fattouhi M., **Di Pietro, A.**, Gnoatto L., Alerani Sole, M., Koopmans, B., Lavrijsen, R. (2023) Using Propagating Spin Wave Spectroscopy to Probe Electric-Field Induced Changes of Surface Anisotropy. (In preparation)

- **Di Pietro, A.**, Yang, B., Picozzi, S., Durin, G. (2023) Character manipulation of DMI via magneto-ionic mechanisms in 2D AX_2 magnets. (In preparation)

References

[1] Jorge Puebla, Junyeon Kim, Kouta Kondou, and Yoshichika Otani. Spintronic devices for energy-efficient data storage and energy harvesting. *Communications Materials*, 1(1), May 2020.

[2] Jia-Mian Hu and Ce-Wen Nan. Opportunities and challenges for magnetoelectric devices. *APL Materials*, 7(8):080905, August 2019.

[3] Alex Hubert and Rudolf Schäfer. *Magnetic Domains*. Springer Berlin Heidelberg, 1998.

[4] J. Stöhr. Exploring the microscopic origin of magnetic anisotropies with x-ray magnetic circular dichroism (XMCD) spectroscopy. *Journal of Magnetism and Magnetic Materials*, 200(1-3):470–497, October 1999.

[5] S. H. Liang, T. T. Zhang, P. Barate, J. Frougier, M. Vidal, P. Renucci, B. Xu, H. Jaffrès, J. M. George, X. Devaux, M. Hehn, X. Marie, S. Mangin, H. X. Yang, A. Hallal, M. Chshiev, T. Amand, H. F. Liu, D. P. Liu, X. F. Han, Z. G. Wang, and Y. Lu. Large and robust electrical spin injection into gaas at zero magnetic field using an ultrathin cofeb/mgo injector. *Physical Review B - Condensed Matter and Materials Physics*, 90:1–9, 2014.

[6] Abderrezak Belabbes, Gustav Bihlmayer, Stefan Blügel, and Aurélien Manchon. Oxygen-enabled control of dzyaloshinskii-moriya interaction in ultrathin magnetic films. *Scientific Reports*, 6:1–9, 2016.

[7] Charles-Elie Fillion, Johanna Fischer, Raj Kumar, Aymen Fassatoui, Stefania Pizzini, Laurent Ranno, Djoudi Ourdani, Mohamed Belmeguenai, Yves Roussigné, Salim-Mourad Chérif, Stéphane Auffret, Isabelle Joumard, Olivier Boulle, Gilles Gaudin, Liliana Buda-Prejbeanu, Claire Baraduc, and Hélène Béa. Gate-controlled skyrmion and domain wall chirality. *Nature Communications*, 13:5257, 9 2022.

[8] Ralph Skomski. *Simple Models of Magnetism*. Oxford University Press, January 2008.

[9] O Boulle, S Rohart, L D Buda-Prejbeanu, E Jué, I M Miron, S Pizzini, J Vogel, G Gaudin, and A Thiaville. Domain wall tilting in the presence of the dzyaloshinskii-moriya interaction in out-of-plane magnetized magnetic nanotracks. *Physical Review Letters*, 111:217203, 2013.

[10] André Thiaville, Stanislas Rohart, Émilie Jué, Vincent Cros, and Albert Fert. Dynamics of dzyaloshinskii domain walls in ultrathin magnetic films. *Epl*, 100, 2012.

[11] Jacob E. Goodman, Joseph O'Rourke, and Csaba D. Tóth. *Handbook of Discrete and Computational Geometry, Third Edition*. Chapman and Hall/CRC, 11 2017.

[12] Robert R Birss. *Symmetry and Magnetism*. North-Holland Publishing Company, 1966.

[13] A. Di Pietro, P. Ansalone, V. Basso, A. Magni, and G. Durin. Gauge theory applied to magnetic lattices. *Europhysics Letters*, 140(4):46003, November 2022.

[14] Arne Vansteenkiste, Jonathan Leliaert, Mykola Dvornik, Mathias Helsen, Felipe Garcia-Sanchez, and Bartel Van Waeyenberge. The design and verification of mumax3. *AIP Advances*, 4:107133, 10 2014.

[15] G. Binasch, P. Grünberg, F. Saurenbach, and W. Zinn. Enhanced magnetoresistance in layered magnetic structures with antiferromagnetic interlayer exchange. *Phys. Rev. B*, 39:4828–4830, Mar 1989.

[16] M. N. Baibich, J. M. Broto, A. Fert, F. Nguyen Van Dau, F. Petroff, P. Etienne, G. Creuzet, A. Friederich, and J. Chazelas. Giant magnetoresistance of (001)fe/(001)cr magnetic superlattices. *Phys. Rev. Lett.*, 61:2472–2475, Nov 1988.

[17] P. Curie. Sur la symétrie dans les phénomènes physiques, symétrie d'un champ électrique et d'un champ magnétique. *Journal de Physique Théorique et Appliquée*, 3(1):393–415, 1894.

[18] L D Landau, J S Bell, M J Kearsley, L P Pitaevskii, E M Lifshitz, and J B Sykes. *Electrodynamics of continuous media*. Elsevier, October 2013.

[19] I. E. Dzyaloshinskiĭ. On the magneto-electrical effects in antiferromagnets. *Soviet physics, JETP*, 10:628–629, 1960.

[20] DN Astrov. The magnetoelectric effect in antiferromagnetics. *Sov. Phys. JETP*, 11(3):708–709, 1960.

[21] Hans Schmid. Multi-ferroic magnetoelectrics. *Ferroelectrics*, 162(1):317–338, January 1994.

[22] Manfred Fiebig. Revival of the magnetoelectric effect. *Journal of Physics D: Applied Physics*, 38(8):R123–R152, April 2005.

[23] W. Eerenstein, N. D. Mathur, and J. F. Scott. Multiferroic and magnetoelectric materials. *Nature*, 442(7104):759–765, August 2006.

[24] J. Van Den Boomgaard, A. M. J. G. Van Run, and J. Van Suchtelen. Magnetoelectricity in piezoelectric-magnetostrictive composites. *Ferroelectrics*, 10(1):295–298, 1976.

[25] H. Ohno, D. Chiba, F. Matsukura, T. Omiya, E. Abe, T. Dietl, Y. Ohno, and K. Ohtani. Electric-field control of ferromagnetism. *Nature*, 408(6815):944–946, December 2000.

[26] D. Chiba, M. Yamanouchi, F. Matsukura, and H. Ohno. Electrical manipulation of magnetization reversal in a ferromagnetic semiconductor. *Science*, 301(5635):943–945, August 2003.

[27] Sasikanth Manipatruni, Dmitri E. Nikonov, Chia-Ching Lin, Tanay A. Gosavi, Huichu Liu, Bhagwati Prasad, Yen-Lin Huang, Everton Bonturim, Ramamoorthy Ramesh, and Ian A. Young. Scalable energy-efficient magnetoelectric spin–orbit logic. *Nature*, 565(7737):35–42, December 2018.

[28] W. Eerenstein, M. Wiora, J. L. Prieto, J. F. Scott, and N. D. Mathur. Giant sharp and persistent converse magnetoelectric effects in multiferroic epitaxial heterostructures. *Nature Materials*, 6(5):348–351, April 2007.

[29] Sarbeswar Sahoo, Srinivas Polisetty, Chun-Gang Duan, Sitaram S. Jaswal, Evgeny Y. Tsymbal, and Christian Binek. Ferroelectric control of magnetism in $BaTio_3Fe$ heterostructures via interface strain coupling. *Phys. Rev. B*, 76:092108, Sep 2007.

[30] Roberto Lo Conte, Zhuyun Xiao, Cai Chen, Camelia V. Stan, Jon Gorchon, Amal El-Ghazaly, Mark E. Nowakowski, Hyunmin Sohn, Akshay Pattabi, Andreas Scholl, Nobumichi Tamura, Abdon Sepulveda, Gregory P. Carman, Robert N. Candler, and Jeffrey Bokor. Influence of nonuniform micron-scale strain distributions on the electrical reorientation of magnetic microstructures in a composite multiferroic heterostructure. *Nano Letters*, 18(3):1952–1961, February 2018.

[31] D. Chiba, M. Sawicki, Y. Nishitani, Y. Nakatani, F. Matsukura, and H. Ohno. Magnetization vector manipulation by electric fields. *Nature*, 455(7212):515–518, September 2008.

[32] Y. Yamada, K. Ueno, T. Fukumura, H. T. Yuan, H. Shimotani, Y. Iwasa, L. Gu, S. Tsukimoto, Y. Ikuhara, and M. Kawasaki. Electrically induced ferromagnetism at room temperature in cobalt-doped titanium dioxide. *Science*, 332(6033):1065–1067, May 2011.

[33] Marine Schott, Laurent Ranno, Hélène Béa, Claire Baraduc, Stéphane Auffret, and Anne Bernand-Mantel. Electric field control of interfacial dzyaloshinskii-moriya interaction in pt/co/alox thin films. *Journal of Magnetism and Magnetic Materials*, 520, 2021.

[34] Hongxin Yang, Olivier Boulle, Vincent Cros, Albert Fert, and Mairbek Chshiev. Controlling dzyaloshinskii-moriya interaction via chirality dependent atomic-layer stacking, insulator capping and electric field. *Scientific Reports*, 8, 8 2018.

[35] Pavel Borisov, Andreas Hochstrat, Xi Chen, Wolfgang Kleemann, and Christian Binek. Magnetoelectric switching of exchange bias. *Physical Review Letters*, 94(11), March 2005.

[36] Xi He, Yi Wang, Ning Wu, Anthony N. Caruso, Elio Vescovo, Kirill D. Belashchenko, Peter A. Dowben, and Christian Binek. Robust isothermal electric control of exchange bias at room temperature. *Nature Materials*, 9(7):579–585, June 2010.

[37] Julius de Rojas, Alberto Quintana, Aitor Lopeandía, Joaquín Salguero, Beatriz Muñiz, Fatima Ibrahim, Mairbek Chshiev, Aliona Nicolenco, Maciej O. Liedke, Maik Butterling, Andreas Wagner, Veronica Sireus, Llibertat Abad, Christopher J. Jensen, Kai Liu, Josep Nogués, José L. Costa-Krämer, Enric Menéndez, and Jordi Sort. Voltage-driven motion of nitrogen ions: a new paradigm for magneto-ionics. *Nature Communications*, 11(1), November 2020.

[38] Uwe Bauer, Lide Yao, Aik Jun Tan, Parnika Agrawal, Satoru Emori, Harry L. Tuller, Sebastiaan Van Dijken, and Geoffrey S.D. Beach. Magneto-ionic control of interfacial magnetism. *Nature Materials*, 14:174–181, 2015.

[39] Aik Jun Tan, Mantao Huang, Can Onur Avci, Felix Büttner, Maxwell Mann, Wen Hu, Claudio Mazzoli, Stuart Wilkins, Harry L. Tuller, and Geoffrey S. D. Beach. Magneto-ionic control of magnetism using a solid-state proton pump. *Nature Materials*, 18(1):35–41, November 2018.

[40] Ki-Young Lee, Sujin Jo, Aik Jun Tan, Mantao Huang, Dongwon Choi, Jung Hoon Park, Ho-Il Ji, Ji-Won Son, Joonyeon Chang, Geoffrey S. D. Beach, and Seonghoon Woo. Fast magneto-ionic switching of interface anisotropy using yttria-stabilized zirconia gate oxide. *Nano Letters*, 20(5):3435–3441, April 2020.

[41] W. Heisenberg. Zur theorie des ferromagnetismus. *Zeitschrift fr Physik*, 49(9-10):619–636, sep 1928.

[42] Felix Bloch. Bemerkung zur elektronentheorie des ferromagnetismus und der elektrischen leitfähigkeit. *Zeitschrift für Physik*, 57(7-8):545–555, 1929.

[43] Neil W Ashcroft and N Mermin. *Solid State Physics*. Brooks/Cole, Florence, KY, January 1976.

[44] Charles L. Cleveland and Rodrigo Medina A. Obtaining a heisenberg hamiltonian from the hubbard model. *American Journal of Physics*, 44:44–46, 1 1976.

[45] *Magnetism - From Fundamentals to Nanoscale Dynamics*. Springer Berlin Heidelberg, 2006.

[46] Gustav Bihlmayer, Paul Noël, Denis V. Vyalikh, Evgueni V. Chulkov, and Aurélien Manchon. Rashba-like physics in condensed matter. *Nature Reviews Physics*, 4(10):642–659, August 2022.

[47] L. Petersen and P. Hedegård. A simple tight-binding model of spin–orbit splitting of sp-derived surface states. *Surface Science*, 459(1-2):49–56, July 2000.

[48] G. Bihlmayer, Yu.M. Koroteev, P.M. Echenique, E.V. Chulkov, and S. Blügel. The rashba-effect at metallic surfaces. *Surface Science*, 600(18):3888–3891, September 2006.

[49] Patrick Bruno. Tight-binding approach to the orbital magnetic moment and magnetocrystalline anisotropy of transition-metal monolayers. *Physical Review B*, 39:865–868, 1989.

[50] Gerrit van der Laan. Microscopic origin of magnetocrystalline anisotropy in transition metal thin films. *Journal of Physics: Condensed Matter*, 10:3239–3253, 4 1998.

[51] E. Abate and M. Asdente. Tight-binding calculation of 3*d* bands of fe with and without spin-orbit coupling. *Phys. Rev.*, 140:A1303–A1308, Nov 1965.

[52] B Dieny and M Chshiev. Perpendicular magnetic anisotropy at transition metal/oxide interfaces and applications. *Reviews of Modern Physics*, 89, 6 2017.

[53] Hans Christoph Siegmann Joachim Stöhr. *Magnetism: From Fundamentals to Nanoscale Dynamics*. Springer Berlin Heidelberg, Berlin, Heidelberg, 1 edition, 2006.

[54] S. Monso, B. Rodmacq, S. Auffret, G. Casali, F. Fettar, B. Gilles, B. Dieny, and P. Boyer. Crossover from in-plane to perpendicular anisotropy in pt/cofe/alo x sandwiches as a function of al oxidation: A very accurate control of the oxidation of tunnel barriers. *Applied Physics Letters*, 80:4157–4159, 2002.

[55] Y. Fan, K. J. Smith, G. Lüpke, A. T. Hanbicki, R. Goswami, C. H. Li, H. B. Zhao, and B. T. Jonker. Exchange bias of the interface spin system at the fe/MgO interface. *Nature Nanotechnology*, 8(6):438–444, June 2013.

[56] Manish K. Niranjan, Chun Gang Duan, Sitaram S. Jaswal, and Evgeny Y. Tsymbal. Electric field effect on magnetization at the fe/mgo(001) interface. *Applied Physics Letters*, 96:1–4, 2010.

[57] H. X. Yang, M. Chshiev, A. Kalitsov, A. Schuhl, and W. H. Butler. Effect of structural relaxation and oxidation conditions on interlayer exchange coupling in fe mgo fe tunnel junctions. *Applied Physics Letters*, 96:2–4, 2010.

[58] Xufeng Zhang, Tianyu Liu, Michael E. Flatté, and Hong X. Tang. Electric-field coupling to spin waves in a centrosymmetric ferrite. *Physical Review Letters*, 113:037202, 7 2014.

[59] A. Hallal, H. X. Yang, B. Dieny, and M. Chshiev. Anatomy of perpendicular magnetic anisotropy in fe/mgo magnetic tunnel junctions: First-principles insight. *Physical Review B - Condensed Matter and Materials Physics*, 88:1–5, 2013.

[60] Kohji Nakamura, Riki Shimabukuro, Yuji Fujiwara, Toru Akiyama, Tomonori Ito, and A. J. Freeman. Giant modification of the magnetocrystalline anisotropy in transition-metal monolayers by an external electric field. *Phys. Rev. Lett.*, 102:187201, May 2009.

[61] Chun-Gang Duan, Julian P. Velev, R. F. Sabirianov, Ziqiang Zhu, Junhao Chu, S. S. Jaswal, and E. Y. Tsymbal. Surface magnetoelectric effect in ferromagnetic metal films. *Phys. Rev. Lett.*, 101:137201, Sep 2008.

[62] Aymen Fassatoui, Jose Peña Garcia, Laurent Ranno, Jan Vogel, Anne Bernand-Mantel, Hélène Béa, Sergio Pizzini, and Stefania Pizzini. Reversible and irreversible voltage manipulation of interfacial magnetic anisotropy in pt / co /oxide multilayers. *Physical Review Applied*, 14:1–11, 2020.

[63] Dustin A. Gilbert, Alexander J. Grutter, Elke Arenholz, Kai Liu, B. J. Kirby, Julie A. Borchers, and Brian B. Maranville. Structural and magnetic depth profiles of magneto-ionic heterostructures beyond the interface limit. *Nature Communications*, 7:12264, 7 2016.

[64] Noel D'Souza, Mohammad Salehi Fashami, Supriyo Bandyopadhyay, and Jayasimha Atulasimha. Experimental clocking of nanomagnets with strain for ultralow power boolean logic. *Nano Letters*, 16(2):1069–1075, January 2016.

[65] Xiang Li, Albert Lee, Seyed Armin Razavi, Hao Wu, and Kang L. Wang. Voltage-controlled magnetoelectric memory and logic devices. *MRS Bulletin*, 43(12):970–977, December 2018.

[66] J. de Rojas, A. Quintana, G. Rius, C. Stefani, N. Domingo, J. L. Costa-Krämer, E. Menéndez, and J. Sort. Voltage control of magnetism with magneto-ionic approaches: Beyond voltage-driven oxygen ion migration. *Applied Physics Letters*, 120(7):070501, February 2022.

[67] Tôru Moriya. Anisotropic superexchange interaction and weak ferromagnetism. *Physical Review*, 120:91–98, 10 1960.

[68] I Dzyaloshinsky. A thermodynamic theory of "weak" ferromagnetism of antiferromagnetics. *Journal of Physics and Chemistry of Solids*, 4:241–255, 1958.

[69] Karin Everschor-Sitte, Jan Masell, Robert M Reeve, and Mathias Kläui. Perspective: Magnetic skyrmions—overview of recent progress in an active research field. *Journal of Applied Physics*, 124(24), 2018.

[70] Naoto Nagaosa and Yoshinori Tokura. Topological properties and dynamics of magnetic skyrmions. *Nature Nanotechnology*, 8:899–911, 2013.

[71] Albert Fert, Vincent Cros, and João Sampaio. Skyrmions on the track. *Nature Nanotechnology 2013 8:3*, 8:152–156, 3 2013.

[72] P. W. Anderson. Antiferromagnetism. theory of superexchange interaction. *Physical Review*, 79(2):350–356, July 1950.

[73] T. Yildirim, A. B. Harris, Amnon Aharony, and O. Entin-Wohlman. Anisotropic spin hamiltonians due to spin-orbit and coulomb exchange interactions. *Phys. Rev. B*, 52:10239–10267, Oct 1995.

[74] A. Fert and Peter M. Levy. Role of anisotropic exchange interactions in determining the properties of spin-glasses. *Phys. Rev. Lett.*, 44:1538–1541, Jun 1980.

[75] S. Mühlbauer. Skyrmion lattice in a chiral magnet (science (2009) (915)). *Science*, 333:1381, 2011.

[76] X. Z. Yu, Y. Onose, N. Kanazawa, J. H. Park, J. H. Han, Y. Matsui, N. Nagaosa, and Y. Tokura. Real-space observation of a two-dimensional skyrmion crystal. *Nature*, 465(7300):901–904, June 2010.

[77] XZ Yu, Naoya Kanazawa, Yoshinori Onose, K Kimoto, WZ Zhang, Shintaro Ishiwata, Yoshio Matsui, and Yoshinori Tokura. Near room-temperature formation of a skyrmion crystal in thin-films of the helimagnet fege. *Nature materials*, 10(2):106–109, 2011.

[78] Jacob Gayles, F Freimuth, T Schena, G Lani, P Mavropoulos, RA Duine, S Blügel, J Sinova, and Y Mokrousov. Dzyaloshinskii-moriya interaction and hall effects in the skyrmion phase of mn 1- x fe x ge. *Physical review letters*, 115(3):036602, 2015.

[79] Takashi Koretsune, Naoto Nagaosa, and Ryotaro Arita. Control of dzyaloshinskii-moriya interaction in mn1-xFexGe: a first-principles study. *Scientific Reports*, 5(1), August 2015.

[80] Hongxin Yang, Olivier Boulle, Vincent Cros, Albert Fert, and Mairbek Chshiev. Controlling dzyaloshinskii-moriya interaction via chirality dependent atomic-layer stacking, insulator capping and electric field. *Scientific Reports*, 8:1–7, 2018.

[81] Hongxin Yang, André Thiaville, Stanislas Rohart, Albert Fert, and Mairbek Chshiev. Anatomy of dzyaloshinskii-moriya interaction at co/pt interfaces. *Physical Review Letters*, 115, 2015.

[82] Hongxin Yang, Gong Chen, Alexandre AC Cotta, Alpha T N'Diaye, Sergey A Nikolaev, Edmar A Soares, Waldemar AA Macedo, Kai Liu, Andreas K Schmid, Albert Fert, et al. Significant dzyaloshinskii–moriya interaction at

graphene–ferromagnet interfaces due to the rashba effect. *Nature materials*, 17(7):605–609, 2018.

[83] Kyoung-Whan Kim, Hyun-Woo Lee, Kyung-Jin Lee, and Mark D Stiles. Chirality from interfacial spin-orbit coupling effects in magnetic bilayers. *Physical review letters*, 111(21):216601, 2013.

[84] F Ibrahim, H X Yang, A Hallal, B Dieny, and M Chshiev. Anatomy of electric field control of perpendicular magnetic anisotropy at fe/{MgO} interfaces. *Physical Review B*, 93, 1 2016.

[85] I. A. Ado, A. Qaiumzadeh, R. A. Duine, A. Brataas, and M. Titov. Asymmetric and symmetric exchange in a generalized 2d rashba ferromagnet. *Physical Review Letters*, 121, 2018.

[86] Ivan A. Ado, A. Qaiumzadeh, A. Brataas, and M. Titov. Chiral ferromagnetism beyond lifshitz invariants. *arXiv*, 2019.

[87] Stewart E. Barnes, Jun'Ichi Ieda, and Sadamichi Maekawa. Rashba spin-orbit anisotropy and the electric field control of magnetism. *Scientific Reports*, 4:1–5, 2014.

[88] A J Schellekens, A van den Brink, J H Franken, H J M Swagten, and B Koopmans. Electric-field control of domain wall motion in perpendicularly magnetized materials. *Nature Communications*, 3, 2012.

[89] K. H. He, J. S. Chen, and Y. P. Feng. First principles study of the electric field effect on magnetization and magnetic anisotropy of feco/mgo(001) thin film. *Applied Physics Letters*, 99, 2011.

[90] Ioan Mihai Miron, Thomas Moore, Helga Szambolics, Liliana Daniela Buda-Prejbeanu, Stéphane Auffret, Bernard Rodmacq, Stefania Pizzini, Jan Vogel, Marlio Bonfim, Alain Schuhl, and Gilles Gaudin. Fast current-induced domain-wall motion controlled by the rashba effect. *Nature Materials*, 10:419–423, 6 2011.

[91] A. D. Caviglia, M. Gabay, S. Gariglio, N. Reyren, C. Cancellieri, and J. M. Triscone. Tunable rashba spin-orbit interaction at oxide interfaces. *Physical Review Letters*, 104:1–17, 2010.

[92] You Ba, Shihao Zhuang, Yike Zhang, Yutong Wang, Yang Gao, Hengan Zhou, Mingfeng Chen, Weideng Sun, Quan Liu, Guozhi Chai, Jing Ma, Ying Zhang, Huanfang Tian, Haifeng Du, Wanjun Jiang, Cewen Nan, Jia-Mian Hu, and Yonggang Zhao. Electric-field control of skyrmions in multiferroic heterostructure via magnetoelectric coupling. *Nature Communications*, 12(1), January 2021.

[93] W. Döring. Mikromagnetismus. In *Ferromagnetism / Ferromagnetismus*, pages 341–437. Springer Berlin Heidelberg, 1966.

[94] William Brown. *Micromagnetics*. J. Wiley, 1963.

[95] Markus Hoffmann and Stefan Blügel. Systematic derivation of realistic spin models for beyond-heisenberg solids. *Physical Review B*, 101, 2020.

[96] Franz Neumann. *Lectures on the theory of the elasticity of solid bodies and light ether*, volume 1. B.G Teubner, 1 edition, 1885.

[97] A. Bogdanov and A. Hubert. Thermodynamically stable magnetic vortex states in magnetic crystals. *Journal of Magnetism and Magnetic Materials*, 138:255–269, 12 1994.

[98] Hongxin Yang, Jinghua Liang, and Qirui Cui. First-principles calculations for dzyaloshinskii–moriya interaction. *Nature Reviews Physics*, 5:43–61, 11 2022.

[99] Giorgio Bertotti. *Hysteresis in Magnetism*. Elsevier, 1998.

[100] Amikam Aharoni. Demagnetizing factors for rectangular ferromagnetic prisms. *Journal of Applied Physics*, 83:3432–3434, 3 1998.

[101] G. A. T. Allan. Critical temperatures of ising lattice films. *Physical Review B*, 1(1):352–356, January 1970.

[102] Ado Dresselhaus S. ,Mildred, Dresselhaus, Gene , Jorio. *Group Theory: Application to the Physics of Condensed Matter*. Springer Berlin Heidelberg, Berlin, Heidelberg, 2008.

[103] Albert Fert, Nicolas Reyren, and Vincent Cros. Magnetic skyrmions: advances in physics and potential applications. *Nature Reviews Materials*, 2:17031, 7 2017.

[104] U. K. Rößler, A. N. Bogdanov, and C. Pfleiderer. Spontaneous skyrmion ground states in magnetic metals. *Nature*, 442(7104):797–801, aug 2006.

[105] Shijiang Luo and Long You. Skyrmion devices for memory and logic applications. *APL Materials*, 9:050901, 5 2021.

[106] A. N. Bogdanov, U. K. Rößler, M. Wolf, and K. H. Müller. Magnetic structures and reorientation transitions in noncentrosymmetric uniaxial antiferromagnets. *Physical Review B*, 66:214410, 12 2002.

[107] A O Leonov, T L Monchesky, N Romming, A Kubetzka, A N Bogdanov, and R Wiesendanger. The properties of isolated chiral skyrmions in thin magnetic films. *New Journal of Physics*, 18:065003, 5 2016.

[108] J.-E. Wegrowe and M.-C. Ciornei. Magnetization dynamics, gyromagnetic relation, and inertial effects. *American Journal of Physics*, 80:607–611, 2012.

[109] T.L. Gilbert. A phenomenological theory of damping in ferromagnetic materials. *IEEE Transactions on Magnetics*, 40(6):3443–3449, 2004.

[110] Oleksandr V Pylypovskyi, Volodymyr P Kravchuk, Oleksii M Volkov, Jürgen Faßbender, Denis D Sheka, and Denys Makarov. Unidirectional tilt of domain walls in equilibrium in biaxial stripes with dzyaloshinskii–moriya interaction. *Journal of Physics D: Applied Physics*, 53(39):395003, July 2020.

[111] AV Khvalkovskiy, V Cros, D Apalkov, V Nikitin, M Krounbi, KA Zvezdin, A Anane, J Grollier, and A Fert. Matching domain-wall configuration and spin-orbit torques for efficient domain-wall motion. *Physical Review B*, 87(2):020402, 2013.

[112] Debanjan Bhowmik, Mark E. Nowakowski, Long You, OukJae Lee, David Keating, Mark Wong, Jeffrey Bokor, and Sayeef Salahuddin. Deterministic domain wall motion orthogonal to current flow due to spin orbit torque. *Scientific Reports*, 5:11823, 7 2015.

[113] Gen Tatara and Hiroshi Kohno. Theory of current-driven domain wall motion: Spin transfer versus momentum transfer. *Physical Review Letters*, 92:1–4, 2004.

[114] Takaya Okuno, Duck-Ho Kim, Se-Hyeok Oh, Se Kwon Kim, Yuushou Hirata, Tomoe Nishimura, Woo Seung Ham, Yasuhiro Futakawa, Hiroki Yoshikawa, Arata Tsukamoto, Yaroslav Tserkovnyak, Yoichi Shiota, Takahiro Moriyama, Kab-Jin Kim, Kyung-Jin Lee, and Teruo Ono. Spin-transfer torques for domain wall motion in antiferromagnetically coupled ferrimagnets. *Nature Electronics*, 2(9):389–393, September 2019.

[115] Mouad Fattouhi, Felipe Garcia-Sanchez, Rocio Yanes, Victor Raposo, Eduardo Martinez, and Luis Lopez-Diaz. Absence of walker breakdown in the dynamics of chiral néel domain walls driven by in-plane strain gradients. *Physical Review Applied*, 18:044023, 10 2022.

[116] Durgesh Kumar, Tianli Jin, Rachid Sbiaa, Mathias Kläui, Subhankar Bedanta, Shunsuke Fukami, Dafine Ravelosona, See-Hun Yang, Xiaoxi Liu, and S.N. Piramanayagam. Domain wall memory: Physics, materials, and devices. *Physics Reports*, 958:1–35, 5 2022.

[117] Stuart Parkin and See-Hun Yang. Memory on the racetrack. *Nature Nanotechnology*, 10:195–198, 3 2015.

[118] Ke Gu, Yicheng Guan, Binoy Krishna Hazra, Hakan Deniz, Andrea Migliorini, Wenjie Zhang, and Stuart S. P. Parkin. Three-dimensional racetrack memory devices designed from freestanding magnetic heterostructures. *Nature Nanotechnology*, 17(10):1065–1071, September 2022.

[119] Mei Li, Bin Xi, Yongjun Liu, and Jie Lu. Enhancement of the walker limit by bulk dzyaloshinskii-moriya interaction. *Physical Review B*, 105:14440, 2022.

[120] Daniel Hill, Valeriy Slastikov, and Oleg Tchernyshyov. Chiral magnetism: a geometric perspective. *SciPost Physics*, 10:078, 3 2021.

[121] Jürg Fröhlich and Urban M. Studer. Gauge invariance and current algebra in nonrelativistic many-body theory. *Rev. Mod. Phys.*, 65:733–802, Jul 1993.

[122] Johan Ernest Mebius. Derivation of the euler-rodrigues formula for three-dimensional rotations from the general formula for four-dimensional rotations, 2007.

[123] Pierre Hohenberg and Walter Kohn. Inhomogeneous electron gas. *Physical Review*, 136(3B):B864–B871, 1964.

[124] Walter Kohn and L. J. Sham. Self-consistent equations including exchange and correlation effects. *Physical Review*, 140(4A):A1133–A1138, 1965.

[125] J. H. Wood and A. Michael Boring. Improved pauli hamiltonian for local-potential problems. *Phys. Rev. B*, 18:2701–2711, Sep 1978.

[126] A H MacDonald and S H Vosko. A relativistic density functional formalism. *Journal of Physics C: Solid State Physics*, 12(15):2977–2990, August 1979.

[127] M. Weinert, R. E. Watson, and J. W. Davenport. Total-energy differences and eigenvalue sums. *Physical Review B*, 32:2115–2119, 1985.

[128] Xindong Wang, Ding Sheng Wang, Wu Ruqian, and A. J. Freeman. Validity of the force theorem for magnetocrystalline anisotropy. *Journal of Magnetism and Magnetic Materials*, 159:337–341, 1996.

[129] The FLEUR project. https://www.flapw.de/.

[130] Daniel Wortmann, Gregor Michalicek, Nadjib Baadji, Markus Betzinger, Gustav Bihlmayer, Jens Bröder, Tobias Burnus, Jussi Enkovaara, Frank Freimuth, Christoph Friedrich, Christian-Roman Gerhorst, Sabastian Granberg Cauchi, Uliana Grytsiuk, Andrea Hanke, Jan-Philipp Hanke, Marcus Heide, Stefan Heinze, Robin Hilgers, Henning Janssen, Daniel Aaaron Klüppelberg, Roman Kovacik, Philipp Kurz, Marjana Lezaic, Georg K. H. Madsen, Yuriy Mokrousov, Alexander Neukirchen, Matthias Redies, Stefan Rost, Martin Schlipf, Arno Schindlmayr, Miriam Winkelmann, and Stefan Blügel. FLEUR. Zenodo, May 2023.

[131] D. Šabani, C. Bacaksiz, and M. V. Milošević. Ab initio methodology for magnetic exchange parameters: Generic four-state energy mapping onto a heisenberg spin hamiltonian. *Phys. Rev. B*, 102:014457, Jul 2020.

[132] R. Pachat, D. Ourdani, J.W. van der Jagt, M.-A. Syskaki, A. Di Pietro, Y. Roussigné, S. Ono, M.S. Gabor, M. Chérif, G. Durin, J. Langer, M. Belmeguenai, D. Ravelosona, and L. Herrera Diez. Multiple magnetoionic regimes in ta/co 20 fe 60 b 20/ hf o 2. *Physical Review Applied*, 15:064055, 6 2021.

[133] Martin Weisheit, Sebastian Fahler, Alain Marty, Yves Souche, Christiane Poinsignon, and Dominique Givord. Electric field-induced modification of magnetism in thin-film ferromagnets. *Science*, 315(5810):349–351, January 2007.

[134] G. H. O. Daalderop, P. J. Kelly, and M. F. H. Schuurmans. Magnetocrystalline anisotropy and orbital moments in transition-metal compounds. *Physical Review B*, 44(21):12054–12057, December 1991.

[135] Kohji Nakamura, Riki Shimabukuro, Yuji Fujiwara, Toru Akiyama, Tomonori Ito, and A. J. Freeman. Giant modification of the magnetocrystalline anisotropy in transition-metal monolayers by an external electric field. *Physical Review Letters*, 102(18), May 2009.

[136] Chris Leighton. Electrolyte-based ionic control of functional oxides. *Nature Materials*, 18(1):13–18, December 2018.

[137] S. Ono, S. Seki, R. Hirahara, Y. Tominari, and J. Takeya. High-mobility, low-power, and fast-switching organic field-effect transistors with ionic liquids. *Applied Physics Letters*, 92(10):103313, March 2008.

[138] A. Manchon, C. Ducruet, L. Lombard, S. Auffret, B. Rodmacq, B. Dieny, S. Pizzini, J. Vogel, V. Uhlíř, M. Hochstrasser, and G. Panaccione. Analysis of oxygen induced anisotropy crossover in pt/co/MOx trilayers. *Journal of Applied Physics*, 104(4):043914, August 2008.

[139] Marcel Schie, Michael P. Müller, Martin Salinga, Rainer Waser, and Roger A. De Souza. Ion migration in crystalline and amorphous hfox. *Journal of Chemical Physics*, 146, 2017.

[140] L. Herrera Diez, Y.T. Liu, D.A. Gilbert, M. Belmeguenai, J. Vogel, S. Pizzini, E. Martinez, A. Lamperti, J.B. Mohammedi, A. Laborieux, Y. Roussigné, A.J. Grutter, E. Arenholtz, P. Quarterman, B. Maranville, S. Ono, M. Salah El Hadri, R. Tolley, E.E. Fullerton, L. Sanchez-Tejerina, A. Stashkevich, S.M. Chérif, A.D. Kent, D. Querlioz, J. Langer, B. Ocker, and D. Ravelosona. Nonvolatile ionic modification of the dzyaloshinskii-moriya interaction. *Phys. Rev. Appl.*, 12:034005, Sep 2019.

[141] M.E. Bridge and R.M. Lambert. Oxygen chemisorption, surface oxidation, and the oxidation of carbon monoxide on cobalt (0001). *Surface Science*, 82(2):413–424, apr 1979.

[142] C.R. Brundle. Oxygen adsorption and thin oxide formation at iron surfaces: An XPS/UPS study. *Surface Science*, 66(2):581–595, sep 1977.

[143] Gary W. Simmons and Daniel J. Dwyer. A LEED-AES study of the initial stages of oxidation of fe (001). *Surface Science*, 48(2):373–392, mar 1975.

[144] L. Herrera Diez, F. García-Sánchez, J.-P. Adam, T. Devolder, S. Eimer, M. S. El Hadri, A. Lamperti, R. Mantovan, B. Ocker, and D. Ravelosona. Controlling magnetic domain wall motion in the creep regime in hesup/supirradiated CoFeB/MgO films with perpendicular anisotropy. *Applied Physics Letters*, 107(3):032401, jul 2015.

[145] Adriano Di Pietro, Rohit Pachat, Lei Qiao, Liza Herrera-Diez, Johannes W. van der Jagt, Silvia Picozzi, Dafiné Ravelosona, Wei Ren, and Gianfranco Durin. iab initio/i study of magneto-ionic mechanisms in ferromagnet/oxide multilayers. *Physical Review B*, 107(17), May 2023.

[146] Roxana Alina One, Hélène Béa, Sever Mican, Marius Joldos, Pedro Brandão Veiga, Bernard Dieny, Liliana D. Buda-Prejbeanu, and Coriolan Tiusan. Route towards efficient magnetization reversal driven by voltage control of magnetic anisotropy. *Scientific Reports*, 11:1–11, 2021.

[147] Joko Suwardy, Minori Goto, Yoshishige Suzuki, and Shinji Miwa. Voltage-controlled magnetic anisotropy and dzyaloshinskii-moriya interactions in {CoNi}/{MgO} and {CoNi}/pd/{MgO}. *Japanese Journal of Applied Physics*, 58:60917, 6 2019.

[148] Z Huang, I Stolichnov, A Bernand-Mantel, J Borrel, S Auffret, G Gaudin, O Boulle, S Pizzini, L Ranno, L Herrera Diez, and N Setter. Ferroelectric control of magnetic domains in ultra-thin cobalt layers. *Applied Physics Letters*, 103:222902, 11 2013.

[149] H. G. Flynn. Transport phenomena. *Physics Today*, 15:96–98, 1962.

[150] Na Wu, Wei Wang, Yu Wei, and Taohai Li. Studies on the effect of nano-sized mgo in magnesium-ion conducting gel polymer electrolyte for rechargeable magnesium batteries. *Energies*, 10, 2017.

[151] T. Liu, Y. Zhang, J. W. Cai, and H. Y. Pan. Thermally robust mo/cofeb/mgo trilayers with strong perpendicular magnetic anisotropy. *Scientific Reports*, 4:1–6, 2014.

[152] S. Ikeda, K. Miura, H. Yamamoto, K. Mizunuma, H. D. Gan, M. Endo, S. Kanai, J. Hayakawa, F. Matsukura, and H. Ohno. A perpendicular-anisotropy cofeb-mgo magnetic tunnel junction. *Nature Materials*, 9:721–724, 2010.

[153] Le Zhi Wang, Xiang Li, Taisuke Sasaki, Kin Wong, Guo Qiang Yu, Shou Zhong Peng, Chao Zhao, Tadakatsu Ohkubo, Kazuhiro Hono, Wei Sheng Zhao, and Kang Long Wang. High voltage-controlled magnetic anisotropy and interface magnetoelectric effect in sputtered multilayers annealed at high temperatures. *Science China: Physics, Mechanics and Astronomy*, 63, 2020.

[154] R Pachat, D Ourdani, J W Van Der Jagt, M Syskaki, A Di Pietro, and M Belmeguenai. Multiple magneto-ionic regimes in ta / cofeb / hfo 2. pages 2–9.

[155] O. Krogh Andersen. Linear methods in band theory. *Phys. Rev. B*, 12:3060–3083, Oct 1975.

[156] John P. Perdew, Kieron Burke, and Matthias Ernzerhof. Generalized gradient approximation made simple. *Physical Review Letters*, 77:3865–3868, 1996.

[157] Weinan Lin, Baishun Yang, Andy Paul Chen, Xiaohan Wu, Rui Guo, Shaohai Chen, Liang Liu, Qidong Xie, Xinyu Shu, Yajuan Hui, Gan.167emMoog Chow, Yuanping Feng, Giovanni Carlotti, Silvia Tacchi, Hongxin Yang, and Jingsheng Chen. Perpendicular magnetic anisotropy and dzyaloshinskii-moriya interaction at an oxide/ferromagnetic metal interface. *Physical Review Letters*, 124, 5 2020.

[158] H X Yang, M Chshiev, B Dieny, J H Lee, A Manchon, and K H Shin. First-principles investigation of the very large perpendicular magnetic anisotropy at fe|{MgO} and co|{MgO} interfaces. *Physical Review B*, 84, 8 2011.

[159] P. Strange, J. B. Staunton, B. L. Györffy, and H. Ebert. First principles theory of magnetocrystalline anisotropy. *Physica B: Physics of Condensed Matter*, 1991.

[160] Bernd Zimmermann, Gustav Bihlmayer, Marie Böttcher, Mohammed Bouhassoune, Samir Lounis, Jairo Sinova, Stefan Heinze, Stefan Blügel, and Bertrand Dupé. Comparison of first-principles methods to extract magnetic parameters in ultrathin films: Co/pt(111). *Physical Review B*, 99, 2019.

[161] M. Heide, G. Bihlmayer, and S. Blügel. Describing dzyaloshinskii-moriya spirals from first principles. *Physica B: Condensed Matter*, 404:2678–2683, 2009.

[162] Piotr Błoński and Jürgen Hafner. Density-functional theory of the magnetic anisotropy of nanostructures: An assessment of different approximations. *Journal of Physics Condensed Matter*, 21, 2009.

[163] G. Kresse and J. Furthmüller. Efficiency of ab-initio total energy calculations for metals and semiconductors using a plane-wave basis set. *Computational Materials Science*, 6:15–50, 7 1996.

[164] G. Kresse and J. Furthmüller. Efficient iterative schemes for ab initio total-energy calculations using a plane-wave basis set. *Phys. Rev. B*, 54:11169–11186, Oct 1996.

[165] William H. Butler. Tunneling magnetoresistance from a symmetry filtering effect. *Science and Technology of Advanced Materials*, 9, 2008.

[166] M Košuth, V Popescu, H Ebert, and G Bayreuther. Magnetic anisotropy of thin fe films on GaAs. *EPL*, 72(5):816–822, December 2005.

[167] A. Kyritsakis, E. Baibuz, V. Jansson, and F. Djurabekova. Atomistic behavior of metal surfaces under high electric fields. *Physical Review B*, 99:205418, 2019.

[168] H. E. Stanley. Dependence of critical properties on dimensionality of spins. *Phys. Rev. Lett.*, 20:589–592, Mar 1968.

[169] Ulrich Nowak. Classical spin models. *Handbook of Magnetism and Advanced Magnetic Materials*, 12 2007.

[170] Gary M Wysin. *Magnetism theory: spin models*. IOP Publishing, 2015.

[171] E. Y. Vedmedenko, R. K. Kawakami, D. D. Sheka, P. Gambardella, A. Kirilyuk, A. Hirohata, C. Binek, O. Chubykalo-Fesenko, S. Sanvito, B. J. Kirby, J. Grollier, K. Everschor-Sitte, T. Kampfrath, C. Y. You, and A. Berger. The 2020 magnetism roadmap. *Journal of Physics D: Applied Physics*, 53, 2020.

[172] Frances Hellman, Materials Sciences Division, Lawrence Berkeley, Axel Hoffmann, Geoffrey S. D. Beach, Eric E Fullerton, Allan H Macdonald, and Daniel C Ralph. Interface-induced phenomena in magnetism. *Reviews of Modern Physics*, 89:025006, 2017.

[173] Benjamin W. Walker, Can Cui, Felipe Garcia-Sanchez, Jean Anne C. Incorvia, Xuan Hu, and Joseph S. Friedman. Skyrmion logic clocked via voltage-controlled magnetic anisotropy. *Applied Physics Letters*, 118, 5 2021.

[174] P. Bak and M. H. Jensen. Theory of helical magnetic structures and phase transitions in mnsi and fege. *Journal of Physics C: Solid State Physics*, 1980.

[175] L. D. Landau and E. M. Lifshitz. *Statistical Physics Part I*. Elsevier, Amsterdam, 3rd edition, 1980. bibtex: landa;b;sp80.

[176] A Ullah, B Balamurugan, W Zhang, S Valloppilly, X Li, R Pahari, L Yue, A Sokolov, D J Sellmyer, and R Skomski. Crystal structure and dzyaloshinskii-moriya micromagnetics. pages 1–5, 2019.

[177] Markus Hoffmann, Bernd Zimmermann, Gideon P Müller, Daniel Schürhoff, Nikolai S Kiselev, Christof Melcher, and Stefan Blügel. Antiskyrmions stabilized at interfaces by anisotropic dzyaloshinskii-moriya interactions. *Nature Communications*, 8:308, 2017.

[178] Helmut Kronmüller. *General Micromagnetic Theory and Applications*. Wiley, 5 2019.

[179] Patrizio Ansalone, Salvatore Perna, Massimiliano d'Aquino, Valentino Scalera, Claudio Serpico, and Vittorio Basso. A local gauge description of the interaction between magnetization and electric field in a ferromagnet. *IEEE Transactions on Magnetics*, 9464:8–11, 2021.

[180] Vittorio Basso and Patrizio Ansalone. Electric field effect on spin waves: Role of magnetic moment current. *Epl*, 130, 2020.

[181] K. Y. Guslienko. Gauge and emergent electromagnetic fields for moving magnetic topological solitons. *Epl*, 113, 2016.

[182] Patrizio Ansalone, E S Olivetti, A Magni, A Sola, and V Basso. Gauge theory applied to chiral magnets. *Epl*, 3, 2022.

[183] E. Wigner and F. Seitz. On the constitution of metallic sodium. *Phys. Rev.*, 43:804–810, May 1933.

[184] Leo J. Grady and Jonathan R. Polimeni. *Discrete Calculus*. Springer London, 2010.

[185] S. Bhagavantam and P. V. Pantulu. Generalized symmetry and neumann's principle. *Proceedings of the Indian Academy of Sciences - Section A*, 66:33–39, 7 1967.

[186] Mois Ilia Aroyo, Juan Manuel Perez-Mato, Cesar Capillas, Eli Kroumova, Svetoslav Ivantchev, Gotzon Madariaga, Asen Kirov, and Hans Wondratschek. Bilbao crystallographic server: I. databases and crystallographic computing programs. *Zeitschrift für Kristallographie - Crystalline Materials*, 221:15–27, 1 2006.

[187] K. P.W. Hall and S. H. Curnoe. Generalized model of mnsi-like spiral magnets. *Physical Review B*, 104:1–9, 2021.

[188] Y. Ishikawa, K. Tajima, D. Bloch, and M. Roth. Helical spin structure in manganese silicide mnsi. *Solid State Communications*, 19:525–528, 7 1976.

[189] Iosif Galanakis. Theory of heusler and full-heusler compounds. *Springer Series in Materials Science*, 222:3–36, 1 2016.

[190] Devinder Singh and Kuldeep Chand Verma. Magnetic properties of heusler alloys and nanoferrites. *Magnetic Skyrmions*, 1 2021.

[191] Kelvin Elphick, William Frost, Marjan Samiepour, Takahide Kubota, Koki Takanashi, Hiroaki Sukegawa, Seiji Mitani, and Atsufumi Hirohata. Heusler alloys for spintronic devices: review on recent development and future perspectives. *Science and Technology of Advanced Materials*, 22(1):235–271, March 2021.

[192] Peter Swekis, Jacob Gayles, Dominik Kriegner, Gerhard H. Fecher, Yan Sun, Sebastian T.B. Goennenwein, Claudia Felser, and Anastasios Markou. Role of magnetic exchange interactions in chiral-type hall effects of epitaxial mnxptsn films. *ACS Applied Electronic Materials*, 3:1323–1333, 2021.

[193] Caner Deger. Strain-enhanced dzyaloshinskii–moriya interaction at co/pt interfaces. *Scientific Reports 2020 10:1*, 10:1–7, 7 2020.

[194] Daniil A. Kitchaev, Irene J. Beyerlein, and Anton Van Der Ven. Phenomenology of chiral dzyaloshinskii-moriya interactions in strained materials. *Physical Review B*, 98:3–8, 2018.

[195] Giovanni Masciocchi, Mouad Fattouhi, Andreas Kehlberger, Luis Lopez-Diaz, Maria-Andromachi Syskaki, and Mathias Kläui. Strain-controlled domain wall injection into nanowires for sensor applications. *Journal of Applied Physics*, 130:183903, 11 2021.

[196] F. Klingbeil, S. D. Stölting, and J. McCord. Sensing of temperature through magnetooptical domain wall susceptibility. *Applied Physics Letters*, 118:092403, 3 2021.

[197] Zhaochu Luo, Aleš Hrabec, Trong Phuong Dao, Giacomo Sala, Simone Finizio, Junxiao Feng, Sina Mayr, Jörg Raabe, Pietro Gambardella, and Laura J. Heyderman. Current-driven magnetic domain-wall logic. *Nature*, 579:214–218, 3 2020.

[198] D. A. Allwood, G. Xiong, C. C. Faulkner, D. Atkinson, D. Petit, and R. P. Cowburn. Magnetic domain-wall logic. *Science*, 309:1688–1692, 9 2005.

[199] Jean Anne Currivan, Youngman Jang, M. D. Mascaro, M. A. Baldo, and C. A. Ross. Low energy magnetic domain wall logic in short, narrow, ferromagnetic wires. *IEEE Magnetics Letters*, 3:3000104–3000104, 2012.

[200] S. Glathe, I. Berkov, T. Mikolajick, and R. Mattheis. Experimental study of domain wall motion in long nanostrips under the influence of a transverse field. *Applied Physics Letters*, 93:2008–2010, 2008.

[201] A. Thiaville, Y. Nakatani, J. Miltat, and N. Vernier. Domain wall motion by spin-polarized current: a micromagnetic study. *Journal of Applied Physics*, 95:7049–7051, 6 2004.

[202] A Mougin, M Cormier, J. P Adam, P. J Metaxas, and J Ferré. Domain wall mobility, stability and walker breakdown in magnetic nanowires. *Europhysics Letters (EPL)*, 78:57007, 6 2007.

[203] Jun-Young Lee, Ki-Suk Lee, and Sang-Koog Kim. Remarkable enhancement of domain-wall velocity in magnetic nanostripes. *Applied Physics Letters*, 91:122513, 9 2007.

[204] Markus Hoffmann, Gideon P. Müller, Christof Melcher, and Stefan Blügel. Skyrmion-antiskyrmion racetrack memory in rank-one dmi materials. *Frontiers in Physics*, 9:668, 11 2021.

[205] Kosuke Karube, Licong Peng, Jan Masell, Xiuzhen Yu, Fumitaka Kagawa, Yoshinori Tokura, and Yasujiro Taguchi. Room-temperature antiskyrmions and sawtooth surface textures in a non-centrosymmetric magnet with s4 symmetry. *Nature Materials*, 20:335–340, 3 2021.

[206] Kaustuv Manna, Yan Sun, Lukas Muechler, Jürgen Kübler, and Claudia Felser. Heusler, weyl and berry. *Nature Reviews Materials 2018 3:8*, 3:244–256, 7 2018.

[207] A. Thiaville, J.M. Garcıa, and J. Miltat. Domain wall dynamics in nanowires. *Journal of Magnetism and Magnetic Materials*, 242-245:1061–1063, 4 2002.

[208] Yonglong Ga, Qirui Cui, Yingmei Zhu, Dongxing Yu, Liming Wang, Jinghua Liang, and Hongxin Yang. Anisotropic dzyaloshinskii-moriya interaction protected by d2d crystal symmetry in two-dimensional ternary compounds. *npj Computational Materials*, 8:128, 6 2022.

[209] Lorenzo Camosi, Nicolas Rougemaille, Olivier Fruchart, Jan Vogel, and Stanislas Rohart. Micromagnetics of antiskyrmions in ultrathin films. *Phys. Rev. B*, 97:134404, Apr 2018.

[210] Qirui Cui, Yingmei Zhu, Yonglong Ga, Jinghua Liang, Peng Li, Dongxing Yu, Ping Cui, and Hongxin Yang. Anisotropic Dzyaloshinskii–Moriya Interaction and Topological Magnetism in Two-Dimensional Magnets Protected by P 4 m 2 Crystal Symmetry. *Nano Lett.*, 22(6):2334–2341, mar 2022.

[211] J. M. D. Coey. *Magnetism and Magnetic Materials*. Cambridge University Press, 1 2001.

[212] S. Ali Nasseri, Eduardo Martinez, and Gianfranco Durin. Collective coordinate descriptions of magnetic domain wall motion in perpendicularly magnetized nanostructures under the application of in-plane fields. *Journal of Magnetism and Magnetic Materials*, 468:25–43, 12 2018.

[213] Danila Amoroso, Paolo Barone, and Silvia Picozzi. Interplay between single-ion and two-ion anisotropies in frustrated 2d semiconductors and tuning of magnetic structures topology. *Nanomaterials*, 11(8):1873, July 2021.

[214] Roland Winkler. Quasi-degenerate perturbation theory. In *Springer Tracts in Modern Physics*, pages 201–205. Springer Berlin Heidelberg, 2003.

Appendix A

The limits of the Hubbard model

A.1 The non-interacting limit $U = 0$

In the following we briefly discuss the non-interacting limit of the Hubbard Hamiltonian discussed in 2.1.1, i.e. a version of eq.(2.1) where we set $U = 0$ implying that the electrons are free to hop on the lattice but their charge does not interact via Coulomb repulsion. We proceed by calculating the free energy for the simplified case of a SC lattice with n.n interaction and site-independent hopping $t_{ij} = t$. For simplicity we suppress the spin index.

$$\mathscr{H} - \mu N = -t \sum_{<i,j>} c_i^\dagger c_j - \mu \sum_i c_i^\dagger c_i \tag{A.1}$$

We introduce this elementary model as it constitutes the starting point for many effective spin models discussed both in this dissertation and in the broader literature. Since the problem in this formulation is translationally invariant, we change to momentum space and diagonalize

$$c_i^\dagger = \frac{1}{\sqrt{V}} \sum_k e^{i\boldsymbol{k}\cdot\boldsymbol{R}_i} c_k^\dagger \tag{A.2}$$

$$\Rightarrow -\frac{t}{V} \sum_{<i,j>} \sum_{k,q} e^{i(\boldsymbol{k}\cdot\boldsymbol{R}_i - \boldsymbol{q}\cdot\boldsymbol{R}_j)} c_k^\dagger c_q - \frac{\mu}{V} \sum_{i,k,q} e^{i\boldsymbol{R}_i\cdot(\boldsymbol{k}-\boldsymbol{q})} c_k^\dagger c_q. \tag{A.3}$$

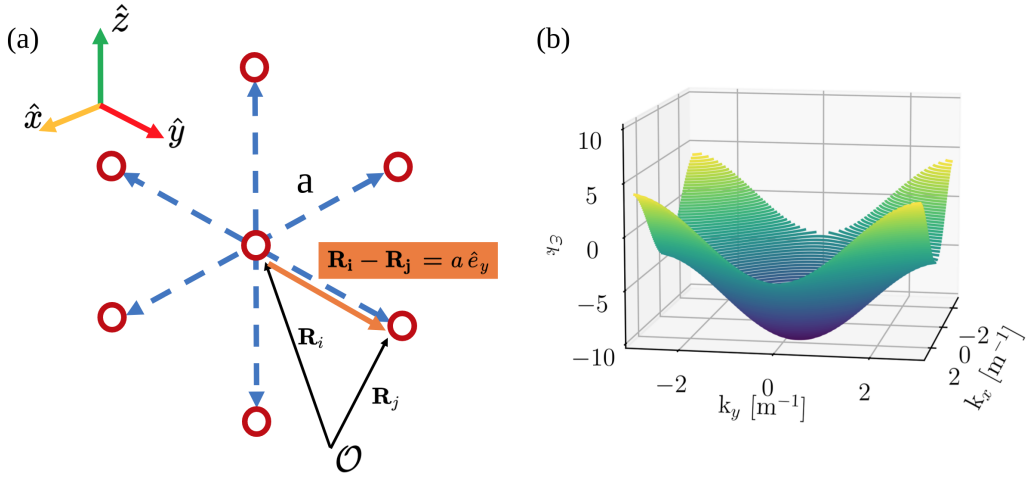

Fig. A.1 (a) Nearest neighbors in the SC lattice (b) Dispersion relation ε_k. To allow for a 3D visualization, the k_z-component is set to 0.

We recall $V\delta_{\boldsymbol{k},\boldsymbol{q}} = \sum_i e^{i\boldsymbol{R}_i(\boldsymbol{k}-\boldsymbol{q})}$ and the fact that we are working on a simple cubic (SC) lattice which allows us to rewrite $\boldsymbol{R}_j$ (see Fig.A.1)

$$\boldsymbol{R}_j - \boldsymbol{R}_i = \pm a\hat{e}_\alpha \tag{A.4}$$

$$\Rightarrow = -t\sum_k \sum_{\alpha=x,y,z} \underbrace{(e^{ia\boldsymbol{k}\cdot\hat{e}_\alpha} + e^{-ia\boldsymbol{k}\cdot\hat{e}_\alpha})}_{=2\cos(k_\alpha a)} c_k^\dagger c_k - \mu\sum_k c_k^\dagger c_k \tag{A.5}$$

$$\Rightarrow = \sum_k (\varepsilon_k - \mu) c_k^\dagger c_k \,, \varepsilon_k = -2t\sum_{\alpha=x,y,z}\cos(k_\alpha a) \tag{A.6}$$

where we have defined the energy as $\varepsilon_k = -2t\sum_{\alpha=x,y,z}\cos(k_\alpha a)$. We have plotted the dispersion relation ε_k in the simplified case of $k_z = 0$ in Fig.A.1 and we immediately recognize the valence band of a metallic material.

A.2 The non-hopping case $t = 0$

Another trivial limit of the Hubbard model is identified by the non-hopping case, where we allow the electrons to interact via Coulomb interaction, but deprive them of the freedom to hop around the lattice sites. This situation is described by the Hamiltonian

$$\mathscr{H} = \sum_i U_i n_{i,\uparrow} n_{i,\downarrow}, \tag{A.7}$$

where $n_{i,\sigma}$ represents the number operator with spin σ on atomic site i. The Hamiltonian is already in diagonal form and a general eigenstate in occupation number basis can be written in terms of Wannier functions [43] as follows

$$|\boldsymbol{x},\sigma\rangle = \left(\prod_{i\in X} c^{\dagger}_{i\uparrow}\right)\left(\prod_{i\in Y} c^{\dagger}_{i\downarrow}\right)|0\rangle\,, \tag{A.8}$$

where X and Y represent the lattice sites occupied by, respectively, $\uparrow$-spins and $\downarrow$-spins. The total number of electrons is fixed and is given by $N = N(\uparrow) + N(\downarrow)$. The eigenenergies are given by the eigenvalue equation

$$\mathscr{H}\,|\boldsymbol{x},\sigma\rangle = \left(\sum_i U_i\right)|\boldsymbol{x},\sigma\rangle = U\,|\boldsymbol{x},\sigma\rangle\,, \tag{A.9}$$

where we have defined $\left(\sum_i U_i\right) := U$. As we can see the physical picture in this case is of an ensemble of localized electron at atomic lattice sites. The fact that flipping pairs of spins leaves the energy invariant generates a huge ground state degeneracy, i.e. there are 2^N equivalent ground states. As we discuss in 2.1.1, this is the precisely the degeneracy that is broken by the perturbational inclusion of the hopping term t.

Appendix B

Quasi degenerate perturbation theory

In the following we provide a brief introduction to the problems and solution strategies of degenerate perturbation theory [214] as they are vastly used in the computation of effective spin models [95]. Assume we are dealing with a Hamiltonian of the form

$$\mathscr{H} = \mathscr{H}_0 + \mathscr{H}', \tag{B.1}$$

where $\mathscr{H}'$ is a perturbational term. We now make the assumption that the spectrum of this Hamiltonian can be partitioned in 2 weakly overlapping subsets of eigenfunctions $\mathrm{A} = \{|\psi_n\}\rangle$ and $\mathrm{B} = \{|\psi_m\rangle\}$. Perturbation theory states that it is possible to find a unitary operator S such that the rotated matrix elements $\tilde{\mathscr{H}}_{nm} = \langle\psi_m|\tilde{\mathscr{H}}|\psi_l\rangle = \langle\psi_m|e^{-S}He^{S}|\psi_l\rangle = 0$ up to a desired order in S (see Fig.B.1). We start by writing the Ansatz

$$\tilde{\mathscr{H}} = e^{-S}\mathscr{H}e^{S} \tag{B.2}$$

and expanding the exponential e^S giving us the rotated Hamiltonian

$$\tilde{\mathscr{H}} = (1 - S + \frac{1}{2}S^2 - \frac{1}{3!}S^3 + \cdots)\mathscr{H}(1 + S + \frac{1}{2}S^2 - \frac{1}{3!}S^3 + \cdots) = \sum_{j=0}^{\infty}\frac{[\mathscr{H}, S]^{(j)}}{j!}. \tag{B.3}$$

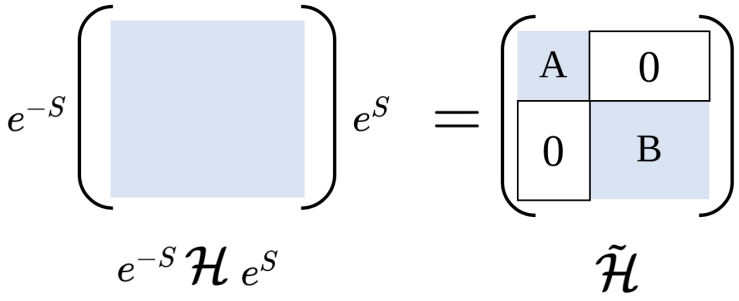

Fig. B.1 Effect of the unitary operator S acting on the matrix H

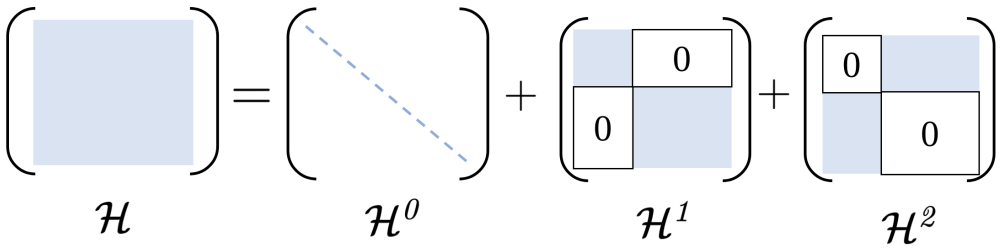

Fig. B.2 Decomposition of a matrix H in a diagonal ($\mathscr{H}^0$), block diagonal ($\mathscr{H}^1$) and non block-diagonal matrix ($\mathscr{H}^2$) component

Much like any matrix, we can separate $\mathscr{H}$ in one diagonal ($\mathscr{H}^0$), 1 block diagonal ($\mathscr{H}^1$) and 1 non block diagonal matrix ($\mathscr{H}^2$) as represented in Fig.B.2

$$\rightarrow \tilde{\mathscr{H}} = \sum_{j=0}^{\infty} \frac{[\mathscr{H}^0 + \mathscr{H}^1, S]^{(j)}}{j!} + \sum_{j=0}^{\infty} \frac{[\mathscr{H}^2, S]^{(j)}}{j!}. \tag{B.4}$$

Given that the decomposition in B.2 can be performed for any matrix, we can also perform it for the rotated matrix $\tilde{\mathscr{H}} = \tilde{\mathscr{H}}_d + \tilde{\mathscr{H}}_n = \left(\begin{array}{c|c} A & 0 \\ \hline 0 & B \end{array}\right) + \left(\begin{array}{c|c} 0 & C \\ \hline D & 0 \end{array}\right)$. Since S is non block diagonal (this is justified a posteriori) we can expect $\tilde{\mathscr{H}}_d$ to contain the following powers of the nested commutator

$$[\mathscr{H}^0 + \mathscr{H}^1, S]^{(j)} \ \forall \text{ j even}, \tag{B.5}$$

$$[\mathscr{H}^2, S]^{(j)} \ \forall \text{ j odd}. \tag{B.6}$$

We begin by noticing that the structure of the j^{th} nested commutator can be inferred by simply multiplying the operators.

$$\left(\begin{array}{c|c} A & 0 \\ \hline 0 & B \end{array}\right) \cdot \left(\begin{array}{c|c} 0 & C \\ \hline D & 0 \end{array}\right) = \left(\begin{array}{c|c} 0 & A \cdot C \\ \hline B \cdot D & 0 \end{array}\right) \Rightarrow \text{ even powers} \tag{B.7}$$

$$\left(\begin{array}{c|c} A & 0 \\ \hline 0 & B \end{array}\right) \cdot \left(\begin{array}{c|c} C & 0 \\ \hline 0 & B \end{array}\right) = \left(\begin{array}{c|c} A \cdot C & 0 \\ \hline 0 & B \cdot D \end{array}\right) \tag{B.8}$$

$$\left(\begin{array}{c|c} 0 & C \\ \hline D & 0 \end{array}\right) \cdot \left(\begin{array}{c|c} 0 & A \\ \hline B & 0 \end{array}\right) = \left(\begin{array}{c|c} C \cdot B & 0 \\ \hline 0 & D \cdot A \end{array}\right) \cdot \tag{B.9}$$

Therefore

$$[\mathscr{H}^0 + \mathscr{H}^1, S] = \left(\begin{array}{c|c} 0 & A \\ \hline 0 & B \end{array}\right) \rightarrow \text{ even powers } \rightarrow \left(\begin{array}{c|c} C & 0 \\ \hline 0 & D \end{array}\right) \tag{B.10}$$

$$[\mathscr{H}^2, S] = \left(\begin{array}{c|c} A & 0 \\ \hline 0 & B \end{array}\right) \rightarrow \text{ odd powers} \rightarrow \left(\begin{array}{c|c} C & 0 \\ \hline 0 & D \end{array}\right) \tag{B.11}$$

On the other hand, the non-block diagonal part of $\tilde{\mathscr{H}}$ (i.e $\tilde{\mathscr{H}_n}$) must contain the following powers of the nested commutators

$$[\mathscr{H}^0 + \mathscr{H}^1, S]^{(j)} \, \forall \text{ j odd}, \tag{B.12}$$

$$[\mathscr{H}^2, S]^{(j)} \, \forall \text{ j even}. \tag{B.13}$$

We can therefore split the even/odd contributions and write

$$\tilde{\mathscr{H}_d} = \sum_{j=0}^{\infty} \frac{[\mathscr{H}^0 + \mathscr{H}^1, S]^{(2j)}}{(2j)!} + \sum_{j=0}^{\infty} \frac{[\mathscr{H}^2, S]^{(2j+1)}}{(2j+1)!}, \tag{B.14}$$

$$\tilde{\mathscr{H}_a} = \sum_{j=0}^{\infty} \frac{[\mathscr{H}^0 + \mathscr{H}^1, S]^{(2j+1)}}{(2j+1)!} + \sum_{j=0}^{\infty} \frac{[\mathscr{H}^2, S]^{(2j)}}{(2j)!}. \tag{B.15}$$

With the above we can formulate a constraint on S that allows to compute its elements at the desired order in S. The requirement on S is that $\tilde{\mathscr{H}_n}(S) = 0$ at all orders of j. Since we assume that S is proportional to the perturbation parameter, we make the following Ansatz

$$S = \sum_n s^{(n)}, \tag{B.16}$$

where $\mathscr{O}(s^{(n)}) = t^n$. We now expand (B.15) and compare order by order in n

$$\tilde{\mathscr{H}}_d = \sum_{j,k=0}^{\infty} \frac{[\mathscr{H}^0 + \mathscr{H}^1, s^{(k)}]^{(2j)}}{(2j)!} + \sum_{j=0}^{\infty} \frac{[\mathscr{H}^2, s^{(k)}]^{(2j+1)}}{(2j+1)!}. \tag{B.17}$$

When comparing the orders we have to keep in mind

$$\mathscr{O}([\mathscr{H}^0, s^{(k)}]^{(j)}) = \mathscr{O}([\mathscr{H}^0, \underbrace{s^{(k)}] \cdots s^{(k)}}_{\text{j-times}}] = jk \tag{B.18}$$

$$\mathscr{O}([\mathscr{H}^{1,2}, s^{(k)}]^{(j)}) = jk + 1 \tag{B.19}$$

Solving at any given order we have

$$[\mathscr{H}^0, s^1] = -\mathscr{H}^2, \tag{B.20}$$

$$[\mathscr{H}^0, s^2] = -[\mathscr{H}^1, s^1], \tag{B.21}$$

$$[\mathscr{H}^0, s^3] = -[\mathscr{H}^1, s^2] - \frac{1}{3}[\mathscr{H}^1, s^1]^{(2)}. \tag{B.22}$$

If we now select a suitable basis in the 2 disjoint sub-spaces A and B introduced above (see Fig.B.1) we have

$$\langle n|s^{(1)}|m\rangle = -\frac{\langle n|\mathscr{H}^{(2)}|m\rangle}{(E_n - E_m)} \tag{B.23}$$

The second order equation follows analogously

$$(E_n - E_m)\langle n|s^{(2)}|m\rangle = -\sum_l \langle n|\mathscr{H}^{(1)}|l\rangle \langle l|s^{(1)}|m\rangle - \langle n|s^{(1)}|l\rangle \langle l|\mathscr{H}^{(1)}|m\rangle \tag{B.24}$$

$$= \sum_l \frac{\langle n|\mathscr{H}^{(1)}|l\rangle \langle l|\mathscr{H}^{(2)}|m\rangle}{E_l - E_m} - \frac{\langle n|\mathscr{H}^{(2)}|l\rangle \langle l|\mathscr{H}^{(1)}|m\rangle}{E_n - E_l} \tag{B.25}$$

Plugging these matrix elements in (B.14) we can recover the effective Hamiltonian. This method can be employed to compute the magnetic interaction terms of the Heisenberg Hamiltonian [95].

Appendix C

Moriya's derivation of DMI

In the following we present a detailed derivation of the DMI term in the framework of the Anderson superexchange model as performed by Moriya in his seminal paper [67]. The one electron Hamiltonian written in terms of annihilation and creation operators is written as follows

$$\mathscr{H} = \mathscr{H}_0 + \mathscr{H}_{SOC} = \sum_n \sum_i \varepsilon_{ni} [c^\dagger_{ni\uparrow} c_{ni\uparrow} + c^\dagger_{ni\downarrow} c_{ni\downarrow}] \tag{C.1}$$

$$\begin{aligned} &+ \sum_{i \neq j} \sum_{n,n',\sigma} b_{ji,n'n} \left(c^\dagger_{n'j\sigma} c_{ni\sigma} + c^\dagger_{ni\sigma} c_{n'j\sigma} \right) + \\ &+ \mathscr{C}^x_{ji,n'n} \left(c^\dagger_{n'j\sigma} c_{ni-\sigma} - c^\dagger_{ni\sigma} c_{n'j-\sigma} \right) - \\ &- i \mathscr{C}^y_{ji,n'n} \left(c^\dagger_{n'j-\sigma} c_{ni\sigma} + c^\dagger_{ni\sigma} c_{n'j-\sigma} \right) + \\ &+ \mathscr{C}^z_{ji,n'n}(2\sigma) \left(c^\dagger_{n'j\sigma} c_{ni\sigma} - c^\dagger_{ni\sigma} c_{n'j\sigma} \right) \end{aligned} \tag{C.2}$$

C.1 The x-component

Expanding the expression (2.88)

$$\begin{aligned} &\sum_\sigma b_{ji,n'n} \left(c^\dagger_{n'j\sigma} c_{ni\sigma} + c^\dagger_{ni\sigma} c_{n'j\sigma} \right) + \mathscr{C}^x_{ji,n'n} \left(c^\dagger_{n'j\sigma} c_{ni-\sigma} - c^\dagger_{ni\sigma} c_{n'j-\sigma} \right) \times \\ &\sum_\eta b_{ij,nn'} \left(c^\dagger_{ni\eta} c_{n'j\eta} + c^\dagger_{n'j\eta} c_{ni\eta} \right) + \mathscr{C}^x_{ij,nn'} \left(c^\dagger_{ni-\eta} c_{n'j\eta} - c^\dagger_{n'j-\eta} c_{ni\eta} \right) \end{aligned} \tag{C.3}$$

By carrying out the multiplication and keeping the terms $\propto \mathscr{C}^x b$, we have

$$\sum_{\sigma\eta} b_{ji,n'n} \mathscr{C}^x_{ij,nn'} \left(c^\dagger_{n'j\sigma} c_{ni\sigma} c^\dagger_{ni-\eta} c_{n'j\eta} - c^\dagger_{ni\sigma} c_{n'j\sigma} c^\dagger_{n'j-\eta} c_{ni\eta} \right) + \\ +(i \leftrightarrow j) \tag{C.4}$$

where the notation $(i \leftrightarrow j)$ indicates a term identical to the first one but with exchanged i and j. We can rearrange the creation operators in order to have j operators first.

$$c^\dagger_{n'j\sigma} c_{ni\sigma} c^\dagger_{ni-\eta} c_{n'j\eta} = c^\dagger_{n'j\sigma} c_{n'j\eta} (\delta_{\sigma,-\eta} - c^\dagger_{ni-\eta} c_{ni\sigma}) \tag{C.5}$$

$$c^\dagger_{ni\sigma} c_{n'j\sigma} c^\dagger_{n'j-\eta} c_{ni\eta} = (\delta_{\sigma,-\eta} - c^\dagger_{n'j-\eta} c_{n'j\sigma}) c^\dagger_{ni\sigma} c_{ni\eta} \tag{C.6}$$

$$\sum_{\sigma\eta} b_{ji,n'n} \mathscr{C}^x_{ij,nn'} \left(c^\dagger_{n'j-\eta} c_{n'j\sigma} c^\dagger_{ni\sigma} c_{ni\eta} - c^\dagger_{n'j\sigma} c_{n'j\eta} c^\dagger_{ni-\eta} c_{ni\sigma} \right) + \\ +(i \leftrightarrow j) \tag{C.7}$$

We used the fact that the term

$$\sum_{i \neq j} \sum_{\sigma} c^\dagger_{n'j\sigma} c_{n'j-\sigma} - c^\dagger_{ni\sigma} c_{ni-\sigma} \tag{C.8}$$

vanishes in the sum over i, j because it is antisymmetric under the exchange of these two indices. We now introduce a new notation for the operator strings of the form

$$\Lambda_A(j,i) := \sum_{\sigma} c^\dagger_{n'j\sigma} \underbrace{c_{n'j-\sigma}}_{position A} c^\dagger_{ni\sigma} c_{ni\sigma} \tag{C.9}$$

Basically the index of Λ indicates the location of the spin index which appears with an opposite sign in the summation. Using this compact notation we have

$$\sum_{\sigma,\eta} c^\dagger_{n'j-\eta} c_{n'j\sigma} c^\dagger_{ni\sigma} c_{ni\eta} = \Lambda_1(j,i) + \Lambda_4(j,i) \tag{C.10}$$

$$\sum_{\sigma,\eta} c^\dagger_{n'j\sigma} c_{n'j\eta} c^\dagger_{ni-\eta} c_{ni\sigma} = \Lambda_3(j,i) + \Lambda_2(j,i) \tag{C.11}$$

This change of notation allows us to write eq.(C.7) as

$$\Rightarrow\ b_{ji,n'n}\mathscr{C}^{x}_{ij,nn'}\left(\Lambda_1(j,i)+\Lambda_4(j,i)-\Lambda_3(j,i)-\Lambda_2(j,i)\right)+(i\leftrightarrow j) \tag{C.12}$$

Furthermore, we notice the following property of the Λ's

$$\Lambda_1(i,j)\leftrightarrow\Lambda_3(j,i) \tag{C.13}$$
$$\Lambda_2(i,j)\leftrightarrow\Lambda_4(j,i) \tag{C.14}$$

Meaning the term with $i\leftrightarrow j$ becomes

$$-b_{ij,nn'}\mathscr{C}^{x}_{ij,nn'}\left(\Lambda_1(j,i)+\Lambda_4(j,i)-\Lambda_3(j,i)-\Lambda_2(j,i)\right) \tag{C.15}$$

Meaning the x-component of our effective Hamiltonian has the form

$$\left(b_{ji,n'n}\mathscr{C}^{x}_{ij,nn'}-b_{ij,nn'}\mathscr{C}^{x}_{ji,n'n}\right)\left(\Lambda_1+\Lambda_4-\Lambda_3-\Lambda_2\right) \tag{C.16}$$

where we have suppressed the i,j indices in the Λ_A to lighten the notation.

C.2 The y-component

Performing the same steps as the x-component we obtain the following form for the y-term

$$i\left(b_{ji,n'n}\mathscr{C}^{y}_{ij,nn'}-\mathscr{C}^{y}_{ji,n'n}b_{ij,nn'}\right)\left(\Lambda_3+\Lambda_4-\Lambda_1-\Lambda_2\right) \tag{C.17}$$

C.3 The z-component

For the z component we cannot use the same Λ notation as for the other 2 components. We can however perform the same steps as for the other 2 cases and obtain:

$$\left(b_{ji,n'n}\mathscr{C}^{z}_{ij,nn'}-\mathscr{C}^{z}_{ji,n'n}b_{ij,nn'}\right)\times \\ \times\sum_{\sigma}(2\sigma)\left(c^{\dagger}_{n'j\sigma}c_{n'j-\sigma}c^{\dagger}_{ni-\sigma}c_{ni\sigma}-c^{\dagger}_{n'j-\sigma}c_{n'j\sigma}c^{\dagger}_{ni\sigma}c_{ni-\sigma}\right) \tag{C.18}$$

One can now easily compare with the spin operators in second quantization and notice

$$(\boldsymbol{S}_j \times \boldsymbol{S}_i)_x = \frac{i}{4}(\Lambda_1 + \Lambda_4 - \Lambda_3 - \Lambda_2) \tag{C.19}$$

$$(\boldsymbol{S}_j \times \boldsymbol{S}_i)_y = \frac{1}{4}(\Lambda_3 + \Lambda_4 - \Lambda_1 - \Lambda_2) \tag{C.20}$$

$$(\boldsymbol{S}_j \times \boldsymbol{S}_i)_z = \frac{i}{4}\sum_{\sigma}(2\sigma)(c^{\dagger}_{n'j\sigma}c_{n'j-\sigma}c^{\dagger}_{ni-\sigma}c_{ni\sigma} - c^{\dagger}_{n'j-\sigma}c_{n'j\sigma}c^{\dagger}_{ni\sigma}c_{ni-\sigma}) \tag{C.21}$$

The effective Hamiltonian for the terms $\propto \mathscr{C}b$ becomes

$$\boldsymbol{D}(j,i)\cdot(\boldsymbol{S}_j \times \boldsymbol{S}_i) \tag{C.22}$$

Where

$$\boldsymbol{D}_{\alpha}(j,i) := \frac{4i}{U}[b_{ji,n'n}\mathscr{C}^{\alpha}_{ij,nn'} - \mathscr{C}^{\alpha}_{ji,n'n}b_{ij,nn'}]. \tag{C.23}$$

This is indeed in accordance with the result shown in [67], and demonstrates how the inclusion of SOC in the one electron Hamiltonain can indeed induce effective spin models where the so called DMI is present. A completely analogous procedure can be employed to calculate the expansion terms of eq.(2.88) that are $\propto \mathscr{C}^2$, yielding the effective Hamiltonian term

$$\boldsymbol{S}^T_j \overset{\leftrightarrow}{\Gamma}(j,i)\boldsymbol{S}_i, \tag{C.24}$$

Where $\overset{\leftrightarrow}{\Gamma}(j,i)$ is a 3×3 matrix of the form

$$\boldsymbol{C}_{ij,nn'}\otimes\boldsymbol{C}_{ji,n'n} + \boldsymbol{C}_{ji,n'n}\otimes\boldsymbol{C}_{ij,nn'} - \mathbb{I}\otimes(\boldsymbol{C}_{ij,nn'}\cdot\boldsymbol{C}_{ji,n'n}) \tag{C.25}$$

Appendix D

The finite difference code to compute exotic DMI terms in thin films

In the following we provide the code used to alter the MuMax3 section in order to include Lifshitz invariant terms of the form reported in eq.(3.53). As discussed in 6.3.2 any arbitrary DMI tensor can be decomposed in an antisymmetric part (iDMI), a symmetric traceless part (anisotropic DMI part) and a diagonal part (bMDI part) part. The additional term corresponding to the symmetric traceless part of DMI is the missing one to allow the calculation of magnetization dynamics in the presence of arbitrary DM contributions.

$$\hat{\boldsymbol{Q}}_{ij} = \underbrace{\begin{pmatrix} 0 & D_a \\ -D_a & 0 \end{pmatrix}}_{\text{iDMI} \rightarrow \textbf{implemented}} + \underbrace{\begin{pmatrix} D_b & D_s \\ D_s & -D_b \end{pmatrix}}_{\textbf{not implemented}} + \underbrace{\begin{pmatrix} D_t & 0 \\ 0 & D_t \end{pmatrix}}_{\text{bDMI} \rightarrow \textbf{implemented}} . \tag{D.1}$$

According to the discussion of Sec.3.3.1, the effective field of a DMI tensor of the form

$$\hat{\boldsymbol{Q}} = \begin{pmatrix} D_b & D_s \\ D_s & -D_b \end{pmatrix} \tag{D.2}$$

has the form

$$\boldsymbol{H}_{\text{eff}}^{(DMI)} = \begin{pmatrix} D_2 \partial_x m_z - D_1 \partial_y m_z \\ -[D_1 \partial_x m_z + D_2 \partial_y m_z] \\ 0 \end{pmatrix} \tag{D.3}$$

which can be translated in discrete form by considering the finite difference implementation of the partial derivative operators (see eqs.(5.79)-5.81)

$$H_{\text{eff},x}^{(DMI)}(i,j,k) = D_2 \frac{m_z(i+1,j,k) - m_z(i-1,j,k)}{2\Delta_x} - D_1 \frac{m_z(i,j+1,k) - m_z(i,j-1,k)}{2\Delta_y} \tag{D.4}$$

$$H_{\text{eff},y}^{(DMI)}(i,j,k) = -D_1 \frac{m_z(i+1,j,k) - m_z(i-1,j,k)}{2\Delta_x} - D_2 \frac{m_z(i,j+1,k) - m_z(i,j-1,k)}{2\Delta_y} \tag{D.5}$$

$$H_{\text{eff},z}^{(DMI)}(i,j,k) = 0 \tag{D.6}$$

```
#include <stdint.h>
#include "exchange.h"
#include "float3.h"
#include "stencil.h"
#include "amul.h"

// Exchange + Dzyaloshinskii-Moriya interaction according to
// Bagdanov and Rössler, PRL 87, 3, 2001. eq.8 (out-of-plane symmetry breaking).
// Taking into account proper boundary conditions.
// m: normalized magnetization
// H: effective field in Tesla
// D: dmi strength / Msat, in Tesla*m
// A: Aex/Msat
extern "C" __global__ void
adddmi(float* __restrict__ Hx, float* __restrict__ Hy, float* __restrict__ Hz,
       float* __restrict__ mx, float* __restrict__ my, float* __restrict__ mz,
       float* __restrict__ Ms_, float Ms_mul,
       float* __restrict__ aLUT2d, float* __restrict__ dLUT2d, uint8_t* __restrict__ regions,
       float cx, float cy, float cz, int Nx, int Ny, int Nz, uint8_t PBC, uint8_t OpenBC) {

    int ix = blockIdx.x * blockDim.x + threadIdx.x;
    int iy = blockIdx.y * blockDim.y + threadIdx.y;
    int iz = blockIdx.z * blockDim.z + threadIdx.z;

    if (ix >= Nx || iy >= Ny || iz >= Nz) {
        return;
    }

    int I = idx(ix, iy, iz);                    // central cell index
    float3 h = make_float3(0.0,0.0,0.0);        // add to H
    float3 m0 = make_float3(mx[I], my[I], mz[I]); // central m
    uint8_t r0 = regions[I];
    int i_;                                     // neighbor index

    if(is0(m0)) {
        return;
    }
```

```
// x derivatives (along length)
{
    float3 m1 = make_float3(0.0f, 0.0f, 0.0f);     // left neighbor
    i_ = idx(lclampx(ix-1), iy, iz);               // load neighbor m if inside grid, keep 0 otherwise
    if (ix-1 >= 0 || PBCx) {
        m1 = make_float3(mx[i_], my[i_], mz[i_]);
    }
    int r1 = is0(m1)? r0 : regions[i_];                // don't use inter region params if m1=0
    float A1 = aLUT2d[symidx(r0, r1)];                 // inter-region Aex
    float D1 = dLUT2d[symidx(r0, r1)];                 // inter-region Dex
    if (!is0(m1) || !OpenBC){                          // do nothing at an open boundary
        if (is0(m1)) {                                 // neighbor missing
            m1.x = m0.x - (-cx * (0.5f*D1/A1) * m0.z); // extrapolate missing m from Neumann BC's
            m1.y = m0.y;
            m1.z = m0.z + (-cx * (0.5f*D1/A1) * m0.x);
        }
        h   += (2.0f*A1/(cx*cx)) * (m1 - m0);          // exchange
        h.x += (D1/cx)*(- m1.z);
        h.z -= (D1/cx)*(- m1.x);
    }
}

{
    float3 m2 = make_float3(0.0f, 0.0f, 0.0f);     // right neighbor
    i_ = idx(hclampx(ix+1), iy, iz);
    if (ix+1 < Nx || PBCx) {
        m2 = make_float3(mx[i_], my[i_], mz[i_]);
    }
    int r2 = is0(m2)? r0 : regions[i_];
    float A2 = aLUT2d[symidx(r0, r2)];
    float D2 = dLUT2d[symidx(r0, r2)];
    if (!is0(m2) || !OpenBC){
        if (is0(m2)) {
            m2.x = m0.x - (cx * (0.5f*D2/A2) * m0.z);
            m2.y = m0.y;
            m2.z = m0.z + (cx * (0.5f*D2/A2) * m0.x);
        }
        h   += (2.0f*A2/(cx*cx)) * (m2 - m0);
        h.x += (D2/cx)*(m2.z);
        h.z -= (D2/cx)*(m2.x);
    }
}

// y derivatives (along height)
{
    float3 m1 = make_float3(0.0f, 0.0f, 0.0f);
    i_ = idx(ix, lclampy(iy-1), iz);
    if (iy-1 >= 0 || PBCy) {
        m1 = make_float3(mx[i_], my[i_], mz[i_]);
    }
    int r1 = is0(m1)? r0 : regions[i_];
    float A1 = aLUT2d[symidx(r0, r1)];
    float D1 = dLUT2d[symidx(r0, r1)];
    if (!is0(m1) || !OpenBC){
```

```
        if (is0(m1)) {
            m1.x = m0.x;
            m1.y = m0.y - (-cy * (0.5f*D1/A1) * m0.z);
            m1.z = m0.z + (-cy * (0.5f*D1/A1) * m0.y);
        }
        h   += (2.0f*A1/(cy*cy)) * (m1 - m0);
        h.y += (D1/cy)*(- m1.z);
        h.z -= (D1/cy)*(- m1.y);
    }
}

{
    float3 m2 = make_float3(0.0f, 0.0f, 0.0f);
    i_ = idx(ix, hclampy(iy+1), iz);
    if  (iy+1 < Ny || PBCy) {
        m2 = make_float3(mx[i_], my[i_], mz[i_]);
    }
    int r2 = is0(m2)? r0 : regions[i_];
    float A2 = aLUT2d[symidx(r0, r2)];
    float D2 = dLUT2d[symidx(r0, r2)];
    if (!is0(m2) || !OpenBC){
        if (is0(m2)) {
            m2.x = m0.x;
            m2.y = m0.y - (cy * (0.5f*D2/A2) * m0.z);
            m2.z = m0.z + (cy * (0.5f*D2/A2) * m0.y);
        }
        h   += (2.0f*A2/(cy*cy)) * (m2 - m0);
        h.y += (D2/cy)*(m2.z);
        h.z -= (D2/cy)*(m2.y);
    }
}

// only take vertical derivative for 3D sim
if (Nz != 1) {
    // bottom neighbor
    {
        i_  = idx(ix, iy, lclampz(iz-1));
        float3 m1  = make_float3(mx[i_], my[i_], mz[i_]);
        m1  = ( is0(m1)? m0: m1 );                          // Neumann BC
        float A1 = aLUT2d[symidx(r0, regions[i_])];
        h += (2.0f*A1/(cz*cz)) * (m1 - m0);                 // Exchange only
    }

    // top neighbor
    {
        i_  = idx(ix, iy, hclampz(iz+1));
        float3 m2  = make_float3(mx[i_], my[i_], mz[i_]);
        m2  = ( is0(m2)? m0: m2 );
        float A2 = aLUT2d[symidx(r0, regions[i_])];
        h += (2.0f*A2/(cz*cz)) * (m2 - m0);
    }
}

// write back, result is H + Hdmi + Hex
```

```
    float invMs = inv_Msat(Ms_, Ms_mul, I);
    Hx[I] += h.x*invMs;
    Hy[I] += h.y*invMs;
    Hz[I] += h.z*invMs;
}                           x
```